Introspecting the Metal Oxides and Metal Free Catalysts for Electrocatalytic Methanol Oxidation Reaction

THESIS

Submitted in partial fulfillment
of the requirements for the degree of
DOCTOR OF PHILOSOPHY

By

Meenu P C
ID No. **2018PHXF0410H**

Under the supervision of

Prof. Sounak Roy

&

Under the Co-supervision of

Prof. Chanchal Chakraborty

Prof. Santanu Prasad Datta

BIRLA INSTITUTE OF TECHNOLOGY AND SCIENCE, PILANI
2024

Declaration of Authorship

I hereby declare that the matter embodied in this thesis entitled **"Introspecting the Metal Oxides and Metal Free Catalysts for Electrocatalytic Methanol Oxidation Reaction"** is the result of investigations carried out by me in the Materials Chemistry Lab, BITS-Pilani, Hyderabad Campus, India, under the supervision of Prof. Sounak Roy and co-supervision of Prof. Chanchal Chakraborty and Prof. Santanu Prasad Datta.

In keeping with the general practice of reporting scientific observations, due acknowledgement has been made whenever the work described is based on the findings of other investigators. Any omission which might have occurred by oversight or error in judgement is regretted.

Signed: 

Date: 09-07-2024

BIRLA INSTITUTE OF TECHNOLOGY AND SCIENCE, PILANI

CERTIFICATE

This is to certify that the thesis entitled, "**Introspecting the Metal Oxides and Metal Free Catalysts for Electrocatalytic Methanol Oxidation Reaction**" submitted by **Meenu P C**, ID No. **2018PHXF0410H** for the award of Ph.D. of the institute embodies original work done by her under my supervision.

Sounak Roy

Supervisor
Prof. SOUNAK ROY
Professor,
Department of Chemistry,
BITS-Pilani, Hyderabad Campus
Date: 09-07-2024

Chanchal Chakraborty

Co-Supervisor
Prof. CHANCHAL CHAKRABORTY
Asst. Professor,
Department of Chemistry
BITS-Pilani Hyderabad Campus
Date: 09-07-2024

Co-Supervisor
Prof. SANTANU PRASAD DATTA
Assoc. Professor,
Department of Mechanical Engineering
BITS-Pilani Hyderabad Campus
Date: 09-07-2024

Dedicated to My Family

Acknowledgements

I find great pleasure in treasuring the chance to uncover the history of a journey that has spanned a long time, encompassing the efforts of many individuals. Among them, some have been by my side from the very start, while others joined me at different junctures. Their unwavering kindness, affection, and support have played a significant role in molding me into the person I am today. I wish to extend my heartfelt thanks to all those who played a crucial role in shaping this thesis.

I consider fortunate indeed to have had the opportunity to pursue my Ph.D. degree under Prof. Sounak Roy, Professor and Head, Department of Chemistry, BITS Pilani Hyderabad campus. His excellent guidance, support and encouragement during this work were immense. I specially acknowledge him for his fruitful advice, continuous monitoring kindness and affection throughout the course of my work.

I would like to express my earnest vote of thanks to one and all who have helped me throughout my Ph.D. tenure with their valuable time, suggestions, and encouragement. Thanks to my co-supervisors Prof. Chanchal Chakraborty, and Prof. Santanu Prasad Datta. My sincere gratitude to Prof. Satyapaul A Singh and Prof. Srikanta Dinda who helped me with the journal preparation and review. My greatfulness to my doctoral advisory committee member, Prof. N Rajesh and Prof. Himanshu Aggarwal for their support and encouragement during this entire period with their valuable comments and ideas. My sincere thanks to Prof. Pralok K Samanta for helping me with the theoretical studies. I would like to thank former DRC convener, Prof. Durba Roy, and current DRC, Prof. Tanmay Chatterjee for their valuable advice. I am thankful to the former HOD, Prof. Manab Chakravarty and entire chemistry department faculty member for their significant interaction and discussion throughout my journey. I acknowledge the vice-chancellor of BITS-Pilani, Prof. Ram Gopal Rao, Prof. G. Sundar, ex-director of the BITS-Pilani Hyderabad Campus, and director Prof. Soumyo Mukherji for allowing me to pursue and complete my Doctoral research work. I would also like to express my sincere gratitude to BITS-Pilani, Hyderabad Campus, for sponsoring the institution fellowship.

My journey in the realm of electrochemistry research would not be complete without acknowledging the indispensable support and guidance of Prof. S M A Shibli, Professor, Department of Chemistry, University of Kerala. He provided me with the initial stepping stone and ignited my passion for research in this field. My sincere thanks to Prof. T S Anirudhan for nurturing me in the field of research during my master's time. I extend my gratitude to the other faculties at the Department of Chemistry, University of Kerala who nourished me to be a better researcher.

I am truly grateful to my senior lab mates Dr. Swapna Challagulla and Dr. Soumitra Payra for their continuous support, valuable suggestions, comments, and criticism. I am also

indebted to my colleague Ms. Reeshma Rameshan for her encouragement and understanding throughout this journey. I wish to extend my heartfelt gratitude to my fellow colleagues in the lab, Bandarupalli Krishna, Saraswati Roy, Aathira B, Arpan Gosh, Ankur Chanda, and Debashish Halder for their constant words of encouragement and steadfast support. Also I must thank Dr. Arun Raj, Dr. Karuna Anna Sajeev, Akhil Chandran P, Paromita Pattnayak, Amita Ann Mathews, Yogesh, Anup K Pradhan, Dhanya V, Dr.Rishika Aggarwal, Dr. Sayantan Halder and Dr. Dinabandhu Patra for their kind support. My sincere thanks to Resmi V L, Akhil S Nair, Haridev, and Krishnendu for helping me with Latex software. I would want to express my gratitude to the research scholars in the chemistry department as well as other departments for their time and effort in making my time on campus a pleasant one. I also appreciate the extended co-operation of the chemistry department, non-teaching staff, and technicians of the central analytical laboratory during my research work.

I have no words to express about my parents Dr. Preetha Rajam R V and Mr. P Chandrasekharan Nair whose unwavering love, encouragement, and unwavering support have been the cornerstone and inspiration throughout my academic journey. I am deeply grateful to my brother Mr. Manu P C and sister-in-law Priyanka Baby for their patience, love, mental support encouragement and motivating presence. I thank to my niece Alyssa and nephew Gerrad for their fun to make smile in our faces even at our tough time. I wish to extend my deepest gratitude to my husband, Dr. Ameen Sha Mashood, for his unwavering love, encouragement, and constant support during the highs and lows of my challenging Ph.D. pursuit. His invaluable assistance in my scientific endeavors, particularly in solving intricate problems in the field of electrochemistry, has been indispensable. I am also indebted to my father-in-law Mashood K and mother-in-law, Late Raheela A, for their unconditional support and desire.

Last but not least I thank myself for successfully completing this journey facing all the chaos, ups and downs that happened throughout this period. My heartfelt gratitude and deep sense of appreciation to all of the people mentioned above, as well as others whose names I may have missed out inadvertently.

Meenu P C

Abstract

The first introductory chapter deals with the idea of methanol economy and the role of electrocatalytic MOR in methanol economy. The technological aspects of MOR in DMFC and methanol assisted HER is explicitly discussed. The chapter sets the tune with the discussion of various descriptors, such as (i) facile red-ox ability of active metal sites, (ii) electron occupancy in e_g orbital, (iii) metal-oxygen covalency, and (iv) defect engineering and lattice strain in enhancing MOR. The significance of Ni based metal oxide in implementing these descriptors for alkaline MOR with the formation of Ni-OOH has been comprehensively mentioned in this chapter.

The first two working chapter (2A and 2B) offers a uniquely comprehensive exploration of structural and surface properties of RP oxides toward methanol oxidation reactions. Solution combustion-synthesized $La_{2-x}Sr_xNiO_{4+\delta}$ (x = 0 – 0.8) Ruddlesden–Popper oxides is explored by optimal doping with bivalent Sr^{2+} in the A site to enable the tetragonal distortion and oxidation of Ni^{2+} to Ni^{3+} which ultimately resulted in enhanced covalent hybridization of Ni 3d – O 2p with a closer proximity of the O 2p band to the Fermi level. This chapter propose a detailed mechanism over $La_{1.4}Sr_{0.6}NiO_{4+\delta}$ considering a lattice oxygen-mediated methanol oxidation reaction, owing to Fermi-level "pinning" at the top of the O 2p band, which facilitated lattice oxygen atoms prone to oxidation. The role of active species of Ni–OOH with the help of lattice oxygen atoms and oxygen vacancies in $La_{1.4}Sr_{0.6}NiO_{4+\delta}$ is studied during the methanol oxidation reaction.

In subsequent chapter 2B, $La_{2-x}Sr_xNi_{1-y}(Mn/Fe/Co)_yO_{4+\delta}$ is explored for enhanced MOR. The optimised $La_{1.4}Sr_{0.6}NiO_{4+\delta}$ is further doped with Co^{2+} in the B site, to enhance the Ni^{3+} with t_{2g}^6 $d_{x^2-y^2}^1$configuration exhibiting a tetragonal distortion with compression in axial bonds and elongation in equatorial bonds. This structural modification fostered an augmented overlap of d_z^2 orbitals with axial O 2p orbitals, leading to a heightened density of states at the Fermi level. Consequently, this facilitated not only elevated electrical conductivity for MOR but also a noteworthy reduction in the charge transfer resistance.

Chapter 3A and 3B is devoted for the exploration of reducible CeO_2 support with doping of Ni, Sr and Zr, ($Ce_{1-x-y}Ni_xSr_yO_{2-\delta}$ and $Ce_{1-x-y}Zr_xNi_yO_{2-\delta}$) for MOR. In Chapter 3A, with the help of structural and surface studies, reducible CeO_2 support in Ni and Sr co-doped, $Ce_{1-x-y}Ni_xSr_yO_{2-\delta}$ solid solution facilitate Ni^{2+} to Ni^{3+} oxidation as well as evolution of lattice oxygen during MOR. The successful synthesis of $Ce_{1-x-y}Ni_xSr_yO_{2-\delta}$ helped in formation of Ni - OOH surface intermediates with Ni in 3+ oxidation state, where the evolved lattice oxygen eased the CO oxidation process in order to bring out the better CO-tolerant methanol oxidation activity. In chapter 3B, the highly reducible CeO_2–ZrO_2 support in the $Ce_{1-x-y}Zr_xNi_yO_{2-\delta}$ solid solution effectively facilitates the Ni^{2+} to Ni^{3+} oxidation process and the evolution of

lattice oxygen during methanol oxidation. Both the study shows the unique importance of the electronic interactions between the active site and the support and involvement of lattice oxygen in the methanol oxidation reaction.

The role of lattice strain in molybdates by doping of Co^{2+} in $NiMoO_4$ is described in chapter 4. The co-existence of two phases α and β along with the creation of strain resulted in structural modification by weakening the bonds between Ni - O and Mo - O in the crystal lattice and activation of lattice oxygen, creating vacancy. The result of optimizing the coordination environment is the formation of Ni-OOH which is a beneficial diffusion path between the catalyst surface and electrolyte, and improved conductivity, favourable for improving MOR performance which was corroborated with DFT studies.

The last working chapter discuss the catalytic efficacy and improved mass activity of morphologically engineered metal-free graphitic carbon nitride towards MOR. The quantum dots show higher methanol oxidation activity due to its abundant edges in nano morphology and maximum atomic percentages of active site of pyridinic N with the thorough probing of electronic properties. The 0D g-C_3N_4 when supported on conducting polyaniline, not only shows higher electrocatalytic methanol oxidation activity but also demonstrates excellent CO tolerance to be a suitable and applicable metal-free anode catalyst in DMFC. The electrostatic interaction between 0D g-C_3N_4 and conducting PANI fibres may have improved the electrical conductivity and methanol adsorption of CNQD-PANI electrocatalyst and also played a role in oxidizing the adsorbed CO to upsurge the CO tolerance.

An overall conclusion of the entire work with a future outlook is portrayed in chapter 6.

Contents

List of Tables

List of Figures

List of Abbreviations

MT	**M**etric **T**onn
eV	**E**lectron volt
keV	**k**ilo electron volt
mV	**M**illivolt
V	**V**olts
mA	**M**illiampere
A	**A**mpere
nm	**N**anometre
μm	**M**icrometre
cm	**C**entimetre
m	**M**etre
km	**K**ilometre
μL	**M**icroliter
mL	**M**illiliter
L	**L**iter
μg	**M**icrogram
mg	**M**illigram
g	**G**ram
T	**T**emperature
°C	**D**egree centigrade
K	**K**elvin
μmol	**M**icromole
mmol	**M**illimole
mol	**M**ole
s	**S**econds

min	**M**inutes
h	**H**ours
Å	**Å**ngstroms
deg	**D**egree
mM	**M**illimolar
M	**M**olar
W	**W**att
KWh	**K**ilo Watt hour
%	**P**ercentage
ppb	**P**arts per billion
ppm	**P**arts per million
R	**R**eflectance
KM	**K**ubelka Munk Factor
XRD	**X**-**R**ay **D**iffraction
ED-XRF	**E**nergy-**D**ispersive **X**-**R**ay **F**luorescence
FE-SEM	**F**ield **E**mission **S**canning **E**lectron **M**icroscope
EDS	**E**nergy **D**ispersive **X**-**R**ay **S**pectroscopy
HR-TEM	**H**igh **R**esolution **T**ransmission **E**lectron **M**icroscope
SAED	**S**elected **A**rea **E**lectron **D**iffraction
UV-Vis	**U**ltraviolet-**V**isible **S**pectroscopy
BJH	**B**arret- **J**oyner **H**alenda
DME	**D**i **M**ethyl **E**ther
FTIR	**F**ourier **T**ransform **I**nfrared **S**pectroscopy
NMR	**N**uclear **M**agnetic **R**esonance
PL	**P**hotoluminescence
GC	**G**as **C**hromatography
CV	**C**yclic **V**oltammetry
LSV	**L**inear **S**weep **V**oltammetry
CA	**C**hrono **A**mperometry
ECSA	**E**lectrochemical **S**urface **A**rea
FE	**F**araday **E**fficiency
DFT	**D**ensity **F**unctional **T**heory
DOS	**D**ensity **O**f **S**tates

XANES	**X**-ray **A**bsorption **N**ear-edge **S**tructures
H_2-TPR	**H_2-T**emperature **P**rogrammed **R**eduction
GCE	**G**lassy **C**arbon **E**lectrode
RP	**R**uddelsden **P**opper
RHE	**R**eversible **H**ydrogen **E**lectrode
EIS	**E**lectrical **I**mpedance **S**pectroscopy
I	**C**urrent
j/J	**C**urrent **D**ensity
DMFC	**D**irect **M**ethanol **F**uel **C**ell
CNNRS	**g**-C_3N_4 **N**ano **S**heets
CNNR	**g**-C_3N_4 **N**ano **R**ods
CNQD	**g**-C_3N_4 **Q**uantum **D**ots
OER	**O**xygen **E**voulution **R**eaction
ORR	**O**xygen **R**eduction **R**eaction
HER	**H**ydrogen **E**volution **R**eaction
PANI	**P**olyaniline
XAFS	**X**ray **A**bsorption **F**ine **S**tructure
XANES	**X**-ray **A**bsorption **N**ear - **E**dge **S**tructures
MOR	**M**ethanol **O**xyidation **R**eaction
IPCC	**I**ntergovernmental **P**ane on **C**limate **C**hange
IEA	**I**nternational **E**nergy **A**gency
GGA	**G**eneralized **G**radient **A**pproximation
PBE	**P**urdew **B**urke and **E**rnzerhof
SAED	**S**elected **A**rea **E**lectron **D**iffraction
MO	**M**etal **O**xide
PEM	**P**roton **E**xchange **M**embrane
MEA	**M**embrane **E**lectrode **A**ssembly

Chapter 1

Introduction

The global population's escalating reliance on energy, driven by factors such as urbanization, rising living standards, and the growing importance of technology, is projected to result in a substantial increase in energy demand. Projections suggest that by 2050, global energy demand will soar to approximately 660 quadrillion British thermal units, marking an annual growth rate of 15% [1]. The relentless demand for energy has led to a significant depletion of fossil fuel reserves. Furthermore, the uncontrolled combustion of fossil fuels has led to the accumulation of greenhouse gases such as CO_2 in the atmosphere. Given the limited availability of fossil fuels and the environmental consequences of their use, there is a pressing need for innovative technologies that provide clean and sustainable energy alternatives to meet the ever-growing energy demands of human society. The primary objective of human civilization in the 21^{st} century is to strike a balance between modern living and environmental harmony by exploring alternative energy sources.

An affordable and practical alternative to traditional fuels is methanol, which contains more H_2 by mass per litre than pure liquid H_2 (98.8 g of H_2 per litre of methanol at room temperature compared to 70.8 g in liquid H_2 at 253 °C) [2]. This characteristic suggests that methanol can serve as a safe carrier fuel for H_2. Methanol boasts a reported octane number of 108.7 compared to gasoline's 91, indicating that the methanol-air mixture can be compressed further before ignition, thereby enhancing engine efficiency and ensuring cleaner emissions. Methanol can leverage existing infrastructure used for gas and diesel, reducing infrastructure and dispensing costs without emitting soot or smoke upon combustion. These unique attributes provide a solution to the pressing issues of depleting fossil fuel reserves and pave the way for a

feasible "Methanol Economy." The distinct qualities of methanol, including its lower flammability risk, high octane fuel with favorable combustion characteristics, and high energy density of approximately 4820 Wh/L, drive the emergence of the methanol economy as a promising future prospect even compared to H_2 [2, 3]. Being a liquid at ambient conditions, methanol can be handled, stored, and transported with ease, utilizing existing infrastructure supporting global methanol trade. In the methanol economy, methanol and dimethyl ether act as substitutes for fossil fuels in the production of fuels, chemicals, and various other raw materials. The concept of a methanol-based economy encompasses economic and technological considerations related to the production, distribution, and utilization of methanol as an energy carrier or fuel across diverse applications. Consequently, the accelerated adoption of methanol in the energy sector has already resulted accounting for 40% of total production. By 2015, emerging energy applications had utilized 75 million metric tonnes of methanol. Worldwide, approximately 200,000 tonnes of methanol are consumed daily, either as a chemical feedstock or as a transportation fuel. Figure 1.1 illustrates global methanol consumption [4].

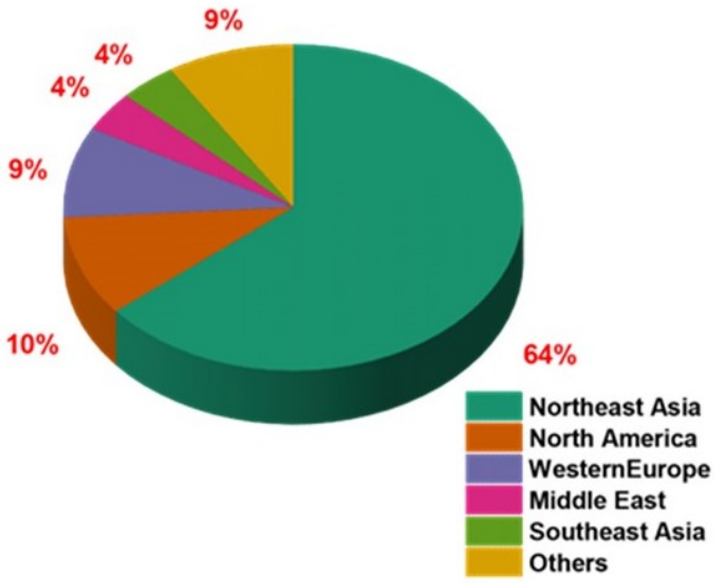

FIGURE 1.1: Global consumption of methanol

The production of methanol primarily relies on syngas in the following manner:

$$CO + 2H_2 \rightarrow CH_3OH \ (\Delta H = -90.84 \text{ kJ/mol}) \tag{1.1}$$

The particular synthesis process is exothermic and occurs at low temperatures and high pressures, primarily facilitated by a copper-based catalyst [5]. The catalysts operate at temperatures

aroun 230 °C and pressures of 50–100 atm, as established by Imperial Chemical Industries (ICI). Another approach involves producing methanol from natural gas (CH_4) directly, leveraging its abundance and ease of extraction. However, this method faces challenges due to methane's chemical properties, including the difficulty of activating the C–H bond [6]. Researchers have also explored utilizing CO_2 for methanol production using suitable catalysts [7–9]. Efforts to reduce the temperature and pressure requirements for methanol synthesis have led to innovative pathways, such as producing methanol via methyl formate and successive hydrogenolysis. This technique involves carbonylation in the liquid phase using sodium or potassium methoxide as a homogeneous catalyst [10].

1.1 Methanol Oxidation Reaction: A Crucial Reaction of Methanol Economy

Methanol oxidation Reaction (MOR) is a vital reaction of great technological relevance in view of its potential use as a fuel in methanol economy. Its importance can be validated by implementing its potential aspect in Direct Methanol Fuel Cell and Methanol Assisted Hydrogen Evolution Reaction.

1.1.1 Direct Methanol Fuel Cell (DMFC)

The idea of methanol economy is viable with the concept of DMFC to hunt for a clean, effective energy source. The best thing is that it can utilise all by-products and even CO_2 can be recycled back to methanol again. DMFC belongs to the subcategory of proton exchange membrane (PEM) fuel cells, where methanol production is harnessed to generate electricity independently of hydrogen reliance. Utilizing DMFC, which leverages affordable methanol over expensive hydrogen, can lead to a substantial reduction in carbon emissions. A DMFC has the potential to offer 2–3 times the energy density of the Li-ion batteries in the future [11, 12]. Figure 1.2 shows a schematic of DMFC components.

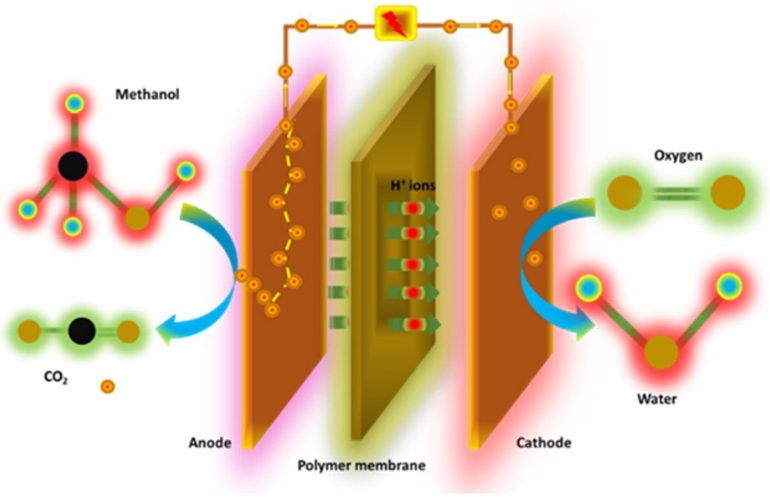

FIGURE 1.2: Schematic diagram showing DMFC components

The complete reaction in a DMFC involves a methanol/water mixture directly fed at the anode compartment, where it undergoes direct oxidation to carbon dioxide. Protons generated at the anode migrate through the polymer electrolyte to the cathode, where they react with oxygen undergoing reduction to produce water. Electrons flow through an external circuit to the cathode, producing electricity, while protons migrate through the PEM to reach the cathode. Conversely, oxygen from the surrounding air undergoes reduction at the cathode, resulting in the production of water and heat through the reaction of oxygen with protons and electrons. This process is referred to as the oxygen reduction reaction. Water vapour at the cathode leaves the cell mainly by diffusion and natural convection. The released heat is dissipated to the methanol solution on the anode side and to the ambient air on the cathode side. MOR in the anodic compartment can be carried out both in acidic and alkaline medium.

Acidic medium

$$\text{Anode reaction :} \quad CH_3OH + H_2O \rightarrow CO_2 + 6H^+ + 6e^- \;\; E_0 = 0.016 \text{ V vs RHE} \tag{1.2}$$

$$\text{Cathode reaction :} \quad \frac{3}{2}O_2 + 6H^+ + 6e^- \rightarrow 3H_2O \;\; E_0 = 1.229 \text{ V vs RHE} \tag{1.3}$$

Alkaline medium

$$\text{Anode reaction :} \quad CH_3OH + OH^- \rightarrow CO_2 + 6e^- + 5H_2O \;\; E_0 = 0.016 \text{ V vs RHE} \tag{1.4}$$

$$\text{Cathode reaction :} \quad \frac{3}{2}O_2 + 6e^- + 3H_2O \rightarrow 6OH^- \;\; E_0 = 1.229 \text{ V vs RHE} \tag{1.5}$$

$$\text{Overall reaction :} \quad CH_3OH + \frac{3}{2}O_2 \rightarrow CO_2 + 3H_2O \tag{1.6}$$

MOR in the anodic compartment is the bottle neck reaction of DMFC with the efficient utilization of methanol.

1.1.2 Methanol Assisted Hydrogen Evolution Reaction

Recently, methanol assisted HER has been regarded as a practical approach to the generation of hydrogen [13–15]. This strategy is similar to the electrochemical water electrolysis, while the methanol addition in electrolytes is the only major difference. This technique has a number of benefits, such as enhanced HER, simplified methanol storage and transportation, less dependency on fossil fuels, and the potential cogeneration of valuable formate. During methanol assisted HER, the hydroxyl groups of methanol lose electrons which would oxidize it completely or partially. Typically, methanol oxidizes over electrodes in fuel cells to produce hydrogen and CO_2 greenhouse gas [16–18]. In this reaction, methanol can be utilized in a selective way for the synthesis of formate or formic acid avoiding the formation of CO_2. This way of utilization of methanol for selective synthesis of specific chemicals, such as formate or formic acid (HCOOH) called selective electrochemical methanol oxidation reaction [19]. On combining selective electrochemical MOR with hydrogen can boost the efficiency of H_2 generation at the cathode by reducing its overpotential while producing products with high added values at the anode for CO_2 replacement as shown in Figure 1.3.

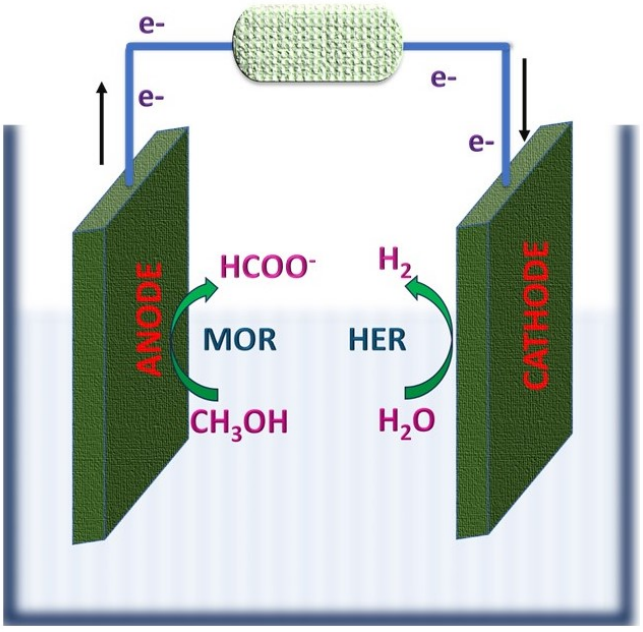

FIGURE 1.3: Schematic diagram showing methanol assisted HER

$$\text{Anode} : CH_3OH + 4OH^- \rightarrow HCOOH + H_2O + 4e^- \quad E_0 = 0.016 \text{ V vs RHE} \tag{1.7}$$

$$\text{Cathode} : 4e^- + H_2O_{(l)} \rightarrow 4OH^-_{(aq)} + 2H_{2(g)} \quad E_0 = 0 \text{ V vs RHE} \tag{1.8}$$

1.2 Fundamentals of MOR

MOR appears to be the bottleneck reaction in DMFC, methanol-assisted HER, and methanol upgradation, in both acidic and alkaline conditions [20–22]. Researchers have explored MOR as a substitutionary pathway to expedite anodic oxidation, aiming to overcome sluggish kinetics and substantial overpotential of OER [23]. The electrocatalytic mechanism for MOR in DMFC involves a six - electron transfer process, proceeding via either a CO pathway or a CO - free pathway, depending on the adsorbates and intermediates formed during the reaction. MOR can occur in both acidic and alkaline mediums, with the latter being preferred due to faster kinetics and reduced risks of corrosive electrode materials. We have discussed the stoichiometric anodic reactions in acidic and alkaline medium in the previous section. In alkaline MOR, CH_3OH oxidation reaction occurs with the help of OH^- ions. The conversion of CO to CO_2 in alkaline media is facilitated by OH^- groups, while in acidic media it is provided by water dissociation. The advantage of alkaline medium over acidic media lies in bisulfate and perchlorate ions inhibiting CH_3OH adsorption or replacing adsorbed OH^- ions, due to sluggish kinetic reactions at high potential. MOR in alkaline medium proceeds through either O - H activation or C - H activation mechanisms [20, 24, 25]. Following is the detailed O - H activation mechanism in basic medium where M is the metal:

$$M + CH_3OH \overset{OH^-}{\rightarrow} M(CH_3OH)_{ads} \tag{1.9}$$

$$M(CH_3OH)_{ads} + OH^- \rightarrow M(CH_3O)_{ads} \tag{1.10}$$

$$M(CH_3O)_{ads} + OH^- \rightarrow M(CH_2O)_{ads} \tag{1.11}$$

$$M(CH_2O)_{ads} + OH^- \rightarrow M(CHO)_{ads} \tag{1.12}$$

$$M(CHO)_{ads} + OH^- \rightarrow M(CO)_{ads} \tag{1.13}$$

$$M(CO)_{ads} + 2OH^- \rightarrow M + CO_2 + H_2O \tag{1.14}$$

CO poisoning in MOR

CO_{ad} is found to be the most stable surface adsorbate among all other methanolic fragments in O-H activation pathway as seen in equation 1.13. It is one of the worst catalyst-deactivating processes, especially for platinum group metal catalysts. CO is more easily combined with the Pt catalyst due to its polar molecule character (the adsorption energy of CO is 134 kJ/mol, while H_2 is 87.9 kJ/mol) [26]. This hinders the electrode kinetics, conductivity and mass transfer, further blocking of catalyst-active sites affecting MOR kinetics. The conventional methods to address the CO-poisoning issue of Pt electrocatalysts include alloying Pt with a second metal [27, 28], creating composite structures, engineering surface strain [29], atomic ensemble effect, etc which enhance the activity and durability for MOR . Switching to non noble metal-based catalyst or to alter MOR mechanism to C-H activation is one of the best alternatives to tackle the CO poisoning issue.

In the case of C-H activation, it occurs with the dissociation of methanol into numerous carbonaceous intermediates (COOH, CH_2OH, COH, CHOH, and HOCOH) through the removal of H in each step from C-H after the adsorption of methanol.

$$M + CH_3OH \overset{OH^-}{\rightarrow} M(CH_3OH)_{ads} \tag{1.15}$$

$$M(CH_3OH)_{ads} + OH^- \rightarrow M(CH_2OH)_{ads} \tag{1.16}$$

$$M(CH_2OH)_{ads} + OH^- \rightarrow M(CHOH)_{ads} \tag{1.17}$$

$$M(CHOH)_{ads} + OH^- \rightarrow M(COH)_{ads} \tag{1.18}$$

$$M(COH)_{ads} + OH^- \rightarrow M(HOCOH)_{ads} \tag{1.19}$$

$$M(HOCOH)_{ads} + OH^- \rightarrow M(COOH)_{ads} \tag{1.20}$$

$$M(COOH)_{ads} + OH^- \rightarrow M(CO_2)_{ads} \tag{1.21}$$

$$M(CO_2)_{ads} + OH^- \rightarrow M + CO_2 + H_2O \tag{1.22}$$

Spectroscopic studies revealed that MOR undergoes parallel pathways in which it proceeds via either a CO pathway or a CO - free pathway involving six electrons. Here CO pathway could be considered analogous to O - H activation pathway whereas CO free pathway could be analogous to the C - H activation pathway. In the case of the CO pathway, CO* is formed after

the deprotonation of COH* or CHO* Then CO* combines with a surface hydroxyl OH* and converts to COOH*, which is further oxidized to CO_2. During the process, in acidic medium OH* is formed by water dissociation and OH- is formed in basic medium On the other hand of CO free pathway, instead of directly deprotonating, potential intermediates like CHO*, COH*, or CH_2O* would engage with OH* to create CHOOH*, $C(OH)_2$*, or H_2COOH*, respectively. These doubly-oxygenated species then undergo dehydrogenation to generate CO_2, either through COOH* or CHOO*. In alkaline media, the easier formation of OH* would efficiently remove the adsorbed carbonous species and result in faster kinetics [30].

Due to the complexity of the reaction mechanism and a consequential sluggish kinetics resulting into higher overpotential the choice of catalytic materials becomes crucially critical. Often studies focus in to exploring the mesoporous and conductive catalysts to enhance the materials' durability and charge transfer efficiency. The porosity is another physical property that enhance surface area, but careful control is needed to achieve the optimal pore size, as small pores may hinder mass transport rates despite increasing surface area [31]. Key characteristics required for practical application of catalytic materials include good electrical conductivity, large surface area, strong bonding with the catalyst, mesoporous structure, efficient water handling, corrosion resistance, and easy catalyst recovery. Despite our foundational understanding, catalysts optimized for commercial viability remain elusive. Consequently, recent efforts have been directed towards more sophisticated approaches to comprehend the role of catalysts and make future predictions. In the subsequent sections, we will employ a more nuanced method to grasp the significance of catalysts in MOR.

1.3 Descriptors of MOR as Guidance to Engineering Efficient Electrocatalysts

A catalytic descriptor is a property of a catalyst or the interface between a catalyst and electrolyte that can be easily adjusted and directly linked to the reaction efficacy. It should serve both an explanatory and predictive role, helping to illuminate the activation processes and provide insights into how to enhance the reaction rate. Several researchers studied and reached a global consensus on the catalytic descriptors influencing the OER. The anodic reaction OER being mechanistically similar to MOR in acidic or alkaline condition, for practical purposes the learning can be extracted for understanding the descriptors of MOR as well. The correlation

between catalytic activity and descriptors has proven invaluable for comprehending fundamental aspects of the MOR, guiding future experimental studies, and facilitating high-throughput computational screening of potential catalysts.

Given the severe reaction conditions of MOR in alkaline or acidic environments at elevated potentials, non-noble metal-based oxides are widely recognized as predominant and promising catalytic materials capable of long-term stability and resistance to CO [32]. Among non-noble metals, Ni-based oxides have garnered significant research interest due to their favourable surface oxidation properties, cost-effectiveness, and abundance. The ability to adjust the electronic structure of Ni by varying its oxidation state and creating vacant 3d orbitals renders it particularly suitable for use in MOR under alkaline conditions [33–35]. In the following sections we will discuss the descriptors such as (i) facile red-ox ability of active metal sites of the catalyst, (ii) electron occupancy, (iii) covalency, and (iv) defect engineering and lattice stain of mostly the Ni based catalysts in influencing the MOR efficacy in terms of overpotentials and current densities

1.3.1 Facile Red-Ox Ability of Active Metal sites

For Ni-based catalysts operating in an alkaline environment, the initial stage involves the creation of a layer of $Ni(OH)_2$, which subsequently undergoes conversion into Ni- OOH, featuring nickel in a 3+ oxidation state. This Ni-OOH layer is recognized as the active phase for catalyzing methanol oxidation. Research indicates that the redox couple of Ni^{2+}/Ni^{3+} plays a pivotal role, as the primary Ni– OOH species generated through surface restructuring can effectively modulate the electronic configuration of active sites, thereby facilitating the methanol oxidation reaction [36]. The sequential reactions are outlined below:

$$Ni(OH)_2 + OH^- \rightarrow Ni(OH)_3 + e^- \tag{1.23}$$

$$Ni(OH)_3 \rightarrow NiOOH + H_2O \tag{1.24}$$

$$NiOOH + (CH_3OH)_{ads} \rightarrow (CH_3O^-)_{ads} + Ni(OH)_2 \tag{1.25}$$

$$NiOOH + (CH_3O^-)_{ads} \rightarrow (CH_2O^-)_{ads} + Ni(OH)_2 \tag{1.26}$$

$$NiOOH + (CH_2O^{-)_{ads}} \rightarrow (CHO^-)_{ads} + Ni(OH)_2 \tag{1.27}$$

$$NiOOH + (CO)_{ads} \rightarrow CO_2 + Ni(OH)_2 \tag{1.28}$$

The facile oxidation of Ni^{2+} to Ni^{3+} and the consequent formation of the crucial intermediate species Ni-OOH are recognized as key descriptors of MOR [37, 38]. When Ni^{2+} undergoes oxidation to Ni^{3+}, it generates an accessible charge-transfer orbital, which becomes available for electron transfer processes during methanol oxidation to CO_2. However, the creation of available charge-transfer orbitals near the Fermi energy level poses a fundamental challenge [39]. One potential solution to this challenge could involve substituting Ni^{2+} ions within a reducible support to facilitate the $Ni^{2+} \rightarrow Ni^{3+}$ oxidation process. Furthermore, if the reducible support exhibits oxophilic properties and has a propensity for adsorbing oxygenated species such as -OOH at lower potentials, it could further enhance the oxidation of CO to CO_2. Among the range of low-cost oxides, CeO_2 is of particular interest as a result of its high surface area, significant surface defects, and high oxygen storage capacity (due to facile redox of Ce^{4+}/Ce^{3+} sites) [40–42]. In this context, a sizable number of reports showing excellent promotional and anti-poisoning activities of CeO_2 for MOR are available in the literature [43, 44].

1.3.2 Electron Occupancy

In non - noble metal-based oxide catalysts, especially in perovskites, the active site metal adopts an octahedral geometry. The d orbitals of transition metals in octahedral coordination split into triply degenerate states of t_{2g} and doubly degenerate states of e_g. During electrocatalytic oxidation, the strength of binding with oxygen-containing intermediates, such as -OOH, on catalytically active metal sites is being found to be depended on the electron occupancy in the e_g states. This is because the $e_g$orbitals of surface transition metal ions in metal oxides participate in σ-bonding with surface adsorbates. Oxides with an e_g occupancy that is too low ($e_g < 1$) bind oxygen-containing intermediates too strongly, while oxides with an e_g occupancy that is too high ($e_g > 1$) bind too weakly. Systematic investigations on perovskites demonstrated that the $e_g$occupancy of the 3d electron can serve as an activity descriptor for the OER [45]. Optimal binding with the oxygen-containing intermediates is achieved when the e_g occupancy is close to unity [45–47].

As stated before, when Ni^{2+} is oxidized to Ni^{3+}, an available charge-transfer orbital is formed which is then available for the electron transfer process during methanol oxidization to CO_2. However, it is fundamentally challenging to create available charge-transfer orbitals near the Fermi energy level in traditional $Ni(OH)_2$ due to these six-coordinated Ni atom without subjecting the material to impractical potential. Wang et al. with a non-stochiometric $Ni(OH)_2$

nanoribbon structure having alternating $\frac{4}{6}$-coordinated Ni edge atoms demonstrated that when the coordination number of Ni is reduced to four, electrons can be delocalized near the Fermi energy level which ultimately generates an available charge-transfer orbital to facilitate the six-electron transfer process during MOR [39]. The nano-ribbons of $Ni(OH)_2$ synthesized by the authors possessed four-coordinated Ni atoms with two dangling bonds, and the structure was perceived as an intermediate configuration between an extended octahedron and square planar as shown in Figure 1.4(a). The electron transfer mechanism was shown by the pictorial demonstration in Figure 1.4(b), which corroborated the isosurface charge results (Figure 1.4(c)). Despite the importance of four-coordinated Ni atoms in the establishment of charge-transfer orbital due to delocalization, they showed that this four-coordinated Ni atom must be paired to a neighbouring six-coordinated Ni atom in order to achieve efficient methanol oxidation.

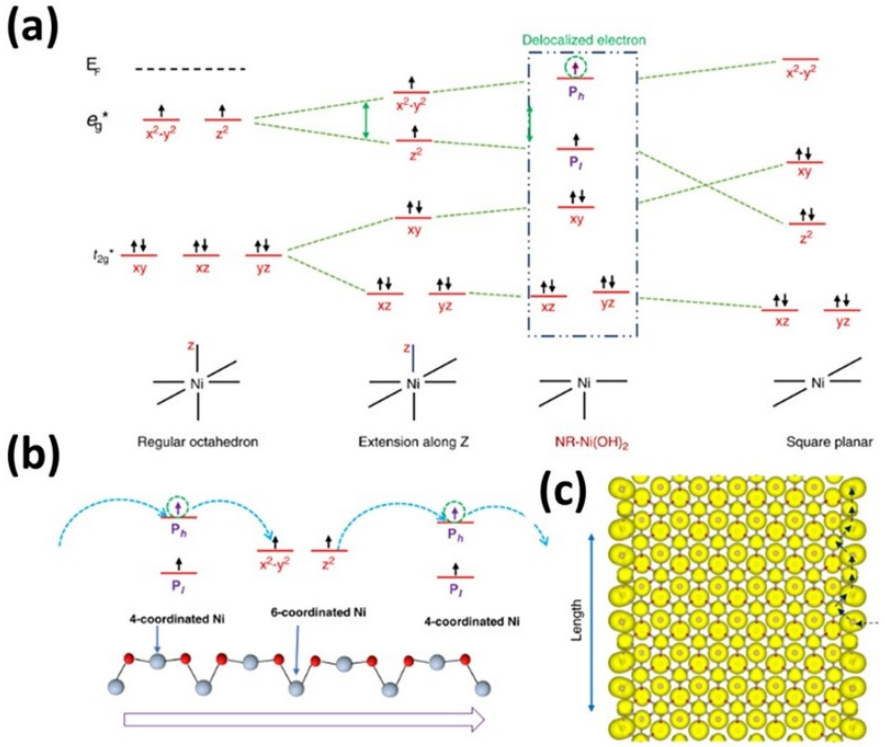

FIGURE 1.4: (a) t_{2g} and e_g electronic orbitals of regular NiO_6 octahedron, NiO_6 octahedron extended along z axis, NR-$Ni(OH)_2$, and NiO_4 square planar (b) charge transfer process on alternating four-six-coordinated arrangement in NR-$Ni(OH)_2$; (c) iso-surface of charge density of NR-$Ni(OH)_2$

Hao et al. have recently explained the importance of the particular descriptor of electron occupancy in e_g orbital in one of their MOR investigations [15]. In a typical NiO, the e_g orbitals are occupied by two spin-up electrons hindering the transfer of electrons into the vacant orbitals of the adsorbed species to form feedback bonds due to the Pauli exclusion principle.

With the oxidation/hydroxylation of the NiO surface, there is only one spin up electron on the NiOOH e_g orbital, which would allow effective electron transfer into the adjacent orbital. They have synthesized Fe_2O_3/NiO heterojunctions with ultrafast solution combustion strategy and demonstrated that the near unity electron occupancy in the e_g of Ni^{3+} provide unique collaborative active sites for the favourable dynamic conversion of methanol to formate and inhibiting further oxidation.

1.3.3 Covalency

The covalency is another crucial feature of the catalyst that is regarded as one of the descriptors to minimize the charge-transfer resistance for any electrocatalytic reaction. The hybridization of the metal d orbitals and O 2p orbitals occur due to the spatial overlap and energetic similarity of the electronic states, which result in σ-bonding states, with largely oxygen character, and σ*-antibonding states with largely metal character. As the Fermi level moves down in energy and closer to the O 2p states, the antibonding states below the Fermi level exhibit greater oxygen character. A stronger covalency of the metal-oxygen bond should shift the insulating character of the material to semi metallic nature and thereby facilitate the MOR activity. The aliovalent substitution in transition metal oxides can result in the redistribution of an electronic density between metal and ligand. The degree of metal–oxygen hybridization is tuned by the choice of transition metal ion and its oxidation state, both of which modify the number of d electrons and the electronegativity of the metal ion [48, 49].

Wang et al. explored coordinated phosphate oxyanions to modify the d-band center of Ni sites and enhance Ni - O covalency, thereby boosting catalytic activity towards MOR. The authors grew different oxyanions (NiOOH-TOx, T= P, S, and Se) on commercial nickel foams to study its effects toward MOR by anionic species [50]. Among the different oxyanions, the coordinated phosphates effectively tailor the d band center of Ni sites and increases Ni-O covalency, promoting the catalytic activity. Dubale et al. developed a surface electronic structure-tuning strategy for the development of a non-noble metal aerogel $Ni_{97}Bi_3$ with unexpected electrocatalytic activity and durability toward MOR [51]. The introduction of atomically dispersed trace amounts of Bi into Ni_xBi_y induced strong electronic effects, which optimally shifted the d-band center of Ni, and thereby enhanced the conductivity of the material.

1.3.4 Defect Engineering and Lattice strain

Defect engineering has been considered as an effective strategy to optimize the number and reactivity of active sites as well as electrical conductivity of catalysts, rendering them to be promising candidates for MOR. Defects cause the crystal lattice's regular arrangement to be disrupted enhancing chemical and physical properties to impact various properties such as conductivity, selectivity, and activity [52–54]. Defect engineering can enhance active sites due to the surface electronic structure modification and optimization of adsorption energy of reaction intermediates. One of the most common defects, vacancies, are those that result from atoms being absent from lattice positions. Oxygen vacancy is widely used in transition metal oxides due to their low formation energy and critically influence the material properties, including the electronic structure and ionic/electronic conductivity. The formation energy of oxygen vacancies increases with the energy difference between the upper edge of the O 2p band and the Fermi level and have a direct influence on the M - O bonds near the oxygen vacancies. Various methods have been used to generate oxygen vacancies in metal oxides during synthesis or post-synthesis treatments which include thermal treatment, reduction processing, cation/anion doping, plasma treatment etc. Among them, both the thermal treatment and reduction processing tune the concentration of oxygen vacancies in oxides by reducing the transitional metal cations to its lower valence state [55–57]. In Ni based oxides for MOR, as Ni - OOH is regarded to be the electrocatalytically active species generated from the oxidation of $Ni(OH)_2$ in alkaline medium, Phan et al. explored on Ni film how structural defect sites on Ni - OOH by the creation of O - vacant sites or - OH vacant sites play active role in the methanol oxidation following formate pathway as pictorially depicted in Figure 1.5(a) [58]. The DFT - calculated energy diagram of vacancy formation established that the generation of O - defect sites is more feasible than the OH^- vacant sites, where the Gibbs free energy (ΔG) in the potential range 1.10 - 1.40 V vs RHE is less than zero for O - defect sites (Figure 1.5(b)). Therefore, the authors created oxygen vacancy in Ni- OOH as shown in Figure 1.5(c) by cycling the catalyst in 1 M KOH at a lower potential of 1.10 – 1.40 V vs RHE, and tried to explore the role of O vacancy following the formate pathway for MOR. They observed a drastic increase in current at potential of 1.32 V vs RHE indicating that MOR occurs in the region of potentials where O - vacancy formation is favourable (Figure 1.5(d)). The onset potentials for methanol oxidation and the Ni- OOH formation perfectly coincided, demonstrating that the methanol oxidation takes place immediately after the electrochemically active O - vacant Ni - OOH species is produced on the surface of the catalyst.

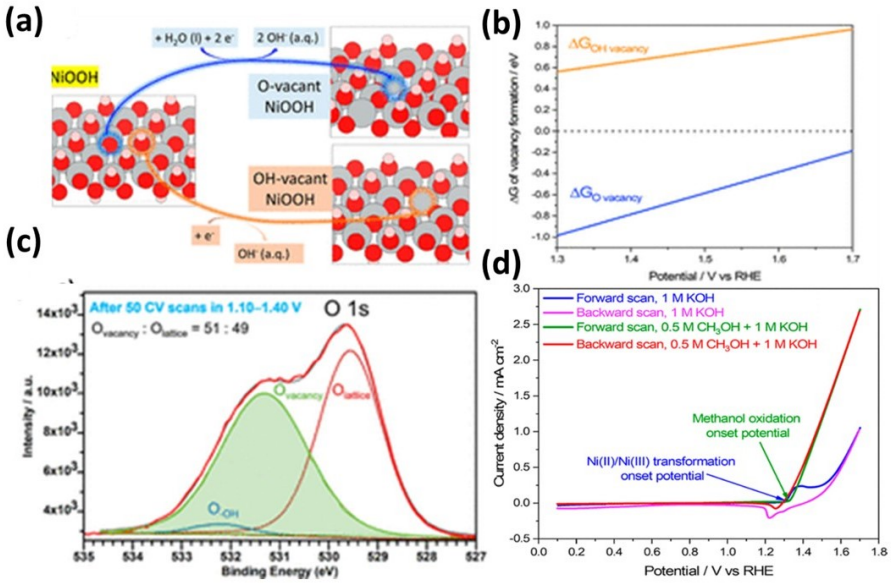

FIGURE 1.5: (a) Schematic depiction of O-vacancy and OH-vacancy formation mechanisms (b) the energy diagram of vacancy formation (c) Deconvoluted O 1s spectra of the Ni film after 50 CV scans between 1.10 - 1.40 V (d) CVs for the Ni film in the absence and presence of 0.5 M CH3OH in 1 M KOH solution at 4 mV s^{-1}

Yang et al. studied the influence of oxygen vacancy in ultra - thin NiO nanosheets which enhanced the electron transport properties of the catalyst [59]. The difference in the annealing time enhanced the oxygen vacancy of NiO. Oxygen vacancy rich NiO exhibited an activity 2.3 times higher than the pristine material. The heightened activity can be attributed to the existence of an oxygen vacancy, generating a novel defect level that acts as a platform for electronic transitions from the valence band to the conduction band (Figure 1.6(a-d)). Boron doped $NiCo_2O_4$ enhanced the electrocatalytic MOR activity and stability of the electrocatalyst by creating oxygen vacancies and reducing the binding strength of intermediate species as reported by Naveen kumar et al. [56]. On replacing Co with B, oxygen vacancies were created in the system that acted as the active sites for methanol adsorption. Moreover, the substitution of B increased the adsorption energy of methanol and also decreased the adsorption energy of the product formate, which further facilitated the oxidation reaction. The authors explored various positions to generate the oxygen vacancies, and the optimal energy configuration indicated a preference for oxygen vacancies to be in proximity to the dopant B. Huang et al. explored cerium oxide supported CoFe - N co-doped carbon nanotubes with abundant oxygen vacancies for MOR [60]. CeO_2 can improve reactants surface adsorption and promote electron transfer behaviour because under oxygen-deficient conditions. CeO_2/CoFe -NCNTs - 2 showed significant catalytic activity for the electrocatalytic methanol oxidation in alkaline electrolytes, achieving a current

density of 281.40 mA cm^{-2} at 1.0 V (vs. Ag/AgCl).

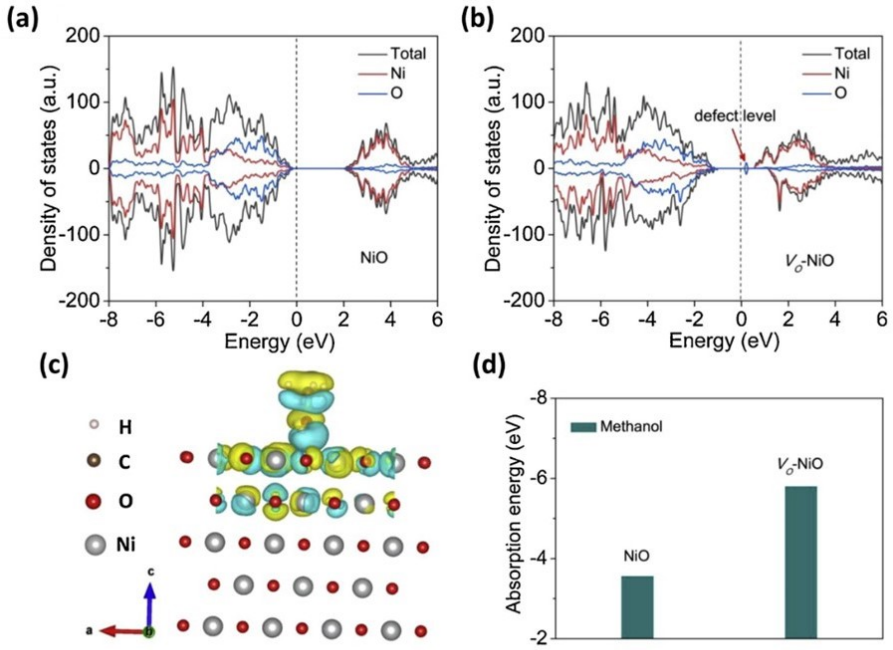

FIGURE 1.6: Calculated DOS of NiO samples without (a) and with (b) oxygen vacancy. (c) Illustration of the adsorption of methanol molecules onto the surface of V_O-NiO sample and the deformation charge density of NiO with oxygen vacancy. (d) Adsorption energy of methanol molecules on the NiO and V_O-NiO samples

Lattice stain is yet another defect that can generate active sites and weaken the adsorption strength of intermediate species, enhancing CO endurance ability and thus contributing to superior MOR performance. Advances in strain engineering lies in their ability to fine-tune complicated catalytic reactions, where minute modifications to surface characteristics and electrical structure might drastically alter desired reaction products' activity and selectivity. The strain effect is aroused by the change of atom-atom bond length or by the induced lattice mismatch [61–63]. Modification of oxide electronic structure by strain can alter oxygen vacancy formation and migration energetics of intermediates and products. Aliovalent metal doping is found to be an efficient strategy to disrupt the symmetric charge distribution around the active metal and induce the lattice strain which further creates vacancy [64]. Moreover, it is also observed that strain engineering minimizes the CO position effect during the MOR by accelerating the reaction CO*→COOH* [64, 65].

1.4 Objectives and Scope of the work

Understanding MOR mechanism is the prerequisite for the rational design of an efficient catalyst to implement in DMFC and methanol assisted HER technology. In the previous section we have summarised the mechanism and different descriptors to improve MOR mechanism via heterogeneous transition metal-based catalysts. The critical analysis of the descriptors can characterize the catalyst's structure-activity relationship by using surface electronic structure. With unremitting efforts, five main descriptors have been identified and put out, which include facile red-ox ability of active metal sites, e_g orbital occupancy, metal-oxygen covalency, defect engineering and lattice stain. Therefore, there remains a significant scope to systematically and thoroughly study the descriptors in Ni based metal oxides for ameliorating the state of the art of MOR.

In Chapter 2A of this thesis, we have systematically enhanced Ni-oxidation states by doping Sr^{2+} in A site, and have probed the MOR mechanism over single-phase $La_{2-x}Sr_xNiO_{4+\delta}$. Aliovalent doping at the A site with rare-earth cations like Sr^{2+} with the molecular formula of has oxidized Ni^{2+} to a higher valency to Ni^{3+} to attain the charge neutrality with a lower electron occupancy with a configuration of $t_{2g}^6 d_z^2$, and also created an elongation along the z-axis. We have also demonstrated that the optimum substitution of Sr^{2+} in $La_{2-x}Sr_xNiO_{4+\delta}$ can enhance the catalytic activity by modifying the extent of Ni - O covalency and electronic conductivity. The optimal aliovalent doping facilitated the extent of overlap of the t_{2g} and e_g orbitals of Ni along with O 2p orbitals, resulting in semi metallic feature of $La_{1.4}Sr_{0.6}NiO_{4+\delta}$. In Chapter 2B, we synthesised $La_{1.4}Sr_{0.6}Ni_{0.9}(Mn/Fe/Co)_{0.1}O_{4+\delta}$ by doping Co, Mn and Fe in B site. With optimal doping of Sr^{2+} in the A site and Co^{2+} in the B site, Ni^{3+} with $t_{2g}^6\ d_{x^2-y^2}^1$ configuration in $La_{1.4}Sr_{0.6}Ni_{0.9}Co_{0.1}O_{4+\delta}$ exhibited a tetragonal distortion with compression in axial bonds and elongation in equatorial bonds. These structural modifications in both studies demonstrated enhanced MOR activity compared to their pristine states.

In Chapter 3A, we doped Ni^{2+} in the fluorite CeO_2 to create higher reducibility in the catalyst as well as oxygen vacancies in CeO_2. This study exhibited with the help of structural and surface probes that the reducible CeO_2 support in Ni and Sr co-doped $Ce_{1-x-y}Ni_xSr_yO_{2-\delta}$ solid-solution can easily facilitate the $Ni^{2+} \rightarrow Ni^{3+}$ oxidation and also release the lattice oxygen during the methanol oxidation reaction. While the Ni^{3+} species facilitated the formation of –OOH surface intermediates, the evolved lattice oxygen facilitated the CO oxidation process, enhancing the CO-tolerant methanol oxidation activity of $Ce_{1-x-y}Ni_xSr_yO_{2-\delta}$. The electrocatalytic activity for

MOR of $Ce_{0.9}Ni_{0.05}Sr_{0.05}O_{2-\delta}$ exhibited a 50% increase compared to pristine CeO_2. In the positive potential of MOR, the Ce^{4+} in CeO_2 was reduced accompanied by parallel oxidation reactions of lattice oxygen evolution ($O_{2-} \rightarrow \frac{1}{2}\ O_2 + 2e^-$) in pristine CeO_2 and $Ni^{2+} \rightarrow Ni^{3+}$ oxidation in Ni-doped materials. A similar idea was extended in chapter 3B of reducible $Ce_{1-x-y}Zr_xNi_yO_{2-\delta}$ solid solution. The highly reducible CeO_2–ZrO_2 support in the $Ce_{1-x-y}Zr_xNi_yO_{2-\delta}$ solid solution effectively facilitated the $Ni^{2+} \rightarrow Ni^{3+}$ oxidation process and the evolution of lattice oxygen during methanol oxidation, resulting in improved CO tolerance and enhanced methanol oxidation activity in $Ce_{1-x-y}Zr_xNi_yO_{2-\delta}$ catalysts.

In chapter 4, another descriptor micro-strain was analysed in pristine $NiMoO_4$ and the Co-doped $Ni_{1-x}Co_xMoO_4$ using diffraction data and HR-TEM micrographs. The results exhibited a notable development of strain in optimally doped mixed-phase $Ni_{0.7}Co_{0.3}MoO_4$ material. Additionally, the presence of Ni^{3+} ions, oxygen vacancies, and ECSA was most pronounced in the specific doped molybdate. This combination resulted in superior electrocatalytic methanol oxidation activity over $Ni_{0.7}Co_{0.3}MoO_4$. Furthermore, the electrocatalytic oxidation of methanol over $Ni_{0.7}Co_{0.3}MoO_4$ yielded the value-added product of formic acid and demonstrated a significant enhancement in methanol oxidation rate reinforced by hydrogen evolution reaction performance.

Chapter 5 discusses a set of completely metal free catalysts. The 2D nano-sheets, 1D nano-rods, and 0D quantum dots of graphitic g C_3N_4 were studied for MOR, and among the three different dimensional g C_3N_4 materials, the quantum dots showed higher methanol oxidation activity due to its abundant edges in nano morphology and maximum atomic percentages of active site of pyridinic N. The 0D g C_3N_4 when supported on conducting polyaniline, not only showed higher electrocatalytic methanol oxidation activity than the commercial Pt/C but also demonstrated excellent CO tolerance to be a suitable and applicable metal-free anode catalyst in direct methanol fuel cell applications.

In the final chapter the complete work has been summarised and a future outlook has been discussed.

Chapter 2A

Electro-Oxidation Reaction of Methanol over $La_{2-x}Sr_xNiO_{4+\delta}$ Ruddlesden–Popper Oxides

2A.1 Introduction

Inorganic materials belonging to the perovskite family, in particular the simple perovskites, have been intensively studied as electrocatalysts for catalyzing relevant electrocatalytic reactions. Ni-based RP oxides, such as $La_2NiO_{4+\delta}$ with a K_2NiF_4 structure, can be considered as promising alternatives for MOR catalysts due to their superior mixed ionic and electronic conductivity in comparison to traditionally used perovskite oxides [66, 67]. The typical structure of $La_2NiO_{4+\delta}$ consists of corner-sharing NiO_6 octahedra of $LaNiO_3$ perovskite layers and alternating LaO rock-salt layers along the c axis, yielding a relatively open structural framework to afford hyper-stoichiometric oxide ions in the interstitial of the rock-salt layer for high oxygen diffusivity and ionic conductivity compared to that of the common electrode materials [68]. During the incorporation of interstitial oxygen atoms, the host structure provides electrons to the surface oxygen and holes in the valence band [69]. Indeed, such interstitial oxygen and holes play an important role in determining the overall electrochemical properties [66]. The layered structure also leads to distinct cationic coordination environments as well as unique anionic defect forms. Although, sufficient work has been done towards understanding the structural properties and charge-transfer kinetics of $La_2NiO_{4+\delta}$ [70–74], few of them have been dedicated to utilizing this

unique charge-transfer mechanism for electrocatalysis [75–77], and no comprehensive investigation exists on exploring $La_2NiO_{4+\delta}$ for MOR.

However, the insufficient room-temperature electrical conductivity of $La_2NiO_{4+\delta}$ has been a performance "bottleneck" that has dogged the efficient and fruitful exploration of electrocatalytic materials. Aliovalent doping at the A site with rare-earth cations like Sr^{2+} with the molecular formula of $La_{2-x}Sr_xNiO_{4+\delta}$ has shown a higher magnitude of electron density than that of pristine $La_2NiO_{4+\delta}$ [78, 79]. Indeed, Sr^{2+} doping in $La_{2-x}Sr_xNiO_{4+\delta}$ would oxidize Ni^{2+} to a higher valency to attain the charge neutrality and consecutively the octahedral Ni^{3+} would show a lower electron occupancy in the e_g level. Suntivich et al. has shown that the e_g orbital of the surface-transition-metal ions participate in σ-bonding with a surface-oxygen-related adsorbate, and its occupancy can be used as a descriptor for anodic oxidation reactions [80]. Importantly, Vojvodic and Nørskov have used, cannily, electron occupancy in e_g as an effective descriptor of the electro-oxidation reaction and have demonstrated that decreasing the e_g-orbital occupancy resulted in a stronger M–O binding energy, facilitating the water-splitting reaction [47]. Experimental investigations have demonstrated that the e_g occupancy close to ~1.2 can promote the best OER [81]. The degree of covalency between transition-metal 3d orbitals and O 2p orbitals has also been probed as a descriptor for the OER for water splitting [82]. This mechanism hinges on a lattice-oxygen-mediated pathway, wherein the lattice oxygen is utilized when the E_F crosses the transition-metal 3d and O 2p - hybridized band. This results in the formation of ligand holes which activate the lattice oxygen to combine with chemisorbed OH and produce O_2^-. A similar mechanism has also shown high electrocatalytic oxygen evolution with RP oxides.

Electrocatalytic MOR is a homologous reaction to OER. However, these descriptors have neither been explored for evaluating the MOR mechanism nor have RP oxides been studied comprehensively as MOR catalysts, despite their promise. Here, in the present work, we have systematically enhanced Ni-oxidation states by doping Sr^{2+} in the A site and have probed the MOR mechanism over single-phase $La_{2-x}Sr_xNiO_{4+\delta}$. We have demonstrated, with the help of experiments and DFT calculations, that the optimum amount of Sr^{2+} substitution in $La_{2-x}Sr_xNiO_{4+\delta}$ promotes high MOR activity by enhancing the extent of Ni–O covalency and electronic conductivity. These theoretical calculations, coupled with experimental observations, indicates that a lattice-oxygen-mediated MOR occurs, enabling the involvement of oxygen-vacant sites via the facile formation of Ni–OOH as a key active intermediate species.

2A.2 Experimental & Theoretical methods

2A.2.1 Synthesis of $La_{2-x}Sr_xNiO_{4+\delta}$ (x = 0 - 0.8)

$La_{2-x}Sr_xNiO_{4+\delta}$ (x = 0 - 0.8) were synthesized using a facile single-step solution combustion method. This is a low temperature-initiated, energy-efficient single-step synthesis, where propellant chemistry is followed between the oxidizer metal nitrates and fuel glycine [83–85]. In a typical synthesis, stoichiometrically appropriate amount of metal precursors, $La(NO_3)_3 \cdot 6H_2O$ (SRL chemicals, 99%), $Sr(NO_3)_2$ (Sigma Aldrich, 99%), $Ni(NO_3)_2 \cdot 6H_2O$ (SD fine, 99%), and fuel $C_2H_5NO_2$ (Sigma Aldrich, 99%) were dissolved in ~50 mL of deionized water in a 300 mL borosilicate dish. The organic fuel glycine complexes with the metal cations in the solution. The homogeneous solution was then introduced into a preheated muffle furnace maintained at 450 °C. In the beginning, the solution boiled with frothing and foaming and underwent dehydration. At the time of complete dehydration, combustion started with a burning flame on the surface, where the metal-fuel complexes decomposed exothermically, with the evolution of CO_2, N_2 and H_2O. Within 10 minutes of combustion, a voluminous solid product was formed, which was left to cool to room temperature, and then ground to a fine powder in a mortar and pestle.

2A.2.2 Synthesis of $La_{1.4}Sr_{0.6}NiO_{4+\delta}$/PANI

PANI, which has been used as a conducting support for $La_{1.4}Sr_{0.6}NiO_{4+\delta}$/PANI for electrocatalytic applications was synthesized as per previous reports [86, 87]. Ammonium persulfate (0.183 g, SRL Chemicals, 98.0%.) was dissolved in 10 mL of 1 M HCl (SRL chemicals, 99%) and was poured cautiously into aniline (0.298 g, Advent chemicals, 98%) dissolved in 10 mL of 1 M HCl. The mixed solution was stirred immediately to initiate the polymerization reaction. The resultant green solution was filtered and washed with water and methanol to remove the oligomers. Finally, it was dried at 70 °C for 12 h in a hot air oven to obtain the solid powder of PANI. The solution-combustion-synthesised ($La_{1.4}Sr_{0.6}NiO_{4+\delta}$) was aged in a 1 M NaOH (Finar, 96%) solution for 24 h. The synthesized PANI powder was added in the alkaline dispersion of $La_{1.4}Sr_{0.6}NiO_{4+\delta}$ in a weight ratio of $La_{1.4}Sr_{0.6}NiO_{4+\delta}$: PANI = 4:1, and was vigorously stirred at room temperature for 24 h. The resultant was filtered, washed with water, and dried at 70 °C for 12 h in a hot air oven to obtain the solid composite.

2A.2.3 Structural, Surface and Electronic Characterisation

The crystal structure of the synthesized $La_{2-x}Sr_xNiO_{4+\delta}$ material was probed by high-resolution powder X-ray diffraction using a Rigaku Ultima IV X-ray diffractometer with Cu K_α radiation $\lambda = 1.5418$ Å at a scan rate of 0.5° min^{-1} and a step size of 0.01°. The average nanocrystalline diameters (D) were calculated from the broadening of the highest peak using Scherrer's formula,

$$D = \frac{0.9\lambda}{B\text{Cos}\theta} \tag{2A.1}$$

where B is the full-width at half-maximum, λ is the wavelength of the radiation, and θ is the corresponding angle. The powder X-ray diffraction patterns were refined with the Fullprof program suite. Rietveld refinements were carried out by varying the parameters, such as the overall scale factor, background and profile parameters, unit-cell lattice parameters, atomic positions, half-width, shape, isotropic thermal parameters, oxygen occupancy, etc. The crystal structure was further probed by HR-TEM (Tecnai G2, F30) under an accelerating potential of 300 kV with a point resolution of 2 Å and line resolution of 1 Å. The XAFS measurements of the pellet of powder samples were carried out at the BL36XU beamline on Spring-8. Structural analysis was performed using the Demeter software platform. The reported crystal data were used for calculating F_{eff}. The surface morphology of the synthesized $La_{2-x}Sr_xNiO_{4+\delta}$ materials was studied using a FE-SEM. The non-stoichiometric oxygen content in the $La_{2-x}Sr_xNiO_{4+\delta}$ series was determined using iodometric titrations [88, 89]. Oxygen over stochiometry of the synthesized RP oxides was directly linked with the $Ni^{3+} \rightarrow Ni^{2+}$ reduction according to the formulation $La_{2-x}Sr_xNi^{2+}_{1-\tau}Ni^{3+}_{\tau}\ O_{4+\frac{\tau}{2}}$, where $\delta = \frac{\tau}{2}$, and the content of $Ni^{3+}(\tau)$ was determined using KI. In a typical titration, 0.1 g of the oxide sample was dissolved in a 4 mL HCl solution containing 1 g excess KI (Finar, 99%). The liberated I_2 due to reduction of Ni^{3+} was titrated against standardized $Na_2S_2O_3$ (Sigma-Aldrich, 99.99%) using a starch solution (ACS, 1% solution, Alfa Aesar) as an indicator. The reactions are summarized below:

$$2Ni^{3+} + 2I^- \rightarrow 2Ni^{2+} + I_2 \tag{2A.2}$$

$$I_2 + 2S_2O_3^{2-} \rightarrow 2I^- + S_4O_6^{2-} \tag{2A.3}$$

$$\text{Summary: } 2Ni^{3+} + 2S_2O_3^{2-} \rightarrow 2Ni^{2+} + S_4O_6^{2-} \tag{2A.4}$$

2A.2.4 Electrocatalytic Methanol Oxidation

Electro-oxidation of methanol was evaluated in a conventional three-electrode glass cell equipped with a $La_{2-x}Sr_xNiO_{4+\delta}$ modified GCE as the working electrode, Ag/AgCl in saturated KCl as the reference electrode, and a Pt electrode as the counter electrode. Aqueous solution of 0.5 M NaOH served as the electrolyte. The cell was connected to the Origaflex OGF 500 electrochemical workstation. CV and CA of the catalysts were investigated in an alkaline electrolyte with different methanol content and at varied potential-sweep rates at room temperature. In all measurements, potential in Ag/AgCl is converted to RHE in 0.5 M NaOH according to the following equation: $E_{RHE} = E_{Ag/AgCl} + 0.059 \times pH + 0.1976$. The final liquid products after CA were analyzed using ^{1}H NMR AV NEO 400 MHz (Bruker). About 0.4 mL of the electrolysis solution, 0.1 mL of D_2O, and 5 mg of 4-nitrophenol (as an internal standard) were added into the NMR tube for identifying the product. An electrochemical impedance study was carried out using a Biologic SP-150 electrochemical workstation, with the conventional three-electrode system in an alkaline mixture of 0.5 M MeOH and 0.5 M NaOH over a frequency range of 40 kHz to 100 MHz with a sinusoidal excitation signal of 10 mV. The resulting Nyquist plots were fitted to the appropriate equivalent circuit using EC-Lab V11.31. The Tafel slope of $La_{2-x}Sr_xNiO_{4+\delta}$ with and without methanol was calculated from the fitting of the linear portion of the Tafel plot. The ECSA was determined by conducting double - step chronoamperometric experiments, wherein the electrode potential was swept between non-faradic potential (1.0 V vs RHE) and faradic potential (1.8 V vs RHE). This was done in the presence of an electrolyte comprising 0.1 M potassium ferricyanide and 0.1 M KCl. This potential is sufficient to oxidize the $[Fe(CN)_6]^{4-}$ (aq) to $[Fe(CN)_6]^{3-}$ (aq). Area under the charging - discharging curve was calculated, and was accordingly plotted with time to obtain the ECSA by using the following Cottrell equation.

$$Q = 2nFAD^{1/2}C_o t^{1/2}\pi^{-1/2} \tag{2A.5}$$

where Q = charge in coulomb F = Faraday constant n = Number of electrons being transferred A = Area of electrode (cm^2) D = Diffusion coefficient of $[K_3Fe(CN)_6]$ ($7.6\times10^{-6} cm^2 s^{-1}$) t = time (s) C_o = concentration of $K_3Fe(CN)_6$ (mol cc^{-1}).

2A.2.5 Electronic-Structure Modelling

Electronic-structure-based geometry-optimization calculations of the pristine $La_2NiO_{4+\delta}$ and doped $La_{2-x}Sr_xNiO_{4+\delta}$ were performed using a plane-wave basis with plane-wave energy cut off of 500 eV and the GGA for the exchange-correlation energy using the PBE [90] functional, as implemented in VASP 5.3.5 [91–93]. The initial coordinates for the geometry optimization of $La_2NiO_{4+\delta}$ were taken from the literature [94]. For all of the calculations, 6×6×3 k-point mesh with Monkhorst-pack scheme were used for geometry optimization and single-point properties calculation, except where 3×6×3 k-point mesh with Monkhorst-pack scheme were used. The DFT (PBE) + U methodology (with an additional Hubbard-like term, U) was used to consider strong on-site Coulomb interaction of localized (3d and 4f) electrons, which were not correctly described by PBE functional. We applied the onsite Coulomb interaction U into all of the GGA calculations with the setting of U_{eff}@La = 5.5 eV, U_{eff}@Ni = 8.33 eV, as reported in previous literature for these kinds of materials [82]. In our calculations, we used $La_{1.5}Sr_{0}.5NiO_{4+\delta}$ to mimic the properties of $La_{1.4}Sr_{0.6}NiO_{4+\delta}$, which simplifies the structure and coordinates of the unit cell.

2A.3 Results and discussion

2A.3.1 Structural, Surface and Electronic properties

The X-ray diffraction patterns in Figure 2A.1 (a) demonstrate that the solution-combustion-synthesized $La_{2-x}Sr_xNiO_{4+\delta}$ oxides crystallized in a phase-pure Ruddlesden Popper structure, consistent with the reported literature [69, 76, 79, 88, 94]. $La_{2-x}Sr_xNiO_{4+\delta}$ oxides for x = 0 - 0.6 exhibited tetragonal symmetry with I4/mmm space group [JCPDS No. 81-0742]. With a higher amount of doping of Sr^{2+} (x = 0.8), the polymorphic $La_{1.2}Sr_{0.8}NiO_{4+\delta}$ crystallized in a lower symmetric orthorhombic structure, with space group Fmmm, along with the primary tetragonal structure [88]. However, there was no impurity of La_2O_3 or NiO phases observed in the XRD patterns of any of $La_{2-x}Sr_xNiO_{4+\delta}$ oxides. The magnified view of the XRD patterns for the (103) and (110) peaks in Figure 2A.1(b) shows a gradual shifting of peaks to a higher angle with increasing Sr^{2+} doping in the lattice, suggesting a shrinking of inter-planar distances of d_{103} and d_{110} due to doping of a smaller cation in the A site [95, 96]. The average nanocrystalline size calculated from the highest-intensity peak of the (103) reflection was found to be approximately 60 nm for the pristine and doped $La_{2-x}Sr_xNiO_{4+\delta}$ oxides.

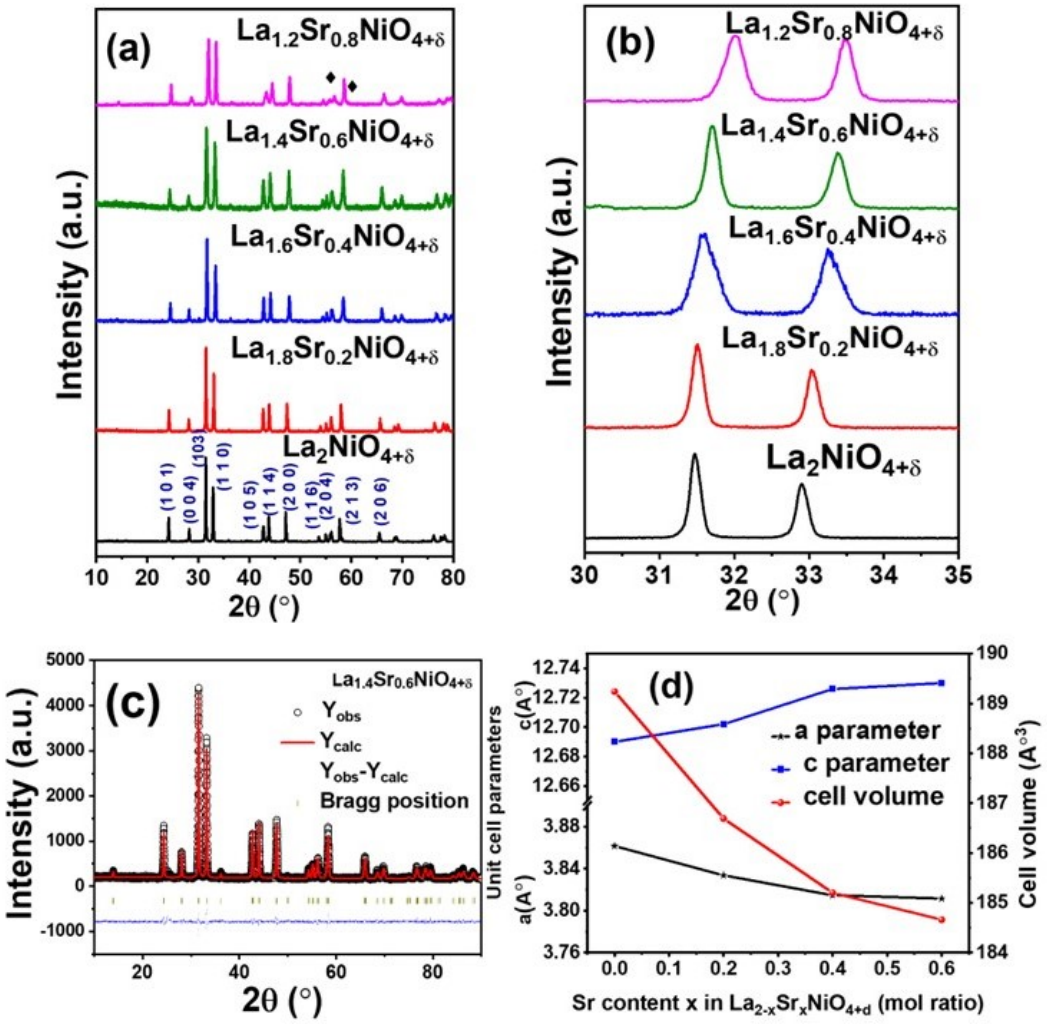

FIGURE 2A.1: (a) Powder XRD patterns of solution-combustion-synthesized $La_{2-x}Sr_xNiO_{4+\delta}$, (b) magnified view of (103) and (110) of $La_{2-x}Sr_xNiO_{4+\delta}$ with Sr^{2+} doping, (c) Rietveld refinement of $La_{1.4}Sr_{0.6}NiO_{4+\delta}$, (d) variation of lattice parameters and unit-cell volume with Sr^{2+} doping doping

To have further insight into the structural information, the powder XRD patterns were refined with Rietveld refinement considering the I4/mmm space group, where La and Sr were randomly distributed at 4e (0,0,z) sites, Ni at 2a (0,0,0) and the two inequivalent oxygen atoms O_1 at 4c (0, 0.5,0) and O_2 at 4e (0,0,z) Wyckoff sites. The powder pattern of $La_{1.2}Sr_{0.8}NiO_{4+\delta}$ was not refined as the particular oxide crystallized in mixed tetragonal and orthorhombic phases. A representative fitting is shown in Figure 2A.1(c), and the refined lattice parameters, along with atomic occupancy, are provided in 2A.1. The reliability factors R_{exp}, R_{wp}, R_p and χ^2 represent satisfactory refinement results. The variation of the lattice constants of $La_{2-x}Sr_xNiO_{4+\delta}$ (x = 0 - 0.6) is shown in Figure 2A.1(d). The lattice constants 'a'/'b' decreased gradually, whereas 'c' increased with an increase in Sr doping. The tetragonal elongation along the 'z' axis of the unit cell is explained by Jahn - Teller distortion. Substitution of trivalent La^{3+} with bivalent

Sr^{2+} in the A site brings about charge neutrality and, therefore, Ni^{2+} oxidizes to Ni^{3+} in the B site. The Ni^{2+} sites in the octahedral environment possess asymmetrical occupancy of the electron in the e_g orbital with $t_{2g}{}^6e_g{}^1$ configuration, which could be responsible for tetragonal elongation [97]. The elongation along the 'z' axis signifies a lesser overlap of d_{z^2} and axial O 2p, whereas compression along the equatorial plane indicates a higher overlap of $d_{x^2-y^2}$ and O 2p with increase in Sr^{2+} up to x = 0.6. The significant shrink along the equatorial plane has also reduced the unit-cell volume upon Sr^{2+} doping [98].

TABLE 2A.1: Rietvield refined lattice parameters and atomic occupancy of $La_{2-x}Sr_xNiO_{4+\delta}$ (x = 0 - 0.6)

	Cell parameters (Å)		**Cell volume**	χ^2	**Occupancy**				
	a= b	c	(**Å**^{3})		La	Ni	Sr	O_1	O_2
$La_2NiO_{4+\delta}$	3.861	12.69	189.2	1.15	1.025	1.000	-	0.985	0.963
$La_{1.2}Sr_{0.8}NiO_{4+\delta}$	3.833	12.70	186.6	2.09	0.674	0.576	0.612	1.060	0.823
$La_{1.6}Sr_{0.4}NiO_{4+\delta}$	3.814	12.72	185.2	1.74	0.747	0.569	0.502	1.136	0.945
$La_{1.4}Sr_{0.6}NiO_{4+\delta}$	3.811	12.73	184.6	1.25	0.480	0.537	0.700	1.163	1.126

To corroborate the tetragonal elongation in substituted oxide, XAFS measurements were performed on $La_2NiO_{4+\delta}$ and $La_{1.4}Sr_{0.6}NiO_{4+\delta}$. XANES at the Ni K-edge are shown in Figure 2A.2 (a). The Ni K-edge spectrum of $La_{1.4}Sr_{0.6}NiO_{4+\delta}$ was shifted from 8340.3 eV (peak top of the edge of the standard sample of $La_2NiO_{4+\delta}$ and $La_{1.4}Sr_0.6NiO_{4+\delta}$) to 8341.0 eV. These results indicate that the oxidation state of Ni ions of $La_{1.4}Sr_{0.6}NiO_{4+\delta}$ was higher than that of $La_2NiO_{4+\delta}$. This was also in accordance with earlier reports [99]. Fitting of the extended X-ray absorption fine-structure region around the Ni ions of $La_2NiO_{4+\delta}$ exhibited Ni–O distances of 1.9130 Å (4-coordinate) and 2.2471 Å (2-coordinate), whereas $La_{1.4}Sr_{0.6}NiO_{4+\delta}$ displayed a distance of 1.8534 Å (4-coordinate) and 2.2890 Å (2-coordinate) (R range 1-2.4 Å, R-factor; 8.0% and 5.7%, k^3 - weighted Fourier transforms of the XAFS data, as shown in Figure 2A.2(b,c). The Ni-O distances confirm the apparent compression along the equatorial plane and tetragonal elongation upon Sr^{2+} doping in the substituted RP oxides. It was difficult to determine definitively the effect of O atoms on $La_{1.4}Sr_{0.6}NiO_{4+\delta}$ (or coordination number around Ni ion) because doping allowed for a more complex Ni-O path, complicating estimations of the Debye-Waller factor. However, Rietveld refinement provided an interesting observation on oxygen occupancy: with higher bivalent-ion doping at the A site, the occupancy of oxygen also became larger (see Table 2A.2). To corroborate this observation, the experimental excess-oxygen content was calculated from iodometric titration. Table 2A.2 shows the amount of oxygen over stoichiometry δ. With the increment of Sr doping from 0.2 to 0.8, over stoichiometric oxygen content was enhanced

gradually from 0.0133 to 0.0290. It could be concluded that the excess oxygen level might be the extra oxygen occupying vacant space in the lattice [88].

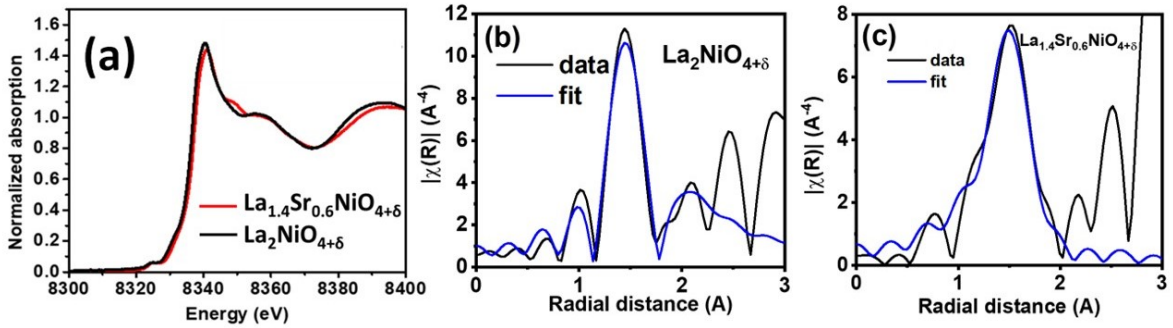

FIGURE 2A.2: (a) Ni K-edge XANES spectra of pristine $La_2NiO_{4+\delta}$ and substituted $La_{1.4}Sr_{0.6}NiO_{4+\delta}$. Fitting of the extended X-ray absorption fine structure region around the Ni ions of (b) $La_2NiO_{4+\delta}$ and (c) $La_{1.4}Sr_{0.6}NiO_{4+\delta}$

The nano-structural features of $La_{1.4}Sr_{0.6}NiO_{4+\delta}$ were probed with HR-TEM micrographs, as shown in Figure 2A.3. The $La_{1.4}Sr_{0.6}NiO_{4+\delta}$ particles in Figure 2A.3(a) exhibited diffuse shapes, with an average size of 93 nm. High-resolution image of $La_{1.4}Sr_{0.6}NiO_{4+\delta}$ in Figure 2A.3(b) showed the lattice fringes with characteristic interplanar distances of 0.268, 0.285 and 0.311 nm, corresponding to (110), (103), (004) planes of tetragonal symmetry, respectively. The corresponding SAED in Figure 2A.3(c) corroborates this tetragonal structure. A similar morphology of the other substituted $La_{2-x}Sr_xNiO_{4+\delta}$ oxides was also observed from FE-SEM micrographs as shown in Figure 2A.4.

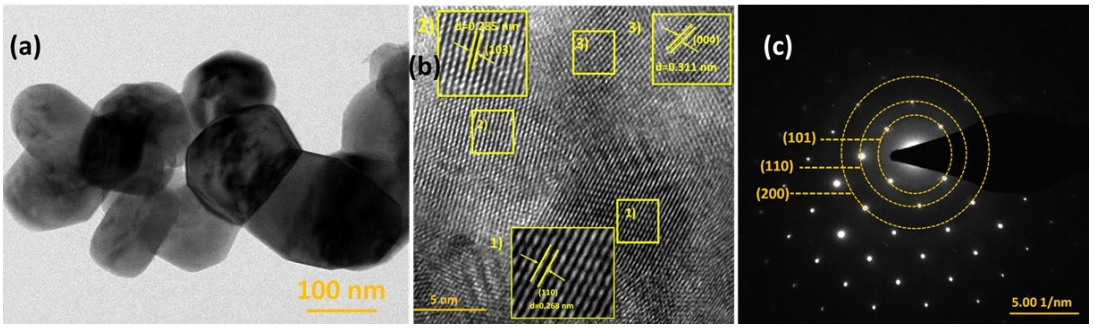

FIGURE 2A.3: HR-TEM images (a,b) and SAED pattern (c) of $La_{1.4}Sr_{0.6}NiO_{4+\delta}$

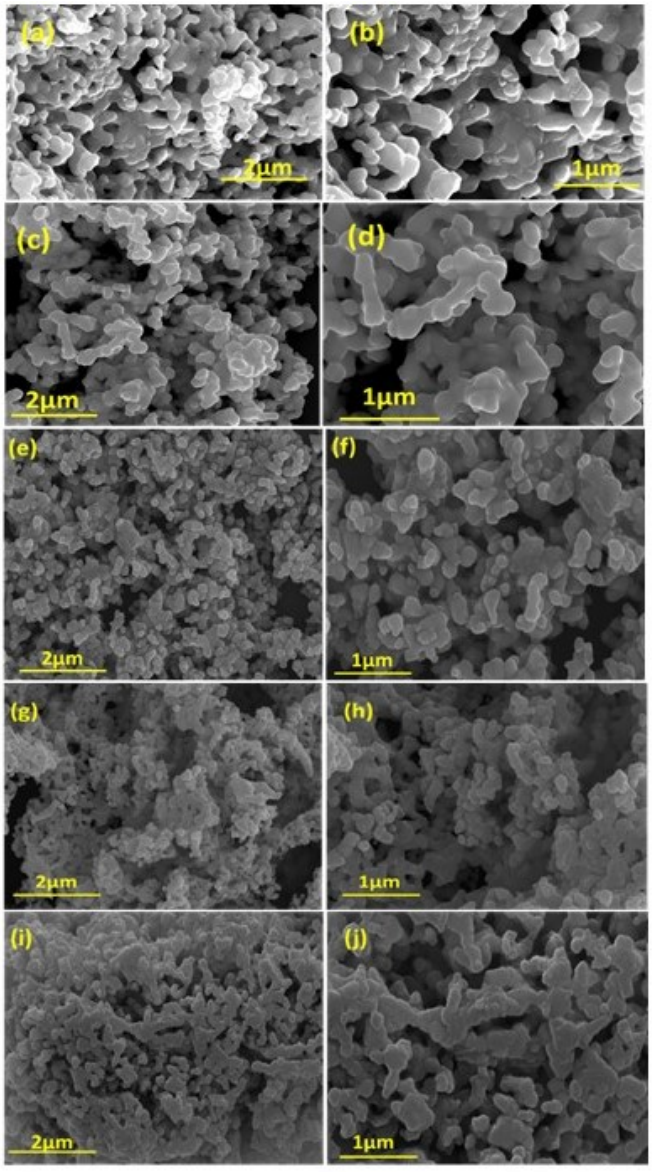

FIGURE 2A.4: SEM images of (a,b) $La_2NiO_{4+\delta}$ (c,d) $La_{1.8}Sr_{0.2}NiO_{4+\delta}$(e,f) $La_{1.6}Sr_{0.4}NiO_{4+\delta}$ (g,h) $La_{1.4}Sr_{0.6}NiO_{4+\delta}$ (i,j)$La_{1.2}Sr_{0.8}NiO_{4+\delta}$

The surface chemical bonding and the elemental electronic states of the elements in $La_{2-x}Sr_xNiO_{4+\delta}$ were probed by XPS analyses. The survey spectra in Figure 2A.5(a) represent the elemental composition, and the core-level spectra of La 3d and Ni 2p (Figure 2A.5(b)) were not analyzed further due to the overlap of Ni $2p_{3/2}$ and La $3d_{3/2}$ satellite peaks [100, 101]. Detailed analyses were carried out with Ni 3p core-level spectra plotted in Figure 2A.5(c). The deconvolution indicates that the pristine $La_2NiO_{4+\delta}$ is comprised of mostly bivalent Ni^{2+}, whereas $La_{2-x}Sr_xNiO_{4+\delta}$ simultaneously contains Ni^{2+} as well as Ni^{3+} due to the Sr^{2+} doping in A site [102, 103]. The pristine $La_2NiO_{4+\delta}$ exhibited 8.6% of Ni^{3+}. The percentage content of Ni^{3+} in $La_{2-x}Sr_xNiO_{4+\delta}$ gradually increased from 17.06% with x = 0.2 to 27.3% with x =

0.8. The Ni^{3+} formation with $3d^7$ electrons accounts for the moderate tetragonal elongation in pristine $La_2NiO_{4+\delta}$, and pronounced elongation in $La_{2-x}Sr_xNiO_{4+\delta}$ as observed in Rietveld refinement and EXAF analysis. The deconvoluted core-level spectra of O 1s in Figure 2A.5(d) shows three distinguishable peaks at 531.2 eV due to lattice oxygen O_L [104–106], at 533.5 eV due to adsorbed oxygen species in the defect sites O_S, and at 534.8 eV corresponding to hydroxyl species of surface-adsorbed water molecules O_W [107, 108]. The surface oxygen content at the defect site was quantified from the area under the curve of surface oxygen with respect to the total area under O 1s core level spectrum (O_T). The total oxygen content is given by $O_T = O_L + O_S + O_W$. Although pristine $La_2NiO_{4+\delta}$ showed defect-site surface-oxygen content around 26.2%, upon higher Sr^{2+} doping (x = 0.6) the defect-site oxygen increased up to 75.08%. However, at Sr^{2+} doping of x = 0.8, the surface oxygen decreased, indicating a lower amount of vacant sites. It can be concluded from core-level O 1s spectra that the vacant sites are maximal for $La_{1.4}Sr_{0.6}NiO_{4+\delta}$, whereas the biphasic structure might have been responsible for the reduced extent of defect sites.

TABLE 2A.2: Over stoichiometric oxygen, defect site oxygen species, Ni^{3+} concentration

Catalysts	**Over stoichiometric oxygen by iodometric titration (δ)**	**Adsorbed oxygen species in the defect sites by core level XPS (O_S)**	**Ni^{3+} concentration estimated by core level XPS %**
$La_2NiO_{4+\delta}$	-	26.2	8.6
$La_{1.8}Sr_{0.2}NiO_{4+\delta}$	0.0133	37.8	17.06
$La_{1.6}Sr_{0.4}NiO_{4+\delta}$	0.0215	45.12	22.2
$La_{1.4}Sr_{0.6}NiO_{4+\delta}$	0.0283	75.08	25.6
$La_{1.2}Sr_{0.8}NiO_{4+\delta}$	0.0290	29.07	27.3

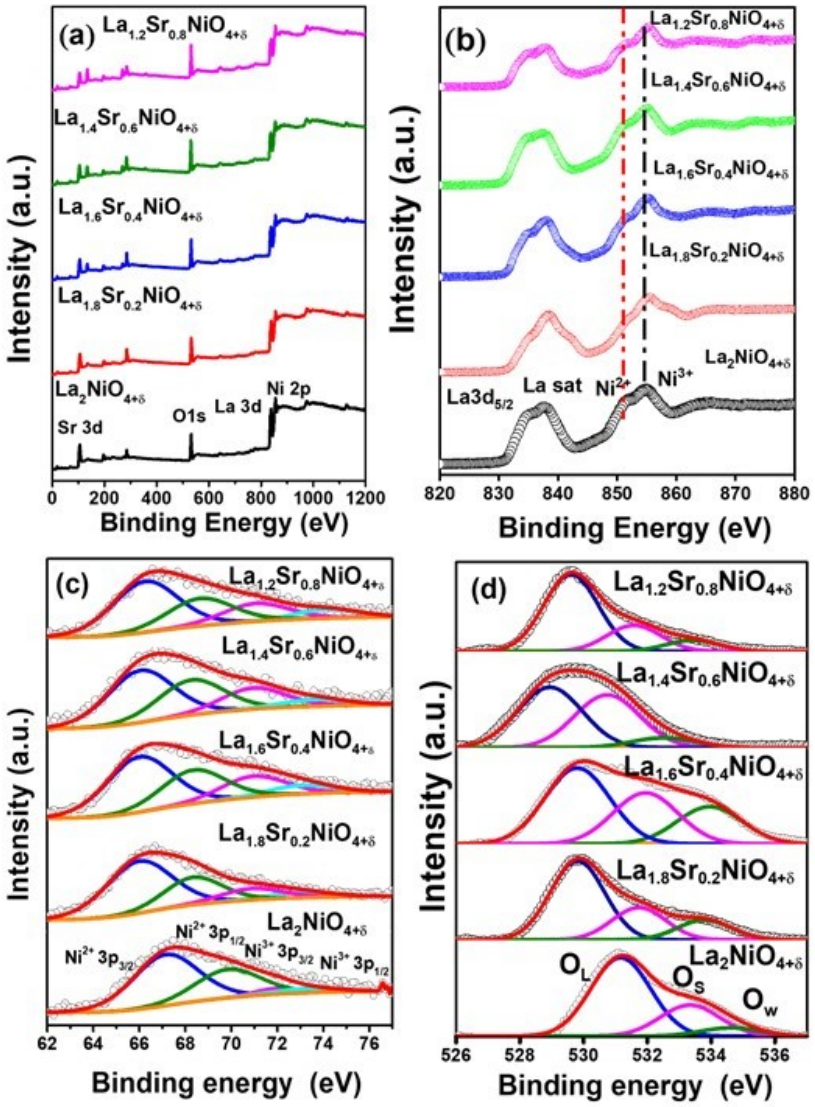

FIGURE 2A.5: (a) XPS survey scan and (b) Ni 2p and La 3d core level spectra (c) Ni 3p and (d) O 1s in $La_{2-x}Sr_xNiO_{4+\delta}$ (x = 0 - 0.8)

2A.3.2 Electrocatalytic Oxidation of Methanol

The activity of solution-combustion-synthesized $La_{2-x}Sr_xNiO_{4+\delta}$ series towards methanol oxidation was investigated from cyclic voltammetry in 0.5 M NaOH at a scan rate of 50 mV s^{-1}. The cyclic voltammograms of $La_{2-x}Sr_xNiO_{4+\delta}$ oxides in the absence of methanol are presented in Figure 2A.6 and exhibit behavior typical of a Ni-based electrode in an alkaline system. A current density observed starting at a potential value between 1.4 V to 1.8 V vs RHE corresponds to the charge-transfer process of a Ni-O/Ni-OOH (Ni^{2+}/Ni^{3+}) redox couple [109]. Due to the increasing number of potential sweeps along the potential 1.0 to 1.9 V vs RHE, a thick layer of Ni - OOH was formed on the lattice surface with Ni in the 3+ oxidation state which was

confirmed from CV studies and XPS [110, 111].

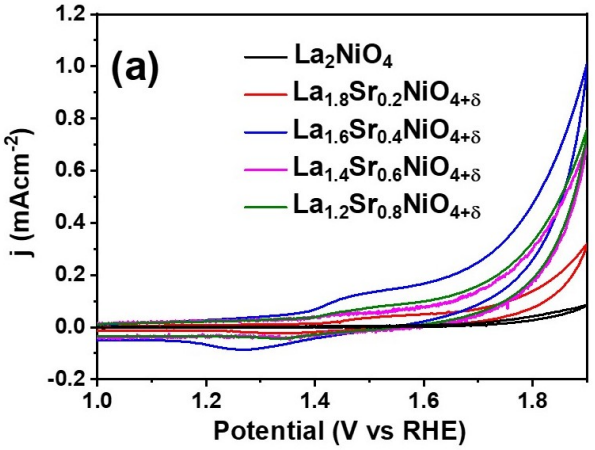

FIGURE 2A.6: CVs of $La_{2-x}Sr_xNiO_{4+\delta}$ 0.5 M NaOH at scan rate 50mV s^{-1} in the absence of methanol

The cyclic voltammogram of $La_{2-x}Sr_xNiO_{4+\delta}$ oxides in 0.5 M NaOH at scan rates from 10 to 100 mV s^{-1} were performed, where the anodic and cathodic current densities increased linearly with the scan rate (cf. Figure 2A.7). A peak shift was observed at a higher scan rate probably due to the less time available for the complete formation of Ni-OOH species [22].

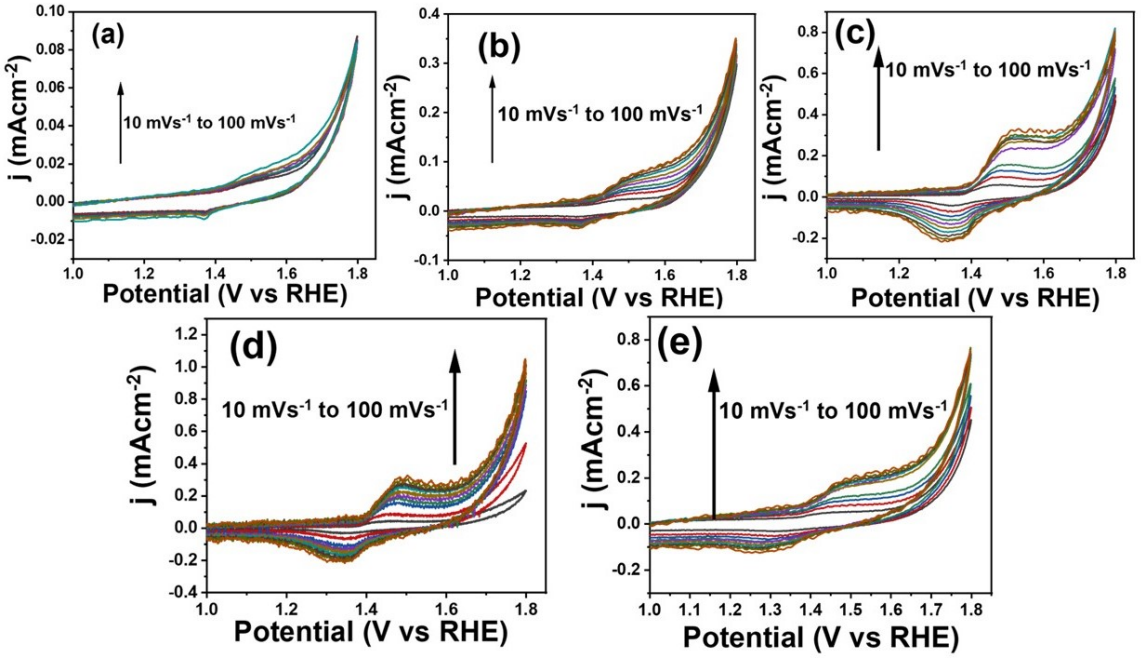

FIGURE 2A.7: CVs of (a) $La_2NiO_{4+\delta}$, (b) $La_{1.8}Sr_{0.2}NiO_{4+\delta}$, (c) $La_{1.6}Sr_{0.4}NiO_{4+\delta}$, (d) $La_{1.4}Sr_{0.6}NiO_{4+\delta}$, and (e) $La_{1.2}Sr_{0.8}NiO_{4+\delta}$ in 0.5 M NaOH at scan rate 10 - 100 mV s^{-1} in the absence of methanol

Further, MOR activity of the synthesized oxides was studied by the addition of 1.5 M MeOH to 0.5 M NaOH electrolyte solution. A significant change in the CV curve is noticed with a characteristic peak showing MOR activity around 1.59 V vs RHE with current densities of 0.10, 0.20, 0.61, and 0.17 mA cm^{-2} for $La_{1.8}Sr_{0.2}NiO_{4+\delta}$, $La_{1.6}Sr_{0.4}NiO_{4+\delta}$, $La_{1.4}Sr_{0.6}NiO_{4+\delta}$, and $La_{1.2}Sr_{0.8}NiO_{4+\delta}$, respectively, as shown in Figure 2A.8a. All the catalysts exhibited a well-separated anodic peak in forward (I_f) and backward scan (I_b) modes. The forward scan peak depends on the amount of MeOH oxidized by the electrode modified by the oxide catalysts. The characteristic hysteresis observed in the backward-scan is attributed to the oxidation of adsorbed electrogenerated intermediate species formed during the forward sweep. This phenomenon has also been reported earlier over the oxidic catalysts [112–116]. It is readily apparent that the trend of MOR activity is increased from $La_2NiO_{4+\delta}$ to $La_{1.4}Sr_{0.6}NiO_{4+\delta}$, and again decreases in $La_{1.2}Sr_{0.8}NiO_{4+\delta}$, with $La_{1.4}Sr_{0.6}NiO_{4+\delta}$ exhibiting the highest extent of MeOH-oxidation behavior, with a maximum current density of 0.61 mA cm^{-2} at 1.59 V vs RHE potential, as shown in Figure 2A.8 and its inset. It should be noted that the OER is also inevitably strong in the same potential window [117]. The comparison of CV traces of MOR and OER in the same potential window over $La_{1.4}Sr_{0.6}NiO_{4+\delta}$ (Figure 2A.8(b)) exhibited that the OER started beyond 1.6 V vs. RHE, whereas the onset anodic potential of MOR was at 1.45 V vs RHE over $La_{1.4}Sr_{0.6}NiO_{4+\delta}$. Further, the Tafel plot in Figure 2A.8(c) displayed a lower Tafel slope (118.9 mV dec^{-1}) for MOR compared to that of OER (303.3 mV dec^{-1}) over $La_{1.4}Sr_{0.6}NiO_{4+\delta}$. The results apparently indicated a much favorable MOR kinetics within the experimental potential window over the synthesized RP oxide. The scan-rate dependency of MOR activity of highly active $La_{1.4}Sr_{0.6}NiO_{4+\delta}$ for MOR was studied, and the results are provided in Figure 2A.8(d). It is observed that the current density of MOR increased with increasing scan rate. The inset of Figure 2A.8(d) demonstrates the linear relationship between the peak current and square root of the scan rate, indicating a diffusion-controlled electrochemical process [118, 119].

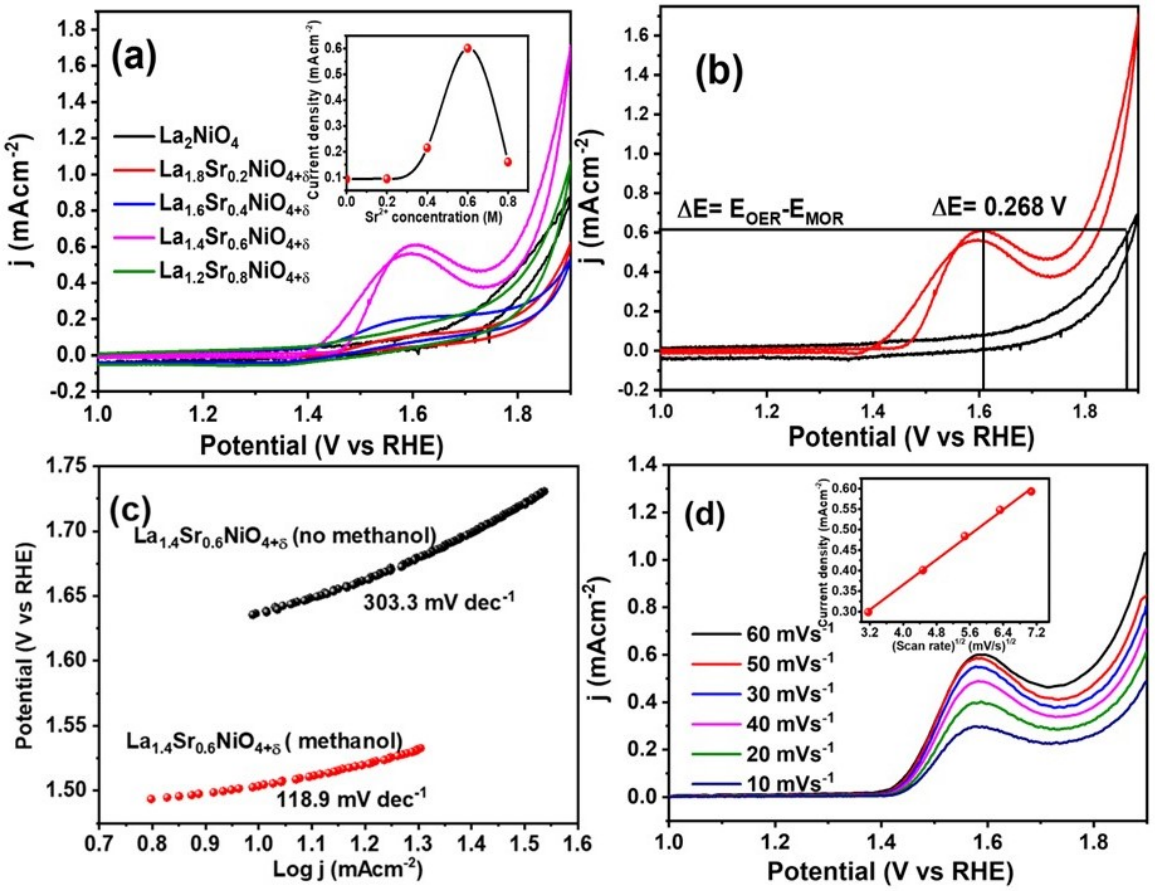

FIGURE 2A.8: CVs of (a) $La_{2-x}Sr_xNiO_{4+\delta}$ series in 0.5 M NaOH and 1.5 M MeOH at scan rate of 50mV s^{-1} (b) CV for $La_{1.4}Sr_{0.6}NiO_{4+\delta}$ in the presence and absence of methanol at a scan rate of 50 mV s^{-1} (c) Tafel plots of $La_{1.4}Sr_{0.6}NiO_{4+\delta}$ for MOR and OER and (d) Scan rate dependent CV study of $La_{1.4}Sr_{0.6}NiO_{4+\delta}$ in 0.5 M NaOH and 1.5 M MeOH

In order to achieve higher current density, as well as better MOR activity, conducting polymer PANI was used as a support of $La_{1.4}Sr_{0.6}NiO_{4+\delta}$ [120–122]. The cyclic voltammograms of $La_{1.4}Sr_{0.6}NiO_{4+\delta}$/PANI composite and unsupported $La_{1.4}Sr_{0.6}NiO_{4+\delta}$ during MOR in alkaline medium (0.5 M NaOH and 1.5 M MeOH at 50 mV s^{-1} scan rate) are provided in Figure 2A.9(a). $La_{1.4}Sr_{0.6}NiO_{4+\delta}$/PANI revealed a significant 5-fold increment in oxidative peak current density for MeOH oxidation at 1.59 V vs RHE, with an increased MOR current density of 3.34 mA cm^{-2}. The strong synergistic oxide-support interaction in $La_{1.4}Sr_{0.6}NiO_{4+\delta}$/PANI may have improved charge transfer between the conducting polymer and the active $La_{1.4}Sr_{0.6}NiO_{4+\delta}$, and thereby enhanced the electron exchange behavior in the composite system for better MOR efficacy. ECSA can also influence the MOR efficacy, and therefore the ECSA was calculated over the pristine and the composite materials (Figure 2A.9(b)) [123–125]. The calculated ECSA of $La_{1.4}Sr_{0.6}NiO_{4+\delta}$/PANI was 0.219 cm^2, an order of magnitude higher value than that of

$La_{1.4}Sr_{0.6}NiO_{4+\delta}$ (0.07 cm^2). This clearly justifies the higher efficacy of the composite material. The electrochemical stability of the catalyst is another vital factor, which was evaluated by CA technique. CA studies of the most active $La_{1.4}Sr_{0.6}NiO_{4+\delta}$ and the composite $La_{1.4}Sr_{0.6}NiO_{4+\delta}$ /PANI were carried out in 0.5 M NaOH and 1.5 M MeOH at MOR potential of 1.61 V vs RHE, as shown in Figure 2A.9(c). The unsupported $La_{1.4}Sr_{0.6}NiO_{4+\delta}$ and the composite $La_{1.4}Sr_{0.6}NiO_{4+\delta}$/PANI exhibited a very stable MOR phenomenon, as they preserved quite constant current density throughout the MOR process for 12 h. An increment of current density was also observed for $La_{1.4}Sr_{0.6}NiO_{4+\delta}$ /PANI catalyst during this CA study. The robust steadiness of the hybrid composite with enhanced current density during MOR activity confirmed the synergistic interaction between and $La_{1.4}Sr_{0.6}NiO_{4+\delta}$ and PANI in the system.

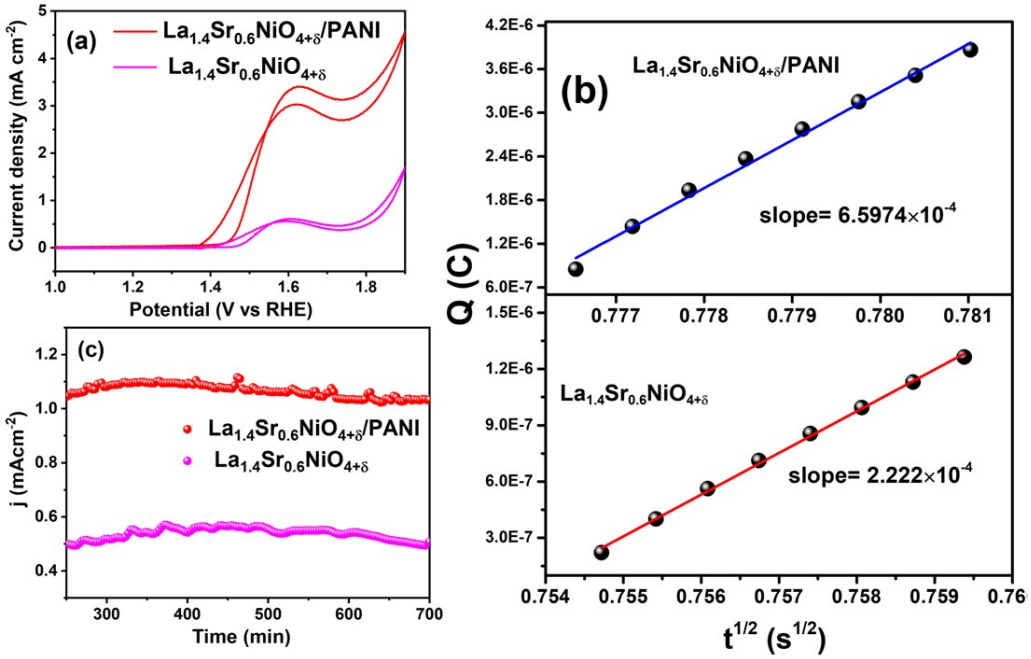

FIGURE 2A.9: CVs of (a) $La_{1.4}Sr_{0.6}NiO_{4+\delta}$ and $La_{1.4}Sr_{0.6}NiO_{4+\delta}$/PANI in 0.5 M NaOH and 1.5 M MeOH at scan rate of 50 mV s^{-1} (b) Plot of charge against time according to Cottrell equation over $La_{1.4}Sr_{0.6}NiO_{4+\delta}$ and $La_{1.4}Sr_{0.6}NiO_{4+\delta}$/PANI and (c) CA of $La_{1.4}Sr_{0.6}NiO_{4+\delta}$ and the composite $La_{1.4}Sr_{0.6}NiO_{4+\delta}$ /PANI in 0.5 M NaOH and 1.5 M MeOH at MOR potential of 1.61 V vs RHE

The well-resolved peak in the backward-scan during MOR over the pristine as well as PANI supported $La_{1.4}Sr_{0.6}NiO_{4+\delta}$ is attributed to the oxidation of adsorbed intermediate species. The gaseous CO could be an intermediate during MOR. Therefore, to confirm CO poisoning or tolerance, a CO-stripping experiment was performed on $La_{1.4}Sr_{0.6}NiO_{4+\delta}$ and $La_{1.4}Sr_{0.6}NiO_{4+\delta}$ /PANI-modified electrodes (Figure 2A.10). Apparently, CV traces were almost identical in the absence or in the presence of feed gaseous CO. This confirmed no evidence of CO poisoning over

the pristine $La_{1.4}Sr_{0.6}NiO_{4+\delta}$ or supported $La_{1.4}Sr_{0.6}NiO_{4+\delta}$ /PANI catalysts, and the peak in the backward-scan during MOR over the materials was due to the oxidation of any adsorbed intermediate species other than CO [126, 127]. Absolute no CO poisoning was a significantly valuable advantage of MOR over the synthesized materials for durable DMFC applications.

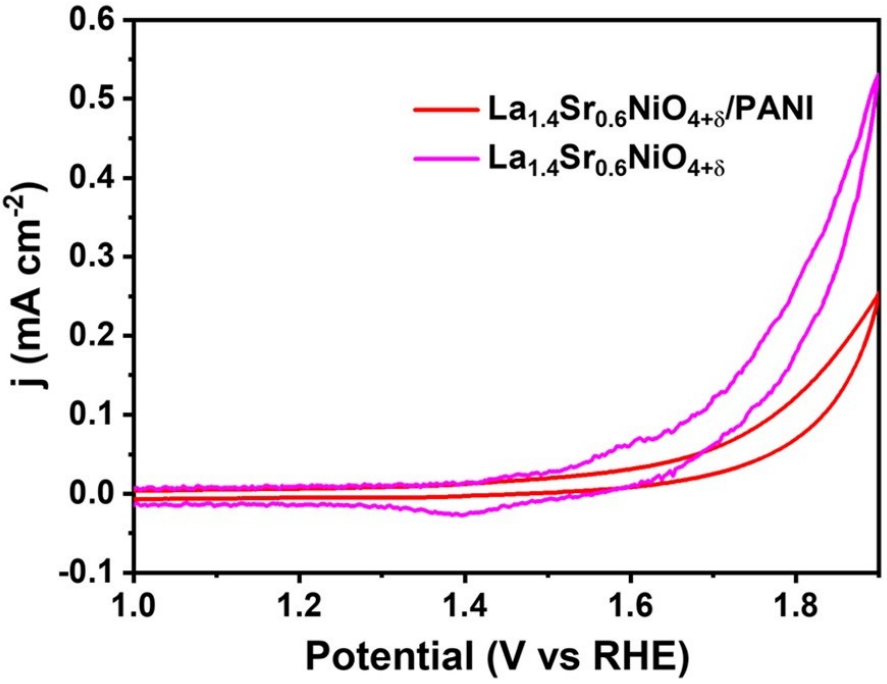

FIGURE 2A.10: (a) CO stripping study of $La_{1.4}Sr_{0.6}NiO_{4+\delta}$and $La_{1.4}Sr_{0.6}NiO_{4+\delta}$ /PANI in 0.5 M NaOH

According to the above electrocatalytic studies, $La_{1.4}Sr_{0.6}NiO_{4+\delta}$ stands out to be the most active catalyst among the $La_{1.4}Sr_{0.6}NiO_{4+\delta}$ oxides. The support PANI could further enhance the MOR efficiency. The higher catalytic efficiency of $La_{1.4}Sr_{0.6}NiO_{4+\delta}$ could originate from its inherent electronic properties. The detailed structural, electronic and surface characterization have already indicated tetragonal distortion in the lattice due to oxidized Ni^{2+} and enhanced surface-adsorbed oxygen at the defect sites of $La_{1.4}Sr_{0.6}NiO_{4+\delta}$. Therefore, next, we probed the MOR mechanism in detail over the most active $La_{1.4}Sr_{0.6}NiO_{4+\delta}$, with the help of DFT and XPS studies.

2A.3.3 Mechanistic Probing

The DFT calculations were carried out on pristine La_2NiO_4 and $La_{1.5}Sr_{0.5}NiO_{4+\delta}$ using plane-wave basis with plane-wave energy and GGA for exchange-correlation energy functional

(see computational details). The computed TDOS for La_2NiO_4 and $La_{1.5}Sr_{0.5}NiO_{4+\delta}$ are shown in Figure 2A.11(a). In the case of pristine La_2NiO_4, the Ni 3d-orbitals split into t_{2g} and e_g, and the occupied orbitals of Ni t_{2g} and e_g along with O 2p orbitals construct the valence band below E_F. On the other hand, the DOS of the unoccupied e_g orbitals above E_F contribute to the conduction band, and the band gap between occupied and unoccupied e_g orbitals are ~4 eV indicating an insulating nature of the pristine oxide. In case of Sr^{2+} doped $La_{1.5}Sr_{0.5}NiO_{4+\delta}$ (Figure 2A.11(b)), there is a clear overlap of the t_{2g} and e_g orbitals of Ni along with O 2p orbitals, and the continuum in the E_F region apparently signifies the semi-metallic feature of $La_{1.4}Sr_{0.6}NiO_{4+\delta}$ [128]. This can happen due to the formation of highly oxidized Ni^{3+} as also has been observed from XAFS and XPS studies due to doping of Sr^{2+} in the A site. The strong hybridization between the Ni 3d states of e_g symmetry and O 2p states lead to the formation of overlapping valance and conduction bands that cross the E_F. With Sr^{2+} doping, the increased overlap between Ni 3d and O 2p states lowers the energy between occupied O 2p states and unoccupied Ni 3d states, and ultimately enhances the Ni 3d - O 2p covalency. The Ni 3d - O 2p hybridisation may be triggered from the closer proximity of Ni^{3+} with the equatorial oxygen, as has been observed from structural investigations. The difference in the bonding between the pristine and Sr^{2+} doped oxides are schematically depicted in Figure 2A.11(c & d). The enhanced covalency due to lattice doping of Sr^{2+} enables $La_{1.4}Sr_{0.6}NiO_{4+\delta}$ to behave as a more active catalyst than the pristine $La_2NiO_{4+\delta}$ analogue. The above theoretical calculations show that the unoccupied e_g band of the highly-oxidized Ni^{3+} shifts downward and overlap with the O 2p band, resulting in band 'hybridization'. The hybridization of these bands may result in Fermi-level 'pinning' at the top of O 2p band [129]. This phenomenon was further explored experimentally by determining the maximum position of the valence band from the onset of the valence band XPS, as shown in Figure 2A.11(e). The binding energies of the onset edge indicate the position of valence-band maxima, and, for all practical purposes, the valence-band spectra obtained from XPS coincide with the DOS [130]. It is apparent that the onset of the valence band is below E_F for pristine $La_2NiO_{4+\delta}$. However, with more extensive doping of Sr^{2+}, the onset edge of the valence band shifted gradually towards the left, indicating pinning of the Fermi level, as well a greater overlap of the valence and conduction bands. It may be inferred that the delocalization of valence-band electrons vis à vis higher covalency facilitated $La_{1.4}Sr_{0.6}NiO_{4+\delta}$ to exhibit highest MOR activity. The higher extent of covalency and mobility of electrons was further probed by an EIS study of $La_{2-x}Sr_xNiO_{4+\delta}$ based electrodes under MOR conditions (0.5 M NaOH and 1.5 M MeOH). The representative Nyquist plots of $La_{2-x}Sr_xNiO_{4+\delta}$ oxides are shown in Figure 2A.11(f). This Figure 2A.11(f) reveals a

large semicircle arc for $La_2NiO_{4+\delta}$ and $La_{1.8}Sr_{0.2}NiO_{4+\delta}$, while smaller semicircles are observed for higher Sr^{2+} doping. $La_{1.4}Sr_{0.6}NiO_{4+\delta}$ exhibited the smallest semicircle at high frequency, indicating the lowest charge-transfer resistance, as well as the highest electronic conductivity, owing to higher covalency of the material. The optimum amount of Sr^{2+} doping has induced the transition from insulator to half-metal, which, in turn, enabled the facile mobility of electrons and the highest degree of MOR activity over $La_{1.4}Sr_{0.6}NiO_{4+\delta}$. The electronic conductivity was further improved by dispersing the $La_{1.4}Sr_{0.6}NiO_{4+\delta}$ over PANI, as can be observed from the inset Nyquist plot of Figure 2A.11(f). The arc of the semicircle in Nyquist plot was greatly decreased for $La_{1.4}Sr_{0.6}NiO_{4+\delta}$/PANI composite compared to $La_{1.4}Sr_{0.6}NiO_{4+\delta}$. This huge reduction of charge-transfer resistance ($\sim$ 20-fold) is due to PANI, which improved the electrical conductivity and ion diffusion during the MOR and as a whole, further enhanced catalytic efficacy [131].

The above results summarise that the close proximity of O 2p centre position to the Fermi Level resulted in Fermi-level pinning at the top of O 2p band. This can significantly influence the lattice-oxygen stability of these oxides by rendering them prone to facile oxidation. Therefore, we propose a lattice-oxygen-mediated methanol-oxidation reaction over the $La_{2-x}Sr_xNiO_{4+\delta}$ oxides as shown in Figure 2A.12(a). The reaction may start with the distorted NiO_6 with oxygen vacancy $\square$ in the lattice. The hydroxyl anion from the electrolyte can be adsorbed on the adjacent site of the catalyst to yield the key intermediate of Ni-OOH species. We have indeed observed the formation of Ni-OOH species on the catalyst surface (vide Figure 2A.5 and 2A.7), and $La_{1.4}Sr_{0.6}NiO_{4+\delta}$ exhibited the highest concentration of Ni-OOH among the oxides. The formation of the Ni-OOH species was further probed by the XPS study of O 1s core-level spectra of the highly efficient $La_{1.4}Sr_{0.6}NiO_{4+\delta}$ after 7h CA studies. The deconvoluted O 1s spectrum of exhausted $La_{1.4}Sr_{0.6}NiO_{4+\delta}$ in Figure 2A.12(b) shows that, in addition to the usual O_L, O_S and O_W peaks, there is an extra peak at 535.5 eV corresponding to the Ni-OOH species on the surface of the catalyst. It must be noted that the corresponding peak of Ni-OOH was not observed in the fresh $La_{1.4}Sr_{0.6}NiO_{4+\delta}$ catalyst. Thus-formed Ni-OOH may enable adsorption of MeOH in the form of Ni-$OOCH_3$. The oxygen vacancy $\square$ in the doped oxides facilitates -OH^- adsorption with a low energy barrier. Incidentally, the oxygen vacancy was found to be highest over $La_{1.4}Sr_{0.6}NiO_{4+\delta}$ (vide Figure 2A.5 and Table 2A.2)

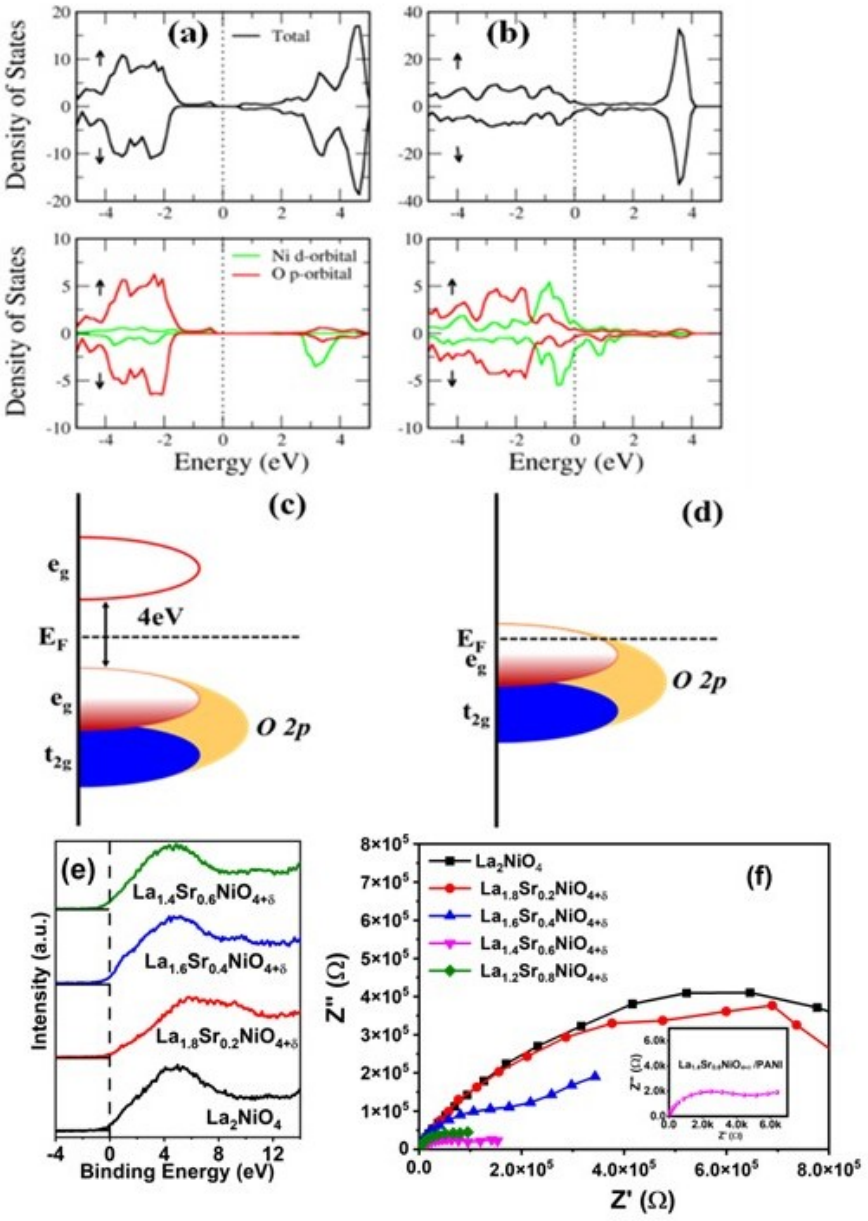

FIGURE 2A.11: (a)Density of states plot for (a) $La_2NiO_{4+\delta}$ and (b) $La_{1.5}Sr_{0.5}NiO_{4+\delta}$, respectively. ↑ and ↓ denote two different spin-states. Schematic representation of Ni 3d-O 2p overlap for (c) $La_2NiO_{4+\delta}$ and (d) $La_{1.4}Sr_{0.6}NiO_{4+\delta}$. (e) Valence band XPS of $La_{2-x}Sr_xNiO_{4+\delta}$ and (f) Nyquist plots of $La_{2-x}Sr_xNiO_{4+\delta}$ oxides. Nyquist plot for $La_{1.4}Sr_{0.6}NiO_{4+\delta}$ /PANI in inset

To validate the product, we have analyzed further the liquid electrolyte obtained after the methanol-oxidation reaction by ^{1}H NMR studies, and the corresponding spectra are shown in Figure 2A.13. The ^{1}H NMR data revealed the presence of the peak around 8.3 ppm, indicating the formation of HCO_2H as one of the products during the methanol-oxidation reaction. The Faradaic efficiency of HCO_2H formed was calculated and tabulated in Table 2A.3. No other liquid product was observed, and the gaseous products were not analyzed over the materials.

The efficient and selective electro-oxidation of methanol to high-value-added HCO_2H over the $La_{1.4}Sr_{0.6}NiO_{4+\delta}$ is also a very important aspect from a commercial and industrial point of view.

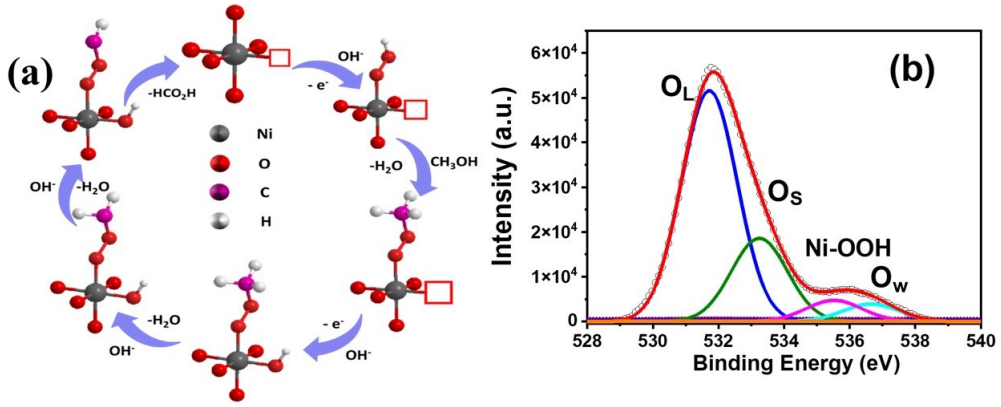

FIGURE 2A.12: (a) Proposed methanol electro-oxidation to HCO_2H over $La_{2-x}Sr_xNiO_{4+\delta}$ involving the lattice oxygen and oxygen vacant sites via formation of the key active species Ni - OOH. (b) O 1s core level spectra of $La_{1.4}Sr_{0.6}NiO_{4+\delta}$ after methanol oxidation reaction to show the formation of Ni-OOH intermediate species

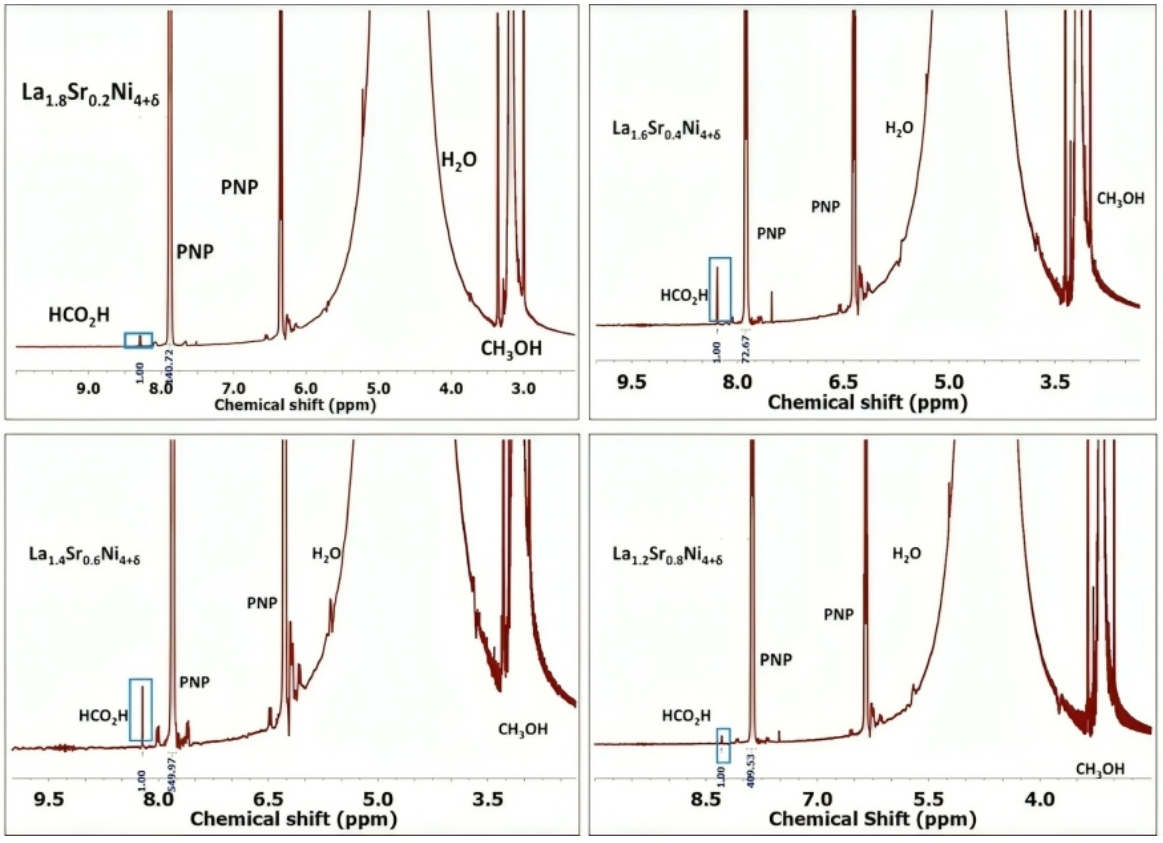

FIGURE 2A.13: ^{1}HNMR spectra after 4h of chronoamperometric study in 1.5 M MeOH and 0.5 M NaOH medium

TABLE 2A.3: Faradaic efficiency of product HCO_2H

Catalysts	**Faradaic efficiency of HCO_2H formation (%)**
$\mathbf{La_{1.8}Sr_{0.2}NiO_{4+\delta}}$	9.3
$\mathbf{La_{1.6}Sr_{0.4}NiO_{4+\delta}}$	8.3
$\mathbf{La_{1.4}Sr_{0.6}NiO_{4+\delta}}$	11.9
$\mathbf{La_{1.2}Sr_{0.8}NiO_{4+\delta}}$	10.4

2A.4 Conclusion

$La_{2-x}Sr_xNiO_{4+\delta}$(x = 0 – 0.8) Ruddlesden Popper oxides were synthesized by a single step single step solution combustion method. Several important conclusions have emerged:

(i) Structural characterization demonstrated that the $La_{2-x}Sr_xNiO_{4+\delta}$ oxides with x = 0 - 0.6 resulted in a single, clean-phase tetragonal structure with I4/mmm space group, whereas higher amount of doping of Sr^{2+} (x = 0.8) crystallized in a lower symmetric orthorhombic phase, along with the primary tetragonal phase. Substitution of trivalent La^{3+} with bivalent $La_{2-x}Sr_xNiO_{4+\delta}$ in the A site invoked charge neutrality, and, therefore, Ni^{2+} was oxidized to Ni^{3+}, exhibiting a compression along the equatorial plane, alongside tetragonal elongation along 'z' axis. The percentage content of Ni^{3+} was found to be highest in $La_{1.4}Sr_{0.6}NiO_{4+\delta}$. A significant amount of oxygen vacancy was also observed in the synthesized materials with a maximum extent of vacancies in $La_{1.4}Sr_{0.6}NiO_{4+\delta}$.

(ii) $La_{1.4}Sr_{0.6}NiO_{4+\delta}$ exhibited the highest efficacy towards methanol oxidation in alkaline medium compared to other synthesized homologous RP oxides. The catalytic efficacy of $La_{1.4}Sr_{0.6}NiO_{4+\delta}$ was further enhanced when PANI was used as the conducting support.

(iii) Mechanistic insights into MOR over the $La_{2-x}Sr_xNiO_{4+\delta}$ oxides were probed, finding that the electronic properties induced by structural deformation and the oxygen defects are due to aliovalent doping in A site. The optimum doping of (Sr^{2+}) in $La_{1.4}Sr_{0.6}NiO_{4+\delta}$ resulted in a high degree of Ni^{3+} 3d - O 2p hybridisation with a close proximity of O 2p centre position to the Fermi level. This not only resulted in higher conductivity but also in Fermi-level pinning taking place at the top of the O 2p band, with facile oxidation of lattice oxygen of $La_{1.4}Sr_{0.6}NiO_{4+\delta}$. Based on these experimental and theoretical findings, we propose an oxygen-vacancy-induced lattice-oxygen-mediated methanol-oxidation reaction mechanism. Taken together, these important overall conclusions point towards RP oxides as being a most promising family of MOR catalysts, capable of further 'tuning', optimization and refinement in our quest to bring about sustainable energy conversion, realize the 'Methanol Economy', and reduce CO_2 emissions.

Chapter 2B

Electro-oxidation Reaction of Methanol over $La_{2-x}Sr_xNi_{1-y}(Mn/Fe/Co)_yO_{4+\delta}$ Ruddlesden-Popper oxides

2B.1 Introduction

The key scientific challenge in MOR using a layered perovskite is to enhance the activity by tunning the structure by creating vacancy, defects and mixed oxidation state. The configuration of La_2NiO_4 creates a relatively open structural framework surface that allows oxygen exchange properties where oxygen from the perovskite layer can occupy interstitial sites of the rock salt layer and diffuse laterally [132–136]. Throughout the process of incorporating interstitial oxygen atoms, the host structure supplies electrons to the surface oxygen while creating holes in the valence band. The presence of interstitial oxygen and holes has a significant impact on determining the comprehensive electrochemical properties.

In chapter 2A, we explored how aliovalent doping at the A site with varied concentrations of rare-earth cation Sr^{2+} can alter the electron density of $La_{2-x}Sr_xNiO_{4+\delta}$ than that of pristine La_2NiO_4 and oxidize Ni^{2+} to a higher valency to attain the charge neutrality, where the octahedral Ni^{3+} sequentially would show a lower electron occupancy in the e_g level. With optimal doping of bivalent $Sr^{2+} = 0.6$, $La_{1.4}Sr_{0.6}NiO_{4+\delta}$ exhibited a very high methanol-oxidation reactivity [132].

This inturn can amend the electrical conductivity of the material with either oxygen deficiency or oxygen excess. On the other hand, this doping can create mixed valence in the B site, which effectively can play a major role in MOR.

In the present work, we try to further explore the MOR activity of $La_{2-x}Sr_xNiO_{4+\delta}$ by doping of Mn, Fe and Co at the B site. Herewith, we enhanced the percentage of Ni to higher oxidation state with the formation of active redox centers (Ni^{2+}/Ni^{3+}) and investigated the MOR mechanism over pure phase $La_{1.4}Sr_{0.6}Ni_{0.9}(Mn/Fe/Co)_{0.1}O_{4+\delta}$. Through a combination of experimental observations and DFT calculations, we have provided evidence that doping at the B site resulted in high MOR activity by further improving electrical conductivity via DOS. The combination of theoretical calculations and experimental observations suggests that MOR occurs with the formation of Ni-OOH as a crucial active intermediate species.

2B.2 Materials and methods

2B.2.1 Synthesis of $La_{1.4}Sr_{0.6}Ni_{0.9}(Mn/Fe/Co)_{0.1}O_{4+\delta}$

A low temperature one step solution combustion synthesis method was adopted for the synthesis of $La_{1.4}Sr_{0.6}Ni_{0.9}(Mn/Fe/Co)_{0.1}O_{4+\delta}$. It involves a propellant chemistry between the oxidizer, metal nitrates, and the fuel glycine [137, 138]. In this method of synthesis, stoichiometrically appropriate amounts of metal precursors, $La(NO_3)_3\cdot 6H_2O$ (SRL chemicals, 99%), $Sr(NO_3)_2$ (Sigma Aldrich, 99%), $Ni(NO_3)_2\cdot 6H_2O$ (SD fine, 99%), $Co(NO_3)_2\cdot 6H_2O$ (Sigma Aldrich, 99%), $Fe(NO_3)_3\cdot 9H_2O$ (Sigma Aldrich, 99%), $Mn(NO_3)_2\cdot 4H_2O$ (Sigma Aldrich, 99%) and fuel $C_2H_5NO_2$ (Sigma Aldrich, 99%) were dissolved in 50 mL of deionized water in a 300 mL borosilicate dish. The mixture was introduced to preheated furnace at 450 °C. In the beginning, the solution boiled vigorously and underwent dehydration, after which the surface ignited. Upon achieving complete dehydration, a combustion process commenced leading to the exothermic decomposition of the metal-fuel complexes, accompanied by the release of CO_2, N_2, and H_2O. The dehydrated product burned with a temperature reaching up to 1000 °C yielding a voluminous product. The resultant mixture was calcined at 1000 °C to obtain pure phased material.

2B.2.2 Structural, Surface and Electronic Characterisation

High-resolution powder XRD using a Rigaku Ultima IV X-ray diffractometer with CuKα radiation ($\lambda = 1.5418$ Å) was adopted to investigate the structural characterization of synthesized $La_{1.4}Sr_{0.6}Ni_{0.9}(Mn/Fe/Co)_{0.1}O_{4+\delta}$ at a scan rate of 0.5° min^{-1} and a step size of 0.01°. The average nanocrystalline diameters (D) were calculated from the broadening of the highest peak using Scherrer's formula,

$$D = \frac{0.9\lambda}{B\text{Cos}\theta} \tag{2B.1}$$

where B is the full-width at half-maximum, λ is the wavelength of the radiation, and θ is the corresponding angle. Fullprof program suite was adopted to refine the powder X-ray diffraction patterns. Rietveld refinements were carried out by systematic variation of various parameters, including the overall scale factor, background and profile parameters, unit-cell lattice parameters, atomic positions, Full width half maxima, shape, isotopic thermal parameters, oxygen occupancy, and other relevant factors. ED-XRF was used to probe the actual atomic ratio of the synthesized $La_{1.4}Sr_{0.6}Ni_{0.9}(Mn/Fe/Co)_{0.1}O_{4+\delta}$, with the help of an Epsilon 1; PAN analytical instrument. HR - SEM was carried out with FE - SEM, (FEI - ApreoS) at 30 kV acceleration. The surface composition, elemental oxidation state and bonding was probed by XPS with the help of Thermo Scientific K-Alpha surface-analysis spectrometer housing Al K_α as the X-ray source (1486.6 eV). The base pressure at the analysing chamber was maintained at 5×10^{-9} mbar. The data profiles were subjected to a nonlinear least-squares curve fitting program with a Gaussian-Lorentzian production function and processed with Avantage software. B.E. of all XPS data was calibrated vs the standard C 1s peak at 284.85 eV.

2B.2.3 Electrocatalytic Oxidation of Methanol

OrigaFlex OGF500 electrochemical workstation was used for the electrocatalytic MOR. A typical three-electrode setup comprising of Hg/HgO (1 M KOH) as the reference, Pt as the counter electrode and GCE as the working electrode was used. The GCE was modified by drop casting the catalyst ink on its surface of area 0.07 cm^2. GCE was polished using 0.05 μm alumina slurry before drop casting the catalyst ink. The catalyst ink was prepared by dispersing the physical mixture of 5 mg of the synthesized catalyst and 2 mg of carbon black in 1 mL of methanol and 10 μL Nafion solution. An aqueous solution of 0.5 M NaOH served as electrolyte.

ECSA was determined by conducting double - step chronoamperometric expert experiments and calculated using Cottrell equation as elobrated chapter 2A.

To evaluate the MOR, CV was carried out in 0.5 M NaOH and 0.5 M MeOH. CA was adopted to study the stability of the catalysts. In all measurements, potential of Hg/HgO is converted to RHE in 0.5 M NaOH according to the following equation: $E_{RHE} = E_{Hg/HgO} + 0.059 \times pH + 0.098$. The concentration of the surface Ni - OOH layers after CV cycles in NaOH medium was calculated with respect to the geometrical surface area according to the following equation

$$I_p = \left[\left(\frac{z^2F^2}{4RT}\right) A\tau^*\nu\right] \tag{2B.2}$$

I_p = Peak current density (mA cm^{-2}), Z = No. of electrons transferred, R = Gas constant, T = Temperature, A = Geometrical area of the electrode (0.07 cm^2) ν = scan rate, and τ^* = surface coverage of Ni - OOH. The liquid products after CA were analysed using ^{1}H NMR (Bruker AV NEO, 400 MHz). For this, about 0.4 mL of electrolysis solution, 0.1 mL of D_2O, and 5 mg of 4-nitrophenol (as an internal standard) were added into the NMR tube to identify the product. EIS study was carried out at 1.56 V vs RHE to study the electron transfer for MOR over a frequency range of 0.1 Hz to 1 MHz with a sinusoidal excitation signal of 10 mV using a Biologic Sp-150 electrochemical workstation with the conventional three-electrode system in an alkaline mixture of 0.5 M MeOH and 0.5 M NaOH.

2B.2.4 Computational Details

The geometry optimization and electronic structure calculations of $La_{1.5}Sr_{0.5}Ni_{0.9}(Mn/Fe/Co)_{0.1}O_{4+\delta}$ were performed using plane-wave basis with plane-wave energy cut-off of 500 eV and GGA for exchange-correlation energy functional in the version of PBE [90] as implemented in VASP 6.3.2 [139–142]. Initial coordinates for geometry optimization of $La_{1.5}Sr_{0.5}NiO_{4+\delta}$ was taken from our previous work on $La_{1.5}Sr_{0.5}Ni_{0.9}M_{0.1}O_4$ materials [132]. $La_{1.5}Sr_{0.5}Ni_{0.9}M_{0.1}O_4$ unit cell (a=7.692 Å, b=19.230 Å, c=12.711 Å, α=β=γ=90°) was created by replacing one of the La with Sr in a 2×5×1 supercell of $La_{1.5}Sr_{0.5}NiO_4$ and then geometry optimization was done. For all the calculation, 4×2×3 k-point mesh with Monkhorst-pack scheme were used. DFT (PBE) + U methodology (with an additional Hubbard-like term, U) was used to consider strong on-site Coulomb interaction of localized electrons (3d and 4f electrons), which is not correctly described by PBE functional. We applied the onsite Coulomb interaction U into all

of the GGA calculations with the setting of U_{eff}@La = 5.5 eV, U_{eff}@Ni = 8.33 as reported in previous literatures [94].

2B.3 Results and Discussion

2B.3.1 Structure, Surface and Electronic Properties of Catalysts

The structural information and phase purity of the solution combustion synthesized $La_{1.4}Sr_{0.6}Ni_{0.9}(Mn/Fe/Co)_{0.1}O_{4+\delta}$ was probed by powder XRD. The representative XRD patterns as shown in Figure 2B.1(a), indicate that the synthesized materials crystallized in phase-pure Ruddlesden Popper structure and are in good agreement with the reported profiles [132, 134, 143–145]. $La_{1.4}Sr_{0.6}Ni_{0.9}(Mn/Fe/Co)_{0.1}O_{4+\delta}$ exhibited a tetragonal symmetry with I4/mmm space group [JCPDS No. 81-0742]. There was no impurity of La_2O_3, NiO, Fe_2O_3, MnO, CoO phases observed in the XRD patterns of any of the synthesized doped oxide.

To have further insight into the structural information, the powder patterns were refined using Rietveld refinement. The refinement employed a pseudo-Voigt profile function, and the background correction was carried out using six polynomial functions. In this context, the I4/mmm space group was considered where La and Sr are randomly distributed at 4e (0,0,0) sites, Ni/Co/Fe/Mn at 2a (0,0,0) and the two inequivalent oxygen atoms, O_1 at 4c (0, 0.5,0) and O_2 at 4e (0, 0, 0) Wyckoff sites. The refinement profiles are shown in Figure 2B.1(b). The black coloured line represents the obtained empirical curve and the superimposed red coloured one designates the fitted curve with theoretically calculated intensities. The apparent fitting and the reliability factors, such as R_{bragg}, and χ^2 ensures the formation of single-phase solid solutions with lattice doping of Sr^{2+} in A site and Mn/Fe/Co in B site of $La_2NiO_{4+\delta}$. The corresponding lattice parameters obtained from refinement and reliability factors R_{bragg} and χ^2 are provided in Table 2B.1. It has been observed in our previous report that the lattice constants 'a'/'b' decreased gradually, whereas 'c' increased with an increase in Sr^{2+} doping at La^{3+} site [132]. This tetragonal elongation along 'z' axis of the unit cell was explained by Jahn - Teller distortion due to the formation of Ni^{3+} in B site. The asymmetrical occupancy of electrons in the e_g orbital, characterized by a low-spin $t_{2g}^6 d_z^2$ configuration, exhibited by the Ni^{3+} sites in an octahedral environment, was identified as the cause of the observed tetragonal elongation. As the Sr^{2+} concentration increased up to x = 0.6 in $La_{1.4}Sr_{0.6}NiO_{4+\delta}$, the elongation along the 'z' axis was an indicative of a reduced overlap between d_{z^2} and axial O 2p orbitals, while the

compression along the equatorial plane suggests an enhanced overlap between $d_{x^2-y^2}$ and O 2p orbitals. However, interestingly here we observe that with further doping of Mn/Fe/Co in B site, this trend reverses and 'c' decreases sharply while 'a'/'b' increases gradually (Figure 2B.1(c)). The increased concentration of Ni^{3+} due to B site doping may cause the switching of electronic configuration over to $t_{2g}^6\ d_{x^2-y^2}^1$ from $t_{2g}^6 d_z^2$. This phenomenon in Ruddlesden Popper phase oxides is already reported [75, 97, 146]. The configuration $t_{2g}^6\ d_{x^2-y^2}^1$ would permit enhanced overlap of dz^2 and axial O 2p while reduced overlap of $d_{x^2-y^2}$ and O 2p orbitals. The significant shrinkage of axial plane and expansion of equatorial planes subsequently increased the unit cell volume of the system, and this was found most profound with Co^{2+} doping in the B site.

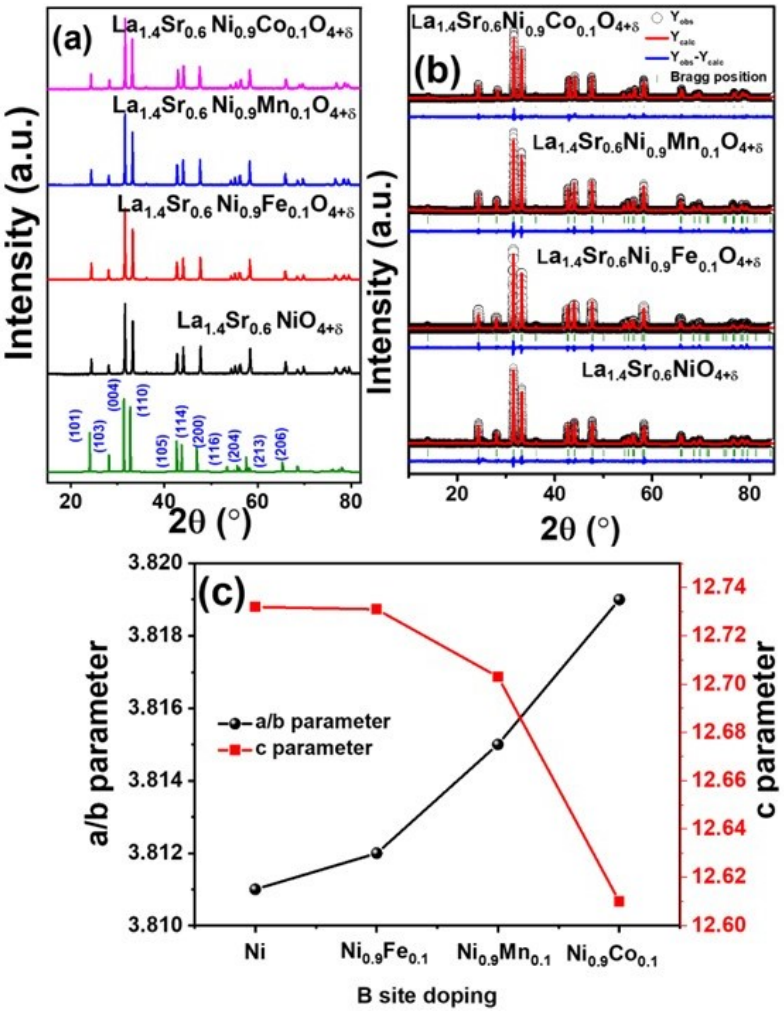

FIGURE 2B.1: (a) Experimentally observed XRD patterns with the simulated one, (b) Rietveld refinement of synthesized $La_{1.4}Sr_{0.6}Ni_{0.9}(Mn/Fe/Co)_{0.1}O_{4+\delta}$ (c) Variation of lattice parameters "a/b" and "c" with B site doping

TABLE 2B.1: Rietveld refine lattice parameters and atom occupancy of $La_{1.4}Sr_{0.6}NiO_{4+\delta}$ and $La_{1.4}Sr_{0.6}Ni_{0.9}(Mn/Fe/Co)_{0.1}O_{4+\delta}$

Catalysts	**Cell parameters (A)**		**Cell volume (A)**	χ^2	$\mathbf{R_{bragg}}$	**Occupancy**					
	a=b	**c**				**La**	**Sr**	**Ni**	**Fe/Mn/Co**	**O_1**	**O_2**
$\mathbf{La_{1.4}Sr_{0.6}NiO_{4+\delta}}$	3.811	12.73	184.6	1.25		0.48	0.70	0.53	-	1.16	1.12
$\mathbf{La_{1.4}Sr_{0.6}Ni_{0.9}Fe_{0.1}O_{4+\delta}}$	3.813	12.73	185.0	3.37	3.46	0.40	0.68	0.21	0.47	1.75	1.32
$\mathbf{La_{1.4}Sr_{0.6}Ni_{0.9}Mn_{0.1}O_{4+\delta}}$	3.815	12.70	184.9	3.58	5.7	0.39	0.55	0.34	0.52	1.84	1.38
$\mathbf{La_{1.4}Sr_{0.6}Ni_{0.9}Co_{0.1}O_{4+\delta}}$	3.819	12.61	185.2	1.19	1.66	0.51	0.66	0.22	0.51	1.76	1.16

The ED-XRF of the prepared catalysts inferred that the actual doping concentration of Sr, Fe, Mn and Co was similar to the theoretically calculated values (Table 2B.2).To further verify the extent of Sr doping on the A site and Co doping on the B site, ICP-OES analysis was conducted with the synthesized material. The ICP results in Table 2B.3 show that the elements fall within the anticipated weight percentage range, exhibiting a margin of ±2%.

TABLE 2B.2: ED-XRF of $La_{1.4}Sr_{0.6}NiO_{4+\delta}$ and $La_{1.4}Sr_{0.6}Ni_{0.9}(Mn/Fe/Co)_{0.1}O_{4+\delta}$

Catalysts	**XRF (wt%)**						**Calculated (wt%)**					
	La	Sr	Ni	Fe	Co	Mn	La	Sr	Ni	Fe	Co	Mn
$\mathbf{La_{1.4}Sr_{0.6}NiO_{4+\delta}}$	62.5	18.0	19.5				63.6	17.1	19.2			
$\mathbf{La_{1.4}Sr_{0.6}Ni_{0.9}Fe_{0.1}O_{4+\delta}}$	61.9	16.6	20.3	1.2			63.6	17.2	17.2	1.8		
$\mathbf{La_{1.4}Sr_{0.6}Ni_{0.9}Mn_{0.1}O_{4+\delta}}$	61.1	16.8	20.7			1.2	63.6	17.2	17.3			1.72
$\mathbf{La_{1.4}Sr_{0.6}Ni_{0.9}Co_{0.1}O_{4+\delta}}$	58.9	18.1	20.4		2.4		63.6	17.1	17.2		1.9	

TABLE 2B.3: ICP-OES of $La_{1.4}Sr_{0.6}NiO_{4+\delta}$and $La_{1.4}Sr_{0.6}Ni_{0.9}Co_{0.1}O_{4+\delta}$

Catalysts	**Wt(%)**			
	La	Sr	Ni	Co
$\mathbf{La_{1.4}Sr_{0.6}NiO_{4+\delta}}$	54.95	14.65	15.77	
$\mathbf{La_{1.4}Sr_{0.6}Ni_{0.9}Co_{0.1}O_{4+\delta}}$	58.9	15.07	14.12	1.9

The nano-structural features of $La_{1.4}Sr_{0.6}Ni_{0.9}(Mn/Fe/Co)_{0.1}O_{4+\delta}$ were probed with HR-SEM images shown in Figure 2B.2. The synthesized materials exhibited a diffuse structure. The EDAX mapping in (Figure 2B.2) demonstrates the homogeneous distribution of Sr, Fe, Co and Mn in $La_2NiO_{4+\delta}$ matrix.

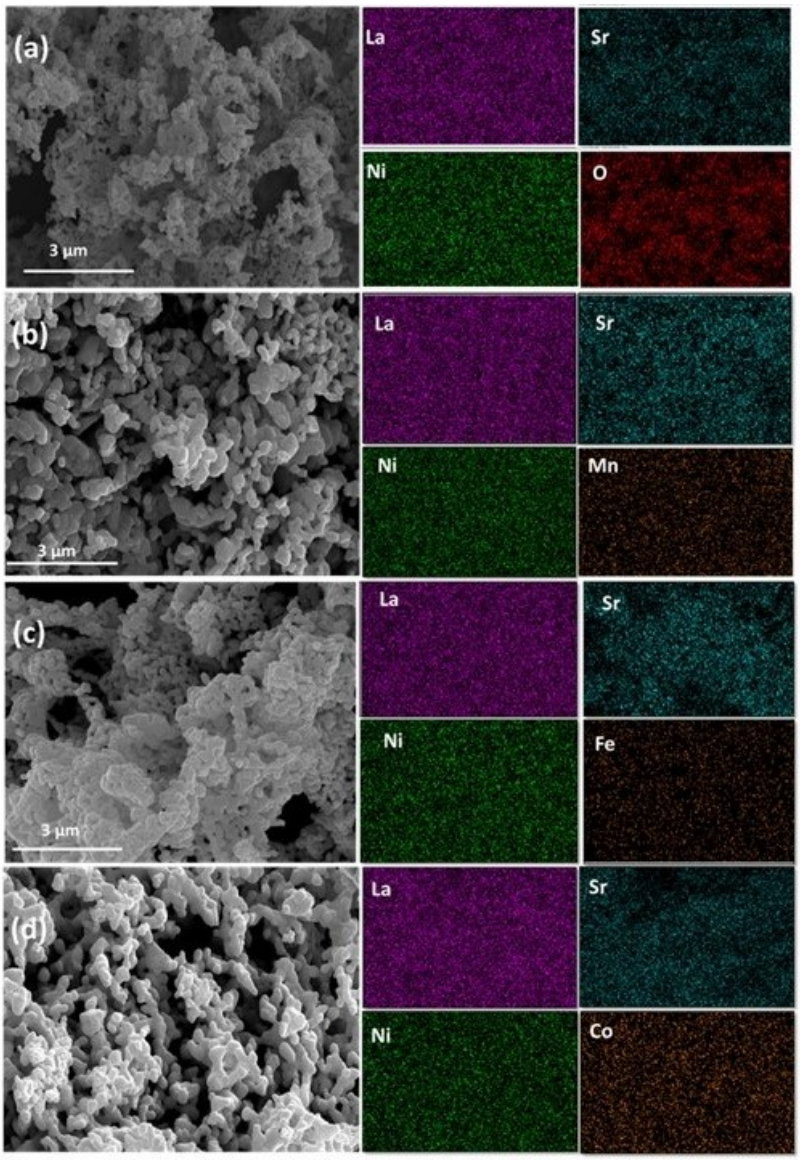

FIGURE 2B.2: (a) FE - SEM images and corresponding EDAX mapping of (a) $La_{1.4}Sr_{0.6}NiO_{4+\delta}$ (b) $La_{1.4}Sr_{0.6}Ni_{0.9}Mn_{0.1}O_{4+\delta}$ (c) $La_{1.4}Sr_{0.6}Ni_{0.9}Fe_{0.1}O_{4+\delta}$ and (d) $La_{1.4}Sr_{0.6}Ni_{0.9}Co_{0.1}O_{4+\delta}$

XPS analysis was employed to probe the surface chemical bonding and electronic states of the elements in solution combustion synthesized $La_{1.4}Sr_{0.6}Ni_{0.9}(Mn/Fe/Co)_{0.1}O_{4+\delta}$. The survey spectra in Figure 2B.3(a) indicate the presence of metals on the surface in their expected atomic ratio. We have considered Ni 3p for deconvolution instead of Ni 2p due to the overlapping peaks of Ni $2p_{3/2}$ and La $3d_{3/2}$ satellites [100, 147–149]. Ni 3p core level spectra of $La_{1.4}Sr_{0.6}NiO_{4+\delta}$ revealed the simultaneous presence of Ni^{2+} and Ni^{3+} due to Sr^{2+} doping (Figure 2B.3(b)). The deconvoluted Ni 3p spectra reveal Ni^{2+} peaks at 66.7 and 68.5 eV, corresponding to the spin-orbital splitting of Ni $3p_{3/2}$ and Ni $3p_{1/2}$, respectively. Likewise, the peaks observed at 71.2 and 73.7 eV correspond to the Ni^{3+} state of Ni $3p_{3/2}$ and Ni $3p_{1/2}$, respectively [150–152]. The partial substitution of Fe, Mn and Co in B site further enhances Ni^{3+} concentration. The

percentage content of Ni^{3+} gradually increased from 24.3% without B site doping to 34.3% with Co doping (vide Table 2B.4). The increase in the proportion of Ni^{3+} formation with B site doping was characterized by $3d^7$ electrons having electronic configuration $t_{2g}^6\ d_{x^2-y^2}^1$ which accounts for the elongation of equilateral 'a'/'b' and compression of axial 'c' as observed from Rietveld refinement of $La_{1.4}Sr_{0.6}Ni_{0.9}(Mn/Fe/Co)_{0.1}O_{4+\delta}$.

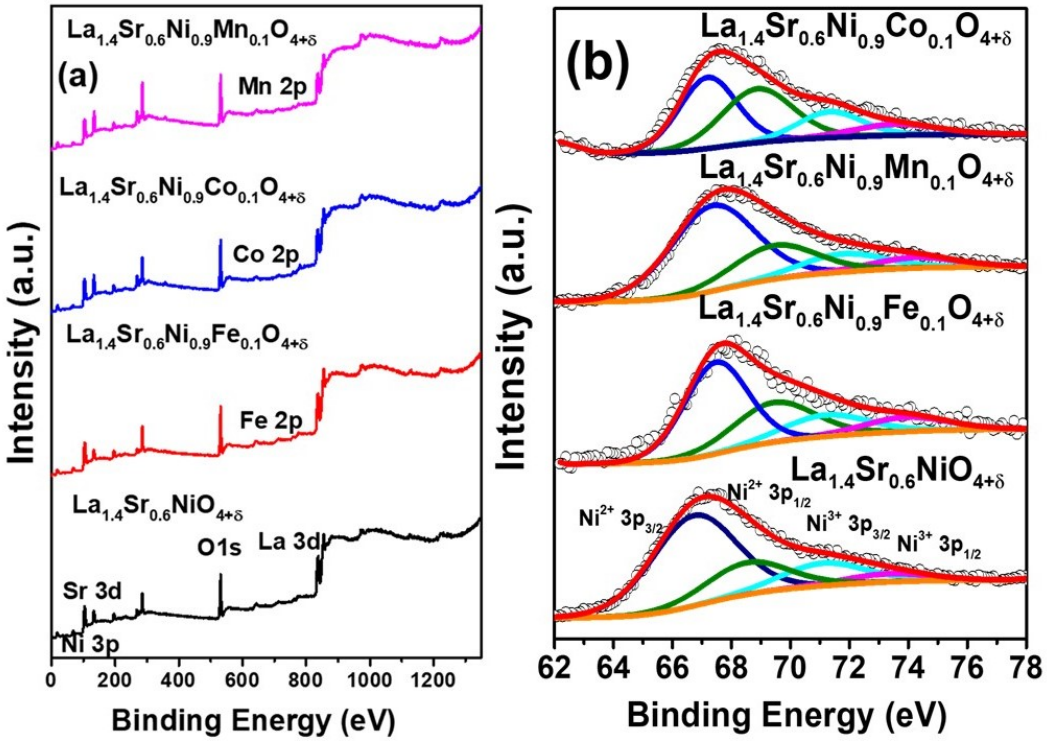

FIGURE 2B.3: (a)XPS survey spectra and (b) Ni 3p core level spectra of $La_{1.4}Sr_{0.6}Ni_{0.9}(Mn/Fe/Co)_{0.1}O_{4+\delta}$

The increase in Ni^{3+} concentration can be attributed to the presence of higher 2+ oxidation states of the dopants (Mn/Fe/Co) in the B site. Illustrated in Figure 2B.4(a), the Fe 2p spectra of $La_{1.4}Sr_{0.6}Ni_{0.9}Fe_{0.1}O_{4+\delta}$ feature two pairs of peaks corresponding to Fe $2p_{3/2}$ and Fe $2p_{1/2}$. Upon deconvolution, the spectra reveal the coexistence of both Fe^{2+} and Fe^{3+} states. The peaks observed at 710.8 and 724.3 eV belong to Fe^{2+} of Fe $2p_{3/2}$ and Fe $2p_{1/2}$, while those at 714.3 and 726.8 eV correspond to Fe^{3+}. Additionally, two satellite peaks were observed at 718.0 and 729.8 eV. Upon deconvolution, the high-resolution Mn 2p spectrum of $La_{1.4}Sr_{0.6}Ni_{0.9}Mn_{0.1}O_{4+\delta}$ (depicted in Figure 2B.4(b)) exhibited the peaks at 639.2 and 654.0 eV attributed to Mn^{2+} of Mn $2p_{3/2}$ and Mn $2p_{1/2}$, whereas Mn^{3+} states were identified at binding energies of 644.1 eV ($2p_{3/2}$) and 655.5 eV ($2p_{1/2}$) [153, 154]. In case of Co 2p spectrum (Figure 2B.4(c)), the spin-orbit doublet of the Co $2p_{3/2}$ and Co $2p_{1/2}$ peaks were further deconvoluted into four distinct peaks. The peaks that appeared at 779.7 and 794.8 eV are assigned with Co^{3+}, while

the ones at 781.0 and 796.3 eV corresponds to Co^{2+} [155–157]. When analysing the distribution of 2+ ions within the B site, it becomes evident that Co^{2+} displayed the highest percentage, reaching 60.99%. In contrast, both Mn^{2+} and Fe^{2+} exhibited lower proportions, accounting for 33.8% and 32.9% respectively. The composition $La_{1.4}Sr_{0.6}Ni_{0.9}Co_{0.1}O_{4+\delta}$, which possessed the highest Co^{2+} concentration, also demonstrated a simultaneous rise in Ni^{3+} concentration, as documented in Table 2B.4.

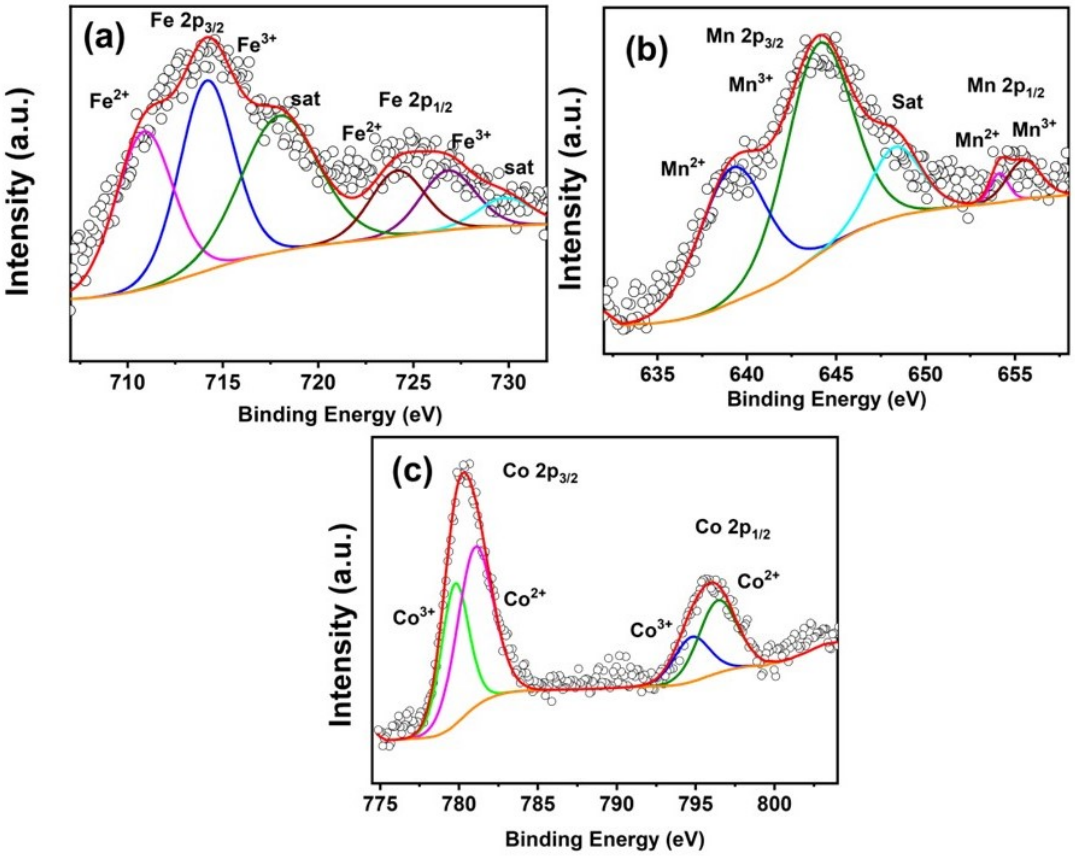

FIGURE 2B.4: (a) Fe 2p core level spectra of $La_{1.4}Sr_{0.6}Ni_{0.9}Fe_{0.1}O_{4+\delta}$ (c) Mn 2p core level spectra of $La_{1.4}Sr_{0.6}Ni_{0.9}Mn_{0.1}O_{4+\delta}$ (d) Co 2p spectra of $La_{1.4}Sr_{0.6}Ni_{0.9}Co_{0.1}O_{4+\delta}$

The deconvoluted core-level spectra of O 1s (Figure 2B.5) show three distinguishable peaks at 531.2, 533.4 and 535.5 eV corresponding to lattice oxygen (O_L), adsorbed oxygen species in the defect sites (O_S), and hydroxyl species of surface-adsorbed water molecules (O_W) [22, 158]. The total oxygen content in the surface was calculated from the area under the curve to the total area of the spectra, where total area is $O_T = O_L + O_S + O_W$. The defective surface oxygen on $La_{1.4}Sr_{0.6}NiO_{4+\delta}$ was 74.1% and it increased to 77.8% with partial doping of Co^{2+} in B site. The highest occurrence of Ni^{3+} and Co^{2+} could be attributed to the formation of the maximum surface oxygen vacancy in $La_{1.4}Sr_{0.6}Ni_{0.9}Co_{0.1}O_{4+\delta}$.

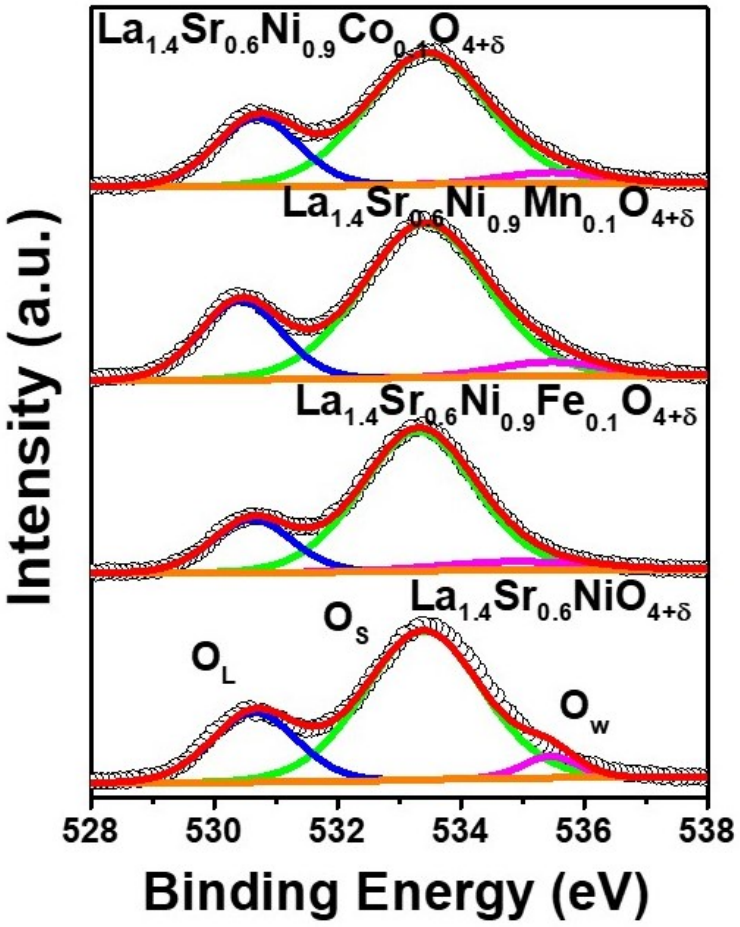

FIGURE 2B.5: (a)O 1s core level spectra of $La_{1.4}Sr_{0.6}Ni_{0.9}(Mn/Fe/Co)_{0.1}O_{4+\delta}$

TABLE 2B.4: Ni^{3+} Concentration, Bivalent concentration of dopants, Defect site oxygen species, and surface –OOH concentration

Catalysts	**Ni^{3+} (%)**	**$Co^{2+}/Fe^{2+}/Mn^{2+}$**	**O_S (%)**	**Surface concentration Ni-OOH** ($\gamma*$) (mol cm^{-2})
$\mathbf{La_{1.4}Sr_{0.6}NiO_{4+\delta}}$	24.3	-	73.1	7.61×10^{-8}
$\mathbf{La_{1.4}Sr_{0.6}Ni_{0.9}Fe_{0.1}O_{4+\delta}}$	27.6	32.9	74.3	1.88×10^{-7}
$\mathbf{La_{1.4}Sr_{0.6}Ni_{0.9}Mn_{0.1}O_{4+\delta}}$	33.3	33.8	75.6	1.16×10^{-7}
$\mathbf{La_{1.4}Sr_{0.6}Ni_{0.9}Co_{0.1}O_{4+\delta}}$	34.3	60.9	77.8	3.67×10^{-7}

Investigation was carried out to examine the influence of ECSA on the activity of MOR Figure (2B.6). The ECSA calculated using Cottrell equation of shows that $La_{1.4}Sr_{0.6}Ni_{0.9}Co_{0.1}O_{4+\delta}$ exhibited the highest ECSA of 9.87 cm^2 compared to other Ruddlesden Popper oxides inferring the better efficacy of the material towards MOR (Table 2B.5).

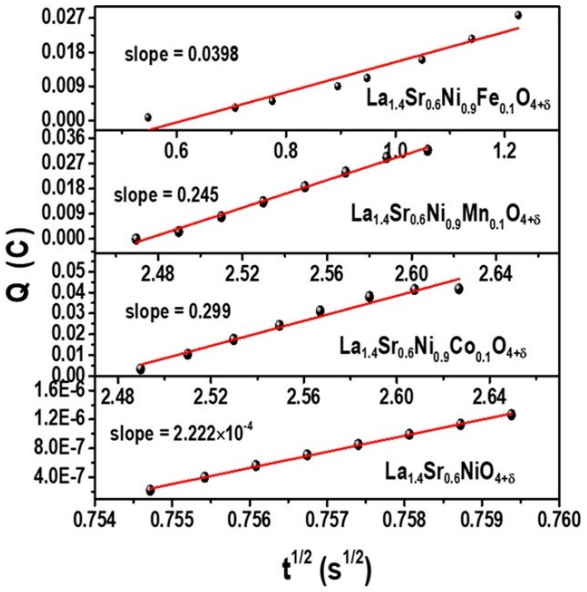

FIGURE 2B.6: Plot of charge against time according to Cottrell equation of $La_{1.4}Sr_{0.6}Ni_{0.9}(Mn/Fe/Co)_{0.1}O_{4+\delta}$

TABLE 2B.5: ECSA of $La_{1.4}Sr_{0.6}Ni_{0.9}(Mn/Fe/Co)_{0.1}O_{4+\delta}$ and $La_{1.4}Sr_{0.6}NiO_{4+\delta}$

Catalysts	**ECSA (cm^2)**
$\mathbf{La_{1.4}Sr_{0.6}NiO_{4+\delta}}$	0.07
$\mathbf{La_{1.4}Sr_{0.6}Ni_{0.9}Fe_{0.1}O_{4+\delta}}$	1.31
$\mathbf{La_{1.4}Sr_{0.6}Ni_{0.9}Mn_{0.1}O_{4+\delta}}$	8.12
$\mathbf{La_{1.4}Sr_{0.6}Ni_{0.9}Co_{0.1}O_{4+\delta}}$	9.87

2B.3.2 Electrocatalytic Oxidation of Methanol

The electrocatalytic activity of $La_{1.4}Sr_{0.6}Ni_{0.9}(Mn/Fe/Co)_{0.1}O_{4+\delta}$ was systematically explored for methanol oxidation reactions with the help of cyclic voltammetry measurements conducted in 0.5 M NaOH and 0.5 M MeOH at a scan rate of 50 mV s^{-1}. Initially, the materials were activated in 0.5 M NaOH by cycling 25 scans within a potential window of 0.8 to 1.8 V vs RHE at a scan rate of 10 - 100 mV s^{-1} prior to the screening of MOR. The cyclic voltammograms obtained in 0.5 M NaOH exhibited a distinguishable peak at 1.49 V vs RHE (labelled as I) in the forward scan and another at 1.15 V vs RHE (labelled as II) in the reverse scan as shown in Figure 2B.7. These peaks demonstrated characteristic behaviour associated with Ni-based electrodes, indicating the oxidation of Ni and the formation of -OOH species linked to Ni^{2+}/Ni^{3+} redox couple. The CV trace in Figure 2B.7 also indicated an additional minor peak at 1.36 V vs RHE (labelled as Peak III) during the forward scan and at 1.26 V vs RHE (labelled as Peak IV) during the reverse scan for $La_{1.4}Sr_{0.6}Ni_{0.9}Co_{0.1}O_{4+\delta}$ [159–161]. The minor peak corresponds to

the oxidation of Co^{3+}/ Co^{4+} and was in accordance with previous findings in the literature. No corresponding peaks were evident for the oxidation of Mn^{2+} or Fe^{2+}.

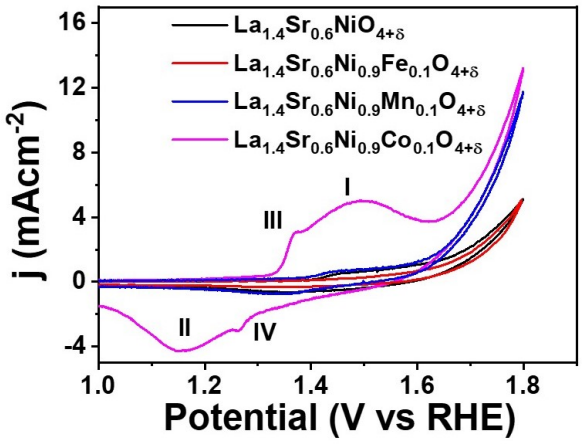

FIGURE 2B.7: CVs of $La_{1.4}Sr_{0.6}O_{4+\delta}$, $La_{1.4}Sr_{0.6}Ni_{0.9}Fe_{0.1}O_{4+\delta}$, $La_{1.4}Sr_{0.6}Ni_{0.9}Mn_{0.1}O_{4+\delta}$ and $La_{1.4}Sr_{0.6}Ni_{0.9}Co_{0.1}O_{4+\delta}$ in 0.5 M NaOH with a scan speed of 50 mV s^{-1}

Interestingly, as the scan rate was elevated from 10 to 100 mV s^{-1}, an increase in peak current density was observed, indicating the formation of a more substantial layer of -OOH species enriched with Ni^{3+} on the catalyst's surface (Figure 2B.8). The surface concentration of these -OOH layers was quantified using peak current densities, revealing that $La_{1.4}Sr_{0.6}Ni_{0.9}Co_{0.1}O_{4+\delta}$ possessed the highest -OOH surface concentration of 3.67×10^{-7} mol cm^{-2} among the catalysts (as tabulated in Table 2B.4). Notably, the highest level of Ni - OOH formation was achieved when the scan rate was 50 mV s^{-1}, designating it as the optimal scan rate for methanol oxidation. At scan rates exceeding this optimal value (ranging from 60 to 100 mV s^{-1}), the oxidation peak associated with Ni^{2+} shifted to higher potentials. Simultaneously, the growth rate of surface Ni - OOH species was compromised in comparison to lower scan rates (as illustrated in Figure 2B.8). This incomplete oxidation of Ni^{2+} could be attributed to limitations in the reaction kinetics, wherein insufficient time was available for the process to achieve completion [22, 162].

The MOR activity of the synthesized $La_{1.4}Sr_{0.6}Ni_{0.9}(Mn/Fe/Co)_{0.1}O_{4+\delta}$ catalysts in 0.5 M NaOH and 0.5 M NaOH electrolyte was carried out at scan rate of 50 mV s^{-1}, and the CV traces are shown in Figure 2B.9(a). With the introduction of methanol, the oxidation peak of Ni and Co became indiscernible, and a rapid surge in current density occurred as a result of methanol oxidation. The methanol oxidation peak was observed after the Ni oxidation peak suggesting the –OOH layer as the active species for MOR. All the catalysts exhibited a distinguishable anodic and cathodic peak in the forward and reverse scan. The surge in anodic peak was observed at 1.58 V vs RHE with current density 6.25 mA cm^{-2} for $La_{1.4}Sr_{0.6}NiO_{4+\delta}$.

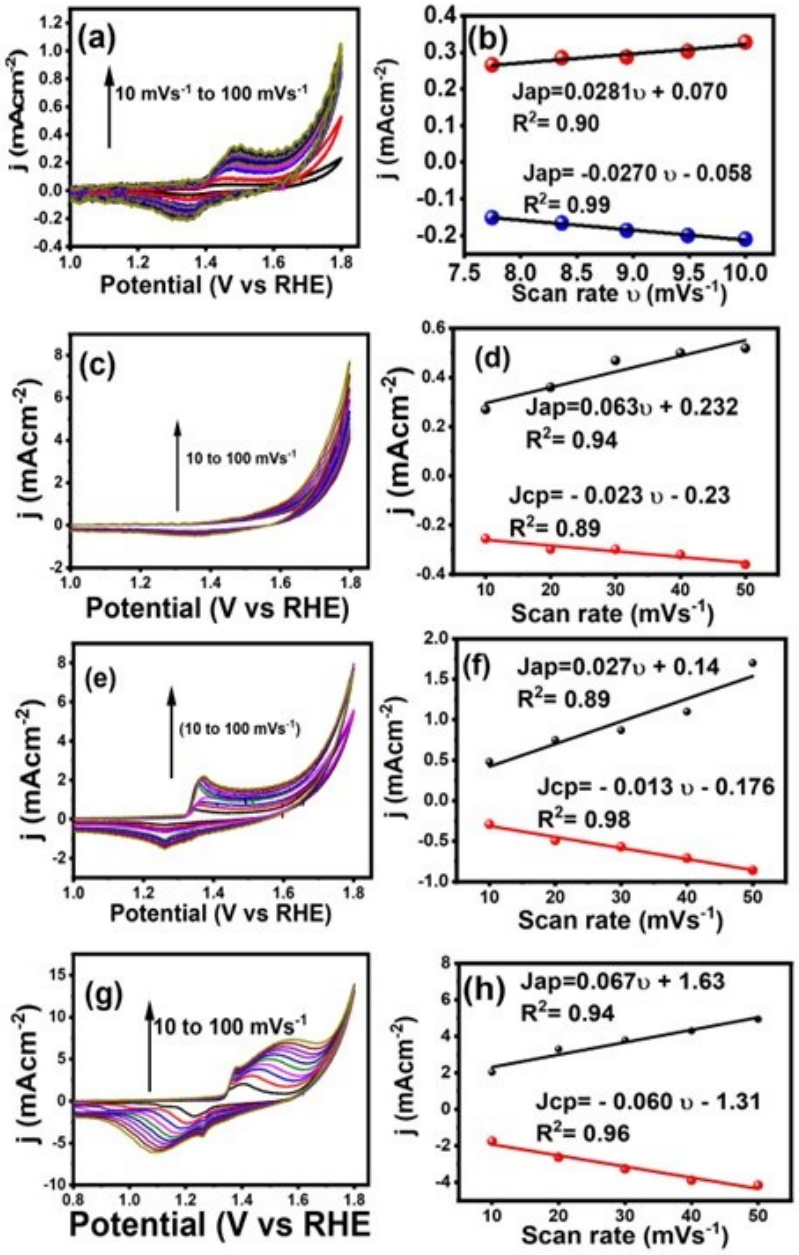

FIGURE 2B.8: CVs of (a) $La_{1.4}Sr_{0.6}O_{4+\delta}$, (b) $La_{1.4}Sr_{0.6}Ni_{0.9}Fe_{0.1}O_{4+\delta}$, (c) $La_{1.4}Sr_{0.6}Ni_{0.9}Mn_{0.1}O_{4+\delta}$ and (d) $La_{1.4}Sr_{0.6}Ni_{0.9}Co_{0.1}O_{4+\delta}$ in 0.5 M NaOH with a scan speed of 10 to 100 mV s^{-1}

With the doping of the B site, the MOR potentials were shifted to a much lower value with enhanced current densities of 7.96, 12.4 and 21.4 mA cm^{-2} for $La_{1.4}Sr_{0.6}Ni_{0.9}Fe_{0.1}O_{4+\delta}$, $La_{1.4}Sr_{0.6}Ni_{0.9}Mn_{0.1}O_{4+\delta}$, $La_{1.4}Sr_{0.6}Ni_{0.9}Co_{0.1}O_{4+\delta}$, respectively. To corroborate the results with the intrinsic activity of all the catalysts, the MOR activity was further normalized with the ECSA, and the obtained data are plotted in Figure 2B.9 (c). The appearance of the anodic peak during the forward scan could be attributed to the oxidation of methanol, whereas the cathodic peak might be associated with the oxidation of the remaining adsorbed species present on the

catalysts' surface. Apparently, the peak current density increased with partial doping of Mn, Fe and Co in the Ni Site, and $La_{1.4}Sr_{0.6}Ni_{0.9}Co_{0.1}O_{4+\delta}$ exhibited the highest current density with a significant lower onset potential. The observed correlation between the formation of surface -OOH species and the MOR current densities provides compelling evidence for the significance of -OOH as the principal catalytic species driving MOR over the Ruddlesden-Popper oxide catalysts. The doping of Co^{2+} in the B site resulted in increasing the surface oxygen vacancy, coupled with heightened Ni^{3+}content. This synergistic effect facilitated the increased formation of –OOH species on the catalyst's surface, thereby enhancing the MOR activity significantly by facilitating easy methanol adsorption on Ni - OOH active sites. It should be noted that the slightly higher onset potential of MOR over the doped Ruddlesden-Popper oxides compared to the theoretical value of the oxygen reduction reaction suggests that while the materials may not directly contribute to the potential application of DMFCs, they hold promise for both the treatment of methanol-rich industrial wastewater and potential utilization in masking or substituting the oxygen evolution reaction for H_2 production.

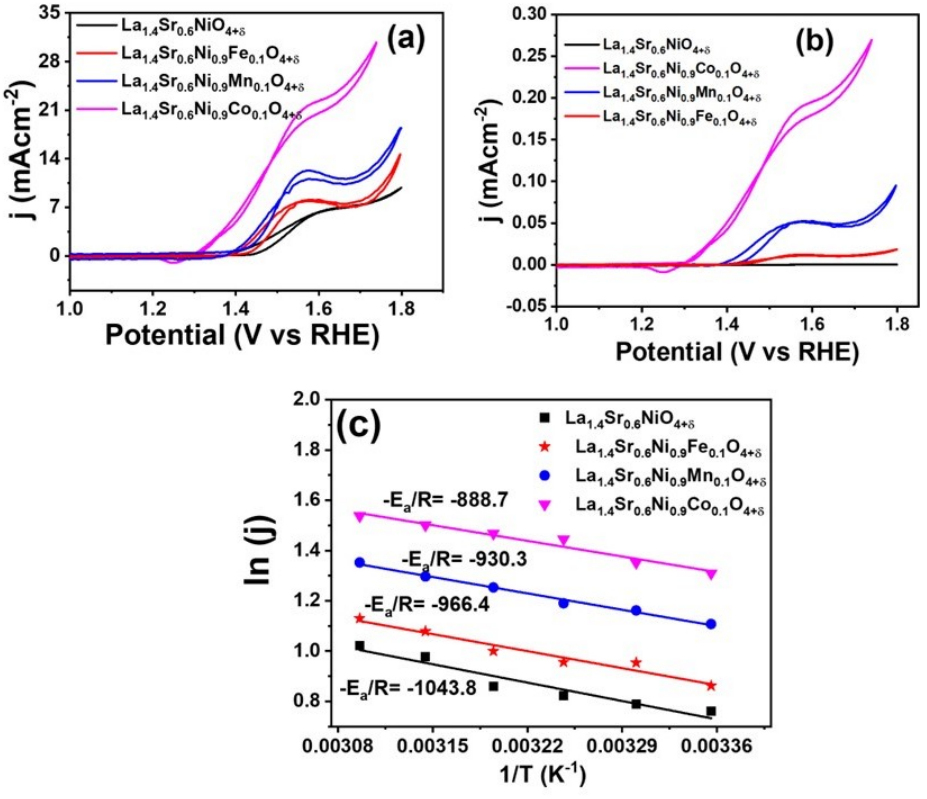

FIGURE 2B.9: (a) CVs of $La_{1.4}Sr_{0.6}NiO_{4+\delta}$ and $La_{2-x}Sr_xNi_{1-y}(Mn/Fe/Co)_yO_{4+\delta}$ in 0.5 M NaOH and 0.5 M MeOH with a scan speed of 50 mV s^{-1} (b) CVs $La_{1.4}Sr_{0.6}NiO_{4+\delta}$ and $La_{2-x}Sr_xNi_{1-y}(Mn/Fe/Co)_yO_{4+\delta}$ in 0.5 M NaOH and 0.5 M MeOH w.r.to ECSA (c) Activation energy plot of $La_{1.4}Sr_{0.6}NiO_{4+\delta}$ and $La_{2-x}Sr_xNi_{1-y}(Mn/Fe/Co)_yO_{4+\delta}$ in 0.5 M NaOH and 0.5 M MeOH

Assessing the catalysts' activity for MOR involves activation energy which is another crucial parameter [163–165]. The activation energy was determined with the help of Arrhenius plot of current density (ln j) vs. temperature (T^{-1}) at methanol oxidation potential over $La_{1.4}Sr_{0.6}Ni_{0.9}(Mn/Fe/Co)_{0.1}O_{4+\delta}$ and $La_{1.4}Sr_{0.6}NiO_{4+\delta}$. The temperature was varied from 25 to 50 °C with a gap of 5 °C in alkaline 0.5 M MeOH electrolyte solution. The slope from the activation energy (E_a) is shown in Figure 2B.9(c). The lowest MOR activation energy of 7.38 kJ mol^{-1} over $La_{1.4}Sr_{0.6}Ni_{0.9}Co_{0.1}O_{4+\delta}$ rationalized its high MOR activity.

2B.3.3 Evaluation of MOR Kinetic Parameters and Stability over $La_{1.4}Sr_{0.6}Ni_{0.9}(Mn/Fe/Co)_{0.1}O_{4+\delta}$

In light of the significant performance exhibited by $La_{1.4}Sr_{0.6}Ni_{0.9}(Mn/Fe/Co)_{0.1}O_{4+\delta}$, an intensive exploration of the kinetic parameters was conducted over the Co doped material. The reaction order of MOR over $La_{1.4}Sr_{0.6}Ni_{0.9}(Mn/Fe/Co)_{0.1}O_{4+\delta}$ was calculated from the methanol concentration studies. Voltammetric responses of $La_{1.4}Sr_{0.6}Ni_{0.9}(Mn/Fe/Co)_{0.1}O_{4+\delta}$ were obtained at different methanol concentration, and a linear relationship was obtained by plotting the current density with methanol concentration in logarithmic scale as shown in the inset of Figure 2B.10(a). The slope was calculated using the equation $\log I = \log nFk + m \log C$, where n is the number of electrons, F is the Faraday constant, k being the reaction constant, m is the reaction order, and C is the concentration of methanol [166]. The reaction order of MOR obtained from the slope of the curve was 0.36 over $La_{1.4}Sr_{0.6}Ni_{0.9}Co_{0.1}O_{4+\delta}$.

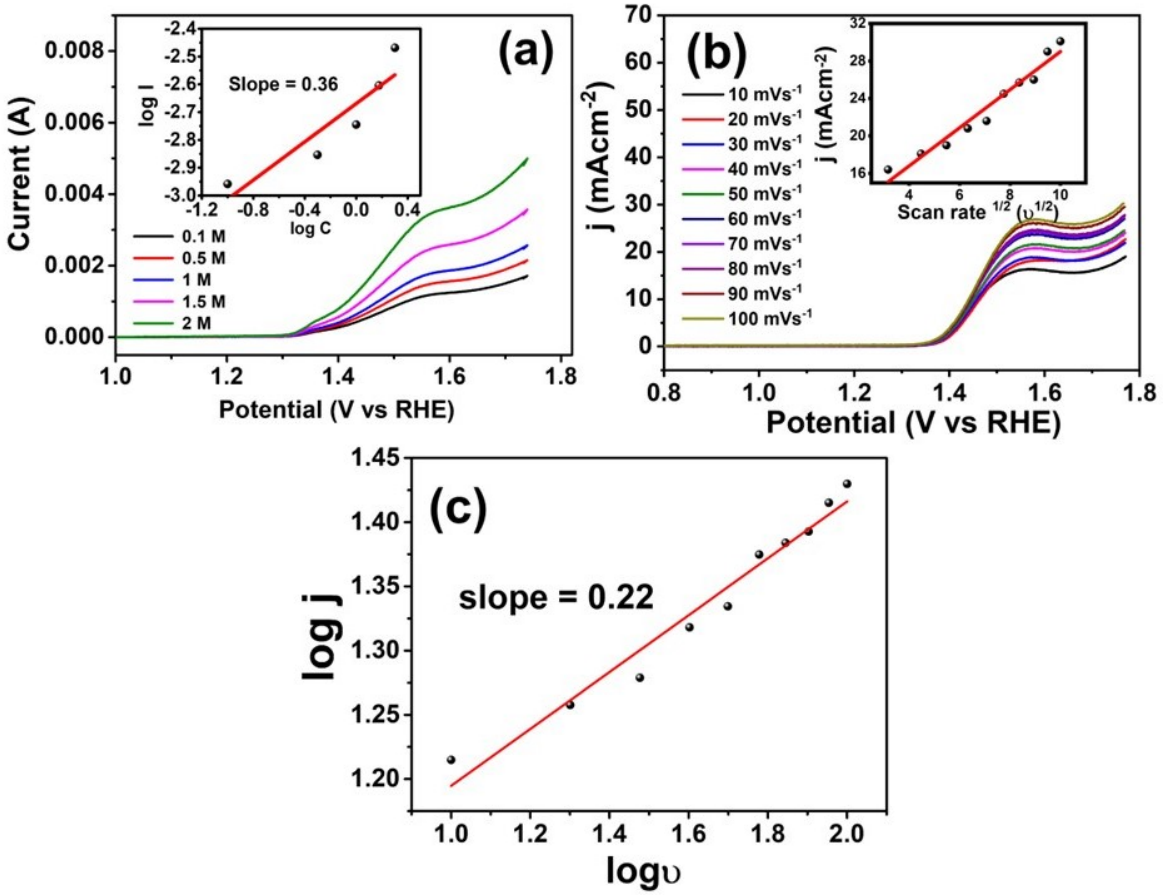

FIGURE 2B.10: (a) Methanol concentration study (inset: log C Vs log I plot MOR showing order of the reaction) (b) scan rate dependent study in 0.5 M NaOH and 0.5 M MeOH (inset square root of scan rate vs current density) and (b) logarithmic plot of scan rate with current density for $La_{1.4}Sr_{0.6}Ni_{0.9}Co_{0.1}O_{4+\delta}$

Next, the scan rate-dependent studies were employed to conduct a detailed kinetic analysis of MOR over the optimized catalyst as shown in Figure 2B.10(b). As the scan rate is increased from 10-100 mV s^{-1}, the current density also increases respectively [167–170]. On plotting the square root of the scan rate against current density, a linear correlation was observed with a regression coefficient (R^2) of 0.97 (Figure 2B.10(b) inset). This suggests that the methanol oxidation reaction over$La_{1.4}Sr_{0.6}Ni_{0.9}Co_{0.1}O_{4+\delta}$ follows a diffusion-controlled pathway, in accordance with the Randles-Sevick equation. The logarithmic curve of peak current density vs. scan rate showed slope of 0.22 confirming the MOR over $La_{1.4}Sr_{0.6}Ni_{0.9}Co_{0.1}O_{4+\delta}$ is a diffusion-controlled process rather than a surface-controlled phenomenon (Figure 2B.10(c)).

Figure 2B.11(a) displays the results obtained from double-step chronoamperometry experiment of $La_{1.4}Sr_{0.6}Ni_{0.9}Co_{0.1}O_{4+\delta}$ conducted under two different potentials [44, 171]. The first step involved applying an oxidation potential of 1.56 V vs RHE for 60 seconds, followed by a second step at 1.0 V for 60 seconds. The experiments were performed both in the presence and

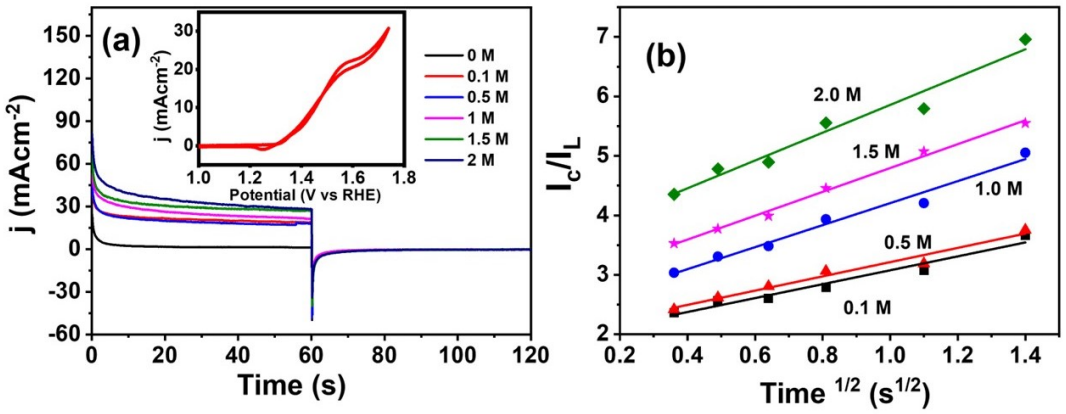

FIGURE 2B.11: (a) Double step chrono amperometry of $La_{1.4}Sr_{0.6}Ni_{0.9}Co_{0.1}O_{4+\delta}$ with and without methanol at 1.56 V and 1.0V vs RHE. (b) I_C vs I_L vs Time (s) of $La_{1.4}Sr_{0.6}Ni_{0.9}Co_{0.1}O_{4+\delta}$

absence of methanol, and the corresponding data were plotted. As methanol concentration was increased, current density increased correspondingly at 1.56 V vs RHE, while there was no increment in current density at 1.0 V vs RHE irrespective of the methanol concentration. The charge value associated with the forward chronoamperometry is significantly higher than that observed for the backward chronoamperometry and also the charge value in the forward scan increased with increase in methanol concentration. The rate constant for methanol electro-oxidation was calculated from the double-step chrono amperometry using the following equation

$$I_c/I_L = \gamma^{1/2}\left[\pi^{1/2}\mathrm{erf}\left(\gamma^{1/2}\right) + \exp\left(-\gamma\right)/\gamma^{1/2}\right] \tag{2B.3}$$

where I_C is the catalytic current of $La_{1.4}Sr_{0.6}Ni_{0.9}Co_{0.1}O_{4+\delta}$ in presence of methanol, I_L is the limiting current in the absence of methanol. γ is the argument of error function and is equal to kC_ot, where k is the rate constant in cc $mol^{-1}s^{-1}$, t being the elapsed time in s, and C_o is the bulk methanol concentration in mol cc^{-1}. The above-mentioned equation can be simplified as the following one by considering the value of $\gamma > 2$.

$$I_c/I_L = \gamma^{1/2}\pi^{1/2} = (kC_0t)^{1/2}\pi^{1/2} \tag{2B.4}$$

The rate constant of MOR can be calculated with the above equation from the plot of I_C/I_L vs $t_{1/2}$ by varying the methanol concentration (Figure 2B.11(b)). The rate constant of MOR over $La_{1.4}Sr_{0.6}Ni_{0.9}Co_{0.1}O_{4+\delta}$ is 1.60 $\times$ 10^3 cc $mol^{-1}s^{-1}$ as calculated from methanol concentration from 0 M to 2 M. The calculated rate constant, which is in line with values reported in the

literature, demonstrates that the catalyst $La_{1.4}Sr_{0.6}Ni_{0.9}Co_{0.1}O_{4+\delta}$ effectively overcomes the kinetic barrier for methanol oxidation and significantly reduces the overpotential within the overall electrocatalytic system [171, 172].

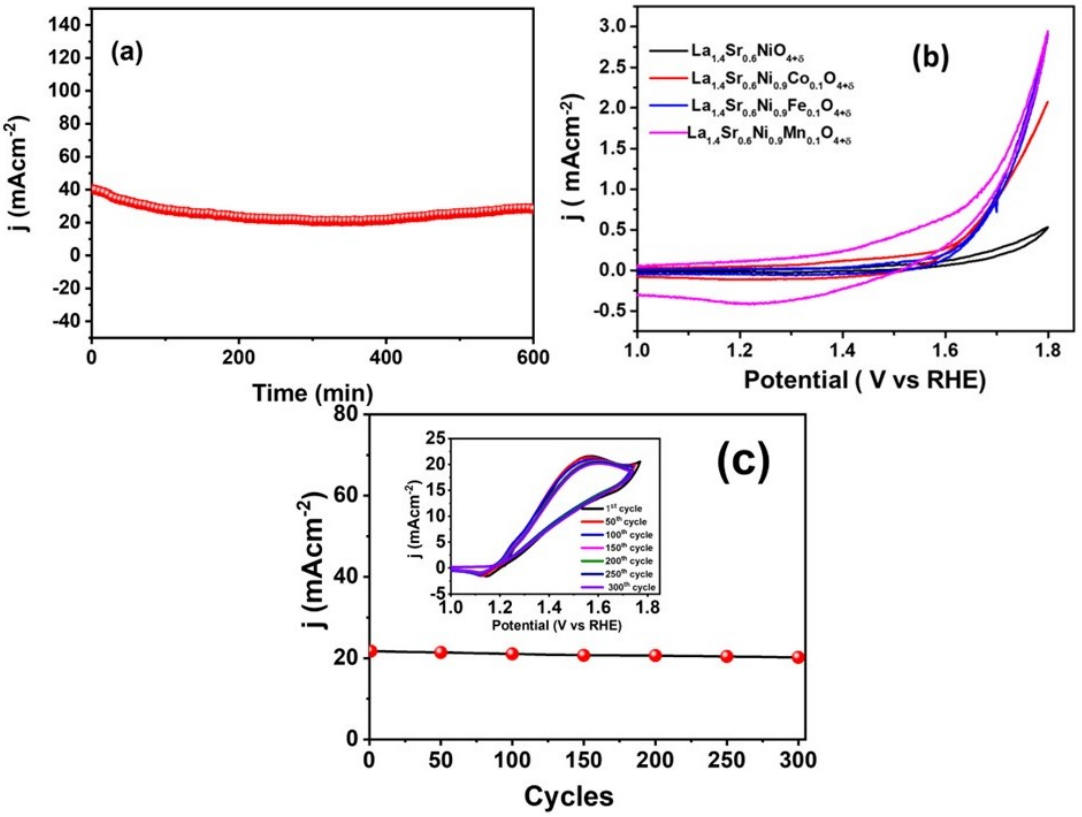

FIGURE 2B.12: (a) CA of $La_{1.4}Sr_{0.6}Ni_{0.9}Co_{0.1}O_{4+\delta}$ at 1.56 V vs RHE in 0.5 M NaOH and 0.5 M MeOH for 10 h (b) CO stripping study of $La_{1.4}Sr_{0.6}Ni_{0.9}(Mn/Fe/Co)_{0.1}O_{4+\delta}$in 0.5 M NaOH (c) Stability study of $La_{1.4}Sr_{0.6}Ni_{0.9}Co_{0.1}O_{4+\delta}$ up to 300 cycles (inset: CV up to 300^{th} cycle)

Long term stability of the catalyst is one of the crucial aspects in evaluating electrocatalysis. The assessment of stability of $La_{1.4}Sr_{0.6}Ni_{0.9}Co_{0.1}O_{4+\delta}$ was conducted with the help of CA and CV studies. Figure 2B.12(a) shows the CA of $La_{1.4}Sr_{0.6}Ni_{0.9}Co_{0.1}O_{4+\delta}$ in 0.5 M NaOH and 0.5 M MeOH for 10 hours at potential of 1.56 V vs RHE. The progressive decline in current density observed during the initial 100 minutes can be attributed to the gradual occupancy of active sites by reaction intermediates. It was observed that current density maintained 95% as the initial current density. The constant and stable long-term current response can be attributed to the highly tolerant nature of $La_{1.4}Sr_{0.6}Ni_{0.9}Co_{0.1}O_{4+\delta}$ against CO poisoning as shown in Figure 2B.12(b) The result of the long-term cyclic stability test by CV analysis for 300 cycles is shown in Figure 2B.12(c). The improved cycling stability further corroborates the high stability and CO tolerant nature of $La_{1.4}Sr_{0.6}Ni_{0.9}Co_{0.1}O_{4+\delta}$ for a prolonged period of time. Following the extended MOR study, the electrolyte was subjected to ^{1}HNMR analysis to assess the composition of the liquid product as shown in Figure 2B.13. The analysis of the data unveiled that the sole liquid product observed during MOR was formic acid with a concentration of 2.46 $\times$ 10^{-6} ppm for $La_{1.4}Sr_{0.6}Ni_{0.9}Co_{0.1}O_{4+\delta}$. The conversion was found to be the highest compared to the other synthesized Ruddlesden Popper oxides as shown in bar plot of Figure 2B.14.

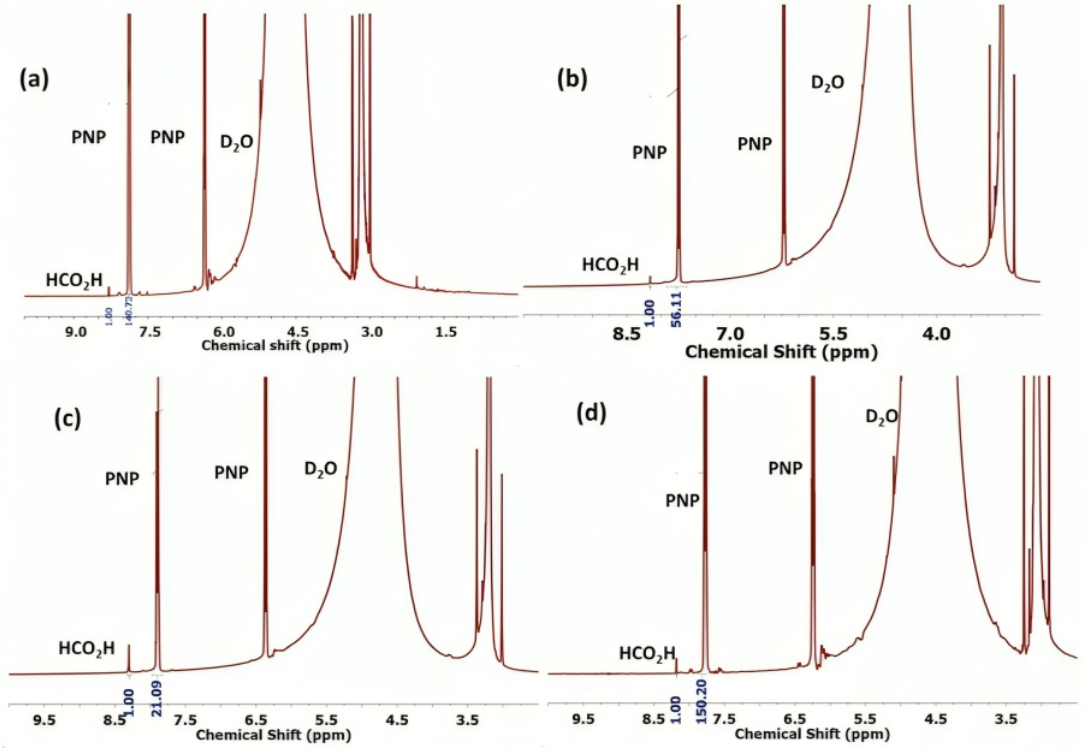

FIGURE 2B.13: ^{1}HNMR spectra of the electrolyte of (a) $La_{1.4}Sr_{0.6}NiO_{4+\delta}$(b) $La_{1.4}Sr_{0.6}Ni_{0.9}Mn_{0.1}O_{4+\delta}$ (c) $La_{1.4}Sr_{0.6}Ni_{0.9}Co_{0.1}O_{4+\delta}$and (d) $La_{1.4}Sr_{0.6}Ni_{0.9}Fe_{0.1}O_{4+\delta}$ after 4 h of CA in 0.5 M MeOH and 0.5 M NaOH medium at MOR potential

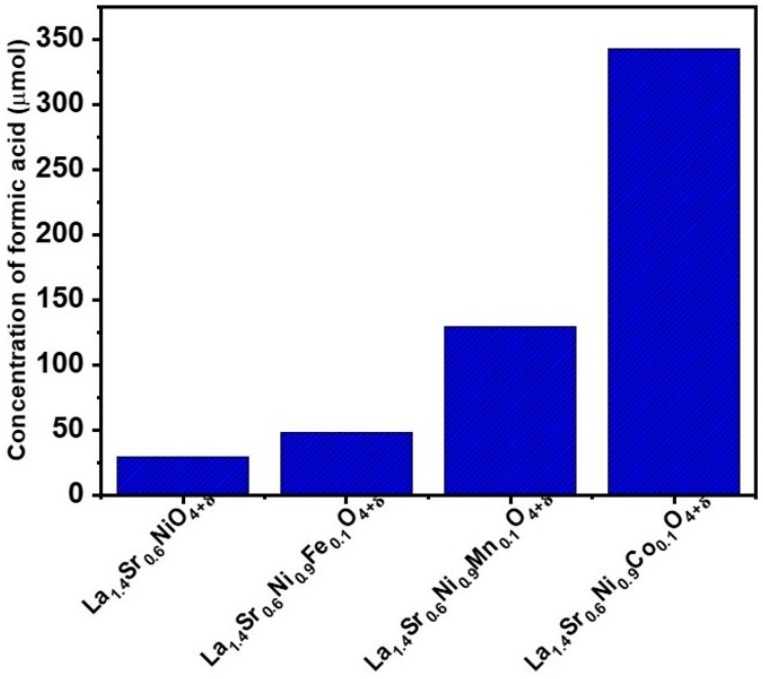

FIGURE 2B.14: Bar plot depicting the concentration of formic acid with respects to the catalysts

2B.3.4 Introspection of the Material's Electronic & Surface Properties in MOR

The electrochemical investigations reveal that $La_{1.4}Sr_{0.6}Ni_{0.9}Co_{0.1}O_{4+\delta}$ emerges as the optimal catalyst for MOR. This significant catalytic performance stems from the carefully tailoring of optimized A-site doping by Sr^{2+} and B-site doping by Co^{2+}. The augmented oxygen vacancy on the catalyst's surface, coupled with the deliberate induction of Ni^{3+}, may synergistically refine the electronic properties of $La_{1.4}Sr_{0.6}Ni_{0.9}Co_{0.1}O_{4+\delta}$, thereby endowing it with a pronounced capability in MOR. Therefore, we endeavored to delve into the MOR activity in light of the material's electronic properties through theoretical calculations, EIS and XPS studies. The DFT calculations were performed on the optimized crystal structures of $La_{1.5}Sr_{0.5}NiO_4$ and $La_{1.4}Sr_{0.6}Ni_{0.9}Co_{0.1}O_{4+\delta}$, as illustrated in Figure 2B.15.

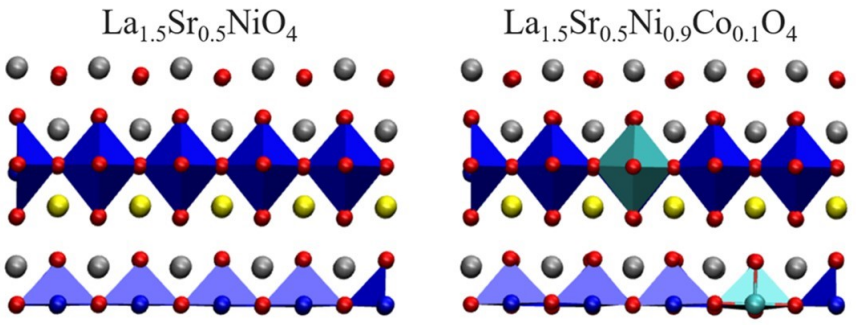

FIGURE 2B.15: Optimized Geometry of $La_{1.5}Sr_{0.5}NiO_4$ and $La_{1.5}Sr_{0.5}Ni_{0.9}Co_{0.1}O_{4+\delta}$. Silver, Red, Blue, Cyan and Yellow spheres denotes La, O, Ni, Co and Sr atoms, respectively

To streamline our computations, we employed $La_{1.5}Sr_{0.5}NiO_4$ as surrogate, capturing the essential traits of $La_{1.4}Sr_{0.6}NiO_{4+\delta}$. In a preliminary approximation, the foremost influencers governing interactions between incoming reactants and a metal surface are expected to arise from the Fermi-level electrons. This principle is rooted in the notion that when the Fermi level aligns with regions of high DOS, it significantly impacts catalytic activity. The outcomes of our DFT investigations (Figure 2B.16) have revealed intriguing insights. Specifically, for the pristine $La_{1.5}Sr_{0.5}NiO_4$, the projected DOS at the Fermi level registers a modest value of 7.2 eV. In contrast, upon doping at the B site with elements such as Fe, Mn, and Co in $La_{1.4}Sr_{0.6}Ni_{0.9}Fe_{0.1}O_{4+\delta}$, $La_{1.4}Sr_{0.6}Ni_{0.9}Mn_{0.1}O_{4+\delta}$, and $La_{1.4}Sr_{0.6}Ni_{0.9}Co_{0.1}O_{4+\delta}$, respectively, the DOS values elevate to 7.8, 8.7, and 10.5 per eV. Strikingly, the $La_{1.4}Sr_{0.6}Ni_{0.9}Co_{0.1}O_{4+\delta}$ compound demonstrates a high DOS at the Fermi level, consequently leading to enhanced catalyst conductivity for the process of MOR.

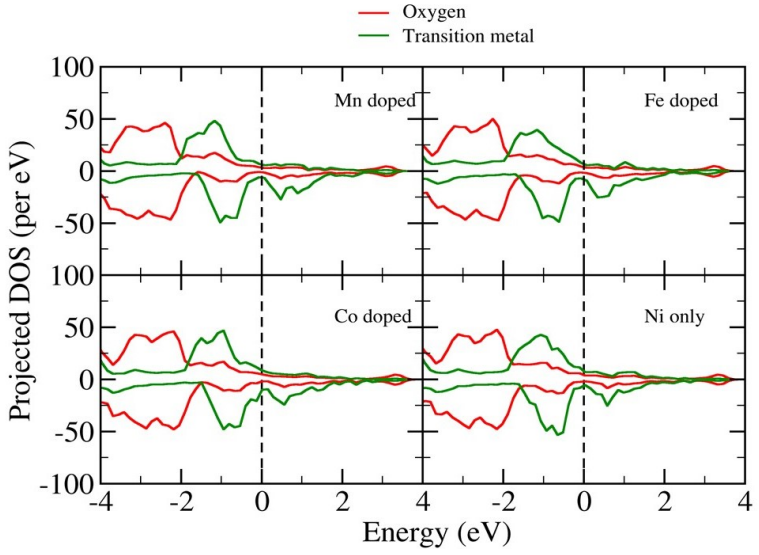

FIGURE 2B.16: DOS plot for $La_{1.4}Sr_{0.6}NiO_{4+\delta}$, $La_{1.4}Sr_{0.6}Ni_{0.9}Fe_{0.1}O_{4+\delta}$, $La_{1.4}Sr_{0.6}Ni_{0.9}Mn_{0.1}O_{4+\delta}$ and $La_{1.4}Sr_{0.6}Ni_{0.9}Co_{0.1}O_{4+\delta}$

In order to further investigate the conductivity of the synthesized catalysts, EIS study was conducted. This would shed light on the movement of electrons at the interface between the electrode and the electrolyte. Figure 2B.17(a) shows the Nyquist plot of $La_{1.4}Sr_{0.6}NIO_{4+\delta}$, $La_{1.4}Sr_{0.6}Ni_{0.9}Mn_{0.1}O_{4+\delta}$, $La_{1.4}Sr_{0.6}Ni_{0.9}Fe_{0.1}O_{4+\delta}$ and $La_{1.4}Sr_{0.6}Ni_{0.9}Co_{0.1}O_{4+\delta}$ in alkaline 0.5 M methanol solution. Among the series, $La_{1.4}Sr_{0.6}Ni_{0.9}Co_{0.1}O_{4+\delta}$ exhibited the smallest semi-circle arc. This can be attributed to its enhanced electrical conductivity and significantly diminished charge transfer resistance. It is important to highlight that the cobalt-doped $La_{1.4}Sr_{0.6}Ni_{0.9}Co_{0.1}O_{4+\delta}$ also displayed a high DOS projection value at the Fermi level due to the better overlap of dz^2 orbitals with O 2p orbitals. These findings strongly indicate a rapid electron transfer process, contributing directly to its superior MOR activity. Equivalent circuits were extracted from the Nyquist plot, as illustrated in Figure 2B.17(b), and the corresponding parameters have been compiled in Table 2B.6. In Figure 2B.17(b), the circuit associated with $La_{1.4}Sr_{0.6}Ni_{0.9}Co_{0.1}O_{4+\delta}$ showcases a dual-phase element arrangement. The initial element pertains to the charge transfer resistance (R_{ct}) and the formation of the double layer (C_{dl}), while the subsequent element corresponds to the adsorption resistance (R_{ad}) and adsorption capacitance (C_{ad}). The R_{ct} value for $La_{1.4}Sr_{0.6}Ni_{0.9}Co_{0.1}O_{4+\delta}$, measured at 263.3 Ω, emerges lower in comparison to other doped Ruddlesden-Popper oxides, affirming its superior electron transfer capability conducive to heightened MOR activity. Moreover, within the secondary phase of the circuit (Figure 2B.17(b)), the lower Rad value (205.9 Ω) for $La_{1.4}Sr_{0.6}Ni_{0.9}Co_{0.1}O_{4+\delta}$, as opposed to counterparts such as $La_{1.4}Sr_{0.6}NiO_{4+\delta}$, $La_{1.4}Sr_{0.6}Ni_{0.9}Fe_{0.1}O_{4+\delta}$, and $La_{1.4}Sr_{0.6}Ni_{0.9}Mn_{0.1}O_{4+\delta}$, underscores its heightened oxidation propensity for adsorbed species like CO, with improved methanol conversion efficacy to CO_2. The circuit employed for $La_{1.4}Sr_{0.6}NiO_{4+\delta}$, $La_{1.4}Sr_{0.6}Ni_{0.9}Fe_{0.1}O_{4+\delta}$, and $La_{1.4}Sr_{0.6}Ni_{0.9}Mn_{0.1}O_{4+\delta}$ differed in configuration (Figure 2B.17(c)), and the fitting parameters detailed in Table 2B.6 affirm the comparatively lower conductivity of these catalysts.

To delve further into the material's conductivity, the analysis was extended to encompass Bode phase and admittance, as depicted in Figures 2B.18(a and b). Remarkably conductive characteristics of $La_{1.4}Sr_{0.6}Ni_{0.9}Co_{0.1}O_{4+\delta}$ are evident from its Bode phase angle plot (Figure 2B.18(b), portraying a phase angle surpassing - 90 °.The diminishing impedance magnitude ($|Z|$) at lower frequencies for $La_{1.4}Sr_{0.6}Ni_{0.9}Co_{0.1}O_{4+\delta}$ indicates a reduction in material resistance and an augmentation in electron flow through the electrode (Figure 2B.18(c)) [173–175].

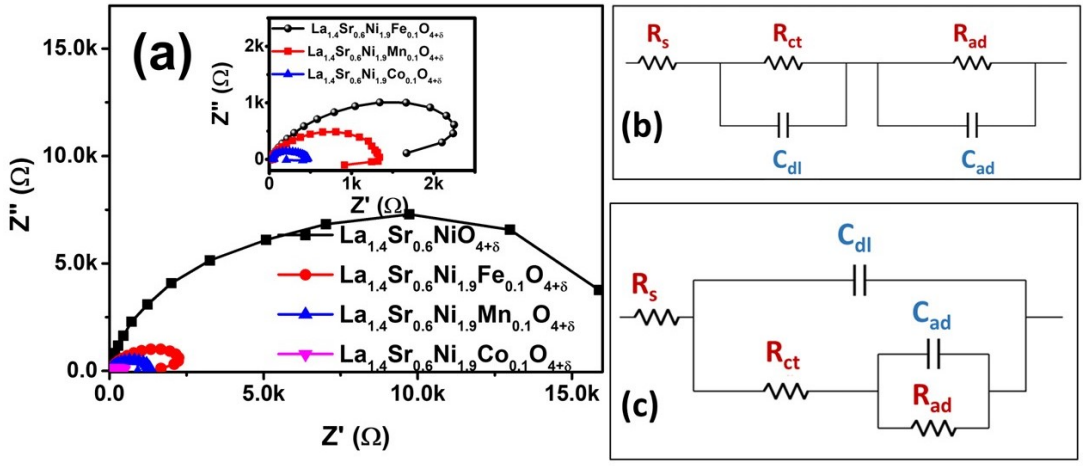

FIGURE 2B.17: (a) Nyquist plots of $La_{1.4}Sr_{0.6}Ni_{0.9}(Mn/Fe/Co)_{0.1}O_{4+\delta}$ (b) Nyquist fitted circuit diagram of $La_{1.4}Sr_{0.6}Ni_{0.9}Co_{0.1}O_{4+\delta}$ (c) Nyquist fitted circuit diagram of $La_{1.4}Sr_{0.6}NiO_{4+\delta}$, $La_{1.4}Sr_{0.6}Ni_{0.9}Fe_{0.1}O_{4+\delta}$ and $La_{1.4}Sr_{0.6}Ni_{0.9}Mn_{0.1}O_{4+\delta}$

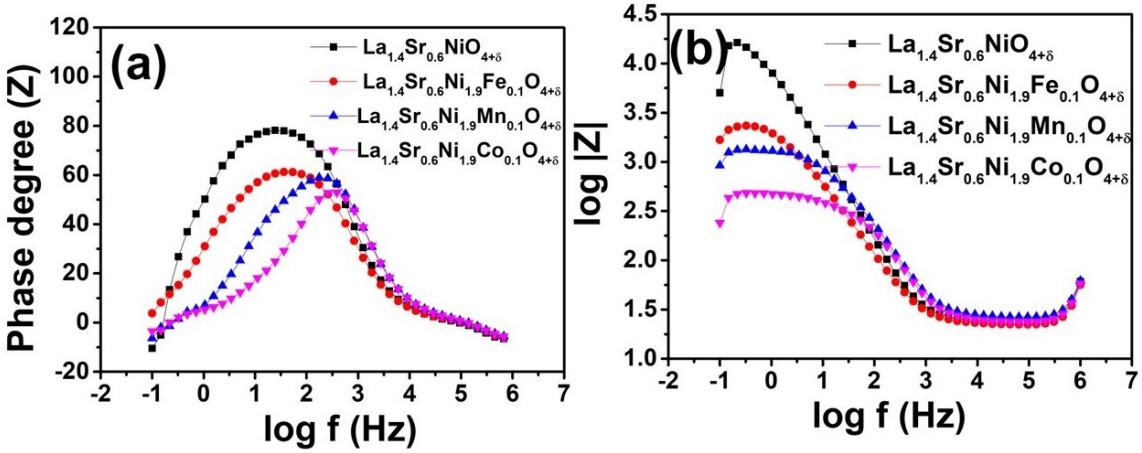

FIGURE 2B.18: (a) Bode Phase angle and (b) Bode admittance plots of $La_{1.4}Sr_{0.6}Ni_{0.9}(Mn/Fe/Co)_{0.1}O_{4+\delta}$

TABLE 2B.6: EIS parameters obtained from fitting of Nyquist plot

Catalysts/ Parameters	$\mathbf{La_{1.4}Sr_{0.6}NiO_{4+\delta}}$	$\mathbf{La_{1.4}Sr_{0.6}Ni_{0.9}Fe_{0.1}O_{4+\delta}}$	$\mathbf{La_{1.4}Sr_{0.6}Ni_{0.9}Mn_{0.1}O_{4+\delta}}$	$\mathbf{La_{1.4}Sr_{0.6}Ni_{0.9}Co_{0.1}O_{4+\delta}}$
$\mathbf{R_s(\Omega)}$	62.57	29.26	25.27	24.23
$\mathbf{R_{ct}(\Omega)}$	7254	821.8	380.2	263.3
$\mathbf{R_{ad}(\Omega)}$	9053	251.4	1717	205.9
$\mathbf{C_{dl}(F)}$	14.91×10^{-7}	7.36×10^{-6}	9.15×10^{-6}	12.48×10^{-6}
$\mathbf{C_{ad}}$ **(F)**	14.5×10^{-6}	1.56×10^{-8}	2.41×10^{-6}	26.8×10^{-6}

To gain a comprehensive understanding, further we examined the O 1s core level spectra subsequent to the reaction. The corresponding data is illustrated in Figure 2B.19. It is noteworthy that an additional peak emerged alongside the regular O_L, O_S, and O_W peaks. Specifically, the peak identified at 534.7 eV corresponds to the Ni-OOH layer, which forms on the catalyst's surface

[173, 176]. The consequential formation of the Ni-OOH layer potentially enhances the catalyst's ability to adsorb MeOH, presumably in the form of Ni-$OOCH_3$. It is important to underscore that among the catalysts studied, $La_{1.4}Sr_{0.6}Ni_{0.9}Co_{0.1}O_{4+\delta}$ exhibits the highest percentage of Ni-OOH content at 47.4%, in contrast to $La_{1.4}Sr_{0.6}Ni_{0.9}Mn_{0.1}O_{4+\delta}$ (25.0%) and $La_{1.4}Sr_{0.6}Ni_{0.9}Fe_{0.1}O_{4+\delta}$ (22.0%). This elevated concentration of Ni-OOH in $La_{1.4}Sr_{0.6}Ni_{0.9}Co_{0.1}O_{4+\delta}$ also plays a pivotal role in augmenting the MOR performance.

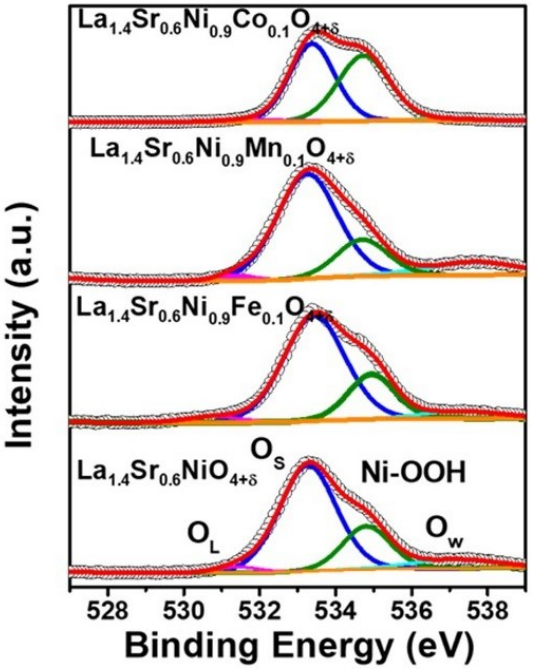

FIGURE 2B.19: O 1s spectra after MOR

2B.4 Conclusion

We have successfully adopted the one step solution combustion synthesis for pure phase tetragonal Ruddlesden Popper $La_{1.4}Sr_{0.6}Ni_{0.9}(Mn/Fe/Co)_{0.1}O_{4+\delta}$ oxide with a space group of I4/mmm. Aliovalent doping of Sr^{2+} in A site and Co^{2+}, Fe^{2+} and Mn^{2+} in B site resulted in enhanced Ni^{3+} concentration with t_{2g}^6 $d_{x^2-y^2}^1$ configuration. Consequently, a distorted tetragonal structure resulted with compressed "c" and elongated "a/b". Overall, a compression in unit cell and a notable presence of surface oxygen with maximum extend was observed in $La_{1.4}Sr_{0.6}Ni_{0.9}Co_{0.1}O_{4+\delta}$. Among the other synthesized oxides, $La_{1.4}Sr_{0.6}Ni_{0.9}Co_{0.1}O_{4+\delta}$ demonstrated the most superior efficiency in catalyzing methanol oxidation in an alkaline medium. The optimum doping of Sr^{2+} in A site and Co^{2+} in B site induced high density of states of 10.5 eV in the fermi level resulting in a metallic character with high conductive nature. The introduction

of Co^{2+} increases the proportion of Ni^{3+} and regulates the electronic structure of the material; creating abundant oxygen vacancies on the surface which is beneficial for its catalytic activity. This endeavor offers a foundation for the creation of diverse, high-performance electrocatalysts for MOR, which are non-Pt-based and can potentially tackle real-world environmental and energy challenges.

Chapter 3A

Electro-oxidation Reaction of Methanol over Reducible $Ce_{1-x-y}Ni_xSr_yO_{2-\delta}$: A Mechanistic Probe of Participation of Lattice Oxygen

3A.1 Introduction

Upon oxidation of Ni^{2+} to Ni^{3+}, an available charge-transfer orbital is formed which is then available for the electron transfer process during methanol oxidation to CO_2. However, it is fundamentally challenging to create available charge-transfer orbitals near the Fermi energy level [32, 36, 39, 177]. A solution to this could be substituting Ni^{2+} in reducible support to facilitate the $Ni^{2+} \rightarrow Ni^{3+}$ oxidation. Moreover, if the reducible support shows oxophilicity and is prone to adsorption of oxygenated species such as Ni - OOH at a lower potential, then it may further promote the oxidation of CO to CO_2 [178]. Among the range of low-cost oxides, CeO_2 is of particular interest as a result of its high surface area, significant surface defects, and high oxygen storage capacity (redox Ce^{4+}/Ce^{3+} sites) [42, 179, 180]. In this context, a sizable number of reports showing excellent promotional and anti-poisoning activities of CeO_2 for MOR are available in the literature [43, 44]. However, most of the reports only focus on the surface

dispersion of active metal on CeO_2 and their limited interactions. Further, the unanswered fundamental questions are: (i) Does the reducible support of CeO_2 facilitate the $Ni^{2+} \rightarrow Ni^{3+}$ oxidation? (ii) Can the formation of Ni - OOH be controlled to accelerate the sluggish kinetics of MOR? (iii) Does the lattice oxygen from reducible support facilitate the CO oxidation? There lies no fundamental report on the exact role of reducibility of the support vis-à-vis the influence of lattice oxygen of CeO_2 in MOR mechanism.

Therefore, in this chapter, we have ionically doped the active site of Ni^{2+} in the fluorite CeO_2 matrix by a novel solution combustion method to yield $Ce_{1-x}Ni_xO_{2-\delta}$. The bivalent Ni^{2+} is expected to create higher reducibility as well as oxygen vacancy in CeO_2. Further, in order to enhance the reducibility and oxygen vacancy, we have co-doped bivalent alkaline earth metal Sr^{2+} in the CeO_2 lattice to produce $Ce_{1-x-y}Ni_xSr_yO_{2-\delta}$. This is the first report on enhanced MOR activity as well as CO tolerance over Ni and Sr co-doped CeO_2 lattice. The mechanistic elucidation showed that Ni^{2+} acted as the active site for CO adsorption, and the lattice oxygen was utilized for CO oxidation. Mere dispersion of Ni and Sr on the surface of CeO_2 or non-reducible Al_2O_3 could not execute the CO oxidation efficiently due to the unavailable lattice oxygen. Detailed ex-situ XPS analysis showed that the Sr co-doping in reducible CeO_2 has helped Ni^{2+} oxidation and facilitated the availability of lattice oxygen. The aim of this work was to investigate the role of lattice oxygen in the electrocatalytic properties, for example, if there is any role of the lattice oxygen in removing the CO poisoning effect during methanol electro-oxidation. We found that, indeed, the suitable reducible oxide can influence $Ni^{2+} \rightarrow Ni^{3+}$ oxidation and thus can form the key active species Ni - OOH and lattice oxygen also plays a crucial role in CO oxidation to exhibit better MOR activity.

3A.2 Methodology

3A.2.1 Synthesis of CeO_2, $Ce_{1-x}Ni_xO_{2-\delta}$ and $Ce_{1-x-y}Ni_xSr_yO_{2-\delta}$

The pristine CeO_2, Ni-doped CeO_2 (where x = 0.03, 0.05, and 0.07), Ni and Sr co-doped CeO_2 ($Ce_{1-x}Ni_xO_{2-\delta}$, where x = 0.05 and y = 0.03, 0.05, and 0.07) catalysts were synthesized by the low-temperature-initiated facile single-step solution combustion method. This self-propagating combustion method utilizes the propellant chemistry involving highly exothermic metathetical chemical reactions between oxidizer and fuel [42, 132]. Here, metal nitrates, $Ce(NO_3)_3 \cdot 6H_2O$ (SRL chemicals, 99%), $Ni(NO_3)_2 \cdot 6H_2O$ (SD fine, 99%), and $Sr(NO_3)_2$

(Sigma Aldrich, 99%) were taken as oxidizer and glycine (Sigma Aldrich, 99%) was used as fuel. Due to the aqueous phase homogeneous precursor, the solution combustion synthesis offers a precise and uniform formulation of the desired composition on the nano scale. In a typical synthesis of $Ce_{1-x-y}Ni_xSr_yO_{2-\delta}$, calculated amounts of $Ce(NO_3)_3 \cdot 6H_2O$, $Ni(NO_3)_2 \cdot 6H_2O$, and $Sr(NO_3)_2$ (Sigma Aldrich, 99%) were dissolved in ~50 mL volume of deionized water in a 300 mL borosilicate dish. The dish containing the redox mixture was introduced into a preheated muffle furnace maintained at 450 °C. Initially, the solution boiled with frothing and underwent dehydration. At the point of complete dehydration, the surface ignited, burning with a flame with a temperature reaching about 1000 °C and yielding a voluminous solid product within a couple of minutes. The chemical reaction for synthesis can be represented as follows:

$$2(1-x-y)Ce(NO_3)_3 \cdot 6H_2O + 2xNi(NO_3)_2 \cdot 6H_2O + 2ySr(NO_3)_3 + 2C_2H_5NO_2 + (3x+3y-2.5-\delta)O_2 \rightarrow 2Ce_{1-x-y}Ni_xSr_yO_{2-\delta} + 4CO_2 + (17-12y)H_2O + (4-x-y)N_2 \quad (3A.1)$$

To benchmark the solution combustion synthesized catalysts, the homologous materials were also synthesized by physical mixing methods. 5%NiO/5%SrO/CeO_2 and 5% NiO/5%SrO/Al_2O_3 were prepared by physical grinding of both of the solution combustion synthesized individual oxides in their respective calculated amount for 2 h with an agate mortar and pestle.

3A.2.2 Structural, Surface and Electronic Characterisation

The actual atomic ratio in the synthesized $Ce_{1-x-y}Ni_xSr_yO_{2-\delta}$ materials were probed by ED-XRF with the help of an Epsilon 1; PAN analytical instrument. The structural characterization of $Ce_{1-x-y}Ni_xSr_yO_{2-\delta}$ (x= 0, 0.03 - 0.07; y = 0.03 - 0.07) was performed with a Rigaku Ultima IV XRD with Cu Kα radiation (λ = 1.5418 Å) at a scan rate of 0.4° min^{-1} and step size of 0.01° in the 2θ range between 10° - 90°. Scherrer's formula,

$$D = \frac{0.9\lambda}{B\cos\theta} \quad (3A.2)$$

where B is the full-width at half-maximum, λ is the wavelength of the radiation, and θ is the corresponding angle was used to calculate the average nanocrystalline diameters (D). Rietveld refinement of the powder diffraction patterns were carried out using Fullprof program suite by varying the overall scale factor, background and profile parameters, unit-cell lattice parameters,

atomic positions, half-width, shape, isotopic thermal parameters, and oxygen occupancy. The surface of the synthesized materials was studied by employing Microtrac BEL Corp mini-II surface area analyzer. Prior to the N_2 sorption measurements at 77 K, samples were degassed in vacuum at 200 °C for 2 h. The specific surface area was estimated using software of the instrument based on the BET equation. HR-SEM was carried out with FE-SEM, (FEI-ApreoS) at 30 kV acceleration. XPS were collected to study the surface composition, elemental oxidation state and bonding with the help of Thermo Scientific K-Alpha surface-analysis spectrometer housing AlK_α as the X-ray source (1486.6 eV). The instrument was operated at 72 W. The base pressure at the analyzing chamber was maintained at 5×10^{-9} mbar. The data profiles were subjected to a nonlinear least-squares curve fitting program with a Gaussian-Lorentzian production function and processed with Avantage software. The B.E. of all XPS data was calibrated vs the standard C 1s peak at 284.85 eV. H_2-TPR was carried out with 50 mg of the synthesized samples. The materials were subjected to reduction under 10% H_2/Ar gas mixture with a flow rate of 30 cc min^{-1} and a heating rate of 10° min^{-1}. H_2 consumption was monitored using a gas chromatograph (Varian 8301).

3A.2.3 Electrocatalytic Oxidation of Methanol

Electrocatalytic oxidation of methanol was performed in a standard three-electrode system using OrigaFlex OGF500 electrochemical workstation. The Hg/HgO electrode in 1 M KOH was used as the reference and a Pt wire was used as the counter electrode. The working electrode was prepared by drop casting the catalyst ink onto the GCE (3 mm, 0.07 cm^2 area). Before drop casting the catalyst ink, the GCE was polished using 0.05 μm alumina slurry. The catalyst ink was prepared by dispersing the physical mixture of 5 mg of the synthesized catalyst and 2 mg of carbon black in 1mL of methanol and 10μL Nafion solution. An aqueous solution of 0.5 M NaOH served as electrolyte. ECSA was determined by conducting double - step chronoamperometric expert experiments and calculated using Cottrell equation as elobrated chapter 2A [123]. CV studies were carried out at different methanol concentrations in alkaline electrolyte medium. The stability of the catalyst was studied for 24 h using CA studies at room temperature. In all measurements, the potential of Hg/HgO is converted to RHE in 0.5 M NaOH according to the following equation: $E_{RHE} = E_{Hg/HgO} + 0.059 \times pH + 0.098$. The concentration of the surface Ni - OOH layers after CV cycles in NaOH medium was calculated with respect to the geometrical

surface area according to the following equation

$$I_p = \left[\left(\frac{z^2F^2}{4RT}\right) A\tau^*\nu\right] \quad (3A.3)$$

I_p = Peak current density ($mAcm^{-2}$), Z = No. of electrons transferred, R = Gas constant, T = Temperature, A = Geometrical area of the electrode (0.07 cm^2) ν = scan rate, and τ^* = surface coverage of Ni - OOH. The liquid products after CA were analysed using ^1H NMR (Bruker AV NEO, 400 MHz). About 0.4 mL of electrolysis solution, 0.1 mL of D_2O, and 5 mg of 4-nitrophenol (as an internal standard) were added into the NMR tube for identifying the product. EIS study was carried out at 1.54 V vs RHE to study the electron transfer for MOR over a frequency range of 0.1 Hz to 500 kHz with a sinusoidal excitation signal of 10 mV using a Biologic Sp-150 electrochemical workstation with the conventional three-electrode system in an alkaline mixture of 0.5 M MeOH and 0.5 M NaOH. The Tafel plot was constructed by using steady-state response and its slope is calculated accordingly.

3A.2.4 CO Oxidation

The CO oxidation experiments were performed over the as-synthesized catalysts in 0.01M NaOH to evaluate the CO tolerance of the materials. The electrochemical cell was made airtight and the electrolyte was purged with Ar for the removal of any dissolved oxygen. Chronoamperometry was carried at different potentials with a continuous purge of 10% CO in N_2 at a flow rate of 5 cc min^{-1}. The evolved gases were quantified using GC (NUCON-5765, India) equipped with a flame ionization detector for CO_2. GC was calibrated using a standard gas mixture (CHEMIX speciality gases and equipment, India) under standard conditions. Ultrapure Ar (99.9%) was used as a carrier gas. Around 300 μL of gas was collected after 15 min of CA at each potential from the headspace of the electrochemical cell with a gas-tight Hamilton syringe and was injected into the GC column. The concentration of CO and CO_2 at each potential were calculated from the area under the peak.

3A.3 Results and discussion

3A.3.1 Structural, Surface and Electronic Properties

The prepared catalysts demonstrated through the ED-XRF analysis that the combustion synthesis yielded an actual doping concentration of Ni and Sr similar to the theoretically calculated values (Figure 3A.1 Table 3A.1).

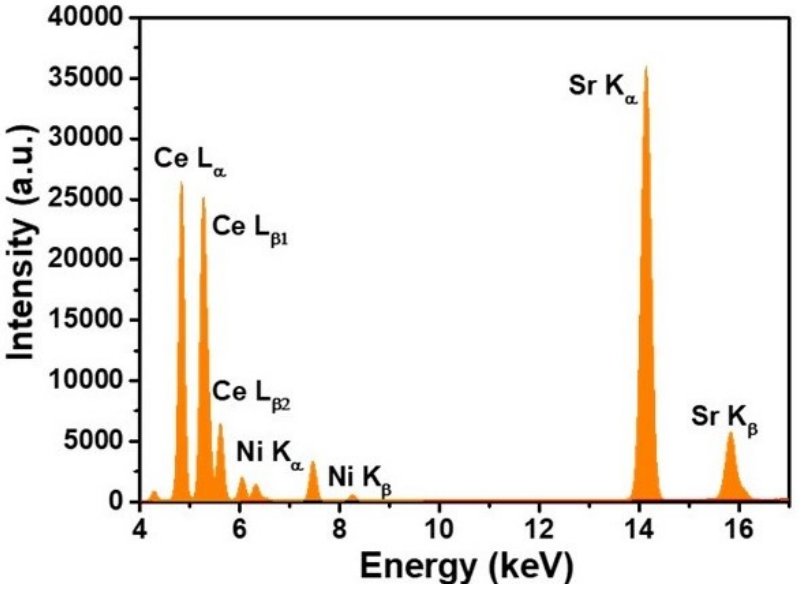

FIGURE 3A.1: Representative ED-XRF Plot of $Ce_{0.9}Ni_{0.05}Sr_{0.05}O_{2-\delta}$

TABLE 3A.1: ED-XRF of $Ce_{1-x-y}Ni_xSr_yO_{2-\delta}$ (x = 0.03 - 0.07; y = 0.03 - 0.07)

Catalysts	**Calculated (%)**			**XRF (%)**		
	Ce	Sr	Ni	Ce	Sr	Ni
$\mathbf{Ce_{0.97}Ni_{0.03}O_{2-\delta}}$	98.7	-	1.2	98.0	-	1.9
$\mathbf{Ce_{0.95}Ni_{0.05}O_{2-\delta}}$	97.5	-	2.10	97.1	-	2.87
$\mathbf{Ce_{0.93}Ni_{0.07}O_{2-\delta}}$	96.9	-	3.05	97.0	-	2.95
$\mathbf{Ce_{0.92}Ni_{0.05}Sr_{0.03}O_{2-\delta}}$	95.8	1.95	2.18	94.6	2.31	3.07
$\mathbf{Ce_{0.9}Ni_{0.05}Sr_{0.05}O_{2-\delta}}$	94.5	3.28	2.19	94.8	2.39	2.84
$\mathbf{Ce_{0.88}Ni_{0.05}Sr_{0.07}O_{2-\delta}}$	93.1	4.63	2.21	92.7	4.68	2.55

The representative XRD patterns of pristine CeO_2, doped $Ce_{0.95}Ni_{0.05}O_{2-\delta}$ and $Ce_{0.9}Ni_{0.05}Sr_{0.05}O_{2-\delta}$ along with the simulated pattern are shown in Figure 3A.2(a). The XRD patterns of the rest of the materials of the series ($Ce_{0.97}Ni_{0.03}O_{2-\delta}$, $Ce_{0.93}Ni_{0.07}O_{2-\delta}$, $Ce_{0.92}Ni_{0.05}Sr_{0.03}O_{2-\delta}$ and $Ce_{0.88}Ni_{0.05}Sr_{0.07}O_{2-\delta}$) are plotted in Figure 3A.2(b). The combustion synthesized pristine and the doped catalysts showed relatively broad XRD peaks indicating a nano-crystalline nature of the materials. The crystallite sizes of the solution combustion synthesized materials calculated using Scherrer's method with respect to the highest intense peak of (111) were 15.19, 8.02, and 5.85 nm for CeO_2, $Ce_{0.95}Ni_{0.05}O_{2-\delta}$, $Ce_{0.9}Ni_{0.05}Sr_{0.05}O_{2-\delta}$, respectively. Apparently, with doping

of Ni and co-doping of Ni and Sr the material became further nano-crystalline in nature [181, 182]. The pristine CeO_2 crystallized in a phase pure cubic fluorite structure with the space group $Fm\bar{3}m$ (JCPDS 34-0394) [179, 180, 183] . Upon Ni doping, $Ce_{1-x}Ni_xO_{2-\delta}$ did not show any additional diffraction peak corresponding to Ni or NiO phases. Even with co-doping of Sr there was complete retention of pure fluorite phase in $Ce_{1-x-y}Ni_xSr_yO_{2-\delta}$without any SrO_x impurity as can be seen from the XRD patterns in Figure 3A.2(a) and Figure 3A.2(b). The absence of any Ni, NiO and SrO_x diffraction peak can be rationalized with the substitutional doping of Ni and Sr cation in the Ce site with a formation of solid solution. This substitutional doping of Ni and Sr in the fluorite lattice by combustion synthesis was further corroborated when the similar loading of Ni and Sr in 5% NiO/CeO_2, 5% $NiO/5\%SrO/CeO_2$ prepared by physical mixing did show a strong evidence of NiO peak at $2\theta = 43.4°$ (JCPDS: 04-0835) and SrOx peak at $2\theta = 37.4°$ (JCPDS: 75-0263) (Figure 3A.2(c). The XRD pattern of 5% $NiO/5\%Sr/Al_2O_3$ is also plotted in Figure 3A.2(c), where the NiO peaks are prominently present.

Further, the Rietveld refinement was carried out with the experimentally collected powder diffraction patterns. A pseudo-Voigt profile function was used and the background correction was done using six polynomial functions. The refinement was carried out by substituting Ni and Sr cation in place of Ce at the Wyckoff sites 4a and oxygen in 8c, and the refinement profiles are shown in Figure 3A.2(d). The black coloured line represents the obtained empirical curve and the superimposed red coloured one designates the fitted curve with theoretically calculated intensities. The apparent fitting and the reliability factors, such as R_{Bragg}, and χ^2 provided in Table 3A.2 ensures the formation of single-phase solid solutions with lattice doping of Ni and Sr in CeO_2 matrix. The corresponding lattice parameters obtained from refinement are also provided in Table3A.2. The Shannon's ionic radii of six coordinated Ni^{2+} is 0.69 Å, whereas Ce^{4+} in CeO_2 is of 0.87 Å [184]. Therefore, a substitutional solid solution would result in a slightly contracted unit cell. The refined lattice parameters and the unit cell volumes of CeO_2 and $Ce_{1-x}Ni_xO_{2-\delta}$ (x = 0.03, 0.05 0.07) in Table 3A.2 indeed indicated a slight shrink in the unit cell size of doped materials compared to the pristine one due to the lattice substitution of Ni in CeO_2. It should be noted that the unit cell of $Ce_{0.9}Ni_{0.05}Sr_{0.05}O_{2-\delta}$ exhibited a slight expansion upon the additional doping of Sr^{2+} (with an ionic radius of 1.18 Å), as evident from the refinement studies presented in Table 3A.2. Even though the X-ray scattering factor of oxygen is low compared to that of cerium, the refined oxygen occupancy obtained from the refinement can give us a trend in the variation of oxygen content. The decrease in oxygen content as point defect is expected as a result of aliovalent substitutional doping. A decrease of oxygen

content from 2.00 in pure CeO_2 to 1.98 in $Ce_{0.95}Ni_{0.05}O_{2-\delta}$ and 1.97 in $Ce_{0.9}Ni_{0.05}Sr_{0.05}O_{2-\delta}$ is evidently significant as shown in Table 3A.2. This further confirms the creation of oxygen vacancy with ionic doping of Ni^{2+} in CeO_2 lattice.

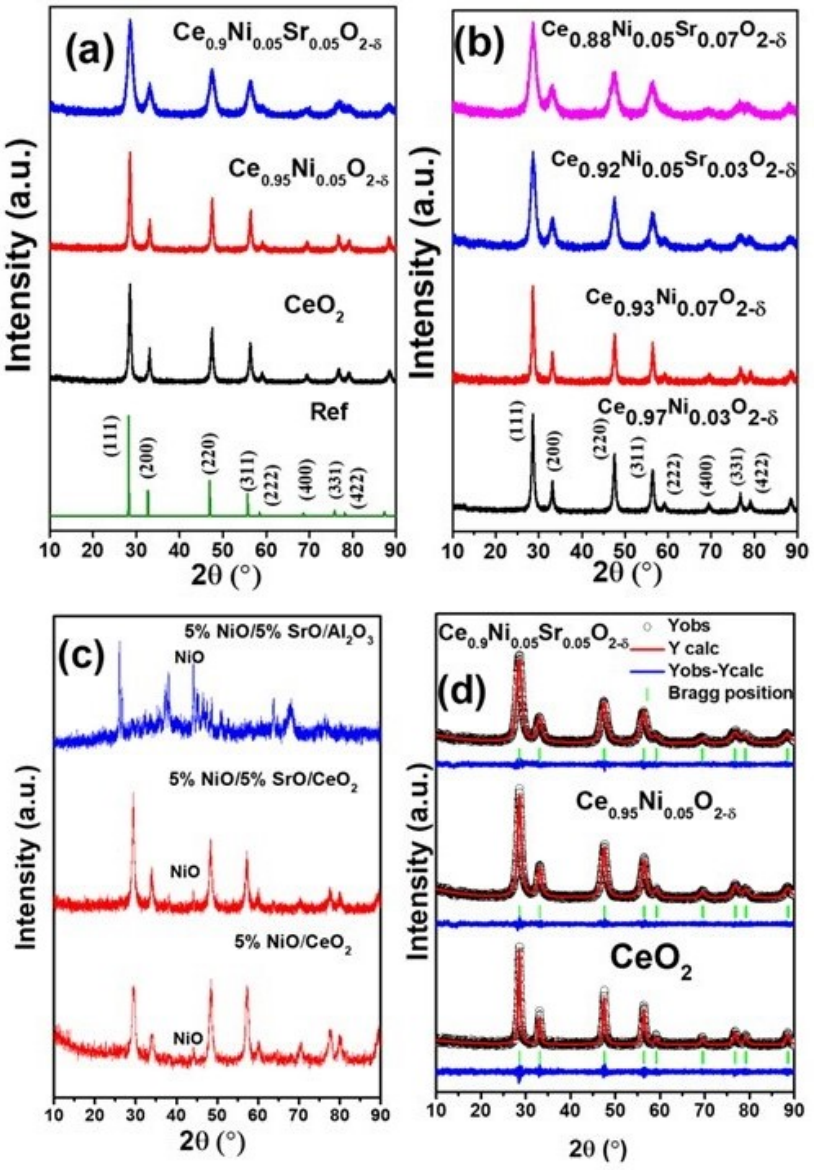

FIGURE 3A.2: (a) XRD patterns of CeO_2, $Ce_{0.95}Ni_{0.05}O_{2-\delta}$ and $Ce_{0.9}Ni_{0.05}Sr_{0.05}O_{2-\delta}$ (b) $Ce_{0.97}Ni_{0.03}O_{2-\delta}$, $Ce_{0.93}Ni_{0.07}O_{2-\delta}$, $Ce_{0.92}Ni_{0.05}Sr_{0.03}O_{2-\delta}$ and $Ce_{0.88}Ni_{0.05}Sr_{0.07}O_{2-\delta}$ (c) 5% NiO/CeO_2, 5% NiO/5%SrO/CeO_2 and 5% NiO/5%SrO/Al_2O_3 and (d) Rietveld refinement of CeO_2, $Ce_{0.95}Ni_{0.05}O_{2-\delta}$ and $Ce_{0.9}Ni_{0.05}Sr_{0.05}O_{2-\delta}$

TABLE 3A.2: Rietveld refine lattice parameters and atom occupancy of CeO_2, $Ce_{1-x}Ni_xO_{2-\delta}$ (x = 0.03, 0.05, 0.07) and $Ce_{0.9}Ni_{0.05}Sr_{0.05}O_{2-\delta}$

Catalysts	**Cell parameters (A)**	**Cell volume ($A^{\circ 3}$)**	χ^2	R_{Bragg}	**Occupancy**				**Wycoff site**			
	a = b=c				Ce	Ni	Sr	O	Ce	Ni	Sr	O
CeO_2	5.411	158.5	4.5	6.18	1.00	-	-	2.00	4a	4a		8c
$Ce_{0.97}Ni_{0.03}O_{2-\delta}$	5.411	158.5	2.6	3.43	1.00	1.02		1.99	4a	4a		8c
$Ce_{0.95}Ni_{0.05}O_{2-\delta}$	5.408	158.2	0.57	0.66	0.97	0.05	-	1.98	4a	4a		8c
$Ce_{0.93}Ni_{0.07}O_{2-\delta}$	5.406	158.0	2.1	3.25	0.96	0.05		1.98	4a	4a		8a
$Ce_{0.9}Ni_{0.05}Sr_{0.05}O_{2-\delta}$	5.416	158.8	0.69	0.76	0.92	0.05	0.05	1.97	4a	4a	4a	8c

The surface morphology along with EDAX pattern of CeO_2, $Ce_{0.95}Ni_{0.05}O_{2-\delta}$ and $Ce_{0.9}Ni_{0.05}Sr_{0.05}O_{2-\delta}$ are shown in Figure 3A.3. The FE-SEM micrograph of pristine CeO_2 was porous in nature. Interestingly, with co-doping of Ni and Sr the morphology was completely different. The EDAX pattern in Figure 3A.3 demonstrates the high distribution of Ni and Sr in the matrix.

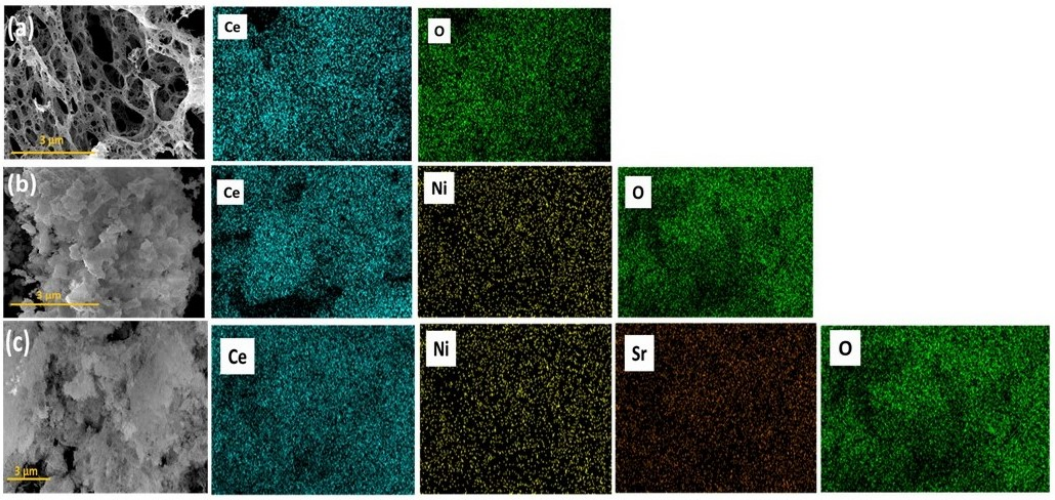

FIGURE 3A.3: FE-SEM and SEM-EDAX of (a) CeO_2, (b) $Ce_{0.95}Ni_{0.05}O_{2-\delta}$and (c) $Ce_{0.9}Ni_{0.05}Sr_{0.05}O_{2-\delta}$

The different surface morphology on doping intrigued us to further study the specific surface area and electrochemically active surface area of the synthesized materials. N_2 adsorption-desorption isotherms of CeO_2, $Ce_{0.95}Ni_{0.05}O_{2-\delta}$ and $Ce_{0.9}Ni_{0.05}Sr_{0.05}O_{2-\delta}$ exhibited type II isotherms indicating the nano porous nature of the materials (Figure 3A.4(a)). The type II adsorption isotherm shows large deviation from Langmuir model of adsorption, and the significant increase in the in the amount of N_2 adsorption at $\frac{P}{Po}$~1 is attributed to the multilayer adsorption. The specific surface area estimated from BET equation were 36.39, 42.87 and 51.36 m^2 g^{-1} for CeO_2, $Ce_{0.95}Ni_{0.05}O_{2-\delta}$ and $Ce_{0.9}Ni_{0.05}Sr_{0.05}O_{2-\delta}$, respectively. It was interesting to find out a subtle increasing specific surface area with co-doping. The pore-size diameter estimated by the BJH model confirmed the presence of mesopores with average pore diameter of ~3 nm [185,

186]. The activity of MOR can be greatly influenced by the ECSA [132, 187, 188]. The ECSA was calculated from the plot in Figure 3A.4(b) obtained from CA studies using the following Cottrell equation. The pristine CeO_2 exhibited the ECSA of 0.82 cm^2, while $Ce_{0.95}Ni_{0.05}O_{2-\delta}$ also showed a similar value of 0.83 cm^2. Surprisingly, $Ce_{0.9}Ni_{0.05}Sr_{0.05}O_{2-\delta}$ possessed a ECSA as high as 2.72 cm^2. It should be noted that as Sr doping increased ECSA with the active sites exposed for further increment in methanol adsorption and oxidation.

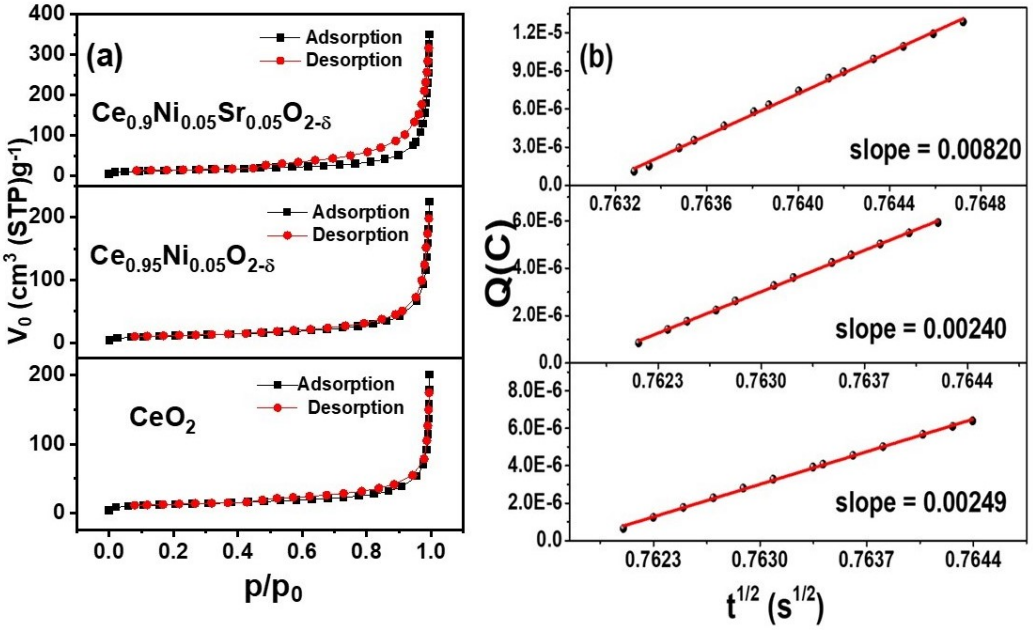

FIGURE 3A.4: (a) N_2 adsorption - desorption isotherm, and (b) Charge vs. time plot of CeO_2, $Ce_{0.95}Ni_{0.05}O_{2-\delta}$ and $Ce_{0.9}Ni_{0.05}Sr_{0.05}O_{2-\delta}$

3A.3.2 Electrocatalytic Oxidation of Methanol

The electrocatalytic activity of MOR of carbon-supported pristine CeO_2 and doped $Ce_{1-x}Ni_xO_{2-\delta}$ and $Ce_{1-x-y}Ni_xSr_yO_{2-\delta}$ were studied at different scan rates in 0.5 M NaOH and 0.5 M MeOH. Before the screening of MOR, the materials were activated in 0.5 M NaOH by cycling 25 scans within a potential window of 0.8 to 1.8 V vs RHE at a scan rate of 10 - 100 mV s^{-1} as in Figure 3A.5.

TABLE 3A.3: Ni - OOH surface concentration

Sample	Surface concentration Ni - OOH (τ^*) mol cm^{-2}
$Ce_{0.95}Ni_{0.05}O_{2-\delta}$	2.1×10^{-9}
$Ce_{0.92}Ni_{0.05}Sr_{0.03}O_{2-\delta}$	5.6×10^{-8}
$Ce_{0.9}Ni_{0.05}Sr_{0.05}O_{2-\delta}$	5.7×10^{-7}
$Ce_{0.88}Ni_{0.05}Sr_{0.07}O_{2-\delta}$	5.5×10^{-9}

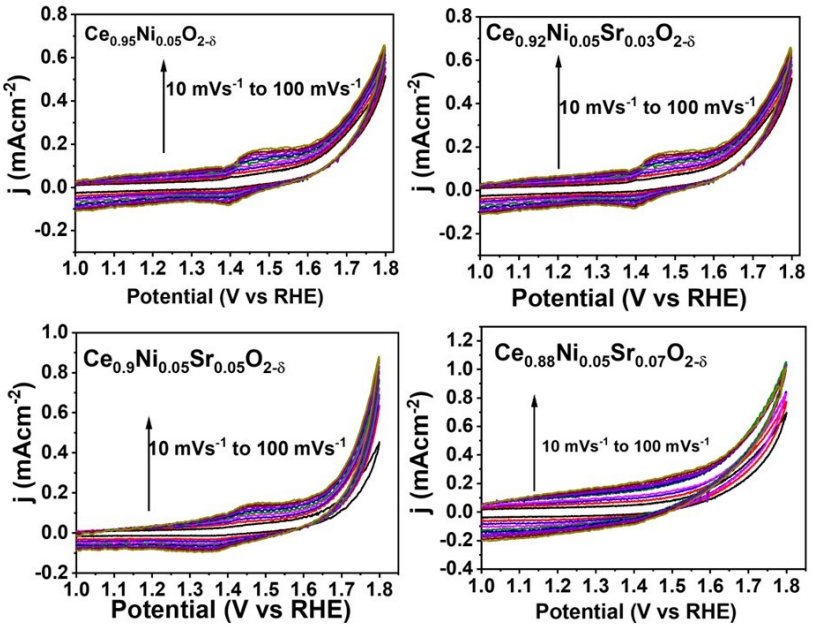

FIGURE 3A.5: CVs of $Ce_{1-x-y}Ni_xSr_yO_{2-\delta}$ (x = 0.05, y = 0.03 - 0.07) in 0.5 M NaOH at the potential scan rates in the range 10 - 100 mV s^{-1}

The CV traces of the CeO_2, $Ce_{0.95}Ni_{0.05}O_{2-\delta}$ and $Ce_{0.9}Ni_{0.05}Sr_{0.05}O_{2-\delta}$ in alkaline media are shown in Figure 3A.6(a). The typical cyclic voltammograms show peaks corresponding to double layer charging, Ni oxidation and Ni - OOH formation in forward cycle, and reduction in reverse scan. A mild peak at 1.39 V vs RHE observed in the presence of 0.5 M NaOH indicated the formation of surface Ni - OOH layer with a red-ox couple of Ni^{2+}/Ni^{3+} as also has been mentioned in earlier reports [187, 189]. The increase of peak current density with the increase in scan rate from 10 to 100 mV s^{-1} suggested the formation of a thicker layer of Ni - OOH species with Ni^{3+} over the materials with a higher scan rate (Figure 3A.5, Table 3A.3). It was interesting to observe that with the doping of Ni and Sr the concentration of Ni - OOH species increased gradually, with $Ce_{0.9}Ni_{0.05}Sr_{0.05}O_{2-\delta}$ exhibiting the highest $-$OOH species concentration of 5.7×10^{-7} mol cm^{-2}. Apparently, the co-doping of Ni and Sr in CeO_2 facilitated the formation of surface Ni - OOH, a key intermediate species for the efficient MOR.

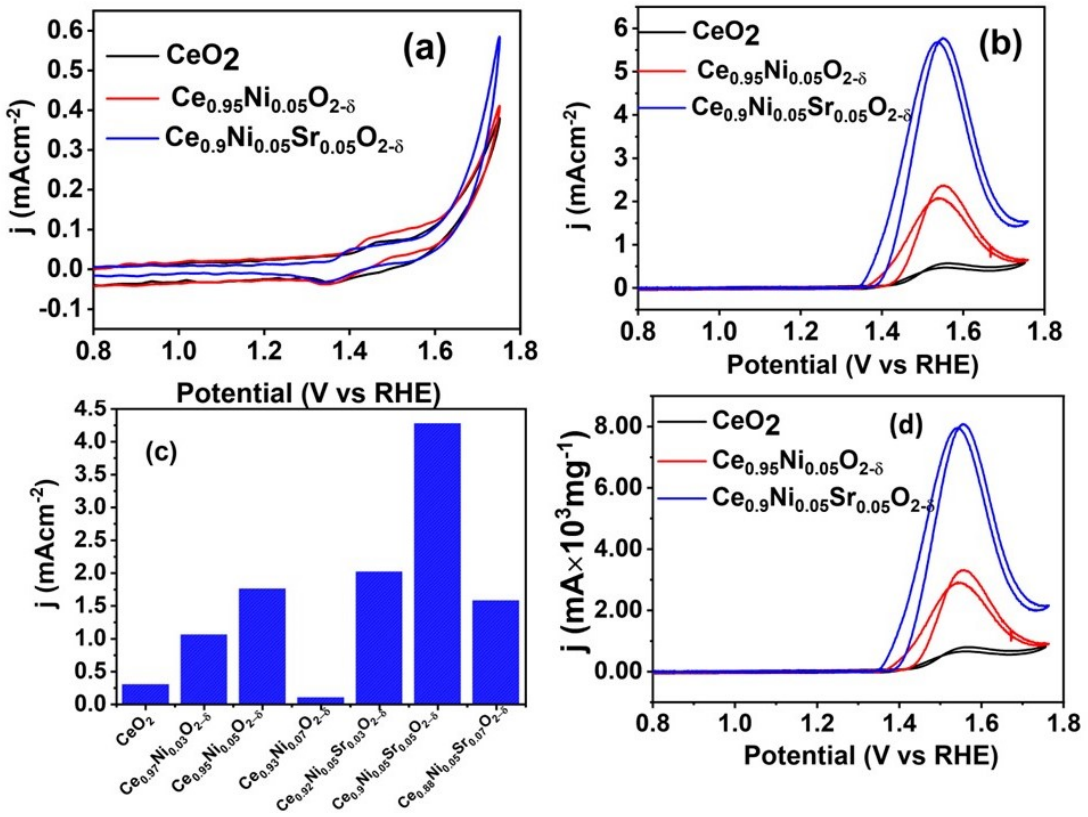

FIGURE 3A.6: CVs of CeO_2, $Ce_{0.95}Ni_{0.05}O_{2-\delta}$ and $Ce_{0.9}Ni_{0.05}Sr_{0.05}O_{2-\delta}$in (a) 0.5 M NaOH, (b) in 0.5 M NaOH and 0.5 M MeOH with a scan speed of 50 mV s^{-1} (c) Bar plot depicting variation of current densities with respect to Ni and Sr co-doping and (d) CVs of CeO_2, $Ce_{0.95}Ni_{0.05}O_{2-\delta}$ and $Ce_{0.9}Ni_{0.05}Sr_{0.05}O_{2-\delta}$ in 0.5 M NaOH and 0.5 M MeOH normalized with catalyst loading

Next, we screened the synthesized material for catalytic MOR activity and the representative CV traces of pristine CeO_2, doped $Ce_{0.95}Ni_{0.05}O_{2-\delta}$ and $Ce_{0.9}Ni_{0.05}Sr_{0.05}O_{2-\delta}$ are plotted in Figure 3A.6(b). With the addition of methanol, the oxidation peak of Ni was obscured and a sharp increase in current density was observed due to the oxidation of methanol. The methanol oxidation peak was observed after onset of Ni^{2+} oxidation peak, suggesting Ni - OOH as the active species for methanol oxidation [190, 191]. All the catalysts exhibited distinguishable and well-separated anodic and cathodic peaks in forward and backward scans. The anodic peak in the forward scan was due to the oxidation of methanol, while the cathodic peak might be due to the oxidation of the rest of the adsorbed species on the surface of the catalyst [170, 192]. The surge in anodic peak was observed at 1.54 V vs RHE with current densities 0.56, 2.36, and 5.76 mA cm^{-2} for CeO_2, doped $Ce_{0.95}Ni_{0.05}O_{2-\delta}$ and $Ce_{0.9}Ni_{0.05}Sr_{0.05}O_{2-\delta}$, respectively. The current density normalized with the amount of catalyst loaded on the surface of glassy carbon is shown in 3A.6(d). Apparently, the peak current density increased with Ni doping in $Ce_{1-x}Ni_xO_{2-\delta}$ up to x = 0.05, and with Sr co-doping in $Ce_{1-x-y}Ni_xSr_yO_{2-\delta}$ up to y = 0.05. The detailed current densities with respect to Ni and Sr co-doping are provided in Figure

3A.6(c). Further enhancement in concentration of Ni and Sr deteriorated the peak current density and $Ce_{0.9}Ni_{0.05}Sr_{0.05}O_{2-\delta}$ emerged as the optimum catalyst for efficient MOR activity. It must be noted that the CV traces in alkaline media exhibited highest formation of Ni - OOH surface species over $Ce_{0.9}Ni_{0.05}Sr_{0.05}O_{2-\delta}$, which apparently helped the particular material demonstrating the best MOR activity [191]. The doping of bivalent cations Ni and Sr in CeO_2 apparently created the intrinsic oxygen vacancy, which facilitated the formation of surface Ni - OOH species in alkaline media for efficient MOR activity.

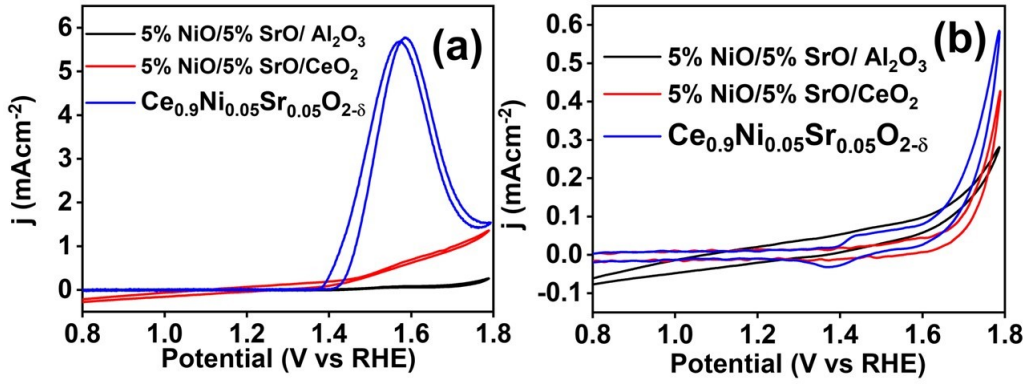

FIGURE 3A.7: CVs of 5% NiO/5%SrO/CeO_2, 5% NiO/5%SrO/Al_2O_3 and $e_{0.9}Ni_{0.05}Sr_{0.05}O_{2-\delta}$ (a) 0.5 M NaOH and 0.5 M MeOH (b) 0.5 M NaOH at scan rate of 50 mV s^{-1}

To corroborate the role of oxygen vacancy, we performed control MOR experiments with 5% NiO/5%SrO/CeO_2 and 5% NiO/5%SrO/Al_2O_3, where the intrinsic oxygen vacancies are comparably negligible. Figure 3A.7(a) shows that the peak current densities are significantly lower in the physical mixtures compared to the ionic solid solution catalysts. Even, the CV traces in alkaline media did not show any evidence of surface Ni - OOH species formation (Figure 3A.7(b)). This clearly indicates that the efficacy of MOR crucially depends on the oxygen vacancy created by the lattice substitution of Ni and Sr in CeO_2, and not on mere surface dispersion of the active sites. When MOR experiment was performed over 5% NiO/5%SrO/Al_2O_3, the material exhibited further deteriorated activity indicating the importance of the reducible support.

The intrinsic oxygen vacancy and the cationic doping may incur covalency vis à vis conductivity in the material. The conductivity plays a significant role in an electrocatalytic process. Therefore, the EIS study was carried out to analyse the electron transfer mechanism taking place at the electrode-electrolyte interface. Figure 3A.8(a) shows the Nyquist plot of CeO_2, $Ce_{0.95}Ni_{0.05}O_{2-\delta}$ and $Ce_{0.9}Ni_{0.05}Sr_{0.05}O_{2-\delta}$ in alkaline 0.5 M methanol solution. With the gradual increase in Ni and Sr co-doping the semi-circle arc lowered steadily attributing to higher electrical conductivity and very less charge transfer resistance indicative of a rapid electron

transfer process in the MOR process. Among the series of materials, $Ce_{0.9}Ni_{0.05}Sr_{0.05}O_{2-\delta}$ exhibited the lowest charge transfer resistance, which directly contributed to its highest MOR activity [193]. Further, we plotted the Bode phase angle (Figure 3A.8(b)) and Bode absolute impedance (Figure 3A.8(c)) to evaluate the RC time constant and admittance value for the synthesized catalysts. The obvious shift in the phase angle peak to a higher frequency region and a decrease in peak height of $Ce_{0.9}Ni_{0.05}Sr_{0.05}O_{2-\delta}$ compared to pristine CeO_2 and $Ce_{0.95}Ni_{0.05}O_{2-\delta}$ in Figure 3A.8(b) as well as the slope at higher frequency from Bode absolute impedance in Figure 3A.8(c) indicate an improved charge transfer efficiency to the adsorbed reactant to facilitate the methanol oxidation reaction over $Ce_{0.9}Ni_{0.05}Sr_{0.05}O_{2-\delta}$. The significantly low RC time constant as well as high admittance value calculated for $Ce_{0.9}Ni_{0.05}Sr_{0.05}O_{2-\delta}$ (vide Table 3A.4) also indicate a seemingly fast electron transfer process over the material for a facile MOR [194–196]. To analyse it further, the corresponding circuits were obtained after fitting the Nyquist plot. Figure 3A.8(d) shows the circuit corresponding to $Ce_{0.95}Ni_{0.05}O_{2-\delta}$ and $Ce_{0.9}Ni_{0.05}Sr_{0.05}O_{2-\delta}$. The first phase element is associated with charge transfer resistance (R_{ct}) and double layer formation (C_{dl}), whereas the second phase element is associated with adsorption resistance (R_{ad}) and adsorption capacitance (C_{ad}) [197, 198]. The corresponding values are provided in Table 3A.4. A lower R_{ct} over $Ce_{0.9}Ni_{0.05}Sr_{0.05}O_{2-\delta}$ (436.3 Ω) compared to $Ce_{0.95}Ni_{0.05}O_{2-\delta}$ (1860 Ω) rationalizes the higher MOR activity over the co-doped catalyst. Also, the lower R_{ad} over $Ce_{0.9}Ni_{0.05}Sr_{0.05}O_{2-\delta}$ (2.4 Ω) compared to $Ce_{0.95}Ni_{0.05}O_{2-\delta}$ (40.9 Ω) in the second phase of the circuit in Figure 3A.8(d) indicates the ease of oxidation of the adsorbed species like CO on the surface of $Ce_{0.9}Ni_{0.05}Sr_{0.05}O_{2-\delta}$. The circuit obtained from fitting the Nyquist data of CeO_2 is plotted in Figure 3A.8(e). Apparently, the circuit constructs in a different manner, and also the R_{ct} and R_{ad} over the pristine material are significantly higher than the doped samples.

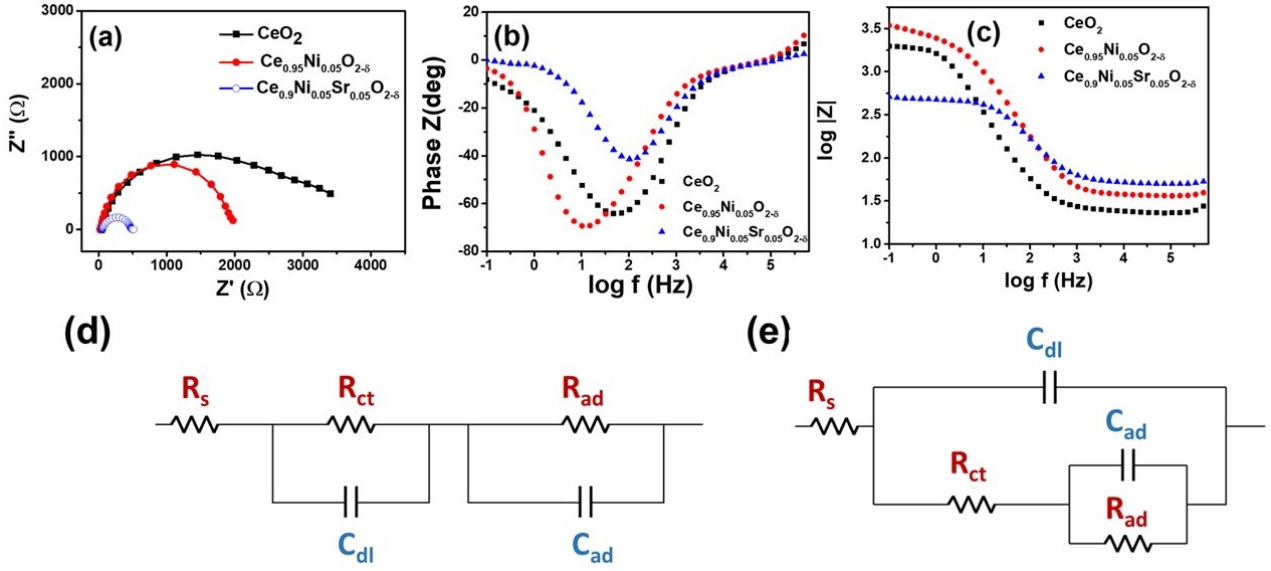

FIGURE 3A.8: (a)Nyquist plots (b)Bode Phase angle (c) Bode Admittance of CeO_2, $Ce_{0.95}Ni_{0.05}O_{2-\delta}$ and $Ce_{0.9}Ni_{0.05}Sr_{0.05}O_{2-\delta}$ Nyquist fitted circuit diagram of (d) $Ce_{0.95}Ni_{0.05}O_{2-\delta}$ and $Ce_{0.9}Ni_{0.05}Sr_{0.05}O_{2-\delta}$ and (e) CeO_2

TABLE 3A.4: EIS parameters obtained from fitting of Nyquist plot

Catalysts / Parameters	**CeO_2**	**$Ce_{0.95}Ni_{0.05}O_{2-\delta}$**	**$Ce_{0.9}Ni_{0.05}Sr_{0.05}O_{2-\delta}$**
$R_s(\Omega)$	36.8	24.4	50.3
$R_{ct}(\Omega)$	2077	1860	436.3
$R_{ad}(\Omega)$	1816	40.9	2.49
C_{dl}(F)	21.4×10^{-6}	52.5×10^{-6}	76.2×10^{-6}
C_{ad}(F)	3.43×10^{-4}	5.2 ×10-5	41.7×10^{-6}
RC Time constant(s)	0.415	2.12×10^{-3}	1.03×10^{-4}
Admittance(S)	0.027	0.040	0.098

3A.3.3 Evaluation of Kinetic Parameters

The data obtained from the voltammetric response of CeO_2, $Ce_{0.95}Ni_{0.05}O_{2-\delta}$ and $Ce_{0.9}Ni_{0.05}Sr_{0.05}O_{2-\delta}$ catalysts towards methanol oxidation reaction were subjected to a detailed kinetic analysis to understand the activity, order and rate determining step of the reaction. The Tafel studies were carried out in a steady state response. A CA response was carried out for 300 s at the catalytically active potential region of MOR (Figure 3A.9(a-c)), and the current density obtained after reaching the steady state (at 150th s) was plotted against the potential with and without iR correction (Figure 3A.9(d-f)).

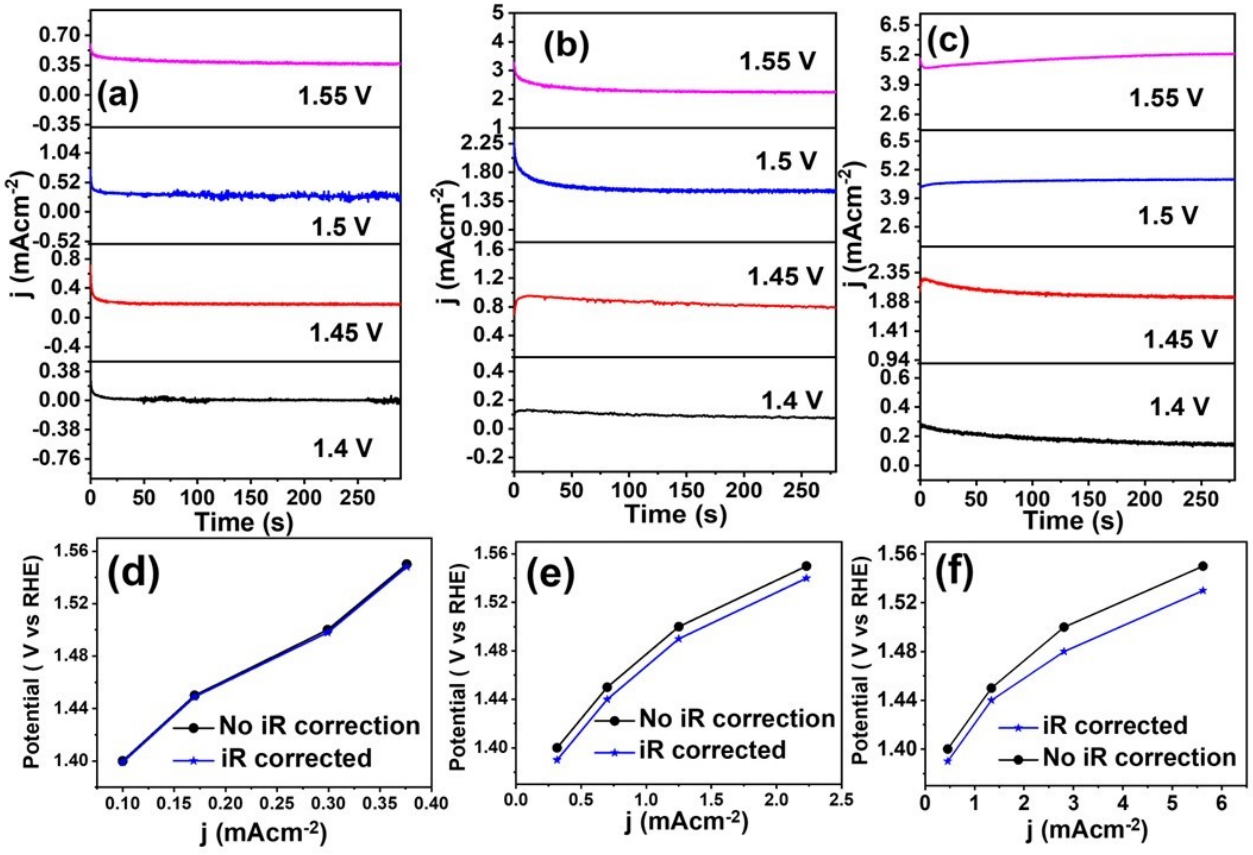

FIGURE 3A.9: CA responses and Plot of current density vs potential (V vs RHE) with and without IR drop correction of (a, d) CeO_2 (b, e) $Ce_{0.95}Ni_{0.05}O_{2-\delta}$ (c, f) $Ce_{0.9}Ni_{0.05}Sr_{0.05}O_{2-\delta}$

The Tafel plots in Figure 3A.10(a) were obtained from the steady state polarization curve constructed using the iR corrected potentials. $Ce_{0.9}Ni_{0.05}Sr_{0.05}O_{2-\delta}$ exhibited a Tafel slope of 126.7 mV dec^{-1}, while $Ce_{0.95}Ni_{0.05}O_{2-\delta}$ and CeO_2 exhibited a slope of 177.2 mV dec^{-1} and 286.0 mV dec^{-1}, respectively. Existing literature propose that the rate determining step of methanol oxidation is the C–H bond dissociation for which the theoretical Tafel slope would be 120 mV dec^{-1} at the methanol oxidation potential [199, 200]. However, the Tafel slope of methanol

oxidation also may show a large deviation from ideal values owing to the adsorbed intermediates on the surface of the catalysts. As observed, Figure 3A.10(a) shows a Tafel slope of 126.7 mV dec^{-1} for $Ce_{0.9}Ni_{0.05}Sr_{0.05}O_{2-\delta}$ near to the theoretical value. On the contrary, $Ce_{0.95}Ni_{0.05}O_{2-\delta}$ and CeO_2 exhibited a high Tafel slope of 177.2 and 286.0 mV dec^{-1} , respectively. This low Tafel slope of $Ce_{0.9}Ni_{0.05}Sr_{0.05}O_{2-\delta}$ is in good agreement with the ideal theoretical value of 120 mV dec^{-1} indicating a single electron transfer for C–H bond dissociation as the rate determining step. The deviation of the Tafel slope from the ideal value in $Ce_{0.95}Ni_{0.05}O_{2-\delta}$ and CeO_2 suggest that the formed oxidative intermediates block the surface of the catalysts preventing accessibility of fresh reactant molecules on the active sites.

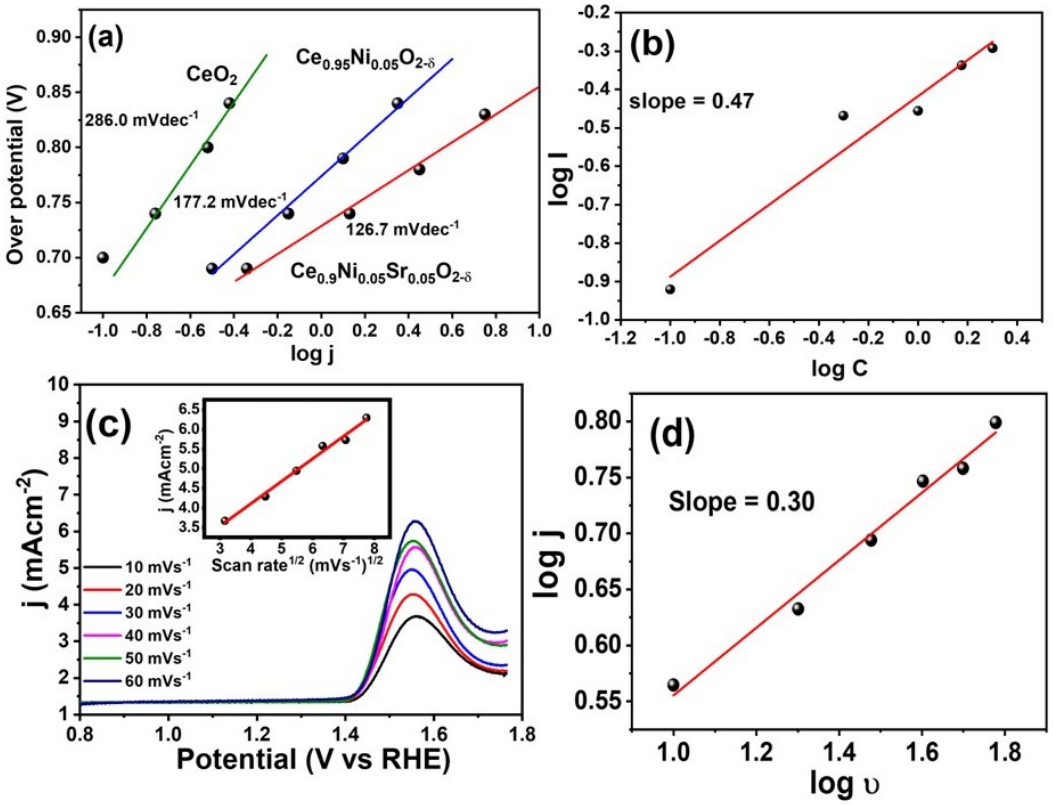

FIGURE 3A.10: (a) Tafel plot of CeO_2, $Ce_{0.95}Ni_{0.05}O_{2-\delta}$ and $Ce_{0.9}Ni_{0.05}Sr_{0.05}O_{2-\delta}$ (b) log C Vs log I plot of $Ce_{0.9}Ni_{0.05}Sr_{0.05}O_{2-\delta}$ for MOR showing order of the reaction (c) scan rate dependent study of $Ce_{0.9}Ni_{0.05}Sr_{0.05}O_{2-\delta}$ in 0.5 M NaOH and 0.5 M MeOH (inset square root of scan rate vs current density) (d) logarithmic plot of scan rate with current density for $Ce_{0.9}Ni_{0.05}Sr_{0.05}O_{2-\delta}$

The reaction order of the electro oxidation of methanol over $Ce_{0.9}Ni_{0.05}Sr_{0.05}O_{2-\delta}$ was calculated from the plot of log I (A) vs. log C (C) using the equation log I (a) = log nFk + m logC, where n is the number of electrons, F is the Faraday constant, k being the reaction constant, m is the reaction order, and C is the concentration of methanol [199]. Voltammetric responses of $Ce_{0.9}Ni_{0.05}Sr_{0.05}O_{2-\delta}$ were obtained at different methanol concentration, and a linear relationship

was obtained by plotting the log I (A) with. log C (M) in Figure 3A.10(b). The slope of 0.47 corresponds to the reaction order = $\frac{1}{2}$ with respect to methanol over $Ce_{0.9}Ni_{0.05}Sr_{0.05}O_{2-\delta}$ [199]. The further kinetic introspection of MOR over the optimized catalyst $Ce_{0.9}Ni_{0.05}Sr_{0.05}O_{2-\delta}$ was done with the help of scan rate dependent studies. When the scan rate was varied in the range of 10 – 100 mV s^{-1} with the catalyst $Ce_{0.9}Ni_{0.05}Sr_{0.05}O_{2-\delta}$, an increase in anodic oxidation current was observed with increasing scan rate. A linear relationship was observed between the square root of scan rate and current density with a regression coefficient R^2 = 0.99 following Randles-Sevick equation (Figure 3A.10(c) and inset) [191]. A slope of 0.30 was obtained from the logarithmic plot of peak current density (mA cm^{-2}) vs. scan rate (mV s^{-1}) (Figure 3A.10(d)). The value is close to the theoretically expected value confirming the MOR over $Ce_{0.9}Ni_{0.05}Sr_{0.05}O_{2-\delta}$ is a diffusion-controlled process rather than a surface controlled phenomenon. Activation energy is another key parameter to assess the MOR activity of the catalysts. This was determined from Arrhenius plot of current density (ln j) vs. temperature (T^{-1}) at methanol oxidation potential of CeO_2, $Ce_{0.95}Ni_{0.05}O_{2-\delta}$ and $Ce_{0.9}Ni_{0.05}Sr_{0.05}O_{2-\delta}$. The temperature was varied from 25 to 50 °C with a gap of 5 °C in 0.5 M NaOH and 0.5 M MeOH electrolyte solution. The activation energy (E_a) was obtained from the slope as in (Figure 3A.11) [201–203]. The doped catalyst $Ce_{0.9}Ni_{0.05}Sr_{0.05}O_{2-\delta}$ exhibited the lowest activation energy of 18.7 kJ mol^{-1}, whereas $Ce_{0.95}Ni_{0.05}O_{2-\delta}$ and CeO_2 exhibited the activation energies of 24.1 and 47.3 kJ mol^{-1}, respectively. The low activation energy of $Ce_{0.9}Ni_{0.05}Sr_{0.05}O_{2-\delta}$ could be attributed to the highly adsorbed -OH in the alkaline medium, which facilitated the formation of surface Ni - OOH on the catalyst to carry forward the MOR with a lower energy barrier [199].

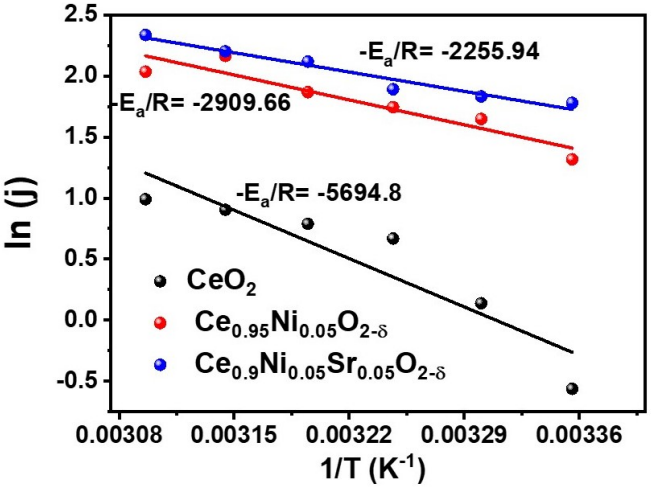

FIGURE 3A.11: Activation Energy plot of MOR over CeO_2, $Ce_{0.95}Ni_{0.05}O_{2-\delta}$, and $Ce_{0.9}Ni_{0.05}Sr_{0.05}O_{2-\delta}$

The durability of the catalyst for methanol oxidation is one of the most important terms of paramount interest. The major challenge is the CO poisoning that deteriorates the long term catalytic activity [204]. The stability of the best catalyst in the series $Ce_{0.9}Ni_{0.05}Sr_{0.05}O_{2-\delta}$ was examined by recording repetitive CVs for 300 scans in 0.5 M NaOH at a scan rate of 50 mV s^{-1} in the presence of 0.5 M methanol (Figure 3A.12(a)). No significant decrease in the peak current density (inset of Figure 3A.12(a) confirmed the stability of $Ce_{0.9}Ni_{0.05}Sr_{0.05}O_{2-\delta}$ towards methanol oxidation reaction. Further, the CA study of $Ce_{0.9}Ni_{0.05}Sr_{0.05}O_{2-\delta}$ was carried out at 1.54 V vs RHE for 12 h duration. Figure 3A.12(b)). shows almost a steady current density indicating a very stable methanol oxidation efficiency for long period of time over $Ce_{0.9}Ni_{0.05}Sr_{0.05}O_{2-\delta}$. A minute drop in the current density with a significantly long-term MOR could be due to the CO poisoning of the Pt counter electrode. A mechanistic introspection of CO tolerance has been addressed in the following section. To confirm the chemical robustness of the material after prolonged period of stability study, XRD pattern of the exhausted catalyst was studied as shown in Figure 3A.13(a). The exhausted $Ce_{0.9}Ni_{0.05}Sr_{0.05}O_{2-\delta}$ maintained its fluorite structure. However, some amorphous nature observed can be attributed to the presence of carbon black in the electrocatalytic ink used during MOR. The surface morphology was retained in the exhausted catalyst with a high dispersion of the dopants (Figure 3A.13(b)). The detailed ex-situ XPS analysis of all the exhausted catalysts (in Figure 3A.16 - 3A.18) unveiled the molecular reaction mechanism. Overall, the observation suggests that the exhausted $Ce_{0.9}Ni_{0.05}Sr_{0.05}O_{2-\delta}$, despite its prolonged stability study, retained its chemical robustness.

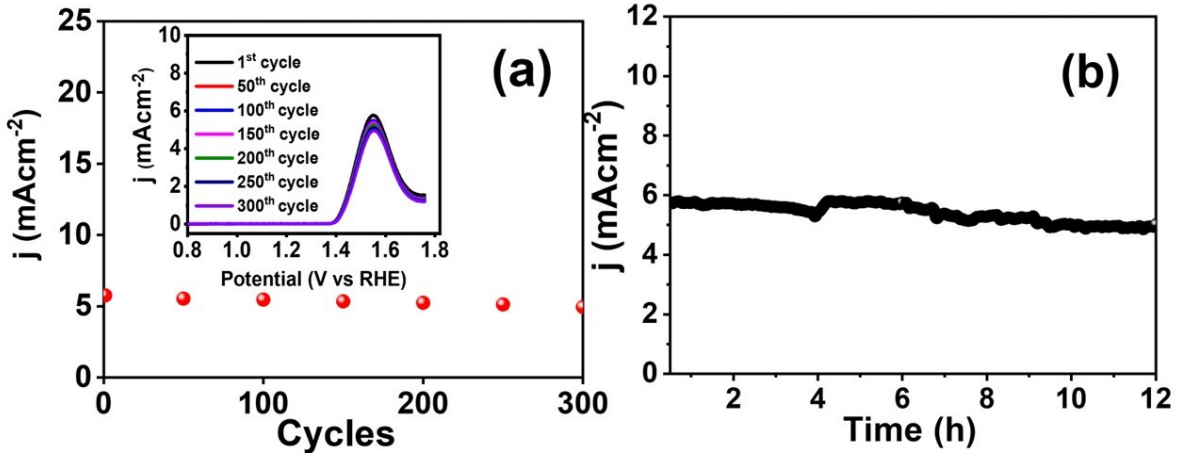

FIGURE 3A.12: Stability study of $Ce_{0.9}Ni_{0.05}Sr_{0.05}O_{2-\delta}$ up to 300 cycles (inset: forward scan up to 300^{th} cycle) (b) CA of $Ce_{0.9}Ni_{0.05}Sr_{0.05}O_{2-\delta}$ at 1.54 V vs RHE in 0.5 M NaOH and 0.5 M MeOH for 12 h

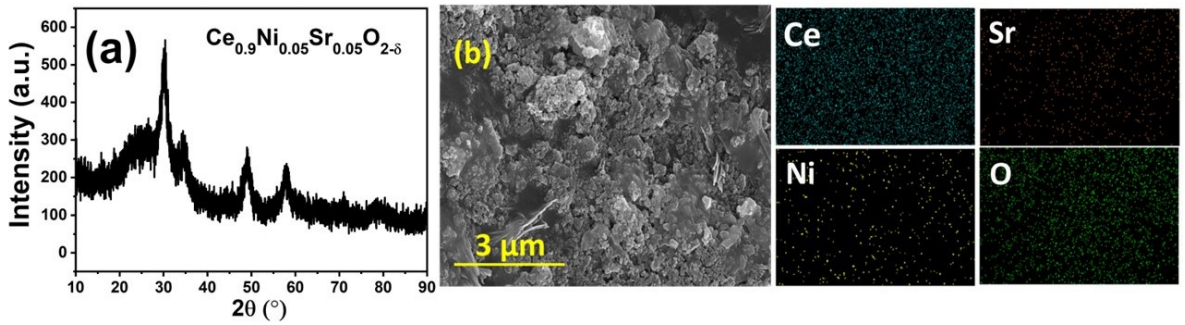

FIGURE 3A.13: (a) XRD, (b) FE-SEM image and EDX map of the exhausted $Ce_{0.9}Ni_{0.05}Sr_{0.05}O_{2-\delta}$

After a prolonged MOR study, the electrolyte was subjected to ^{1}HNMR to evaluate the liquid product. The corresponding spectra are shown in Figure 3A.14. The data revealed the formation of formic acid at 8.3 ppm as the only liquid product during MOR and no other liquid product was observed. Concentration of formic acid produced over CeO_2, $Ce_{0.95}Ni_{0.05}O_{2-\delta}$ and $Ce_{0.9}Ni_{0.05}Sr_{0.05}O_{2-\delta}$ at 1.4, 1.6 and 1.8 V vs RHE is represented in Figure 3A.15.

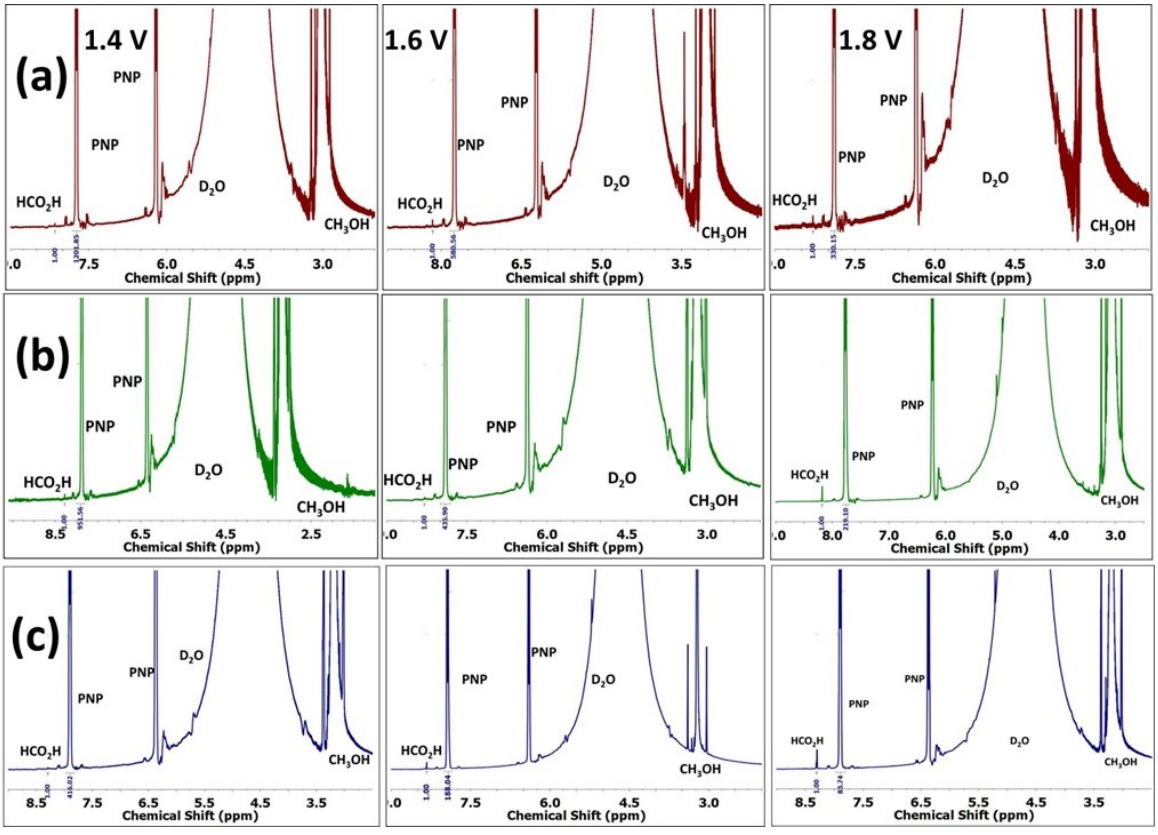

FIGURE 3A.14: ^{1}HNMR spectra of the electrolyte of (a) CeO_2, (b) $Ce_{0.95}Ni_{0.05}O_{2-\delta}$ and (c) $Ce_{0.9}Ni_{0.05}Sr_{0.05}O_{2-\delta}$ after 4 h of CA in 0.5 M MeOH and 0.5 M NaOH medium

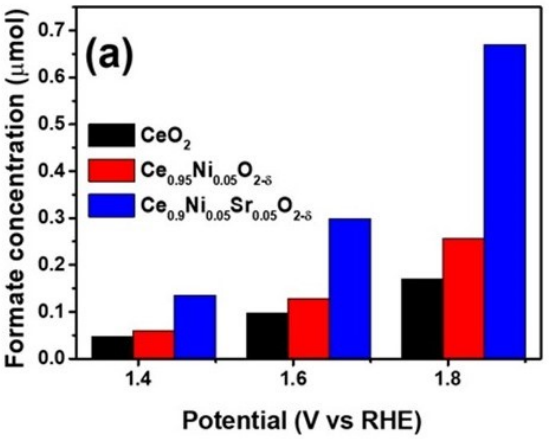

FIGURE 3A.15: Concentration of formic acid produced over CeO_2, $Ce_{0.95}Ni_{0.05}O_{2-\delta}$ and $Ce_{0.9}Ni_{0.05}Sr_{0.05}O_{2-\delta}$ at 1.4, 1.6 and 1.8 V vs RHE

3A.3.4 Mechanistic Probe and Involvement of Lattice Oxygen

The high current density and long-term stability of $Ce_{0.9}Ni_{0.05}Sr_{0.05}O_{2-\delta}$ towards methanol oxidation intrigued us to probe the mechanism of the reaction over the material. As electro-oxidation is a surface bound phenomenon, the electronic environment of the surface elements was thoroughly mapped before and after MOR via ex-situ XPS studies. The surface atomic percentages of the elements before and after MOR obtained from XPS studies are provided in Table 3A.5.

TABLE 3A.5: Surface atomic percentages of elements before and after MOR from XPS

Catalysts	Before reaction (Atm%)				After reaction (Atm%)			
	Ce	Sr	Ni	O	Ce	Sr	Ni	O
CeO_2	18.49			81.51	7.49			92.51
$Ce_{0.95}Ni_{0.05}O_{2-\delta}$	17.54		0.34	82.12	8.22		1.10	90.68
$Ce_{0.9}Ni_{0.05}Sr_{0.05}O_{2-\delta}$	15.33	1.69	0.18	82.17	3.47	0.25	0.36	95.92

The high-resolution core level Ce 3d spectra of as-prepared CeO_2, $Ce_{0.95}Ni_{0.05}O_{2-\delta}$ and $Ce_{0.9}Ni_{0.05}Sr_{0.05}O_{2-\delta}$ before the MOR are shown in Figure 3A.16(a). Each Ce 3d spectrum contains 10 peaks with first 5 peaks labelled as v corresponding to Ce $3d_{5/2}$ and next 5 peaks labelled as u corresponding to Ce $3d_{3/2}$ [42, 205]. The well separated peaks labelled as v‴ and u‴ at 901.8 and 918.1 eV are the characteristics for Ce^{4+} ($3d_{5/2}$ and $3d_{3/2}$) corresponding to Ce $3d^94f^0O2p^6$ final states configuration. The other two doublets labelled as v-u (at 884.8 and 904.5 eV) and v″-u″ (892.4 and 911.0 eV) correspond to primary photoionization from Ce^{4+} with Ce $3d^94f^2O2p^4$ and Ce $3d^94f^1O2p^5$ final states, respectively. The additional peaks labelled as v^o -u^o and v′-u′ at binding energies of 881.3 and 903.6 eV and 886.6 and 909.3 eV, respectively correspond to Ce $3d^94f^1O2p^5$ and $3d^94f^1O2p^6$ final states in 3+ oxidation states [206]. The

relative surface concentration (C) of Ce^{3+} and Ce^{4+} were estimated from deconvoluted peak areas (A) with the help of the following equations:

$$A_{Ce^{4+}} = A_v + A_u + A_{u''} + A_{v''} + A_{v'''} + A_{u'''} \tag{3A.4}$$

$$A_{Ce^{3+}} = A_{v'} + A_{u'} + A_{v^0} + A_{u^0} \tag{3A.5}$$

$$C_{Ce^{3+}} = \frac{A_{Ce^{3+}}}{A_{Ce^{3+}} + A_{Ce^{4+}}} \tag{3A.6}$$

The deconvoluted Ce 3d spectra confirmed the presence of Ce in both 4+ and 3+ states in as-prepared CeO_2, $Ce_{0.95}Ni_{0.05}O_{2-\delta}$ and $Ce_{0.9}Ni_{0.05}Sr_{0.05}O_{2-\delta}$ as can be seen in Table 3A.6. Apparently, with doping of Ni and Sr the concentration of Ce^{3+} increased gradually in the synthesized materials. Figure 3A.16(b) demonstrated the Ce 3d spectra of the exhausted catalysts CeO_2, $Ce_{0.95}Ni_{0.05}O_{2-\delta}$ and $Ce_{0.9}Ni_{0.05}Sr_{0.05}O_{2-\delta}$ after MOR. Interestingly, the relative concentration of Ce^{4+} and Ce^{3+} was changed with higher abundance of Ce^{3+} in the exhausted catalysts compared to the as-prepared ones. The reduction of $Ce^{4+} \rightarrow Ce^{3+}$ was observed to be maximum over $Ce_{0.9}Ni_{0.05}Sr_{0.05}O_{2-\delta}$. As positive potential of MOR causes the oxidation to happen, the reduction of Ce^{4+} in CeO_2 must be accompanied by parallel oxidation reaction(s). These parallel oxidation reactions could be rationalized by lattice oxygen evolution ($O^{2-} \rightarrow \frac{1}{2}$ $O_2 + 2e^-$) in pristine CeO_2 as well as $Ni^{2+} \rightarrow Ni^{3+}$ oxidation in Ni-doped materials. Owing to ceria having a highly reducible oxide lattice oxygen evolution is a reasonable phenomenon. In fact, the easily available lattice oxygen can increase the CO oxidation rate to make the catalysts CO tolerant.

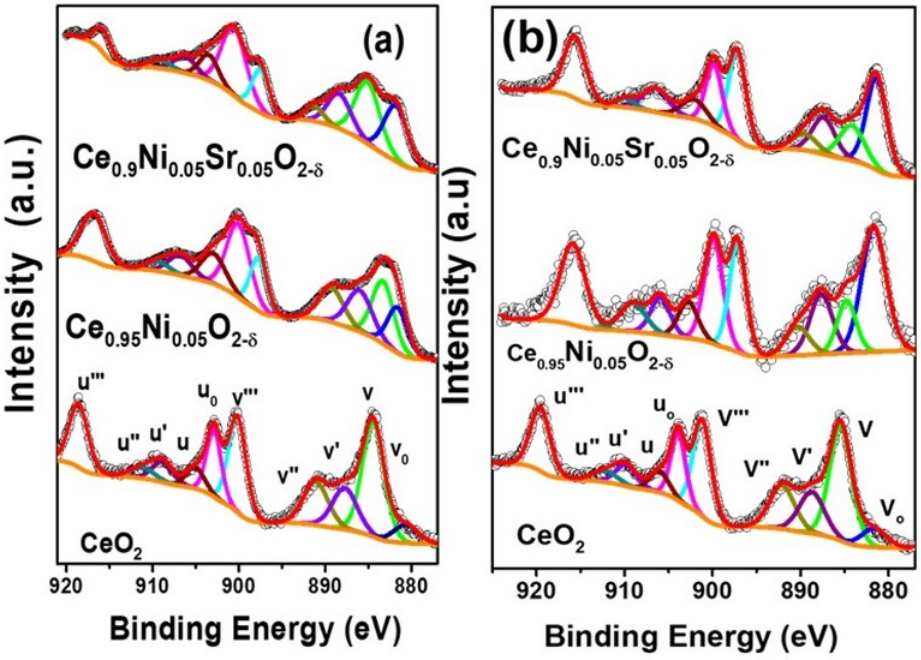

FIGURE 3A.16: Ce 3d core level spectra (a) before and (b) after MOR

To probe the Ni oxidation state and its further oxidation during MOR, we have mapped the Ni 2p core level XPS spectra for as-prepared and exhausted $Ce_{0.95}Ni_{0.05}O_{2-\delta}$ and $Ce_{0.9}Ni_{0.05}Sr_{0.05}O_{2-\delta}$ (Figure 3A.17). The Ni 2p spectra in Figure 3A.17(a) for the as-prepared catalysts exhibit two main peaks corresponding to spin orbital coupling Ni $2p_{3/2}$ and $2p_{1/2}$. The deconvoluted spectra of as-prepared materials exhibited co-existence of Ni^{2+} (at 855.5 and 872.3 eV) and Ni^{3+} (at 857.3 and 873.3 eV) substituted in CeO_2 matrix [187, 207]. Table 3A.6 shows that the concentration of Ni^{3+} became higher with Sr co-doping. Two shakeup satellite peaks were also observed at 861.3 and 865.0 eV in the as-prepared materials [207, 208]. Ni 2p core level XPS spectra for the exhausted $Ce_{0.95}Ni_{0.05}O_{2-\delta}$ and $Ce_{0.9}Ni_{0.05}Sr_{0.05}O_{2-\delta}$ are plotted in Figure 3A.17(b) . Apparently, the abundance of Ni^{3+} was significantly enhanced in exhausted catalysts after MOR (Table 3A.6). It can be concluded that the facile $Ce^{4+} \rightarrow Ce^{3+}$ reduction has facilitated the $Ni^{2+} \rightarrow Ni^{3+}$ oxidation during MOR over the Ni doped catalysts. Thus, formed Ni^{3+} enabled formation of the key surface intermediate species Ni - OOH for efficient methanol oxidation reaction.

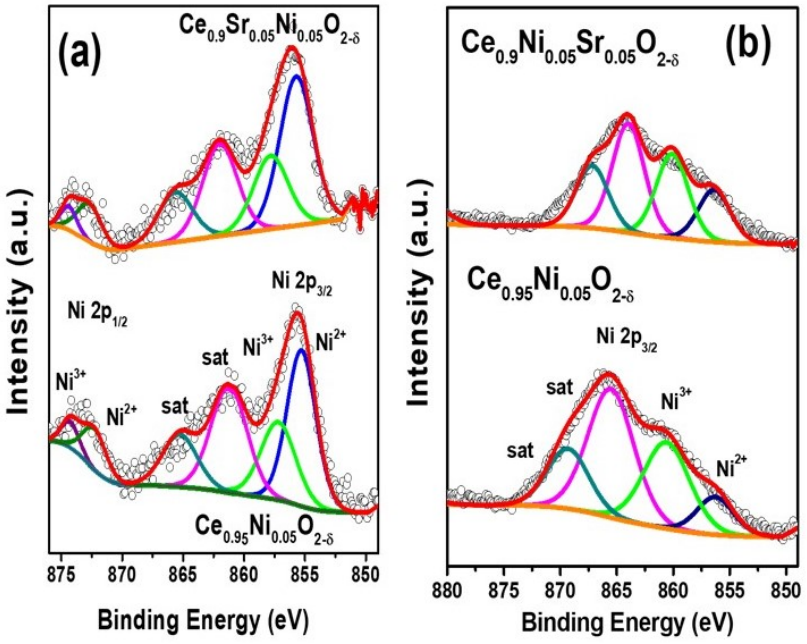

FIGURE 3A.17: Ni 2p core level spectra (a) before and (b) after MOR

Further, we evaluated the O 1s core level spectra of as-prepared and exhausted CeO_2, $Ce_{0.95}Ni_{0.05}O_{2-\delta}$ and $Ce_{0.9}Ni_{0.05}Sr_{0.05}O_{2-\delta}$ (Figure 3A.18). The deconvoluted O 1s of the fresh catalysts in Figure 3A.18(a) did show three distinguishable peaks at 530.0, 532.5, and 534.2 eV corresponding to lattice oxygen (O_L), surface oxygen vacancy (O_V), and hydroxyl species of surface-adsorbed water molecules (O_W) respectively [59, 209–211]. As expected, to compensate the charge balance there was a gradual increase in surface oxygen vacancy with co-doping of aliovalent Ni and Sr in CeO_2. Moreover, the broadly distributed peak corresponding to O_V in $Ce_{0.9}Ni_{0.05}Sr_{0.05}O_{2-\delta}$ could be due to the presence of surface oxygen vacancy in the vicinity of Ce^{3+} [212]. Post MOR, the O 1s spectra of the exhausted catalysts CeO_2, $Ce_{0.95}Ni_{0.05}O_{2-\delta}$ and $Ce_{0.9}Ni_{0.05}Sr_{0.05}O_{2-\delta}$ are plotted in Figure 3A.18(b). Apparently, the deconvoluted O 1s spectra of $Ce_{0.95}Ni_{0.05}O_{2-\delta}$ and $Ce_{0.9}Ni_{0.05}Sr_{0.05}O_{2-\delta}$ exhibited an extra peak at 533.2 eV corresponding to the surface bound intermediate Ni - OOH species formed during methanol oxidation in addition to the usual O_L, O_V and O_W peaks [213]. While the relative intensity of the peak corresponding to Ni - OOH was highest in $Ce_{0.9}Ni_{0.05}Sr_{0.05}O_{2-\delta}$, it was not at all observed in case of pure CeO_2. It was also observed a shift of Ni - OOH to higher binding energy from $Ce_{0.95}Ni_{0.05}O_{2-\delta}$ to $Ce_{0.9}Ni_{0.05}Sr_{0.05}O_{2-\delta}$. It must be noted that a prominent occurrence of Ni - OOH layer with a red-ox couple of Ni^{2+}/Ni^{3+} was also observed in CV traces of $Ce_{0.9}Ni_{0.05}Sr_{0.05}O_{2-\delta}$ earlier. We can infer that the high extent of reduction of $Ce^{4+} \rightarrow Ce^{3+}$ in $Ce_{0.9}Ni_{0.05}Sr_{0.05}O_{2-\delta}$ during MOR has facilitated the Ni^{2+} oxidation to Ni^{3+} and consequently expedited the formation of intermediate Ni - OOH species for better methanol oxidation.

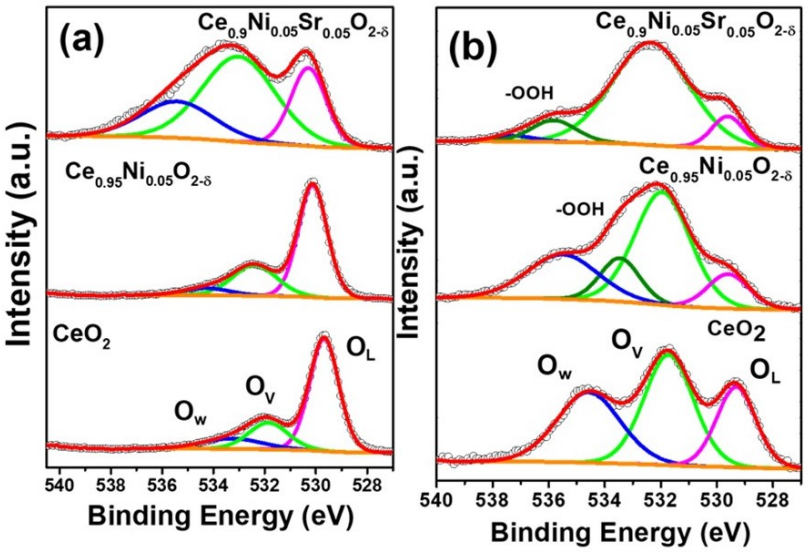

FIGURE 3A.18: O 1s core level spectra (a) before and (b) after MOR

TABLE 3A.6: Concentration (%) of Ce^{3+}, and Ni^{3+} before and after MOR

Catalysts	**Ce^{3+}**		**Ni^{3+}**	
	Before MOR	**After MOR**	**Before MOR**	**After MOR**
CeO_2	18.4	27.9	-	-
$Ce_{0.95}Ni_{0.05}O_{2-\delta}$	20.5	46.0	22.4	62.6
$Ce_{0.9}Ni_{0.05}Sr_{0.05}O_{2-\delta}$	33.7	64.8	42.0	77.9

To corroborate the facile reduction of $Ce^{4+} \rightarrow Ce^{3+}$ accompanied by the evolution of lattice oxygen (as indicated by the XPS analyses), we probed the reducibility of Ce^{4+} with the help of H_2-TPR experiments. The H_2-TPR data in Figure 3A.19(a) shows three peaks at 511, 639 and 935 °C associated with pristine CeO_2. While the merged low-temperature peaks correspond to the reduction of surface-bound $Ce^{4+} \rightarrow Ce^{3+}$, the higher temperature peak is assigned to the bulk reduction of Ce^{4+} [214–218]. Apparently, the lattice oxygen in the bulk CeO_2 reacts with feed H_2 at higher temperature, whereas the weakly coordinated surface oxygen of CeO_2 easily reacts with H_2 at lower temperature [216]. The doped materials, $Ce_{0.95}Ni_{0.05}O_{2-\delta}$ and $Ce_{0.9}Ni_{0.05}Sr_{0.05}O_{2-\delta}$ exhibited three distinguishable peaks. Whereas the first peak may correspond to the reduction of Ni^{2+}, the second and the third peaks correspond to the surface and bulk reduction of $Ce^{4+} \rightarrow Ce^{3+}$, respectively [219, 220]. Evidently, the co-doping of Sr and Ni significantly decreased the reduction temperature of bulk Ce^{4+} compared to the other two catalysts, indicating an easy evolution of lattice oxygen in $Ce_{0.95}Ni_{0.05}O_{2-\delta}$ to react with the feed H_2 [221].

The higher reducibility of Ce^{4+} $Ce_{0.9}Ni_{0.05}Sr_{0.05}O_{2-\delta}$ might have also facilitated the lattice oxygen evolution in the positive potential window, which in turn probably helped to increase

the CO tolerance of the material. Gaseous CO, which is an oxidation intermediate of methanol oxidation, gets adsorbed and blocks the active sites as poison. By utilizing evolved lattice oxygen, a facile CO oxidation reaction at lower potential can render the material more tolerant to CO by converting it to CO_2. Therefore, CO oxidation in an inert atmosphere was performed over $Ce_{0.9}Ni_{0.05}Sr_{0.05}O_{2-\delta}$ at a potential range from 1.25 to 1.75 V vs RHE and the gaseous product CO_2 was measured using GC. Figure 3A.19(b) shows the % CO oxidation and Figure 3A.19(c) shows the formation of CO_2 over CeO_2, $Ce_{0.95}Ni_{0.05}O_{2-\delta}$ and $Ce_{0.9}Ni_{0.05}Sr_{0.05}O_{2-\delta}$ as function of anodic potential. It is worth mentioning that the catalysts exhibited CO oxidation potentials that were considerably lower than the potential required for the oxygen evolution reaction from water. The highest CO oxidation was observed over $Ce_{0.9}Ni_{0.05}Sr_{0.05}O_{2-\delta}$ outperforming the other two materials. It can be inferred that the facile lattice oxygen evolution owing to higher reducibility of Ce^{4+} has helped the CO oxidation over $Ce_{0.9}Ni_{0.05}Sr_{0.05}O_{2-\delta}$. Based on the observation, the overall methanol oxidation reaction over $Ce_{0.9}Ni_{0.05}Sr_{0.05}O_{2-\delta}$ can be expressed as:

$$Ce_{0.9}Ni_{0.05}Sr_{0.05}O_{2-\delta}+xCH_3OH+xH_2O \rightarrow Ce^{4+}_{0.9-x}Ce^{3+}_{x}Ni_{0.05}Sr_{0.05}O_{2-\delta}+xCO_2+3xH_2 \quad (3A.7)$$

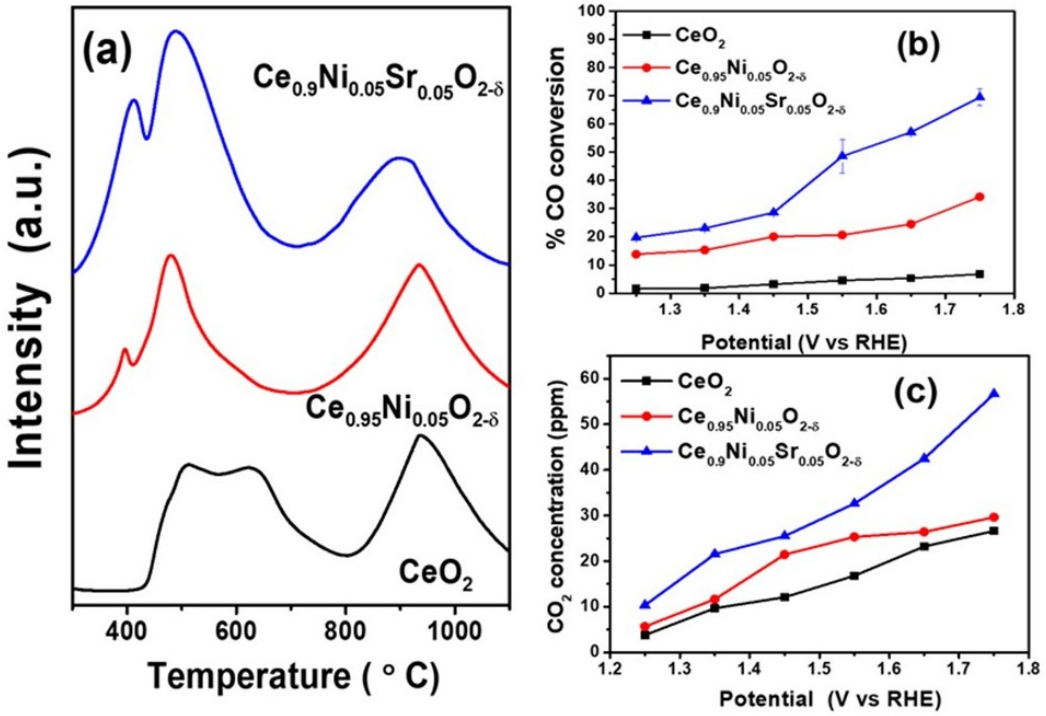

FIGURE 3A.19: a) H_2-TPR over CeO_2, $Ce_{0.95}Ni_{0.05}O_{2-\delta}$, and $Ce_{0.9}Ni_{0.05}Sr_{0.05}O_{2-\delta}$ (b) Percentage of CO conversion and (c) CO_2 concentration in ppm at different potentials

3A.4 Conclusion

$Ce_{1-x-y}Ni_xSr_yO_{2-\delta}$ (x = 0 – 0.07, y = 0 – 0.07) synthesized by solution combustion method crystallized in a phase pure fluorite phase. The materials were nano-crystalline in nature with a high surface area and porosity. The co-doping of aliovalent Ni and Sr has created a sizable oxygen vacancy in the ceria lattice. The electrocatalytic oxidation of methanol was found to be highest over $Ce_{0.9}Ni_{0.05}Sr_{0.05}O_{2-\delta}$. The kinetic evaluation showed that the diffusion-controlled methanol oxidation goes through the C-H bond scission as rate-determining step over $Ce_{0.9}Ni_{0.05}Sr_{0.05}O_{2-\delta}$. The order of the overall reaction was found to be half. The detailed mechanistic introspection revealed that the co-doping of Sr with Ni has facilitated the reduction of $Ce^{4+} \rightarrow Ce^{3+}$ in $Ce_{0.9}Ni_{0.05}Sr_{0.05}O_{2-\delta}$ during anodic oxidation reaction. The higher reducibility of the support has facilitated the $Ni^{2+} \rightarrow Ni^{3+}$ oxidation, which in turn helped to yield the key intermediate species of Ni - OOH to expedite the sluggish kinetics of MOR. Additionally, the low charge transfer resistance over $Ce_{0.9}Ni_{0.05}Sr_{0.05}O_{2-\delta}$ also facilitated the electrocatalytic activity. The high reducibility of ceria further helped in lattice oxygen evolution, which was consumed for CO oxidation reaction at low anodic potential and enhanced the CO tolerance and durability of $Ce_{0.9}Ni_{0.05}Sr_{0.05}O_{2-\delta}$ towards -methanol oxidation reaction. The overall conclusions points towards the importance of electronic interactions between the active site and support and involvement of lattice oxygen in methanol oxidation reaction in order to realize the 'Methanol Economy' in future.

Chapter 3B

Unveiling the Mechanistic Significance of Reducibility and Lattice Oxygen Evolution in the $Ce_{1-x-y}Zr_xNi_yO_{2-\delta}$ Catalyst for Methanol Electro-Oxidation

3B.1 Introduction

Research has indicated that the redox couple of Ni^{2+}/Ni^{3+} plays a crucial role in facilitating MOR by promoting the formation of key Ni - OOH species through surface reconstruction, which, in turn, modulates the electronic structure of active sites. The oxidation of $Ni^{2+} \rightarrow Ni^{3+}$ creates charge-transfer orbitals that enable electron transfer during the methanol oxidation process to CO_2. However, the creation of available charge-transfer orbitals near the Fermi energy level poses a fundamental challenge. One potential solution is substituting Ni^{2+} in a reducible support to facilitate $Ni^{2+} \rightarrow Ni^{3+}$ oxidation. Furthermore, if the reducible support exhibits oxophilic properties, then it readily adsorbs oxygenated key MOR species such as Ni - OOH at lower potentials. Among the various reducible oxides, CeO_2 has attracted particular interest due to its high surface area, significant surface defects, and notable oxygen storage capacity characterized by redox Ce^{4+}/Ce^{3+} sites [42, 180]. We have seen in chapter 3A, how reducible

support of CeO_2 facilitates the $Ni^{2+} \rightarrow Ni^{3+}$ oxidation and shows oxophilicity which is prone to adsorption of oxygenated species and creating Ni - OOH at a lower potential and further promote the oxidation of CO to CO_2 [222]. Even though ZrO_2 cannot be efficiently reduced by H_2, several kinds of research showed that oxygen storage capacity can significantly be enhanced by the insertion of ZrO_2 in CeO_2 lattice by forming the $Ce_{1-x}Zr_xO_2$ solid solution [223, 224]. Though the exact origin of the enhanced redox properties, particularly, the mechanism of the reduction process is still a matter of debate, there is general agreement that the $Ce_{1-x}Zr_xO_2$ solid solution creates mobile lattice oxygen available for reduction [225]. However, the concept of utilizing a reducible $Ce_{1-x}Zr_xO_2$ solid solution support to enhance the oxidation of the active site $Ni^{2+} \rightarrow Ni^{3+}$ and thereby improve the kinetics of MOR has not been investigated in the literature. The main objective of this study in this chapter is to synthesize a pure phase solid solution of $Ce_{1-x-y}Zr_xNi_yO_{2-\delta}$ and evaluate its performance and understanding the significance of the reducibility of the material in the methanol oxidation reaction. This study not only introduces a novel material system and optimization method for developing cost-effective and efficient catalysts for MOR but also offers valuable insights into the underlying mechanistic aspects.

3B.2 Materials and Methods

3B.2.1 Synthesis of CeO_2, $Ce_{1-y}Ni_yO_{2-\delta}$ and $Ce_{1-x-y}Zr_xNi_yO_{2-\delta}$

The single-step solution combustion method was adopted to synthesize pristine CeO_2, $Ce_{1-y}Ni_yO_{2-\delta}$ (where y = 0.05), and $Ce_{1-x-y}Zr_xNi_yO_{2-\delta}$ (where x=0.35, 0.55 and y=0.05) catalysts. Metal nitrates such as $Ce(NO_3)_3 \cdot 6H_2O$ (SRL chemicals, 99%), $Ni(NO_3)_2 \cdot 6H_2O$ (SD fine, 99%), and $Zr(NO_3)_2 \cdot 6H_2O$ (SD fine, 99%) were used as oxidizers, while glycine (Sigma Aldrich, India) was used as fuel. This combustion method involves highly exothermic metathetical chemical reactions between the oxidizers and fuel and utilizes propellant chemistry. The stoichiometrically calculated amount of the oxidizers and fuel glycine were dissolved in approximately 50 mL of deionized water in a 300 mL borosilicate dish. The dish containing the redox mixture was then placed into a preheated muffle furnace maintained at 450 °C. Initially, the solution boiled and foamed, undergoing dehydration. Upon complete dehydration, the surface ignited, burning with a flame, and the temperature reached about 1000 °C, resulting in a

voluminous solid product. The chemical reaction for the synthesis can be represented as follows:

$$2(1-x-y)Ce(NO_3)_3.6H_2O + 2yNi(NO_3)_2.6H_2O + 2xZrO(NO_3)_3 + 2C_2H_5NO_2 + (3x+3y-2.5-\delta)O_2 \rightarrow 2Ce_{1-x-y}Zr_xNi_yO_{(2-\delta)} + 4CO_2 + (17-12y)H_2O + (4-x-y)N_2 \quad (3B.1)$$

To benchmark the solution combustion synthesized catalysts, the homologous materials were also synthesized by physical mixing methods. 5%NiO/35%ZrO_2/CeO_2 and 5% NiO/35%ZrO_2/Al_2O_3 were prepared by physical grinding of both the solution combustion synthesized individual oxides in their respective calculated amount for 2 h with an agate mortar and pestle.

3B.2.2 Structural, Surface and Electronic Characterisation

ED-XRF was used to study the actual atomic ratio of the synthesized $Ce_{1-x-y}Zr_xNi_yO_{2-\delta}$ materials with the help of an Epsilon 1; PAN analytical instrument. The structural characterisation of $Ce_{1-x-y}Zr_xNi_yO_{2-\delta}$ was performed with a Rigaku Ultima IV XRD having Cu K_α radiation (λ = 1.5418 Å) at a scan rate of 0.4° min^{-1} and step size of 0.01° in the 2θ range between 10° - 90°. Scherrer's formula,

$$D = \frac{0.9\lambda}{B\text{Cos}\theta} \quad (3B.2)$$

where B is the full-width at half-maximum, λ is the wavelength of the radiation, and θ is the corresponding angle was used to calculate the average nanocrystalline diameters (D). Fullprof program suite was used for Rietveld refinement of the powder diffraction patterns by varying the overall scale factor, background and profile parameters, unit-cell lattice parameters, atomic positions, half width, shape, isotopic thermal parameters, and oxygen occupancy. HR-TEM (JOEL - JEM 2100F) was further used to probe the crystal structure of the catalysts. The microscope was operated with an accelerating potential of 200 kV with a point resolution of 0.19 nm and line resolution of 0.1 nm. The sample for the analysis was prepared by dispersing about 1- 2 mg in methanol and drop casting over copper grid (200 mesh). Microtrac BEL Corp mini-II surface area analyzer was employed to study the surface of the synthesized materials. The samples were degassed in vacuum at 200 °C for 2 h prior to the N_2 sorption measurements at 77 K. BET equation was used to estimate the specific surface area. The high-resolution

scanning electron microscopy was carried out with FE-SEM, (FEI-ApreoS) at 30 kV acceleration. XPS were collected to study the surface composition, elemental oxidation state and bonding with the help of Thermo Scientific K-Alpha surface-analysis spectrometer housing Al K_α as the X-ray source (1486.6 eV). The instrument was operated at 72 W. The base pressure at the analysing chamber was maintained at 5×10^{-9} mbar. The data profiles were subjected to a nonlinear least-squares curve fitting program with a Gaussian-Lorentzian production function and processed with Avantage software. The B.E. of all XPS data was calibrated vs the standard C 1s peak at 284.85 eV. The H_2 TPR was carried out with 50 mg of sample. The sample was subjected to reduction under 10% H_2/Ar gas mixture with a flow rate of 30 ml min^{-1} and a heating rate of 10 ^oC min^{-1}. H_2 consumption was monitored using a gas chromatography (Varian GC 8301).

3B.2.3 Electrocatalytic Oxidation of Methanol

Origa Flex OGF500 electrochemical workstation with three electrode system was used to carry out electrocatalytic oxidation of methanol. The working electrode was prepared by drop casting the catalyst ink onto a GCE (3 mm, 0.07 cm^2 area). Before drop casting the catalyst ink, the GCE was polished using 0.05 μm alumina slurry. The catalyst ink was prepared by dispersing the physical mixture of 5 mg of the synthesized catalyst and 2 mg of carbon black in 1 mL of methanol and 10 μL Nafion solution. The final catalyst loading on the GCE was 0.05 mg. Hg/HgO in 1 M KOH electrode was used as reference and a Pt wire was used as the counter electrode. Aqueous solutions of 0.5 M NaOH served as electrolyte. The ECSA was derived from the chronoamperometric expert studies and calculated using Cottrell equation as elaborated in chapter 2A [123]. CV studies were carried out at 0.5 M methanol concentration in alkaline electrolyte medium. CA for 10 h and cycle studies for 300 cycles were conducted to study the stability at room temperature. The liquid products after CA were analysed using ^1H NMR (Bruker AV NEO, 400 MHz). About 0.4 mL of electrolysis solution, 0.1 mL of D_2O, and 5 mg of 4-nitrophenol (as an internal standard) were added into the NMR tube to identify the product. In all measurements, potential in Hg/HgO is converted to RHE according to the following equation: $E_{RHE} = E_{Hg/HgO} + 0.059 \times pH + 0.098$. The concentration of the surface Ni - OOH layers after CV cycles in NaOH medium was calculated with respect to the geometrical surface area according to the following equation

$$I_p = \left[\left(\frac{z^2F^2}{4RT}\right) A\tau^*\nu\right] \quad (3B.3)$$

I_p = Peak current density ($mAcm^{-2}$), Z = No. of electrons transferred, R = Gas constant, T = Temperature, A = Geometrical area of the electrode (0.07 cm^2) ν = scan rate, and τ^* = surface coverage of Ni - OOH. The Tafel plot was constructed by using steady state response and its slope is calculated accordingly. EIS study was carried out to study the electron transfer for MOR over a frequency range of 1000 kHz to 50 mHz with a sinusoidal excitation signal of 10 mV using a Biologic Sp-150 electrochemical workstation with the conventional three-electrode system in an alkaline mixture of 0.5 M methanol and 0.5 M NaOH.

3B.2.4 CO Oxidation

CO tolerance of the materials were performed over the as-synthesized catalysts in 0.5 M NaOH. The electrochemical cell was made airtight and the electrolyte was purged with Ar for the removal of any dissolved oxygen. Chronoamperometry was carried at different potentials with a continuous purge of 10% CO in N_2 at a flow rate of 10 cc min^{-1}1. The evolved gases were quantified using gas chromatography (NUCON-5765) equipped with a flame ionization detector for CO_2. GC was calibrated using a standard gas mixture (CHEMIX speciality gases and equipment, India) under standard conditions. Ultrapure Ar (99.9%) was used as a carrier gas. Around 100 μL of gas was collected after 15 min of CA at each potential from the headspace of the electrochemical cell with a gas-tight Hamilton syringe and was injected into the GC column. The concentration of CO and CO_2 at each potential were calculated from area under the peak.

3B.3 Results and Discussion

3B.3.1 Structure and Surface Properties of the Synthesized Catalysts

The catalysts synthesized through solution combustion process exhibited concentrations of Ni and Zr that were similar to the values theoretically calculated as shown in Figure 3B.1 and Table 3B.1. The crystal structure of CeO_2, $Ce_{1-y}Ni_yO_{2-\delta}$ and $Ce_{1-x-y}Zr_xNi_yO_{2-\delta}$ were investigated by powder XRD as shown in Figure 3B.2(a) exhibited the typical characteristics peaks of the phase pure cubic fluorite lattice for all the synthesized materials [JCPDS 34-0394]. The crystallite size of pristine CeO_2 was found to be 15.19 nm, whereas $Ce_{0.4}Zr_{0.55}Ni_{0.05}O_{2-\delta}$ exhibited a significantly smaller crystallite size of 4.7 nm (details are in Table 3B.1). No extra peak corresponding to metallic Ni or NiO or ZrO_2 confirmed the formation of the solid solution

[42, 179, 180]. Further with doping in the solid solutions, there was apparent shifting of the peaks at higher angle with doping (Figure 3B.2(b)). The Shannon's ionic radii of six coordinated Ni^{2+} and Zr^{4+} are 0.69 and 0.72 Å, respectively, whereas the ionic radius of six coordinated Ce^{4+} in CeO_2 is of 0.87 Å. Therefore, a substitutional solid solution would result in a slightly contracted unit cell and d_{111} spacing leading to the appearance of the peaks at higher angle. The XRD patterns of $Zr_{0.95}Ni_{0.05}O_{2-\delta}$, 5%NiO/35%$ZrO_2$/$CeO_2$ and 5%NiO/35%ZrO_2/Al_2O_3 are plotted in Figure 3B.2(c). Evidently, the separate characteristic peaks of NiO (JCPDS-04-0835) and ZrO_2(JCPDS-79-1769) were observed in the XRD pattern of 5%NiO/35%ZrO_2/CeO_2.

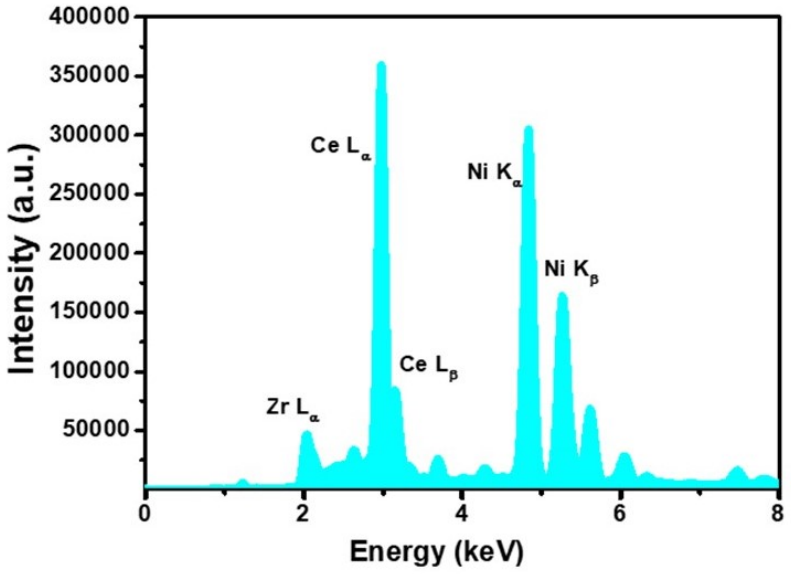

FIGURE 3B.1: Representative ED-XRF Plot of $Ce_{0.6}Zr_{0.35}Ni_{0.05}O_{2-\delta}$

TABLE 3B.1: ED-XRF and crystallite size of $Ce_{1-x-y}Zr_xNi_yO_{2-\delta}$ (x = 0.35, 0.55, y = 0.05)

Catalysts	**Crystallite size (nm)**	**Calculated (%)**			**XRF (%)**		
		Ce	Zr	Ni	Ce	Zr	Ni
CeO_2	15.19						
$Zr_{0.95}Ni_{0.05}O_{2-\delta}$	16.4		96.7	3.27		97.1	2.84
$Ce_{0.95}Ni_{0.05}O_{2-\delta}$	8.02	97.5	-	2.10	97.1	-	2.87
$Ce_{0.6}Zr_{0.35}Ni_{0.05}O_{2-\delta}$	14.33	70.6	21.5	2.47	75.0	21.3	3.61
$Ce_{0.4}Zr_{0.55}Ni_{0.05}O_{2-\delta}$	4.67	51.3	45.9	2.70	60.6	36.4	2.95

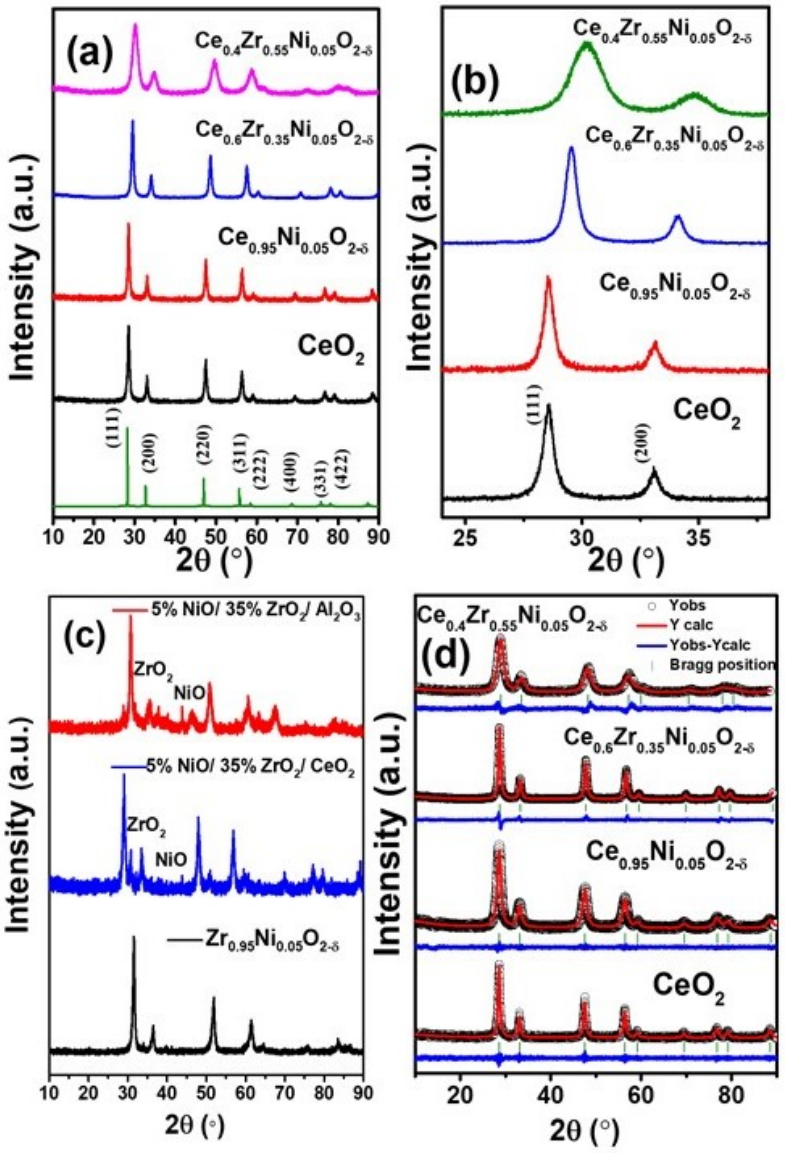

FIGURE 3B.2: (a) XRD patterns, (b) zoomed in version of XRD patterns of CeO_2, $Ce_{0.95}Ni_{0.05}O_{2-\delta}$, $Ce_{0.6}Zr_{0.35}Ni_{0.05}O_{2-\delta}$ and $Ce_{0.4}Zr_{0.55}Ni_{0.05}O_{2-\delta}$, (c) XRD patterns of $Zr_{0.95}Ni_{0.05}O_{2-\delta}$, 5%NiO/35%$ZrO_2$/$CeO_2$ and 5%NiO/35%ZrO_2/Al_2O_3 and (d) Rietveld refinement patterns of CeO_2, $Ce_{0.95}Ni_{0.05}O_{2-\delta}$, $Ce_{0.6}Zr_{0.35}Ni_{0.05}O_{2-\delta}$ and $Ce_{0.4}Zr_{0.55}Ni_{0.05}O_{2-\delta}$

To elucidate the information on the volume of unit cell and other lattice parameters, Rietveld refinements were carried out on the diffraction patterns by substituting Ni and Zr in place of Ce at the Wyckoff sites 4a and oxygen in 8c, and the refinement profiles are shown in Figure 3B.2(d). In the Figure, the black coloured line represents the experimentally obtained data, whereas the superimposed red coloured line designates the fitted curve with the theoretically calculated intensities, and the blue curve at the bottom signifies the difference between them. The reliability factors of fitting, such as R_{Bragg}, and χ^2 provided in Table 3B.2 shows the goodness of fitting. Apparently, the cubic unit cell length of pristine CeO_2 (a = 5.411 Å) decreased with

Ni doping (a = 5.408 Å) in $Ce_{0.95}Ni_{0.05}O_{2-\delta}$, and was further decreased to 5.38 and 5.34 Å in $Ce_{0.6}Zr_{0.35}Ni_{0.05}O_{2-\delta}$ and $Ce_{0.4}Zr_{0.55}Ni_{0.05}O_{2-\delta}$, respectively. The gradual decrease in the unit cell length and corresponding shrinkage of cell volume confirmed the formation of the solid solution with lattice doping of Ni and Zr ions in the cubic fluorite unit cell. Although oxygen has a lower X-ray scattering factor than cerium, we can still use the refined oxygen occupancy obtained from the refinement to observe the trend in the variation of oxygen content. Aliovalent substitutional doping of bivalent Ni^{2+} in place of Ce^{4+} is expected to cause a decrease in oxygen content as a point defect. A decrease of oxygen content from 2.00 in pure CeO_2 to 1.98 in $Ce_{0.95}Ni_{0.05}O_{2-\delta}$ is evidently visible in Table 3B.2 further corroborating the lattice substitution. Greater oxygen vacancy levels may exert a pronounced influence on the MOR activity of the doped materials.

TABLE 3B.2: Rietveld refine lattice parameters and atom occupancy of CeO_2, $Ce_{1-y}Ni_yO_{2-\delta}$ (y = 0 0.05) and $Ce_{1-x-y}Zr_xNi_yO_{2-\delta}$ (x = 0.35, 0.55, y = 0.05)

Catalysts	Cell parameters (A)	**Cell volume**	χ^2	**Occupancy**				**Wyckoff site**			
	a=b=c	**($A^{\circ 3}$)**		Ce	Ni	Zr	O	Ce	Ni	Zr	O
CeO_2	5.411	158.5	4.5	1.00	-	-	2.00	4a			8c
$Ce_{0.95}Ni_{0.05}O_{2-\delta}$	5.408	158.2	0.57	0.97	0.054	-	1.98	4a	4a		8c
$Ce_{0.6}Zr_{0.35}Ni_{0.05}O_{2-\delta}$	5.38	156.0	1.45	0.60	0.050	0.34	1.65	4a	4a	4a	8c
$Ce_{0.4}Zr_{0.55}Ni_{0.05}O_{2-\delta}$	5.34	152.6	1.58	0.40	0.052	0.54	2.07	4a	4a	4a	8c

The nano structural features as well as the alteration in the lattice distance due to the substitutional doping was probed by HR-TEM. Both the pristine CeO_2 and the representative doped solid solution $Ce_{0.6}Zr_{0.35}Ni_{0.05}O_{2-\delta}$ exhibited a diffused porous structure (Figure 3B.3(a,d). The interplanar distance, observed through XRD, was further investigated using HR-TEM analysis. CeO_2 displayed interplanar distances of 0.302 nm and 0.266 nm for the (111) and (200) planes, respectively (Figure 3B.3(b)), while $Ce_{0.6}Zr_{0.35}Ni_{0.05}O_{2-\delta}$ exhibited shrunk interplanar distances of 0.299 nm and 0.263 nm for the corresponding planes (Figure 3B.3(e)). The corresponding SAED patterns also verified the presence of these lattice planes (Figure 3B.3(c,f)).

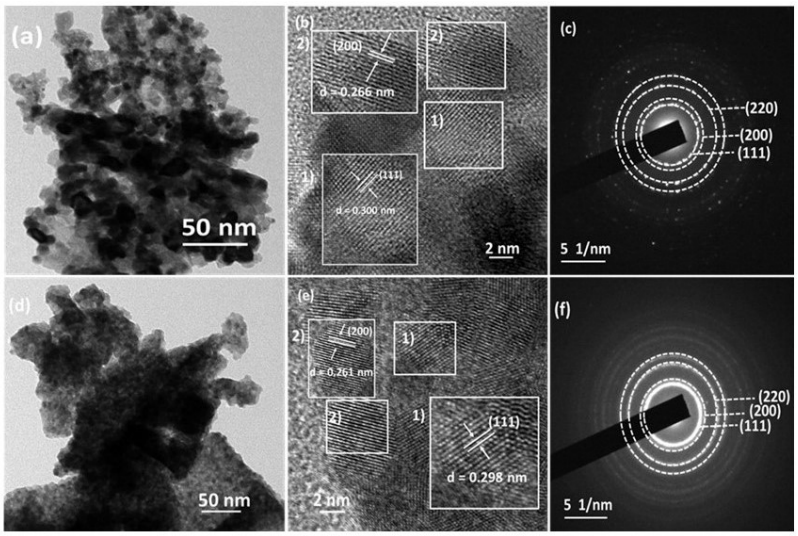

FIGURE 3B.3: HR-TEM images of (a, b) CeO_2, (d, e) $Ce_{0.6}Zr_{0.35}Ni_{0.05}O_{2-\delta}$ and SAED pattern of (c) CeO_2, (f) $Ce_{0.6}Zr_{0.35}Ni_{0.05}O_{2-\delta}$

Electrocatalysis being a surface phenomenon, next we studied the surface properties of the combustion synthesized materials. The FE-SEM micrographs in Figure 3B.4 show the surface morphology of pristine CeO_2, , $Ce_{0.6}Zr_{0.35}Ni_{0.05}O_{2-\delta}$, and $Ce_{0.4}Zr_{0.55}Ni_{0.05}O_{2-\delta}$. The pristine CeO_2 showed a porous surface, whereas on doping with Ni and Zr the morphology changed to flaky. The EDAX elemental mapping showed a very high distribution of Ni and Zr along with Ce throughout the matrix.

Further, the surface area was studied, and all the materials exhibited a type II isotherm with a negligible hysteresis in N_2 adsorption - desorption isotherms specifying the macro porous nature of the surface (Figure 3B.5(a)). The average surface area estimated from BET equation was found to be 35 – 40 $m^2\ g^{-1}$ for the pristine as well as the doped materials, whereas the average pore diameter estimated from BJH plot was 46 nm. The ECSA plays an important role in electrocatalytic activity of a material, and it was calculated with the help of CA studies using the Cottrell equation (Figure 3B.5(b)). The pristine CeO_2 and the only Ni doped $Ce_{0.95}Ni_{0.05}O_{2-\delta}$ exhibited the ECSA of 0.82 and 0.83 cm^2, respectively. Interestingly, with co-doping of Zr in $Ce_{0.6}Zr_{0.35}Ni_{0.05}O_{2-\delta}$ the ECSA was increased to 1.84 cm^2 while $Ce_{0.4}Zr_{0.55}Ni_{0.05}O_{2-\delta}$ exhibited ECSA of 1.50 cm^2. This increased electrochemical active surface area indicates the potential efficacy of the doped materials towards enhanced MOR activity.

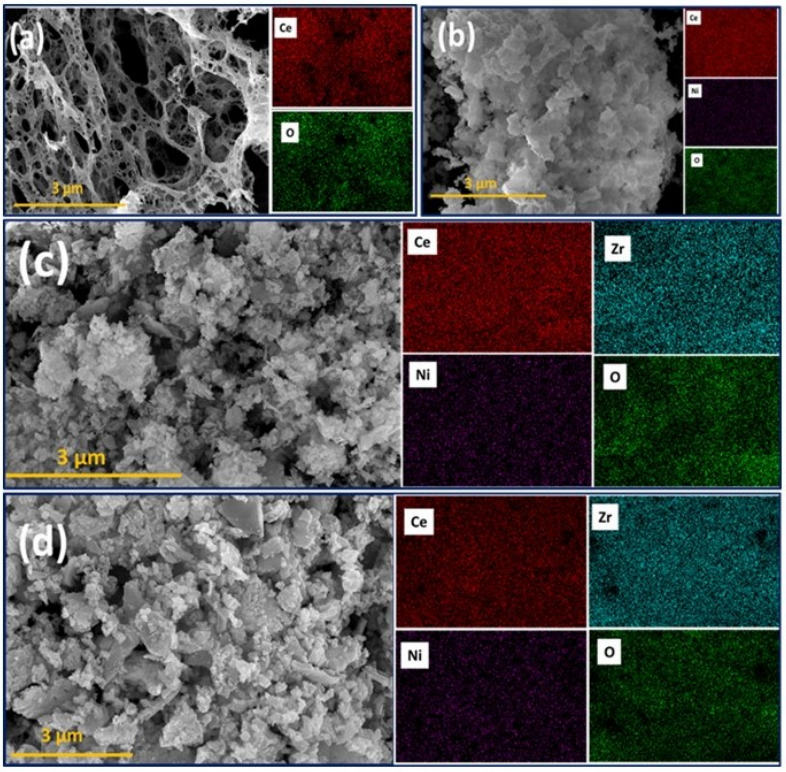

FIGURE 3B.4: FE-SEM images and EDAX of (a) CeO_2, (b) $Ce_{0.95}Ni_{0.05}O_{2-\delta}$, (c) $Ce_{0.6}Zr_{0.35}Ni_{0.05}O_{2-\delta}$ and (d) $Ce_{0.4}Zr_{0.55}Ni_{0.05}O_{2-\delta}$

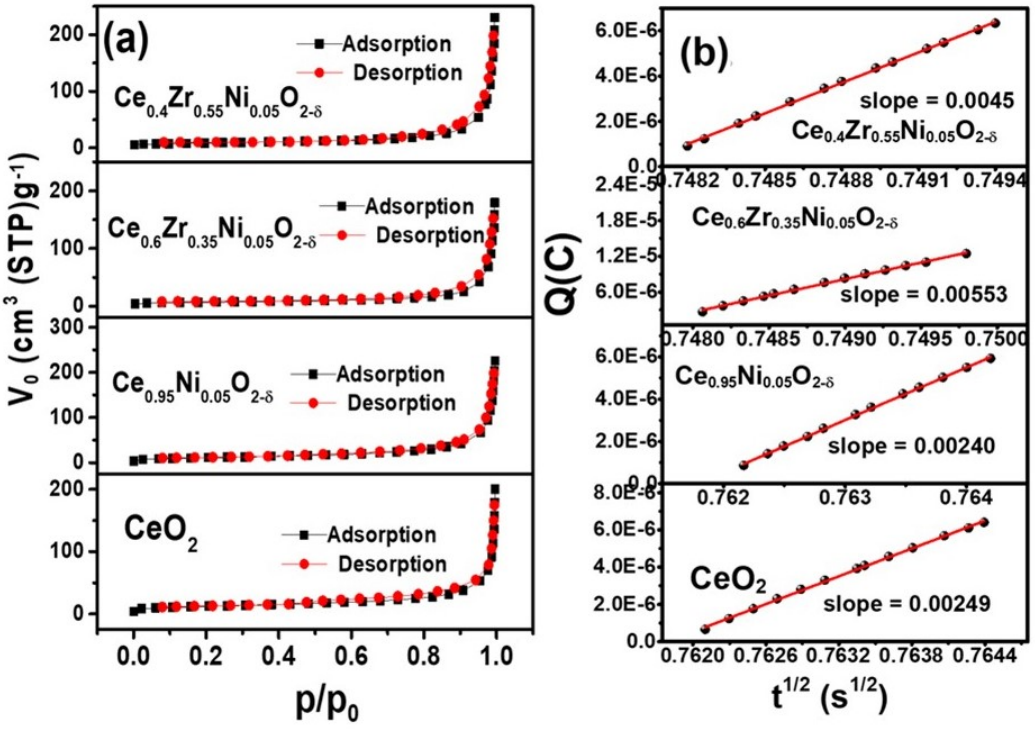

FIGURE 3B.5: (a)N_2 adsorption - desorption isotherm, and (b) Charge vs. time plot of CeO_2 $Ce_{0.95}Ni_{0.05}O_{2-\delta}$, $Ce_{0.6}Zr_{0.35}Ni_{0.05}O_{2-\delta}$ and $Ce_{0.4}Zr_{0.55}Ni_{0.05}O_{2-\delta}$

3B.3.2 Evaluation of Electrocatalytic Oxidation of Methanol

To evaluate the MOR activity of pristine CeO_2, doped $Ce_{0.95}Ni_{0.05}O_{2-\delta}$ and $Zr_{0.95}Ni_{0.05}O_{2-\delta}$ as well as $Ce_{0.6}Zr_{0.35}Ni_{0.05}O_{2-\delta}$ and $Ce_{0.4}Zr_{0.55}Ni_{0.05}O_{2-\delta}$ in alkaline medium, CV curves were recorded in 0.5 M NaOH and 0.5 M MeOH solution. The materials were first activated by cycling several scans in a potential window of 1.0 – 1.8 V vs. RHE in alkaline 0.5 M NaOH electrolyte solution before the MOR. The CV traces in alkaline solution without methanol in Figure 3B.7 show almost no significant peak in case of pristine CeO_2 and a prominent anodic peak at 1.43 V vs RHE and counter cathodic peak at 1.36 V vs RHE in the doped materials. The anodic peak may correspond to the formation oxyhydroxides (Ni - OOH) species associated with the oxidation of higher valency Ni, while the counter cathodic peak is might be associated with the corresponding reduction process of Ni - OOH suggesting a red-ox Ni^{2+}/Ni^{3+} process in the experimental potential window [22, 39, 187, 226–229]. Formation of thicker layer of Ni - OOH with Ni^{3+} was further supported when the corresponding peak current density increased gradually with the increase in the scan rate from 10 to 100 mV s^{-1} (Figure 3B.6) over the doped materials. It was interesting to observe that the surface concentration of Ni - OOH species was higher in $Ce_{0.95}Ni_{0.05}O_{2-\delta}$ compared to $Zr_{0.95}Ni_{0.05}O_{2-\delta}$. The Ni - OOH surface concentration determined with respect to the geometrical surface area according to the Butler-Volmer equation as mentioned in experimental section. With doping of Zr the surface concentration of Ni - OOH species was further increased, and $Ce_{0.6}Zr_{0.35}Ni_{0.05}O_{2-\delta}$ exhibited the highest Ni - OOH species concentration of 8.9 $\times 10^{-8}$ mol cm^{-2} (Table 3B.3). However, lower concentration of Ni - OOH species was observed with the highest Zr doped material, $Ce_{0.4}Zr_{0.55}Ni_{0.05}O_{2-\delta}$. Apparently, the optimum Ni and Zr co-doping in CeO_2 has created oxygen vacancy, which in turn facilitated the in situ formation of the key intermediate species of Ni - OOH for efficient methanol oxidation reaction [39, 230]. Interestingly, the surface concentration of formed Ni - OOH was significantly lower in the physical mixtures of 5%NiO/35%ZrO_2/CeO_2 and 5%NiO/35%ZrO_2/Al_2O_3, which are incidentally possessing no or significantly low oxygen vacancy (Figure 3B.6, Table 3B.3). The absence of Ni - OOH species formation on the surface of 5%NiO/35%ZrO_2/CeO_2 and 5%NiO/35%ZrO_2/Al_2O_3 was clearly depicted in CV traces in 0.5 M NaOH.

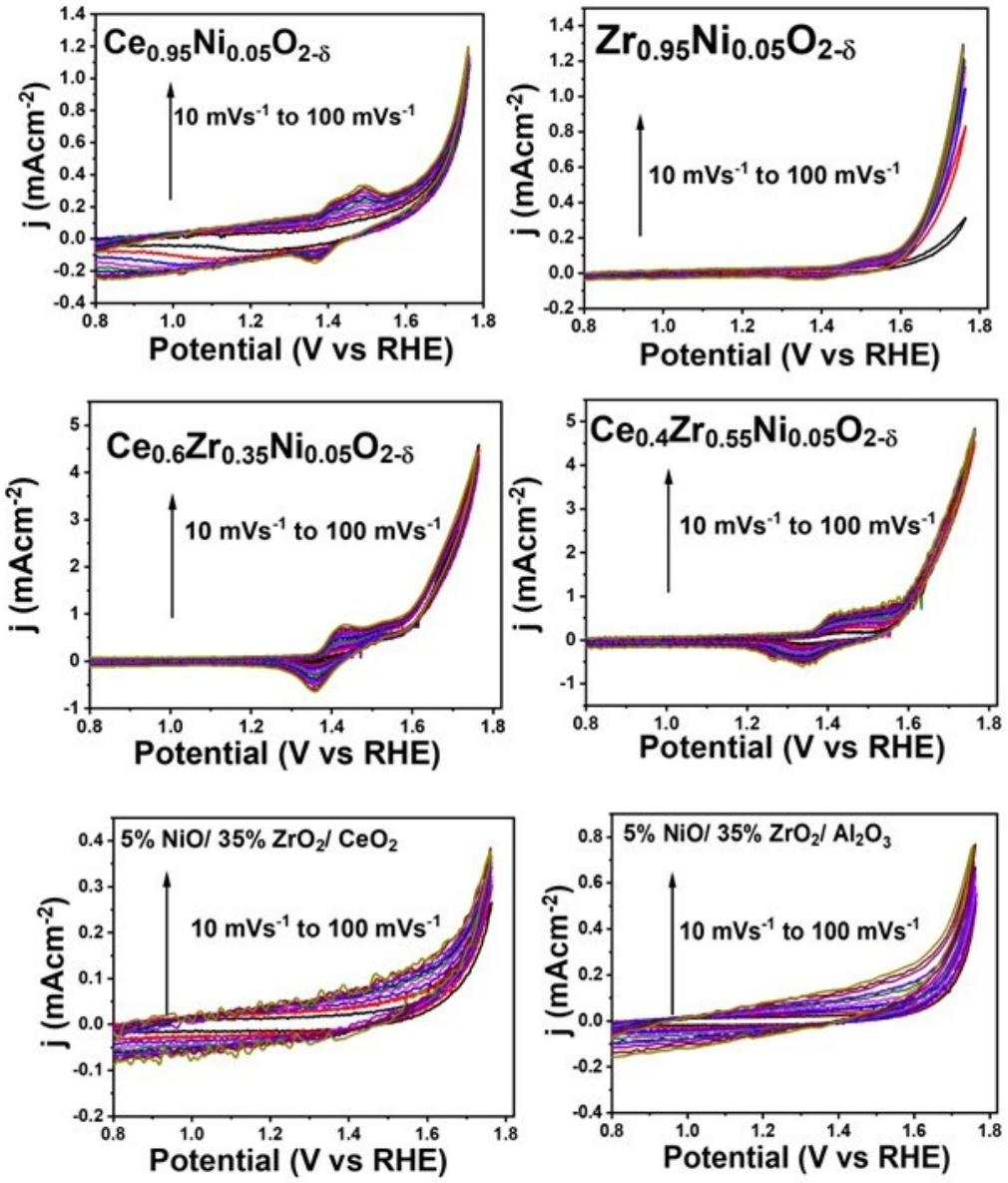

FIGURE 3B.6: CVs of $Ce_{1-x-y}Zr_xNi_yO_{2-\delta}$ in 0.5 M NaOH at the potential scan rates in the range 10 - 100 mVs^{-1}

Next, we screened the materials for MOR and the CV traces in presence of methanol in alkaline electrolyte are provided in Figure 3B.7(b). Apparently, a noticeable enhancement in the peak current density was observed in the CV curves manifesting an outstanding electrochemical response of the catalytic materials towards MOR. The distinguished anodic peak in the forward scan is assigned to the extent of oxidation of adsorbed methanol, whereas the peak in backward scan is considered to be responsible for the oxidation of absorbed intermediates from MOR [170, 231, 232]. It should be also noted that the peak associated with the Ni - OOH formation was almost obscured due to the high peak current density associated with the MOR. The characteristic MOR peak current density at 1.60 V vs RHE in the forward scan has significantly

TABLE 3B.3: Ni - OOH surface concentration

Sample	**Surface concentration Ni - OOH (τ^*) mol cm^{-2}**
$Ce_{0.95}Ni_{0.05}O_{2-\delta}$	2.1×10^{-9}
$Zr_{0.95}Ni_{0.05}O_{2-\delta}$	7.9×10^{-9}
$Ce_{0.6}Zr_{0.35}Ni_{0.05}O_{2-\delta}$	8.9×10^{-8}
$Ce_{0.4}Zr_{0.55}Ni_{0.05}O_{2-\delta}$	8.4×10^{-8}
5%NiO/35%ZrO_2/CeO_2	1.24×10^{-8}
5%NiO/35%ZrO_2/Al_2O_3	1.20×10^{-8}

increased in case of $Ce_{0.95}Ni_{0.05}O_{2-\delta}$ (2.43 mA cm^{-2}) compared to pristine CeO_2 (0.63 mA cm^{-2}). In fact, the current density of MOR was also higher in the case of $Ce_{0.95}Ni_{0.05}O_{2-\delta}$ than $Zr_{0.95}Ni_{0.05}O_{2-\delta}$. With optimum doping of Zr in $Ce_{0.6}Zr_{0.35}Ni_{0.05}O_{2-\delta}$, the current density was found be highest with 13.12 mA cm^{-2}. And the current density reduced with further doping of Zr in $Ce_{0.4}Zr_{0.55}Ni_{0.05}O_{2-\delta}$ (9.04 mA cm^{-2}). $Ce_{0.6}Zr_{0.35}Ni_{0.05}O_{2-\delta}$ exhibited the highest current density signifying the optimized doping increased the number of electrocatalytic active sites, hence by improving the intrinsic catalytic activity towards MOR. Based on the observation that the MOR peak in the CV traces occurred after the formation of the Ni - OOH associated with the Ni^{2+}/Ni^{3+} oxidation peak, it can be concluded that the Ni - OOH species formed in situ are the active species, as previously reported in the literature [39, 233]. Further corroboration can be provided by the fact that the MOR current density showed a clear proportionality with the surface concentration of the Ni - OOH species over the solution combustion synthesized catalysts.

The high concentration of surface bound Ni - OOH species helped $Ce_{0.6}Zr_{0.35}Ni_{0.05}O_{2-\delta}$ to exhibit the best MOR activity. The physical mixtures of 5%NiO/35%ZrO_2/CeO_2 and 5%NiO/35%ZrO_2/Al_2O_3 did not show any significant MOR activity (Figure 3B.7(c and d)). The variation in MOR current density with doping of Zr and Ni is depicted in a bar plot in Figure 3B.8. It should be noted that the onset potential of MOR over $Ce_{0.6}Zr_{0.35}Ni_{0.05}O_{2-\delta}$ exhibits superiority to those of similar Ni-based materials (Table 3B.4). Further, we compared the MOR activity of $Ce_{0.6}Zr_{0.35}Ni_{0.05}O_{2-\delta}$ with those of bare GCE and standard 20%Pt/C (Figure 3B.9). Bare GCE did not show any MOR activity, whereas 20% Pt/C exhibited a lower current density of 9.32 mA cm^{-2}, however, at lower onset potential. The elevated onset potential compared with the theoretical value of the oxygen reduction reaction suggests that while the material may not directly contribute to the potential application of DMFCs, it holds promise for both the treatment of methanol-rich industrial wastewater and potential utilization in masking or substituting the oxygen evolution reaction for H_2 production.

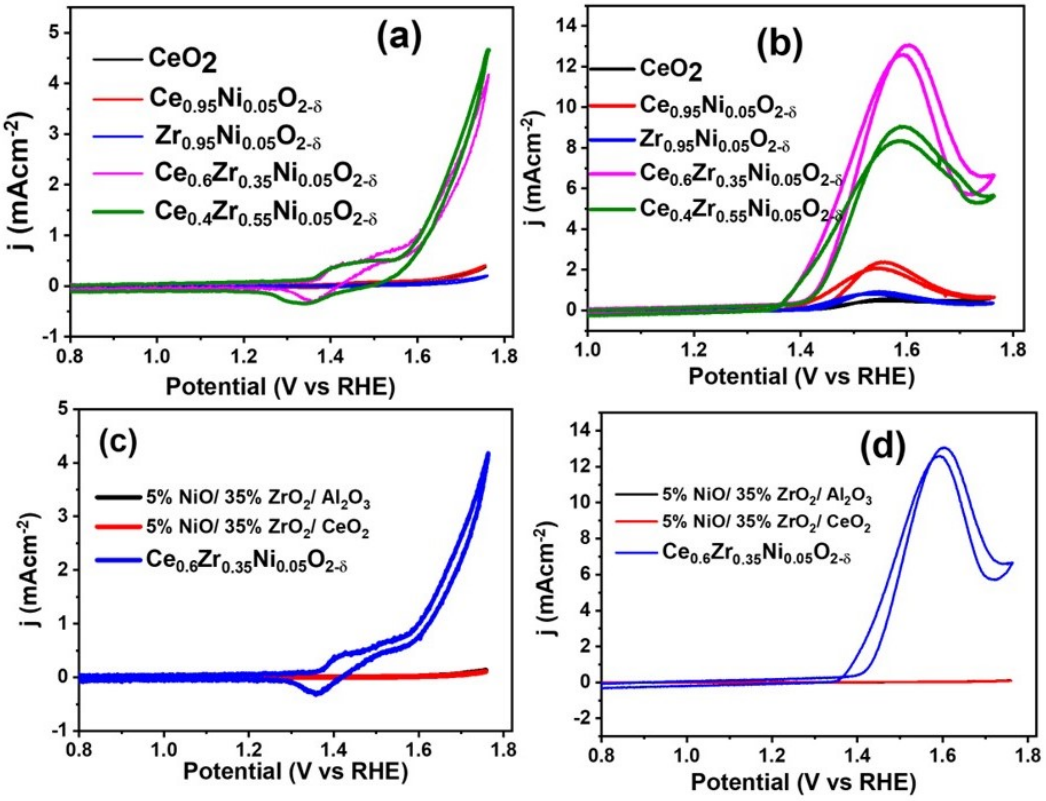

FIGURE 3B.7: CVs of CeO_2, $Ce_{0.95}Ni_{0.05}O_{2-\delta}$, $Zr_{0.95}Ni_{0.05}O_{2-\delta}$, $Ce_{0.6}Zr_{0.35}Ni_{0.05}O_{2-\delta}$, and $Ce_{0.4}Zr_{0.55}Ni_{0.05}O_{2-\delta}$ in (a) 0.5 M NaOH with a scan speed of 50 mV s^{-1}, (b) in 0.5 M NaOH and 0.5 M MeOH with a scan speed of 50 $mVss^{-1}$, CVs of $Ce_{0.6}Zr_{0.35}Ni_{0.05}O_{2-\delta}$, 5% NiO/35%$ZrO_2$/$CeO_2$ and 5% NiO/35%ZrO_2/Al_2O_3 in (c) 0.5 M NaOH and (d) 0.5 M NaOH and 0.5 M MeOH with a scan speed of 50 mV s^{-1}

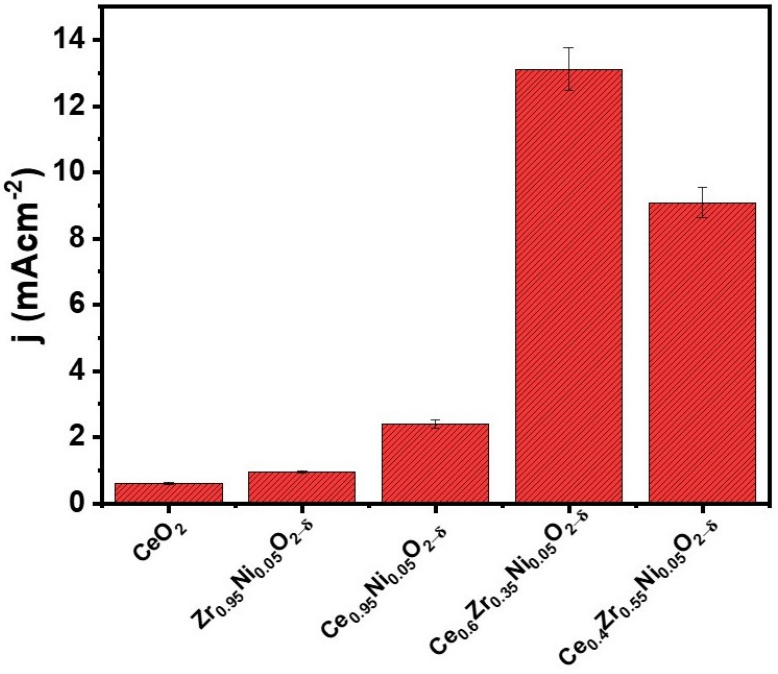

FIGURE 3B.8: Bar plot depicting variation of current densities with respect to Ni and Zr co-doping

TABLE 3B.4: Comparison table showing superior onset potential of $Ce_{0.6}Zr_{0.35}Ni_{0.05}O_{2-\delta}$ over other Ni-based catalysts

Catalysts	**Electrolyte**	**Onset potential (V vs RHE)**	**Ref**
Boron doped $NiCu_2O_4$	1M KOH+ 1M MeOH	1.39	[234]
CeO_2-NiO	1M KOH+ 1M MeOH	1.43	[235]
$NiSe_2$/NC-450	1M KOH+ 0.5 M MeOH	1.33	[236]
NiZn1000@CuO	1M KOH+ 1.5 M MeOH	1.41	[237]
Ni/$CuCo_2O_4$	1M KOH+ 0.5 M MeOH	1.35	[238]
Ni-WC/C	1M KOH+ 0.5 M MeOH	1.3	[239]
NiCoSn alloy	1M KOH+ 1M MeOH	1.35	[240]
NiO NS@NW/NF	1M KOH+ 0.5 M MeOH	1.45	[241]
Ni/NiO	1M KOH+ 1M MeOH	1.38	[226]
Ni-Ni-2	1M KOH+ 1M MeOH	1.4	[242]
$La_{1.4}Sr_{0.6}NiO_{4+\delta}$/PANI	0.5M NaOH+ 1.5M MeOH	1.36	[132]
$Ce_{0.9}Ni_{0.05}Sr_{0.05}O_{2-\delta}$	0.5 M NaOH+ 0.5 M MeOH	1.35	[222]
$Ce_{0.6}Zr_{0.35}Ni_{0.05}O_{2-\delta}$	0.5 M NaOH+ 0.5 M MeOH	1.35	This work

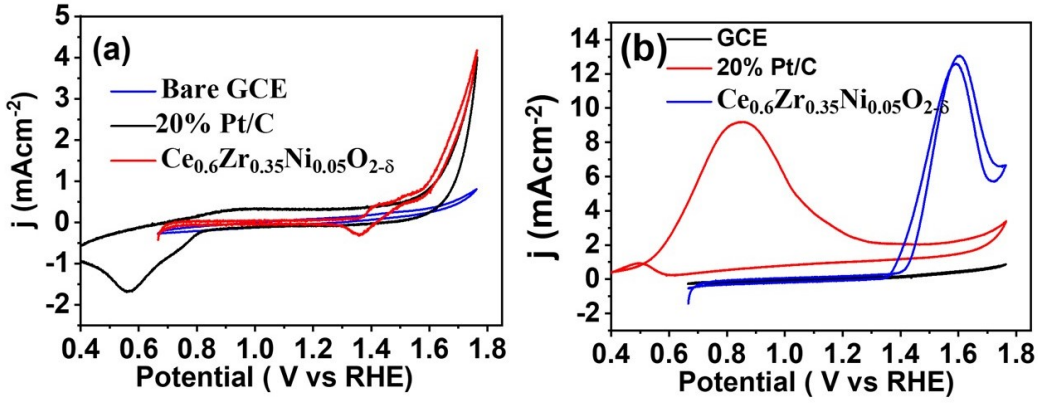

FIGURE 3B.9: CVs of $Ce_{0.6}Zr_{0.35}Ni_{0.05}O_{2-\delta}$, 20% Pt/C, Bare GCE in (a) 0.5 M NaOH (b) 0.5 M NaOH and 0.5 M MeOH

The above discussion rationalized the significance of the formation of surface bound Ni - OOH species due to the high oxygen vacancy and its primary influence towards efficient methanol oxidation activity over the co-doped catalysts. The charge transfer resistance invoked by oxygen vacancy is another crucial factor to tailor the surface electronic configuration vis à vis conductivity of the material for efficient electrocatalytic activity [243–245]. Therefore, EIS measurement was carried out in alkaline 0.5M MeOH solution to probe the electrical conductivity and charge - transfer behavior on the electrode - electrolyte interface. A distinct semicircular arc was observed over the catalytic materials in the measured frequency range, as depicted in Figure 3B.10(a). This can be attributed to the combined effects of charge transfer resistance and double - layer capacitance at high frequency, along with intermediate adsorption at low frequency. As the doping of Ni and Zr increased gradually, the semicircle arc decreased, suggesting a significantly faster electron transfer rate. To elaborate more regarding the impedance of the material, Bode phase and admittance have been studied (Figure 3B.10(b - c)). The Bode admittance plot illustrates that a reduction in the impedance magnitude (Z) in the low-frequency range indicates a decrease in the material's resistance and an enhanced electron flow through the electrode [174, 175]. This behaviour was observed in $Ce_{0.6}Zr_{0.35}Ni_{0.05}O_{2-\delta}$ compared to other materials (Figure 3B.10(b)). $Ce_{0.6}Zr_{0.35}Ni_{0.05}O_{2-\delta}$ demonstrates highly conductive behaviour based on its bode phase angle plot (Figure 3B.10(c)) showing a phase angle less than -90 °C, which signifies a maximum possible phase shift between voltage and current and indicates an insulator behaviour. Further analysis of the system was carried out with circuit fitting (Figure 3B.10(d)) and evaluating the parameters generated from the circuit (Table 3B.5). The initial phase element in the circuit represents the parallel combination of charge transfer resistance (R_{ct}) and double-layer capacitance. The significantly lower R_{ct} value of $Ce_{0.6}Zr_{0.35}Ni_{0.05}O_{2-\delta}$ (548.5 Ω) compared to other materials indicates improved charge transfer during MOR on this optimized oxide. Additionally, the lower adsorption resistance (R_{ad}) value of 92.8 Ω highlights the enhanced oxidation ease of CO species adsorbed on the catalyst's surface [246, 247].

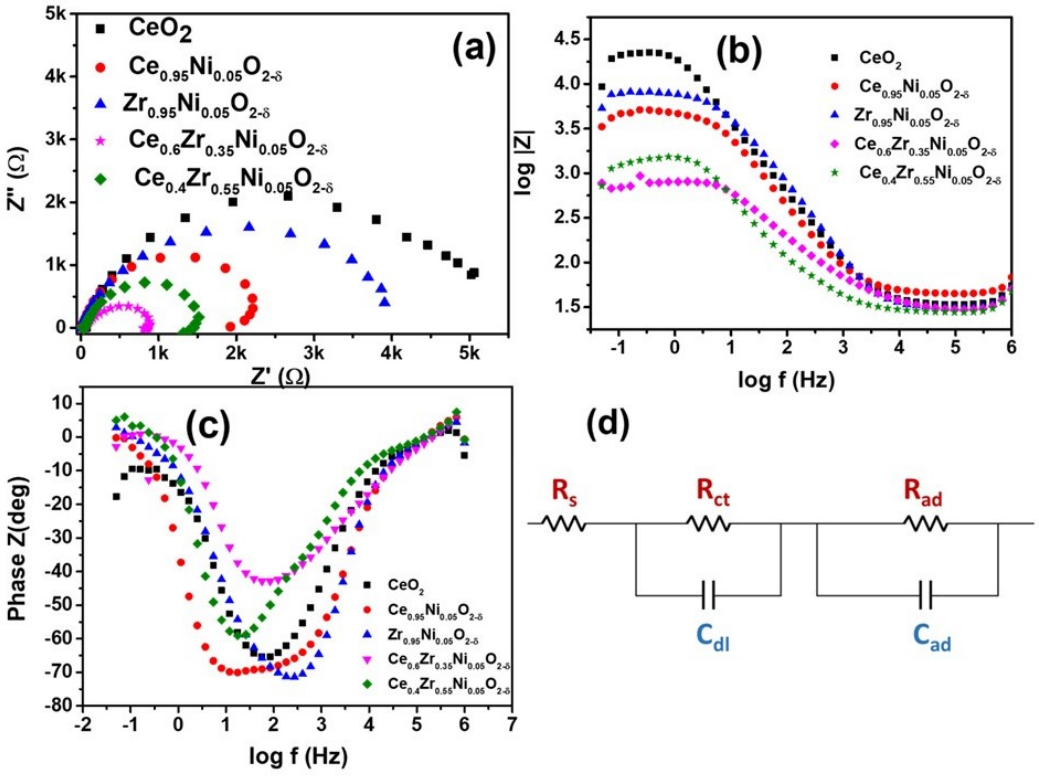

FIGURE 3B.10: (a) Nyquist plot (b) Bode absolute impedance, and (c) Bode phase angle plots of CeO_2, $Ce_{0.95}Ni_{0.05}O_{2-\delta}$, $Zr_{0.95}Ni_{0.05}O_{2-\delta}$, $Ce_{0.6}Zr_{0.35}Ni_{0.05}O_{2-\delta}$ and $Ce_{0.4}Zr_{0.55}Ni_{0.05}O_{2-\delta}$ (d) Nyquist fitted circuit diagram

TABLE 3B.5: EIS parameters obtained from fitting of Nyquist plot

Catalysts	**CeO_2**	**$Ce_{0.95}Ni_{0.05}O_{2-\delta}$**	**$Zr_{0.95}Ni_{0.05}O_{2-\delta}$**	**$Ce_{0.6}Zr_{0.35}Ni_{0.05}O_{2-\delta}$**	**$Ce_{0.4}Zr_{0.55}Ni_{0.05}O_{2-\delta}$**
R_s (Ω)	45.7	35.8	32.1	30.7	28.7
R_{ct} (Ω)	2178	1710	6090	548.5	1368
R_{ad} (Ω)	3720	9.01	1830	92.8	230.6
C_{dl} (F)	5.65×10^{-6}	11.5×10^{-6}	5.59×10^{-6}	29.7×10^{-6}	24.9×10^{-6}
C_{ad} (F)	16.53×10^{-6}	26.8×10^{-6}	5.98×10^{-6}	72.1×10^{-6}	91.5×10^{-6}

3B.3.3 Evaluation of the Kinetic Parameters

In order to evaluate the kinetic parameters of the MOR, such as order of the reaction, rate constant, rate determining step, Tafel slope, activation energy was calculated over the synthesized catalysts CeO_2, $Ce_{0.95}Ni_{0.05}O_{2-\delta}$, $Ce_{0.6}Zr_{0.35}Ni_{0.05}O_{2-\delta}$ and $Ce_{0.4}Zr_{0.55}Ni_{0.05}O_{2-\delta}$. The existing literature suggests that ideally a theoretical Tafel slope of $\sim$ 120 mV dec^{-1} is an indicator of splitting of the first C-H bond of CH_3OH as a rate determining step in the overall methanol electro oxidation reaction [166, 248, 249] Whereas, a large deviation from the ideal theoretical value may happen due to the adsorption of intermediates on the surface of the catalyst [250]. A CA response was carried out for 250 s at the catalytically active potential region of MOR (Figure 3B.11). The current density obtained after reaching the steady state (at 150 s) was plotted against the potential with and without iR correction with R as uncompensated resistance (Figure 3B.12). The Tafel studies were carried out using the steady state polarization curve constructed using the iR corrected potentials [251].

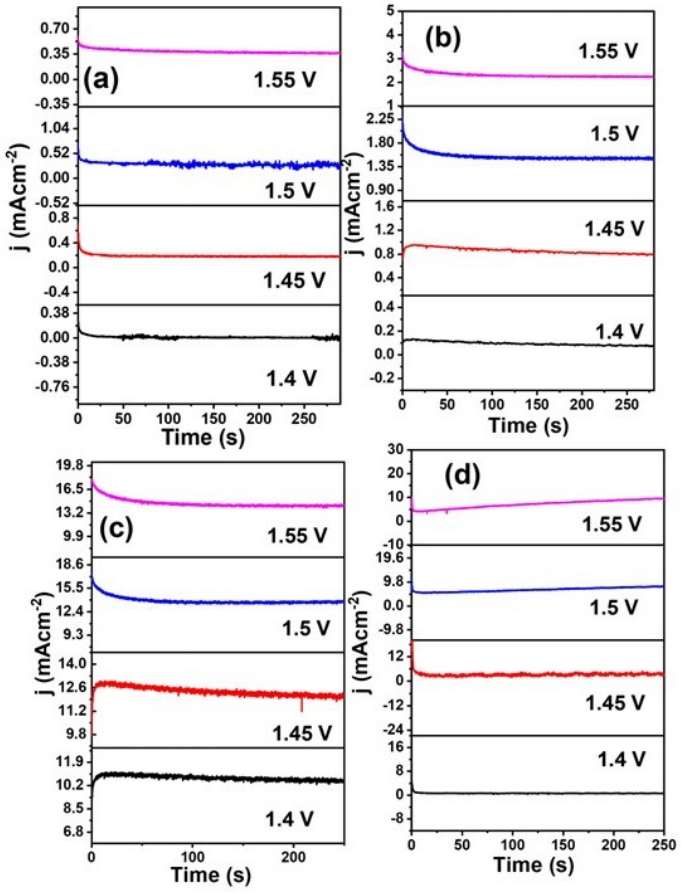

FIGURE 3B.11: CA responses of (a)CeO_2, (b) $Ce_{0.95}Ni_{0.05}O_{2-\delta}$, (c) $Ce_{0.6}Zr_{0.35}Ni_{0.05}O_{2-\delta}$ and (d) $Ce_{0.4}Zr_{0.55}Ni_{0.05}O_{2-\delta}$ for 250 s at catalytically active region.

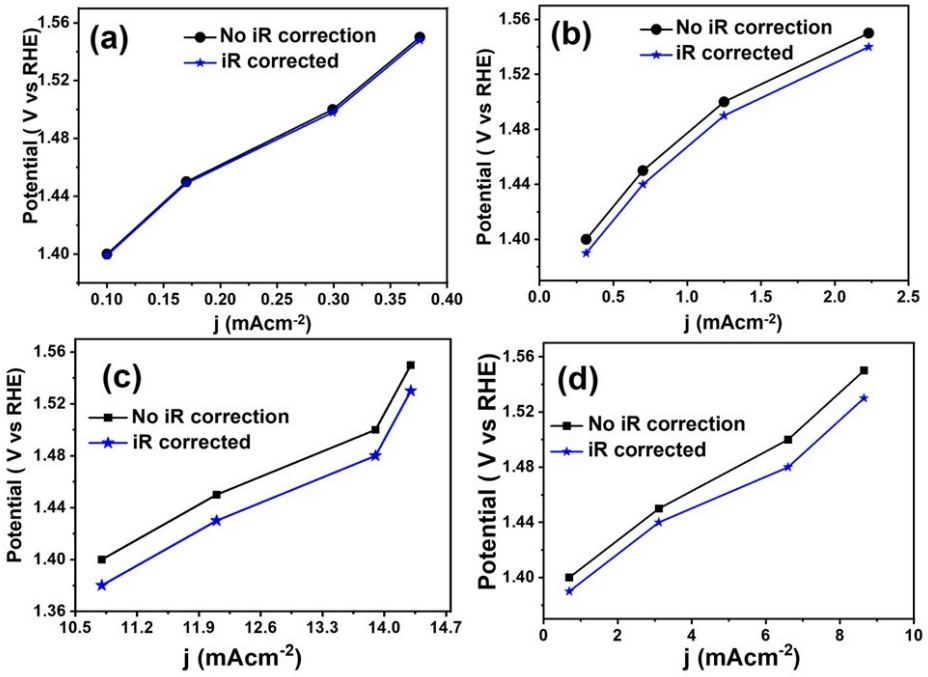

FIGURE 3B.12: Plot of current density vs potential with and without iR drop correction of (a)CeO_2, (b) $Ce_{0.95}Ni_{0.05}O_{2-\delta}$, (c) $Ce_{0.6}Zr_{0.35}Ni_{0.05}O_{2-\delta}$ and (d) $Ce_{0.4}Zr_{0.55}Ni_{0.05}O_{2-\delta}$ for 250 s at catalytically active region.

The Tafel plot depicted in Figure 3B.13(a) exhibits a lower slope of 112.5 mV dec^{-1} over $Ce_{0.6}Zr_{0.35}Ni_{0.05}O_{2-\delta}$, demonstrating excellent conformity with the theoretical value. However, a significant deviation was observed with the other catalysts in the series. The study concludes that the C-H bond dissociation could be the rate determining step over the optimized $Ce_{0.6}Zr_{0.35}Ni_{0.05}O_{2-\delta}$ catalysts, whereas the intermediates formed during MOR gets strongly attached over the surface of other catalysts. As $Ce_{0.6}Zr_{0.35}Ni_{0.05}O_{2-\delta}$ turned out to be the champion catalyst by outperforming the other materials, further evaluation of the kinetic parameters was carried out only with the optimized material. The reaction order of the electro-oxidation of methanol over $Ce_{0.6}Zr_{0.35}Ni_{0.05}O_{2-\delta}$ was calculated using the equation log I = log nFk + m logC, where F is Faraday constant, k being reaction constant, m is the reaction order, and C is the concentration of methanol [252]. Voltammograms were collected with different concentration of methanol (Figure 3B.13(b)), and a linear relationship was obtained from the voltammetric responses of $Ce_{0.6}Zr_{0.35}Ni_{0.05}O_{2-\delta}$ at different methanol concentration by plotting log I vs. log C with a slope of 0.37 at peak potential (1.60 V vs RHE) (inset of Figure 3B.13(b)). The results indicate that the overall MOR order is $\frac{1}{2}$ with respect to methanol over $Ce_{0.6}Zr_{0.35}Ni_{0.05}O_{2-\delta}$. Next, the kinetic evaluation of the optimized catalyzed was carried out by varying the scan rate from 10 to 60 mV s^{-1} in 0.5 M MeOH and 0.5 M NaOH electrolyte. Figure 3B.13(c) shows that the anodic current density increased with the increase in scan rate and a linear

relationship was observed when square root of scan rate was plotted with the current density. The observed linear relationship between the square root of scan rate and current density in the inset of Figure 3B.13(c) with a regression coefficient $R^2 = 0.99$ indicates that the MOR over $Ce_{0.6}Zr_{0.35}Ni_{0.05}O_{2-\delta}$ undergoes a diffusion-controlled pathway by following the Randles-Sevick equation. From the logarithmic curve of peak current vs scan rate in Figure 3B.13(d) a slope of 0.57 was obtained. The value is close to the theoretically expected value of 0.50 confirming the MOR over $Ce_{0.6}Zr_{0.35}Ni_{0.05}O_{2-\delta}$ is a diffusion-controlled process rather than a surface-controlled phenomenon [167, 253].

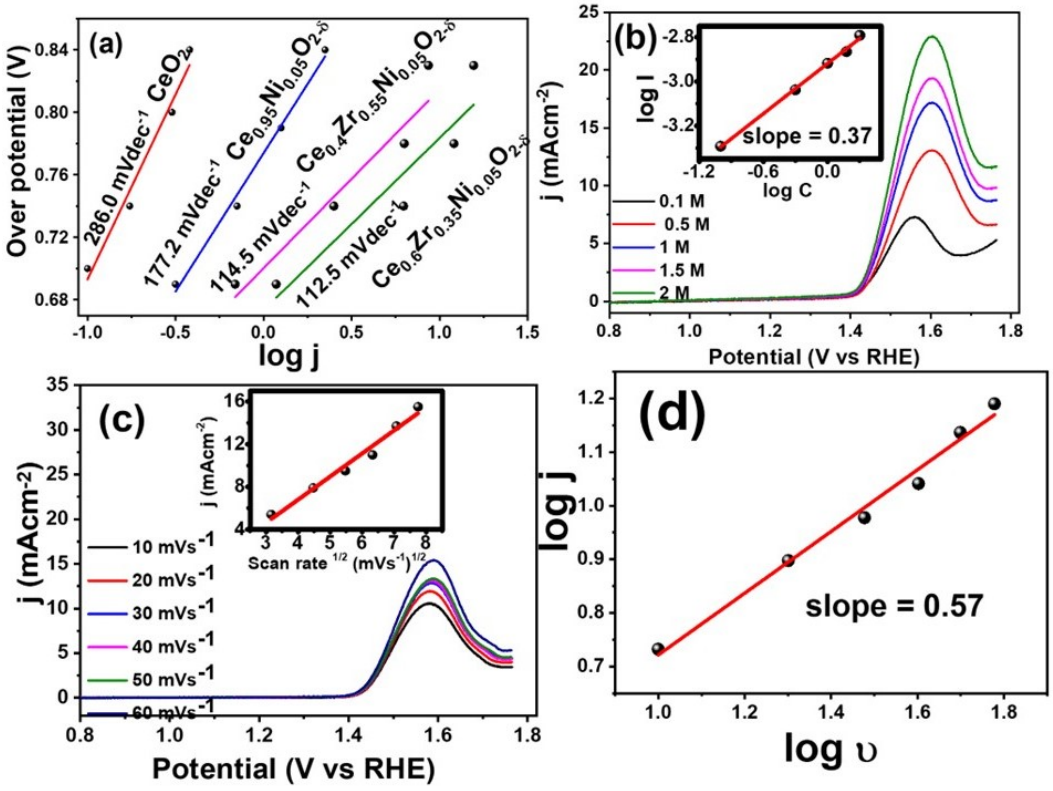

FIGURE 3B.13: (a) Tafel plot of CeO_2, $Ce_{0.95}Ni_{0.05}O_{2-\delta}$, $Ce_{0.6}Zr_{0.35}Ni_{0.05}O_{2-\delta}$ and $Ce_{0.4}Zr_{0.55}Ni_{0.05}O_{2-\delta}$ (b) Methanol concentration study of $Ce_{0.6}Zr_{0.35}Ni_{0.05}O_{2-\delta}$ (log C Vs log I plot of $Ce_{0.6}Zr_{0.35}Ni_{0.05}O_{2-\delta}$ for MOR of showing order of the reaction) (c) scan rate dependent study of $Ce_{0.6}Zr_{0.35}Ni_{0.05}O_{2-\delta}$ in 0.5 M NaOH and 0.5 M MeOH (inset square root of scan rate vs current density) (d) logarithmic plot of scan rate with current density for $Ce_{0.6}Zr_{0.35}Ni_{0.05}O_{2-\delta}$

Double step chronoamperometry was carried out by setting the two-step potentials at MOR oxidation potential (i.e at 1.60 V vs RHE for 60 s and at 1.0 V for 60 s) in presence and in absence of methanol, and the obtained data are plotted in Figure 3B.14(a). The current density was found to increase with an increase in the concentration of methanol at MOR oxidation potential, decreases rapidly at 1.0 V vs RHE, and becomes almost equal and steady irrespective of methanol concentration. The forward and backward potential step chrono amperometry of the modified electrode in absence of methanol showed an almost symmetrical chronoamperogram, whereas the charge value associated with the forward chronoamperometry is significantly higher than that observed for the backward chronoamperometry (inset of Figure 3B.14(a)) demonstrating the irreversible nature of electro oxidation of methanol over $Ce_{0.6}Zr_{0.35}Ni_{0.05}O_{2-\delta}$ [44]. Further, the rate constant for methanol electro-oxidation was calculated using the Equation:

$$I_c/I_L = \gamma^{1/2}\left[\pi^{1/2}\mathrm{erf}\left(\gamma^{1/2}\right) + \exp\left(-\gamma\right)/\gamma^{1/2}\right] \tag{3B.4}$$

where I_C is the catalytic current of $Ce_{0.6}Zr_{0.35}Ni_{0.05}O_{2-\delta}$ in presence of methanol, I_L is the limiting current in the absence of methanol. γ is the argument of error function and is equal to kC_ot, where k is the rate constant in cc $mol^{-1}s^{-1}$, t being the elapsed time in s, and C_o is the bulk methanol concentration in mol cc^{-1}. The above-mentioned equation can be simplified as the following one by considering the value of $\gamma > 2$.

$$I_c/I_L = \gamma^{1/2}\pi^{1/2} = (kC_0t)^{1/2}\pi^{1/2} \tag{3B.5}$$

The slope derived from the Figure 3B.14(b) with different methanol concentration from 0 M to 2 M shows that the rate constant of MOR over $Ce_{0.6}Zr_{0.35}Ni_{0.05}O_{2-\delta}$ is 7.30×10^4 cc mol^{-1} s^{-1}. The calculated rate constant is comparable with the values reported in the literature and clearly indicates that the catalyst $Ce_{0.6}Zr_{0.35}Ni_{0.05}O_{2-\delta}$ efficiently surpasses the kinetic barrier for methanol oxidation as well as competently reduce the overpotential for the overall electrocatalytic system [44, 169, 254, 255].

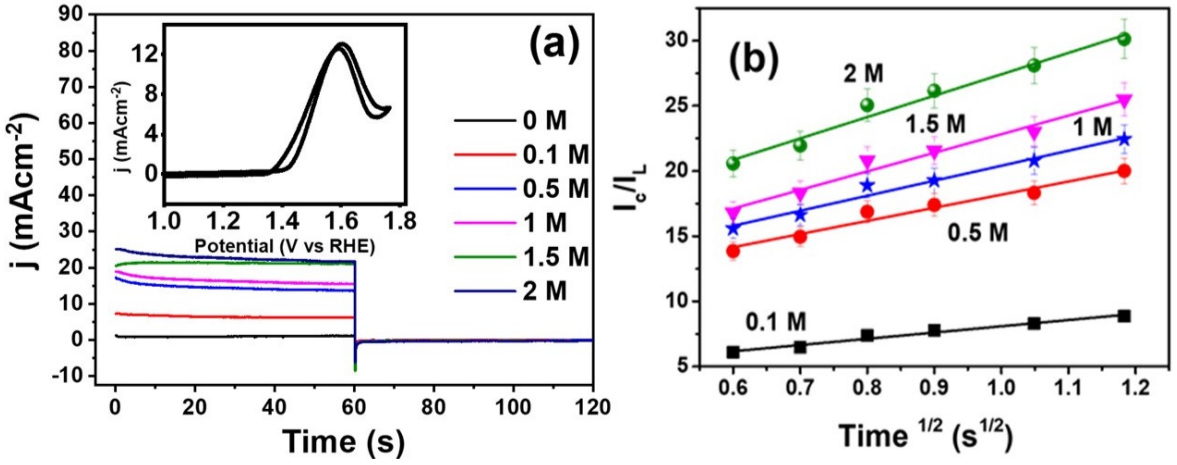

FIGURE 3B.14: (a) Double step chronoamperometry of $Ce_{0.6}Zr_{0.35}Ni_{0.05}O_{2-\delta}$ with and without methanol at 1.6 V and 1.0V vs RHE. (b) I_c vs $_L$ vs Time (s)

Another key parameter for MOR reaction is the activation energy of the catalysts. Arrhenius plot of current density (ln j) vs. temperature (T^{-1}) at methanol oxidation potential of CeO_2, $Ce_{0.95}Ni_{0.05}O_{2-\delta}$, $Ce_{0.6}Zr_{0.35}Ni_{0.05}O_{2-\delta}$, and $Ce_{0.4}Zr_{0.55}Ni_{0.05}O_{2-\delta}$ was adopted to determine the activation energy. The temperature was varied from 25 to 50 °C with a gap of 5 °C in 0.5 M NaOH and 0.5 M MeOH electrolyte solution [256]. The activation energy (E_a) was obtained from the slope of Figure 3B.15. The the optimized catalyst $Ce_{0.6}Zr_{0.35}Ni_{0.05}O_{2-\delta}$ exhibited an MOR activation energy of 21.1 kJ mol^{-1}. $Ce_{0.4}Zr_{0.55}Ni_{0.05}O_{2-\delta}$ and $Ce_{0.95}Ni_{0.05}O_{2-\delta}$ showed a slightly enhanced activation energy of 23.5 and 24.1 kJ mol^{-1}, respectively. Whereas the pristine CeO_2 demonstrated a comparatively very high activation energy of 47.3 kJ mol^{-1}. A lower activation energy indicates a faster MOR kinetics over $Ce_{0.6}Zr_{0.35}Ni_{0.05}O_{2-\delta}$.

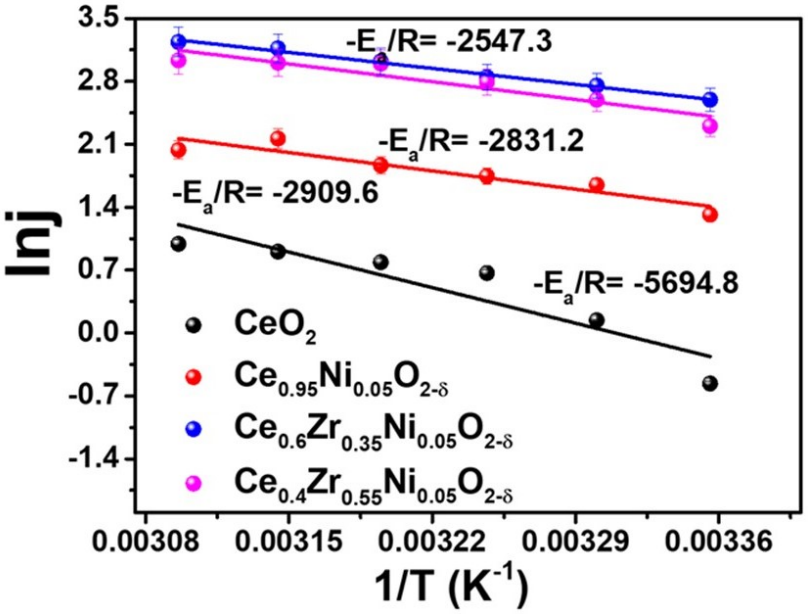

FIGURE 3B.15: Activation Energy plot of MOR over CeO_2, $Ce_{0.95}Ni_{0.05}O_{2-\delta}$, $Ce_{0.6}Zr_{0.35}Ni_{0.05}O_{2-\delta}$ and $Ce_{0.4}Zr_{0.55}Ni_{0.05}O_{2-\delta}$

It is prime for an electrode material is to retain its potential stability vis à vis durability for a prolonged period of time against the major challenge of CO poisoning for practical applicability. The long-term stability of the catalyst was first confirmed using cycle study up to 300 cycles at a scan rate of 50 mV s^{-1}. It was observed that the current density was maintained 99% of the initial current density for $Ce_{0.6}Zr_{0.35}Ni_{0.05}O_{2-\delta}$ (Figure 3B.16(a)). Further, the CA studies for 10 h at 1.6 V vs RHE in 0.5 M NaOH and 0.5 M MeOH electrolyte solution was carried out to confirm the stability of the catalyst. Figure 3B.16(b) shows a stable and constant current response of $Ce_{0.6}Zr_{0.35}Ni_{0.05}O_{2-\delta}$ during 10 h of MOR indicating the high tolerable nature of the materials against CO poisoning. The results depict that the stability retained establishing the high CO tolerance of the materials and indicating the prospective of practical applications. After the prolonged MOR study, the electrolyte was subjected to ^{1}HNMR to evaluate the liquid products. The corresponding spectra are shown in Figure 3B.17. The data revealed the formation of formic acid at 8.3 ppm as the only liquid product during MOR and concentration of formic acid produced over CeO_2, $Ce_{0.95}Ni_{0.05}O_{2-\delta}$, $Ce_{0.6}Zr_{0.35}Ni_{0.05}O_{2-\delta}$ and $Ce_{0.4}Zr_{0.55}Ni_{0.05}O_{2-\delta}$ were calculated to be 0.0097, 0.128, 1.74 and 0.285 μmol respectively

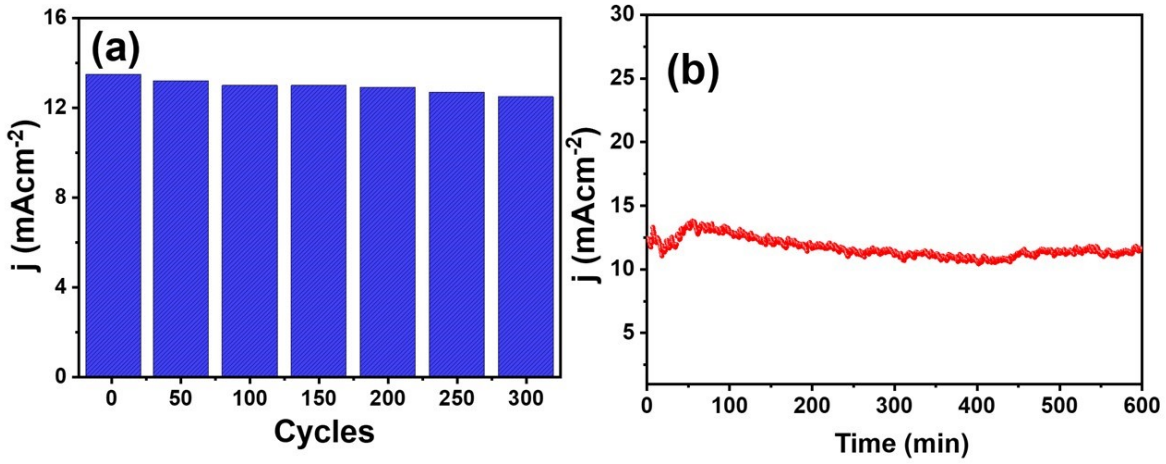

FIGURE 3B.16: (a) Stability study of $Ce_{0.6}Zr_{0.35}Ni_{0.05}O_{2-\delta}$ up to 300 cycles (b) CA of $Ce_{0.6}Zr_{0.35}Ni_{0.05}O_{2-\delta}$ at 1.6 V vs RHE in 0.5 M NaOH and 0.5 M MeOH for 10 h

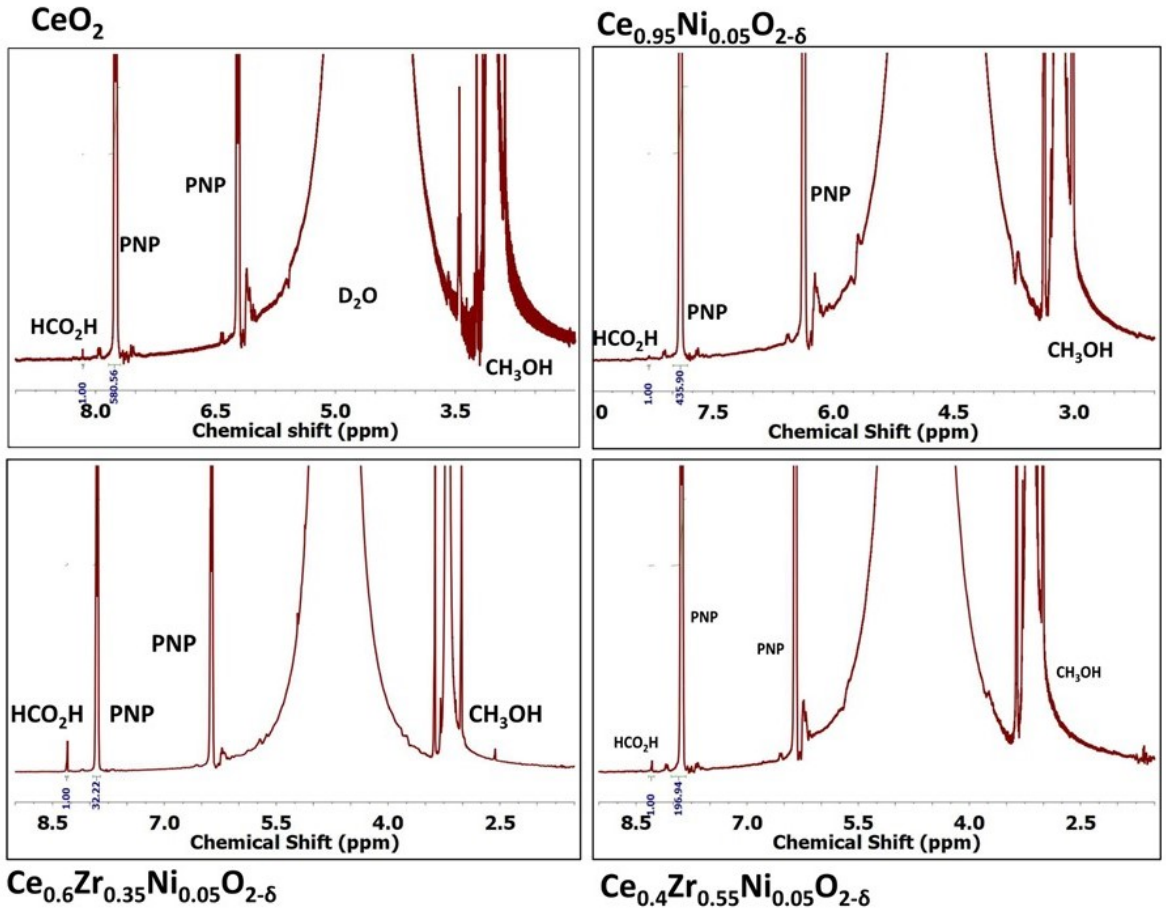

FIGURE 3B.17: ^{1}HNMR spectra of the electrolyte of CeO_2, $Ce_{0.95}Ni_{0.05}O_{2-\delta}$, $Ce_{0.6}Zr_{0.35}Ni_{0.05}O_{2-\delta}$ and $Ce_{0.4}Zr_{0.55}Ni_{0.05}O_{2-\delta}$after 4 h of CA in 0.5 M MeOH and 0.5 M NaOH medium.

Further, to confirm the reproducibility of the catalyst, we have carried out three cycles of single $Ce_{0.6}Zr_{0.35}Ni_{0.05}O_{2-\delta}$ electrode by changing the electrolyte as shown in Figure 3B.18(a). It has been observed that for the first two instances there was absolutely no change in the current density, however at the third run there was a nominal deduction of the current density. The stability of $Ce_{0.6}Zr_{0.35}Ni_{0.05}O_{2-\delta}$ was also compared with the bare GCE and standard catalyst (20% Pt/C) (Figure 3B.18(b)). It has been observed that the current density of 20% Pt/C significantly dropped only within an hour probably due to the electrocatalyst poisoning by chemisorbed carbonaceous species formed during the methanol oxidation. In case of bare GCE, there was no indication of MOR as current density was near to almost zero.

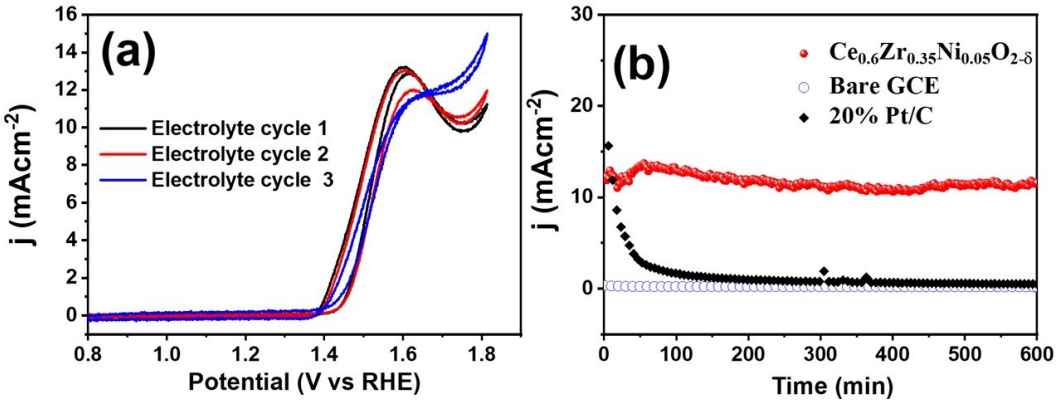

FIGURE 3B.18: (a) CVs of $Ce_{0.6}Zr_{0.35}Ni_{0.05}O_{2-\delta}$ single electrode by changing the electrolyte three times (0.5 M NaOH + 0.5M MeOH) at scan rate of 50 mV s^{-1} (b)Stability study of $Ce_{0.6}Zr_{0.35}Ni_{0.05}O_{2-\delta}$, 20 %Pt/C and bare GCE in 0.5 M NaOH and 0.5 M MeOH for 10 h

The XRD pattern of the exhausted $Ce_{0.6}Zr_{0.35}Ni_{0.05}O_{2-\delta}$ catalyst was studied to confirm the chemical robustness of the material after prolonged period of stability study (Figure 3B.19(a)). Fluorite structure was retained by the catalyst with minute amorphous carbon black from the electrocatalytic ink. The surface morphology as shown in Figure 3B.19(b,c) was retained in the exhausted catalyst as observed from FE-SEM images.

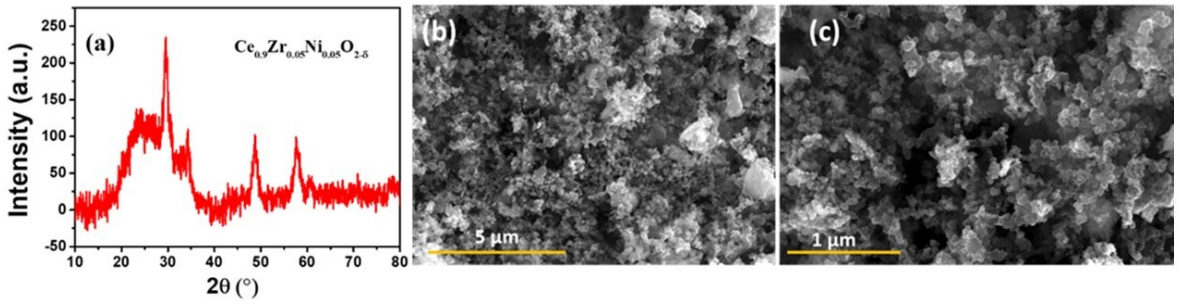

FIGURE 3B.19: (a) XRD (b, c) FE-SEM image of the exhausted $Ce_{0.6}Zr_{0.35}Ni_{0.05}O_{2-\delta}$ after 10 h of MOR

3B.3.4 Redox properties and mechanistic probe

The intriguing findings regarding the MOR activity, which can be attributed to the precise tuning of doping within the solid solution, have captivated our interest in exploring the underlying redox properties of the materials in correlation with the mechanism of the MOR reaction. Ex-situ XPS was employed to map the surface composition of the solid solution catalysts before and after the MOR process. Figure 3B.20 illustrates the Ce 3d XPS patterns, revealing multiple distinctive bands arising from various Ce 4f energy level occupancies. The Ce 3d core level spectra of all oxides exhibited a total of 10 peaks, as depicted in Figure 3B.20 (a). The first five peaks, labelled as **v** correspond to the Ce $3d_{5/2}$ level, while the subsequent five peaks, labelled as **u** correspond to the spin-orbit splitting of Ce $3d_{3/2}$ [130, 212, 257–259]. The peaks at 900.0 and 918.7 eV labelled as v‴ and u‴ are the characteristic Ce^{4+} ($3d_{5/2}$ and $3d_{3/2}$) peak corresponding to $3d^94f^0O2p^6$ final states configuration. The doublets at 884.4 and 904.8 labelled as v - u corresponds to Ce $3d^94f^2O2p^4$ configuration, whereas peaks at 891.0 and 911.4 eV (v″-u″) corresponds to Ce $3d^94f^1O2p^5$ final states of Ce^{4+} oxidation state [130, 180]. Peaks at binding energies 880.5 - 902.8 and 887.7- 909.4 eV labelled as v_0 - u_0 and v′ -u′ corresponds to Ce $3d^94f^2O2p^5$ and Ce $3d^94f^1O2p^6$ final states of Ce^{3+} oxidation states. The relative surface concentration of Ce^{3+} was calculated using the following equations:

$$A_{Ce^{4+}} = A_v + A_u + A_{u''} + A_{v''} + A_{v'''} + A_{u'''} \tag{3B.6}$$

$$A_{Ce^{3+}} = A_{v'} + A_{u'} + A_{v^0} + A_{u^0} \tag{3B.7}$$

$$C_{Ce^{3+}} = \frac{A_{Ce^{3+}}}{A_{Ce^{3+}} + A_{Ce^{4+}}} \tag{3B.8}$$

The presence of both Ce^{4+} and Ce^{3+} observed in the as-prepared oxides is tabulated in Table 3B.6. Apparently, the concentration of lower valent Ce^{3+} increased gradually with the extent of Ni and Zr doping. Higher Ce^{3+} percentage is an indicator of the formation of enhanced oxygen vacancy that might have improved the catalytic properties [260–262]. Interestingly, the core level Ce 3d XPS data of the exhausted catalysts after MOR (shown in Figure 3B.20(b)) exhibited higher abundance of Ce^{3+} concentration than the corresponding as prepared catalysts and the highest occurrence of Ce^{3+} was observed in the exhausted $Ce_{0.6}Zr_{0.35}Ni_{0.05}O_{2-\delta}$. During the MOR process, where a positive potential promotes oxidation, the reduction of $Ce^{4+} \rightarrow Ce^{3+}$ must occur alongside parallel oxidation reactions. These parallel oxidation reactions can be attributed to the evolution of lattice oxygen (O_2- $\rightarrow \frac{1}{2}\ O_2 + 2e^-$) in or/and the oxidation of

$Ni^{2+} \rightarrow Ni^{3+}$ in Ni-doped materials. Due to the high reducibility of ceria in the ceria-zirconia solid solution the evolution of lattice oxygen is a plausible phenomenon. In fact, the evolution of lattice oxygen enables CO oxidation, making the catalysts more tolerant to CO [43, 263].

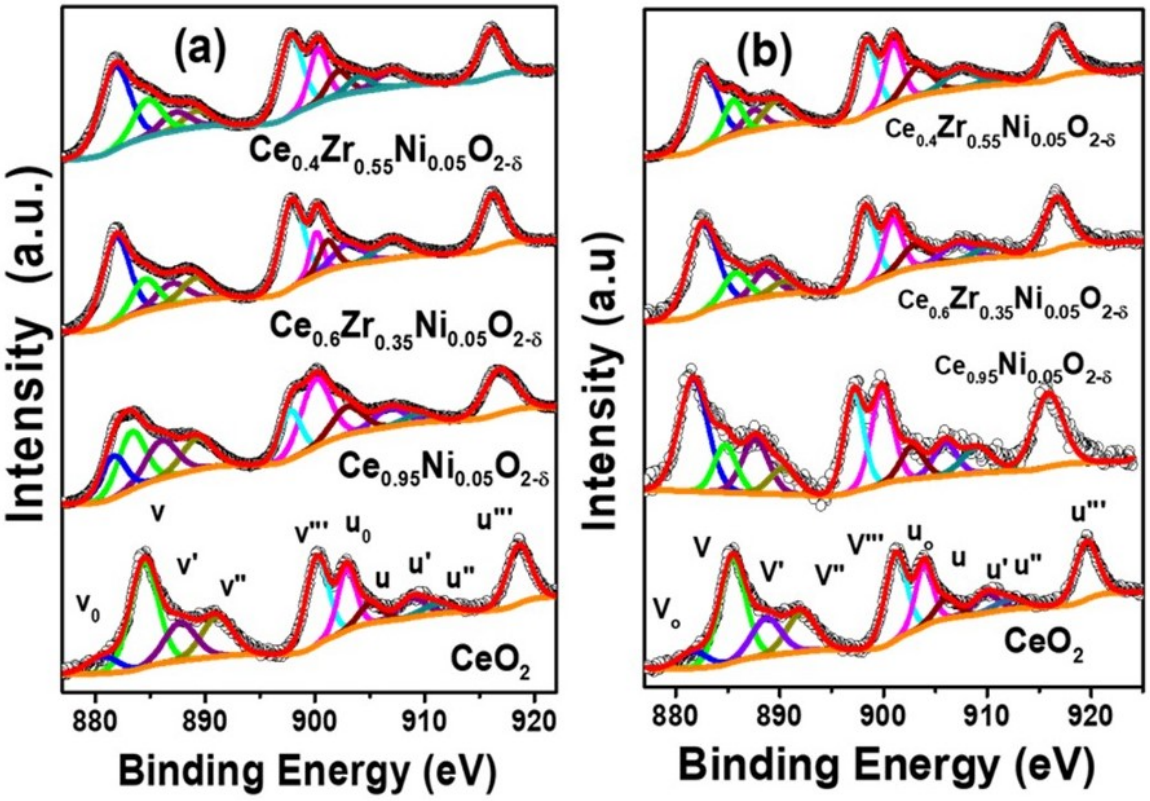

FIGURE 3B.20: Ce 3d core level spectra (a) before and (b) after MOR

In order to investigate the oxidation state of Ni and its subsequent changes during the MOR process, we conducted mapping of the Ni 2p core level XPS for as-prepared and exhausted samples of $Ce_{0.95}Ni_{0.05}O_{2-\delta}$, $Ce_{0.6}Zr_{0.35}Ni_{0.05}O_{2-\delta}$ and $Ce_{0.4}Zr_{0.55}Ni_{0.05}O_{2-\delta}$ (Figure 3B.21). The Ni 2p spectra of both the as-prepared and exhausted catalysts exhibited distinct Ni $2p_{3/2}$ and Ni $2p_{1/2}$ components. The deconvoluted spectra confirmed the presence of Ni^{2+} (855.1 and 872.5 eV) and Ni^{3+} (857.1 eV and 874.2 eV) species [264, 265]. Additionally, two satellite peaks were observed at higher binding energies of 861.3 and 865.3 eV [265]. Table 3B.6 revealed a gradual increase in Ni^{3+} content from 22.4% to 49.7% with increasing Zr doping in the as-prepared catalysts. Notably, there was an enhancement in Ni^{3+} content after the MOR process in the exhausted catalyst. It can be inferred that the reduction of $Ce^{4+} \rightarrow Ce^{3+}$ simultaneously oxidized $Ni^{2+} \rightarrow Ni^{3+}$ during MOR under positive potential. The formation of Ni^{3+} species acted as active sites for the generation of the Ni - OOH layer and subsequent MOR reactions.

Among the solid solutions, this phenomenon was apparently most prominent over the optimized $Ce_{0.6}Zr_{0.35}Ni_{0.05}O_{2-\delta}$ catalyst.

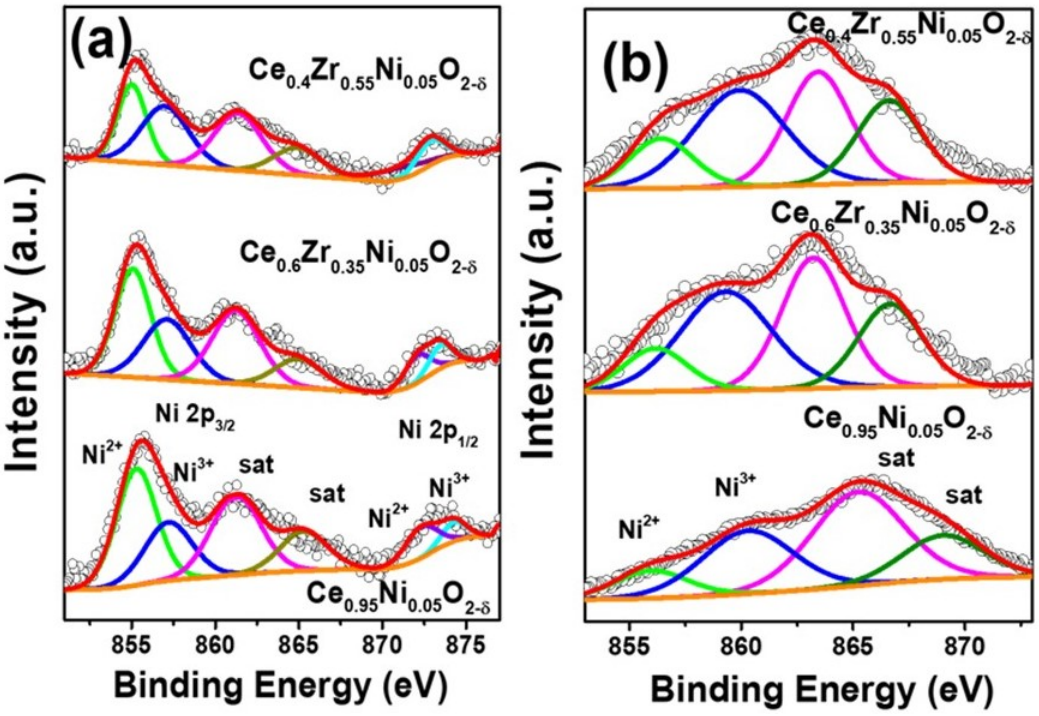

FIGURE 3B.21: Ni 2p core level spectra (a) before and (b) after MOR

Figure 3B.22 displays the deconvoluted O 1s spectra of the as-synthesized fresh solid solution catalysts. The three typical peaks at binding energies of 529.7, 531.9, 533.4 eV correspond to the lattice oxygen (O_L), surface oxygen vacancy (O_S), and hydroxyl species of surface-adsorbed water molecules (O_W) respectively [266, 267]. Apparently, the introduction of bivalent Ni^{2+} resulted in the significant increase of oxygen vacancy (O_S) due to the charge compensation. The O 1s core level spectra of the post MOR exhausted catalysts exhibited four distinct peaks (Figure 3B.22(b)). The peaks at 529.5, 531.9, 533.4, 535.8 correspond to O_L, O_S, Ni - OOH and O_W, respectively. The extra peak labelled as Ni - OOH corresponds to the intermediate that is formed during MOR [268, 269]. There was a minute shift of the peak corresponding to O_W and Ni - OOH to a higher binding energy, probably due to the change in the electronic environment caused by the higher doping of Zr in the CeO_2 lattice. It was interesting to observe the decrease in the surface concentration of lattice oxygen (O_L) after the MOR reaction (Table 3B.6). This corroborates our claim that the reduction of $Ce^{4+} \rightarrow Ce^{3+}$ during MOR is not only facilitating the parallel oxidation of $Ni^{2+} \rightarrow Ni^{3+}$ but also helping the evolution of lattice oxygen, and thereby reducing the surface concentration of O_L. Presence of optimal concentration of Zr in the lattice of $Ce_{0.6}Zr_{0.35}Ni_{0.05}O_{2-\delta}$ apparently exhibited the maximum extent of Ce^{4+} reduction

vis à vis Ni^{2+} oxidation and oxygen evolution. The evolution of lattice oxygen during MOR increased surface oxygen vacancy, promoting the formation of the key intermediate species Ni - OOH. The evolved oxygen likely aids in the oxidation of the intermediate CO, thus making the catalyst CO-tolerant.

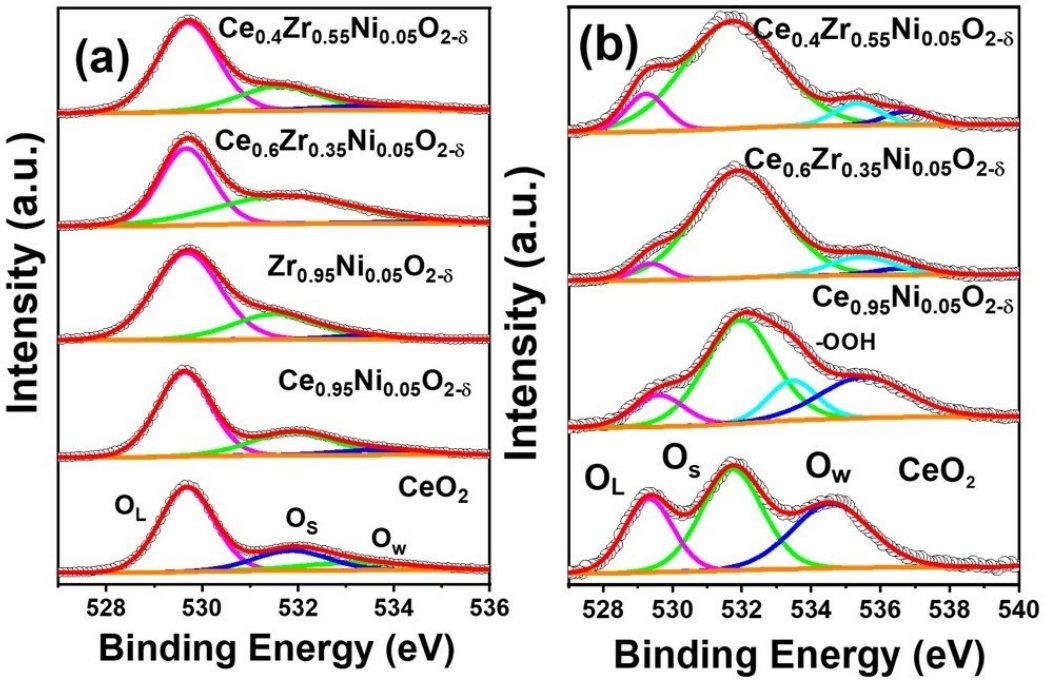

FIGURE 3B.22: O 1s core level spectra (a) before and (b) after MOR

TABLE 3B.6: Concentration (%) of Ce^{3+}, and Ni^{3+} before and after MOR

Catalysts	**Ce^{3+} (%)**		**Ni^{3+} (%)**		**Lattice oxygen (%)**	
	Before	After	Before	After	Before	After
CeO_2	18.4	27.9			30.2	19.4
$Ce_{0.95}Ni_{0.05}O_{2-\delta}$	20.5	46.0	22.4	62.6	65.6	15.7
$Ce_{0.6}Zr_{0.35}Ni_{0.05}O_{2-\delta}$	41.0	49.0	42.5	68.7	51.2	5.0
$Ce_{0.4}Zr_{0.55}Ni_{0.05}O_{2-\delta}$	41.6	48.7	44.3	63.2	58.2	11.2

The above discussion leads to the fundamental property of high reducibility of ceria-zirconia solid solution [270–272]. To corroborate the facile reduction of $Ce^{4+} \rightarrow Ce^{3+}$ accompanied by the evolution of lattice oxygen (as indicated by the XPS analyses), we probed the reducibility of Ce^{4+} in the pristine and the solid solutions with the help of H_2-TPR experiments. Figure 3B.23 shows the H_2 TPR over CeO_2, $Ce_{0.95}Ni_{0.05}O_{2-\delta}$, $Ce_{0.6}Zr_{0.35}Ni_{0.05}O_{2-\delta}$, and $Ce_{0.4}Zr_{0.55}Ni_{0.05}O_{2-\delta}$. Three distinct peaks were observed at 511.0, 639.0 and 934.6 °C labelled as u, v and w, respectively over pristine CeO_2. The low-temperature peaks labelled as u and v corresponds to Ce^{4+} to Ce^{3+} reduction in the surface, while w is assigned to bulk reduction of Ce^{4+} to Ce^{3+} [273–275]. On the contrary, $Ce_{0.95}Ni_{0.05}O_{2-\delta}$ exhibited three peaks at 395, 480 and 934.6 °C denoted as

u_1, v and w corresponding to the reduction of Ni^{2+}, surface Ce^{4+} and bulk Ce^{4+}. Apparently, the introduction of Ni in the CeO_2 matrix promotes the reducibility of the material at lower temperatures. Notably, the consumption of H_2 further increases at lower temperatures over $Ce_{0.6}Zr_{0.35}Ni_{0.05}O_{2-\delta}$, and $Ce_{0.4}Zr_{0.55}Ni_{0.05}O_{2-\delta}$ indicating a very high reducibility of the solid-solution with the introduction of Zr in the lattice. The amount of H_2 consumed by the pristine CeO_2 was 0.128 mmol g^{-1}, whereas the H_2 consumption over the optimized catalysts was found to be 0.320 mmol g^{-1}.

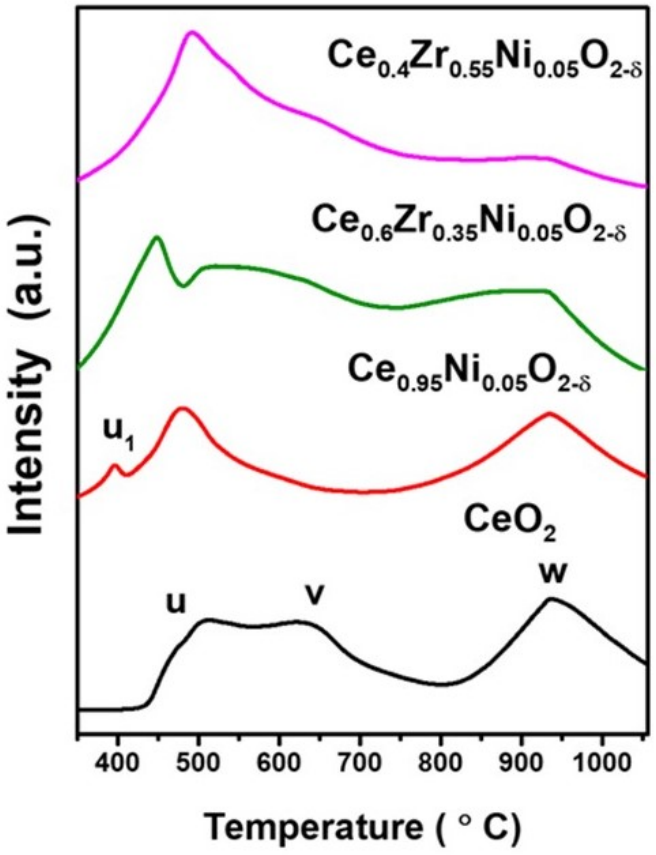

FIGURE 3B.23: H_2 TPR over CeO_2, $Ce_{0.95}Ni_{0.05}O_{2-\delta}$, $Ce_{0.6}Zr_{0.35}Ni_{0.05}O_{2-\delta}$, and $Ce_{0.4}Zr_{0.55}Ni_{0.05}O_{2-\delta}$

Gaseous CO, an intermediate oxidation product of methanol during MOR, tends to adsorb and block the catalyst active sites, acting as a poison. A favorable oxidation of adsorbed CO to gaseous CO_2 would keep the active site clean. We observed that the increased reducibility of the solid-solution catalysts played a crucial role in facilitating lattice oxygen evolution within the positive potential window. The evolved oxygen may react with the adsorbed CO to enhance the material's CO tolerance. To investigate this phenomenon, a series of CO stripping and CO oxidation experiments were conducted in an inert atmosphere on $Ce_{1-x-y}Zr_xNi_yO_{2-\delta}$, spanning

a potential range from 1.20 to 1.75 V vs RHE. From the CO stripping experiment it is clearly evident that $Ce_{0.6}Zr_{0.35}Ni_{0.05}O_{2-\delta}$ exhibited the highest CO oxidation on its surface at potential of 1.2 V vs RHE (Figure 3B.24(a)). Correspondingly, the oxidation of CO was carried out and the percentage of CO oxidation over CeO_2, $Ce_{0.6}Zr_{0.35}Ni_{0.05}O_{2-\delta}$, and $Ce_{0.4}Zr_{0.55}Ni_{0.05}O_{2-\delta}$ as a function of anodic potential (significantly lower than the potential required for oxygen evolution from water) is plotted in Figure 3B.24(b). Interestingly, $Ce_{0.6}Zr_{0.35}Ni_{0.05}O_{2-\delta}$ exhibited the highest degree of CO oxidation, surpassing the other three materials. The ease of lattice oxygen evolution, facilitated by the increased reducibility of Ce^{4+}, contributes significantly to the highest CO oxidation of $Ce_{0.6}Zr_{0.35}Ni_{0.05}O_{2-\delta}$. Based on these observations, the overall MOR over $Ce_{0.6}Zr_{0.35}Ni_{0.05}O_{2-\delta}$ can be expressed as:

$$Ce_{0.6}Zr_{0.35}Ni_{0.05}O_{2-\delta} + xCH_3OH + H_2O \rightarrow Ce^{4+}_{0.6-z}Ce^{3+}_{z}ZrNiO_{2-\delta} + xCO_2 + 3xH_2(\delta' > \delta) \quad (3B.9)$$

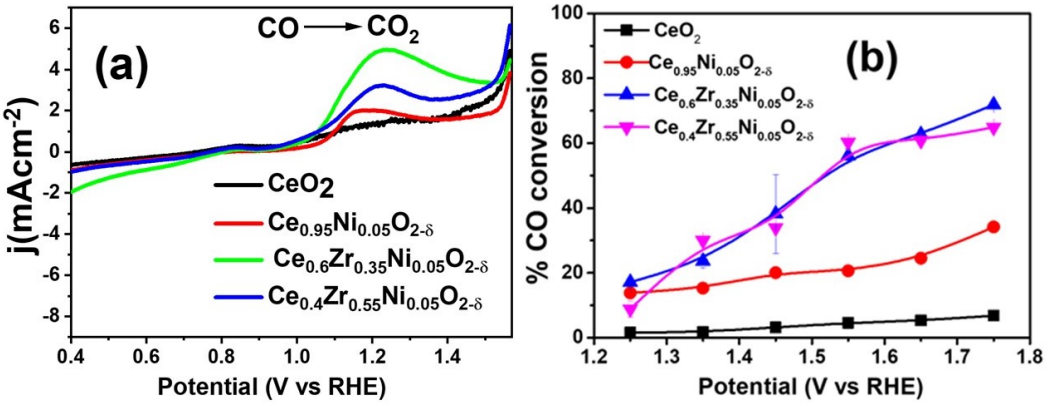

FIGURE 3B.24: (a) CO stripping and (b) Percentage of CO conversion at different potentials of CeO_2, $Ce_{0.95}Ni_{0.05}O_{2-\delta}$, $Ce_{0.6}Zr_{0.35}Ni_{0.05}O_{2-\delta}$, and $Ce_{0.4}Zr_{0.55}Ni_{0.05}O_{2-\delta}$

3B.4 Conclusion

Atomistically dispersed Ni in $Ce_{1-x-y}Zr_xNi_yO_{2-\delta}$ (x = 0.35, 0.55 and y=0.05) synthesized using the solution combustion method exhibited a pure fluorite phase upon crystallization with significant oxygen vacancies. The oxygen vacancies contributed to the high electrochemical surface area of the materials. The combustion synthesized solid-solutions possessed a nanocrystalline structure with a large surface area and porosity. Among the compositions tested, $Ce_{0.6}Zr_{0.35}Ni_{0.05}O_{2-\delta}$ demonstrated the highest electrocatalytic activity for methanol oxidation

with a current density of 13.12 mA cm^{-2}. The kinetic evaluation indicated that the rate-determining step for methanol oxidation involved the cleavage of the C-H bond, which occurred via diffusion control on $Ce_{0.6}Zr_{0.35}Ni_{0.05}O_{2-\delta}$. The overall reaction followed a half-order rate law with an activation energy of 21.1 kJ mol^{-1} over the optimized catalyst $Ce_{0.6}Zr_{0.35}Ni_{0.05}O_{2-\delta}$. Detailed ex-situ spectroscopic analysis revealed that $Ce_{0.6}Zr_{0.35}Ni_{0.05}O_{2-\delta}$ exhibited a facile $Ce^{4+} \rightarrow Ce^{3+}$ reduction along with parallel $Ni^{2+} \rightarrow Ni^{3+}$ oxidation and lattice oxygen evolution. The formation of Ni^{3+} as well as evolution of lattice oxygen during MOR increased surface oxygen vacancy, and thereby promoted the formation of the key intermediate species Ni - OOH to facilitate the sluggish kinetics of methanol oxidation. The evolved oxygen likely aided the oxidation of the intermediate CO, thus making the catalyst CO tolerant. Overall, these findings underscore the significance of electronic interactions between the active site and the support, as well as the involvement of lattice oxygen, in realizing a future "Methanol Economy".

Chapter 4

Engineering lattice strain in Co - doped $NiMoO_4$ for boosting Methanol Oxidation Reaction

4.1 Introduction

Methanol, the fuel used in DMFCs, boosts ease of storage, transport, and refilling, offering an energy density surpassed only by hydrogen. Generally, in fuel cells, methanol oxidizes over electrodes to yield hydrogen and CO_2 greenhouse gas. However, the primary hurdle to implementing DMFC technology in large-scale applications stems from inherent limitations associated with the MOR at the anodic compartment, including frequently sluggish kinetics and low power density. On a different note, the coupling of the electrochemical HER with MOR represents an innovative approach to achieve energy-efficient hydrogen generation, along with the co-generation of the valuable formate or formic acid. By integrating selective MOR with water electrolysis and reducing the voltage required for water electrolysis, it becomes possible to enhance the efficiency of hydrogen generation at the cathode, while simultaneously generating high-value products at the anode, potentially substituting CO_2. Therefore, designing and developing novel catalytic electrode materials is clearly an important parameter for effective, durable and efficient MOR activity. Noble metals, particularly electrocatalysts based on Pt and Pd, are commonly employed compounds known for their strong catalytic activity in MOR. However, despite their significant potential for sustainable energy conversion, their widespread use is hindered by their

expensive price tag and scarcity, structural and chemical instability and by - products of CO intermediate poisoning. Among transition metal - based catalysts utilized for the MOR to switch from noble metals, nickel-based materials demonstrate both high catalytic activity and cost - effectiveness. Studies have shown that Ni^{2+} tends to be converted to the high - valence Ni^{3+} during the reaction process to form the Ni^{2+}/Ni^{3+} coexistence generating highly active surface-intermediate species referred to as Ni - OOH for electrocatalytic oxidation of methanol [276–279]. It is well known that the combination of two or more transition metal oxide can exhibit a synergistic contribution in catalytic activity towards methanol oxidation by bifunctional mechanism of MOR and resistance to CO poisoning which is much better than simple individual oxides ref. Nanostructured nickel molybdates are one such example that is ideal for anode materials in MOR. Doping of the Fe/Co/Mn atom into the $NiMoO_4$ nanostructure were proven to improve the catalytic activity by creating lattice strain. Lattice-strain engineering via lattice compression or tension is an effective way to enhance electrocatalytic activity by manipulating surface electron configuration [280, 281]. This method can alter the intrinsic interatomic distances as well as modulate the electronic structure of the active centre, affecting the binding energy of adsorption and in turn the catalytic reaction kinetics. One method for artificial introduction of strain by traces in the system is by doping of heteroatom. Heteroatoms alter interatomic bond lengths by either stretching or compressing them through competing coordination. This process induces local lattice strain within the nanomaterial, precisely adjusting both the electronic structure of the metal surface and promoting the intrinsic activity of the reaction site. In this work, $Ni_{1-x}Co_xMoO_4$ nano rods were synthesized hydrothermally and characterized considering that the doping of Co^{2+} ions play a significant role in MOR via creation of lattice strain in the system. The optimal doping of Co doping resulted in a mixture of α and β-$NiMoO_4$, which not only induced the maximum lattice strain but also facilitated the formation of Ni^{3+} and oxygen vacancies, the crucial species for the generation of Ni - OOH intermediates during MOR.

4.2 Materials and Methods

4.2.1 Synthesis of $Ni_{1-x}Co_xMoO_4$ (x = 0, 0.1, 0.3, 0.5)

$Ni_{1-x}Co_xMoO_4$ was prepared by one step facile hydrothermal synthesis. In this typical synthesis of $NiMoO_4$, 2 mmol of $Ni(NO_3)_2 \cdot 6H_2O$ (SD fine, 99%), Na_2MoO_4 (SD Fine Chem Limited, India) were dissolved in 30 mL of DI water and stirred for 30 min to obtain a homogeneous

mixture. The solution was then transferred to 50 ml Teflon lined stainless steel autoclave and maintained at 160 °C for 15 h in oven. After naturally cooling to room temperature, the obtained precipitate was washed well with a copious amount of deionized water and then dried overnight at 80 °C in vacuum oven to obtain a dehydrated sample. The powder was grinded well and calcined at 450 °C for 2h. For the Co doped sample, to the abovementioned procedure, various concentrations of $Co(NO_3)_2 \cdot 6H_2O$(99%, SRL chemicals) (0.2 mmol, 0.6 mmol and 1 mmol) were added, resulting in compounds with $Ni_{1-x}Co_xMoO_4$ stoichiometry [282, 283].

4.2.2 Structural, Surface and Electronic Characterization

The actual atomic ratio of the synthesized $Ni_{1-x}Co_xMoO_4$ materials was studied using ED-XRF with the help of an Epsilon 1, PAN analytical instrument. Phase purity and crystalline nature of the as-prepared samples were analysed by XRD using a Rigaku Ultima IV XRD with Cu Kα radiation ($\lambda = 1.5418$ Å) at a scan rate of 0.4° min^{-1} and step size of 0.01° in the 2θ range between 10° - 60°. The average nanocrystalline diameters (D) were calculated from the broadening of the highest peak using Scherrer's formula,

$$D = \frac{0.9\lambda}{B\text{Cos}\theta} \tag{4.1}$$

where β is the full-width at half-maximum, λ is the wavelength of the radiation, and θ is the corresponding angle. The surface morphology was characterised by high-resolution scanning electron microscopy with FE-SEM, (FEI-ApreoS) at 30 kV acceleration. To probe the crystal structure and lattice strain created in the catalysts, HR-TEM (JEOL-JEM 2100F) was further used. The microscope was operated with an accelerating potential of 200 kV with a point resolution of 0.19 nm and a line resolution of 0.1 nm. The sample for the analysis was prepared by dispersing about 1–2 mg in methanol and drop-casting over a copper grid (200 mesh). XPS were collected to study the surface composition, elemental oxidation state, and bonding with the help of a Thermo Scientific K-α surface-analysis spectrometer housing Al Kα as the X-ray source (1486.6 eV). The instrument was operated at 72 W. The base pressure at the analyzing chamber was maintained at 5×10^{-9} mbar. The data profiles were subjected to a nonlinear least-squares curve fitting program with a Gaussian–Lorentzian production function and processed with Avantage software. The BE of all XPS data was calibrated versus the standard C 1s peak at 284.85 eV. Microtrac BEL Corp mini-II surface area analyzer was employed to study the surface area of the synthesized materials. The samples were degassed in vacuum at 200 °C for 2 h before

the N_2 sorption measurements at 77 K. BET equation was used to estimate the specific surface area.

4.2.3 Computational Details

The geometry optimization and electronic structure calculations of the $Ni_{1-x}Co_xMoO_4$ was performed using plane-wave basis with plane-wave energy cutoff of 500 eV and GGA for exchange-correlation energy functional in the version of PBE [284–286]. For all the calculation, 4×4×4 k-point mesh with Monkhorst-pack scheme were used.

4.2.4 Electrocatalytic Oxidation of Methanol

Electro-oxidation of methanol was evaluated in a conventional three-electrode glass cell equipped with $Ni_{1-x}Co_xMoO_4$ modified glassy carbon electrode as the working electrode, Hg/HgO in 1 M KOH electrode as the reference electrode, and a Pt wire as the counter electrode. The working electrode was prepared by drop-casting the catalyst ink onto a GCE (3 mm, 0.07 cm^2 area). Before drop casting the working electrode was polished with 0.05µm alumina slurry. The catalyst ink was prepared by dispersing the physical mixture of 5 mg of the synthesized catalyst and 2 mg of carbon black in 1 mL of methanol and 10 µL of Nafion solution. Aqueous solutions of 0.5 M NaOH served as the electrolyte. MOR was evaluated using cyclic voltammetric studies (CV) in 0.5 M NaOH and 0.5 M MeOH. Stability study was carried out using CA at MOR potential and cycle studies. Hydrogen Evolution Reaction HER was also studied using LSV and CA. In all measurements, potential of Hg/HgO is converted to RHE in 0.5 M NaOH according to the following equation: $E_{RHE} = E_{Hg/HgO} + 0.059 \times pH + 0.098$. The liquid products after CA were analysed using ^1H NMR (Bruker AV NEO, 400 MHz). For this, about 0.4 mL of electrolysis solution, 0.1 mL of D_2O, and 5 mg of 4-nitrophenol (as an internal standard) were added into the NMR tube for identifying the product. The ECSA was determined by conducting double - step chronoamperometric experiments, wherein the electrode potential was swept between non-faradic potential (1.0 V vs RHE) and faradic potential (1.8 V vs RHE). This was done in the presence of an electrolyte comprising 0.1 M potassium ferricyanide and 0.1 M KCl. This potential is sufficient to oxidize the $[Fe(CN)_6]^{4-}$ (aq) to $[Fe(CN)_6]^{3-}$ (aq). Area under the charging - discharging curve was calculated, and was accordingly plotted with time to obtain

the ECSA by using the following Cottrell equation.

$$Q = 2nFAD^{1/2}C_o t^{1/2}\pi^{-1/2} \tag{4.2}$$

where Q = charge in coulomb F = Faraday constant n = Number of electrons being transferred A = Area of electrode (cm^2) D = Diffusion coefficient of $[K_3Fe(CN)_6]$ (7.6×10^{-6} cm^2 s^{-1}) t = time (s) C_o = concentration of $K_3Fe(CN)_6$ (mol cc^{-1}). EIS study was carried out at 1.77 V vs RHE to study the electron transfer for MOR over a frequency range of 500 kHz to 0.1Hz with a sinusoidal excitation signal of 10 mV with the conventional three-electrode system in an alkaline mixture of 0.5 M MeOH and 0.5 M NaOH at 10 mV s^{-1} using a Biologic Sp-150 electrochemical workstation.

4.3 Results and Discussion

4.3.1 Structure, Surface and Electronic Properties of Catalysts

The structural information of the hydrothermal synthesized $Ni_{1-x}Co_xMoO_4$ was probed by powder XRD. The representative XRD patterns as shown in Figure 4.1(a) indicate that $NiMoO_4$ crystallized in monoclinic phase with space group c12/m1 (JCPDS- 33-0948). No secondary phases such as NiO or MoO_3 were found in the XRD pattern, which infers the formation of phase pure compound. With the increase of the Co doping amount, the characteristic peaks belonging to α - $NiMoO_4$ broadened and slightly became amorphous in nature. As $NiMoO_4$bis doped with Co^{2+}, an extra peak at $2\theta = 26.5°$(♦) was observed corresponding to (002) plane of β - $NiMoO_4$ [287–289]. The intensity of (002) plane gradually increased with Co doping, and $Ni_{0.5}Co_{0.5}MoO_4$ exhibited the maximum formation of β- $NiMoO_4$ among the synthesized catalysts. From the structural point of view, α - $NiMoO_4$ and β-$NiMoO_4$, both exhibit monoclinic structure, but in the α-form, Ni^{2+} and Mo^{6+} ions both occupy the octahedral sites $[MoO_6]$, while in the β - form, Ni^{2+} still in octahedral sites, however Mo^{6+} ions are in the tetrahedral sites $[MoO_4]$ [290, 291]. Figure 4.1(b) shows the percentage composition of α and β phases of $NiMoO_4$ with Co doping. The actual bulk concentration of the elements derived from the ED-XRF data matched well with the theoretically calculated values (Table 4.1). The crystallite size of pristine $NiMoO_4$ calculated from the Scherrer's formula was found to be 36.2 nm, whereas $Ni_{0.9}Co_{0.1}MoO_4$, $Ni_{0.7}Co_{0.3}MoO_4$ and $Ni_{0.5}Co_{0.5}MoO_4$ exhibited reduction in its crystallite size to 32.0, 28.4 and

27.9 nm, respectively. The co-existence of the mixed phases due to the aliovalent doping of Co played a pivotal role in creating lattice strain in the system. The presence of micro strain (ε) was calculated using the equation $\varepsilon = B/4\tan\theta$, where B is the full-width at half-maximum, and θ represents the corresponding diffraction angle. It was determined that the micro strain increased from 3.8 μm/m in pristine $NiMoO_4$ to a maximum of 4.6 μm/m in $Ni_{0.7}Co_{0.3}MoO_4$. However, further doping of Co in $Ni_{0.5}Co_{0.5}MoO_4$ led to a slight reduction in micro strain to 4.5 μm/m. The variation of micro strain with Co doping is also presented in Figure 4.1(b).

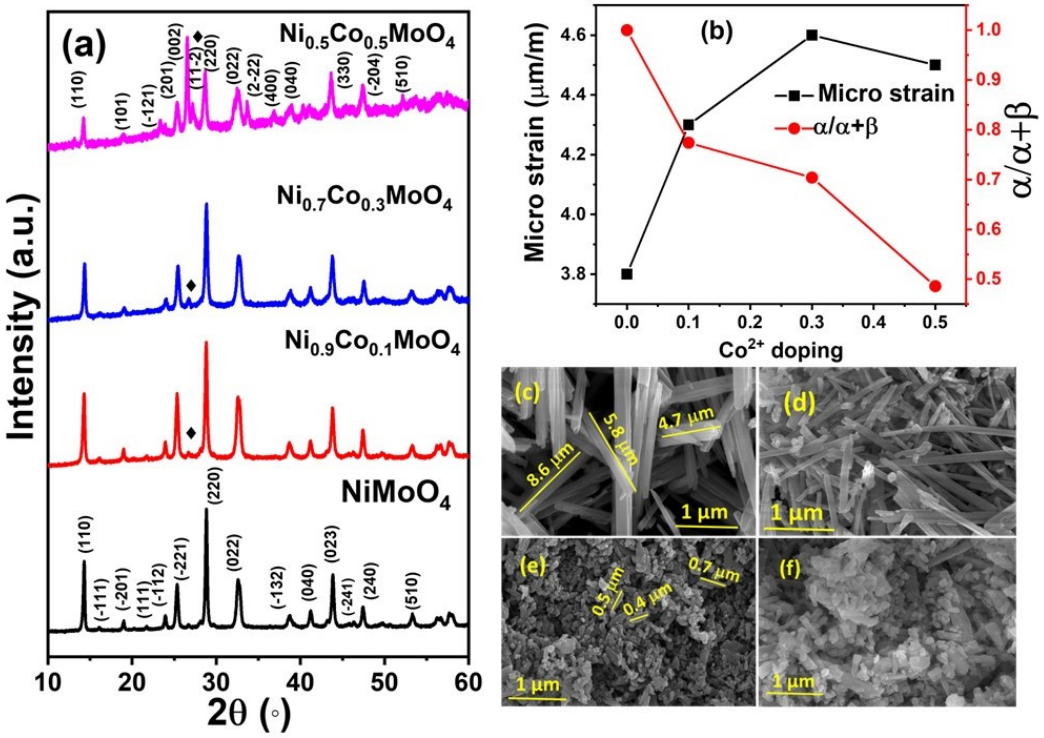

FIGURE 4.1: (a) XRD pattern if $NiMoO_4$ and $Ni_{1-x}Co_xMoO_4$ (b) Variation of micro strain and phase ratio with Co^{2+} doping and (c,d,e,f) FE-SEM images of (c) $NiMoO_4$, (d) $Ni_{0.9}Co_{0.1}MoO_4$, (e) $Ni_{0.7}Co_{0.3}MoO_4$, (f) $Ni_{0.5}Co_{0.5}MoO_4$

TABLE 4.1: ED-XRF of $NiMoO_4$ and $Ni_{1-x}Co_xMoO_4$

Sample	**Calculated (%)**			**XRF (%)**		
	Ni	Mo	Co	Ni	Mo	Co
$NiMoO_4$	37.9	62.0		42.0	57.9	
$Ni_{0.9}Co_{0.1}MoO_4$	41.2	55.8	3.0	34.1	62.0	3.8
$Ni_{0.7}Co_{0.3}MoO_4$	26.5	60.0	13.5	26.5	62.0	11.4
$Ni_{0.5}Co_{0.5}MoO_4$	20.5	54.9	24.5	24.8	62.0	24.9

The morphological features of the pristine and the doped materials were analysed by FE-SEM. The FE-SEM micrographs in Figure 4.1(c-f) shows the nano-structural features of $Ni_{1-x}Co_xMoO_4$. The pristine $NiMoO_4$ exhibited long rod-like morphology with an average length

of ∼5.6 µm as seen in Figure 4.1(c). However, the average length of the rods decreased with increasing doping of Co, and it was found to be ∼0.5 µm over $Ni_{0.7}Co_{0.3}MoO_4$ (Figure 4.1(d)). The similar features have also been observed earlier [292–294]. The rod like morphology crumbled with further increase in Co doping, and $Ni_{0.5}Co_{0.5}MoO_4$ exhibited agglomerated particles (4.1(f)). The EDAX mapping in Figure 4.2 demonstrates the homogeneous distribution of Co in $NiMoO_4$ matrix.

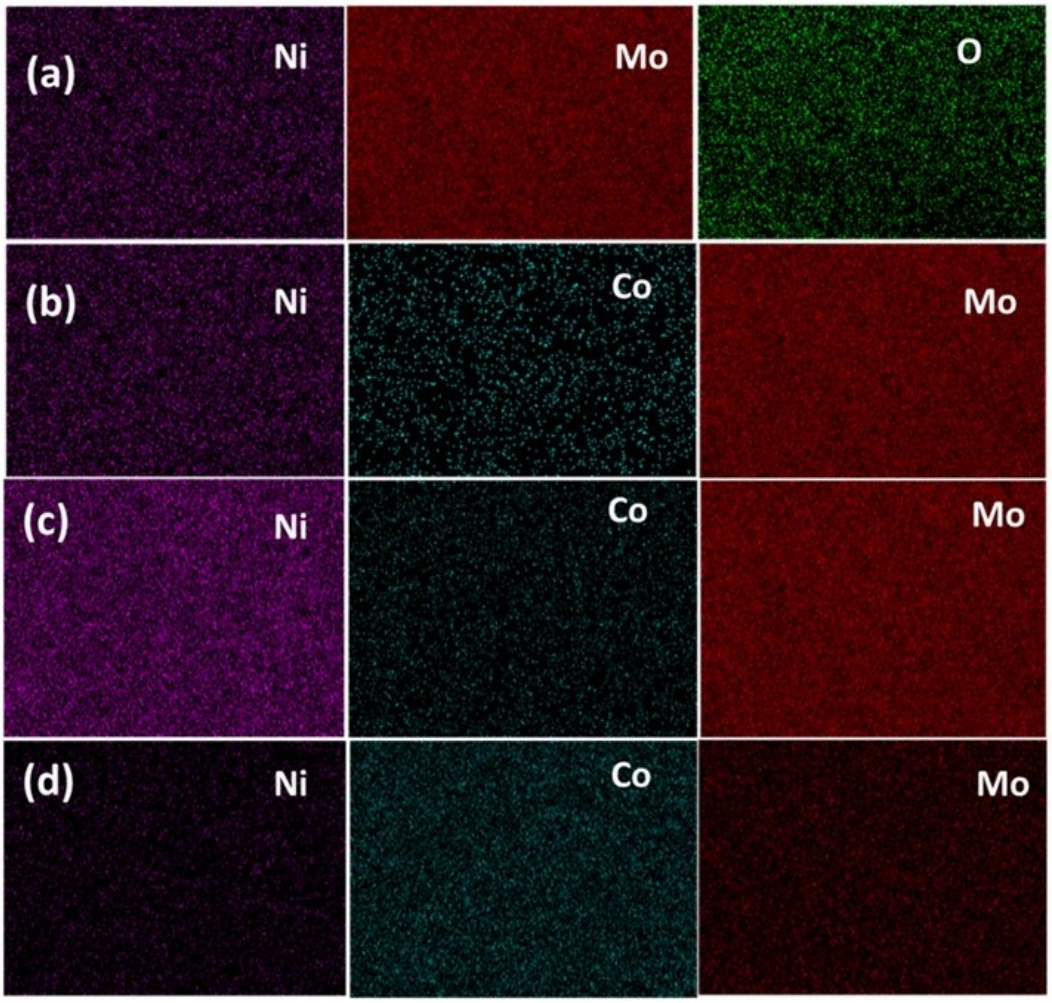

FIGURE 4.2: EDAX Mapping of (a) $NiMoO_4$ (b) $Ni_{0.9}Co_{0.1}MoO_4$ (c) $Ni_{0.7}Co_{0.3}MoO_4$ (d) $Ni_{0.5}Co_{0.5}MoO_4$

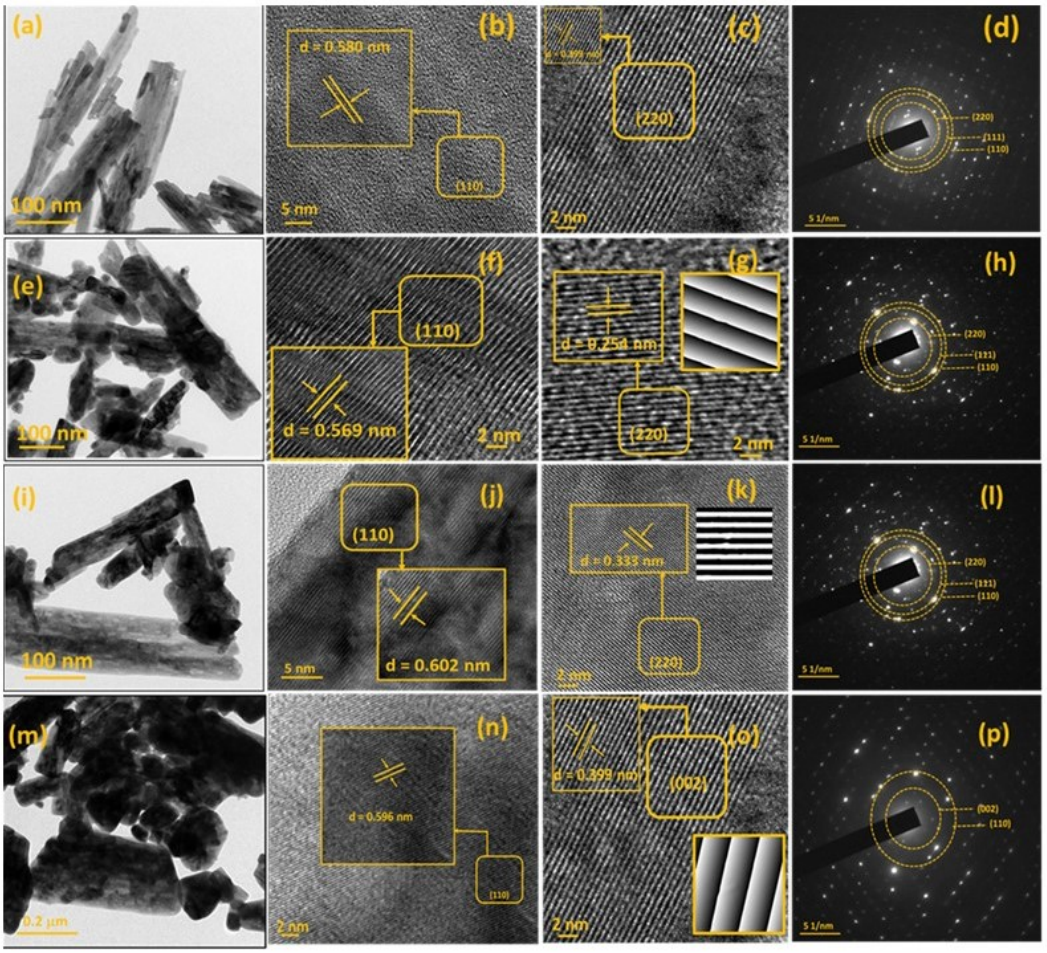

FIGURE 4.3: HR-TEM images and SAED pattern of (a-d) $NiMoO_4$ (e-h) $Ni_{0.9}Co_{0.1}MoO_4$ (i-l) $Ni_{0.7}Co_{0.3}MoO_4$ (m-p) $Ni_{0.5}Co_{0.5}MoO_4$

The nano structural features and the lattice strain in the system created by Co doping was investigated by HR-TEM analysis as shown in Figure 4.3. The HR-TEM micrographs of $NiMoO_4$ in Figure 4.3(a) confirmed the presence of irregular long rods as depicted in FE-SEM images. The interplanar distance of 0.399 and 0.580 nm corresponding to (220) and (110) planes calculated from the fringe distances shown in Figure 4.3(b, c) confirms the monoclinic α phase of pristine $NiMoO_4$. SAED pattern in Figure 4.3(d) also corroborates the same. Interestingly, a minor shrink in the (220) and (110) interplanar distances were observed with aliovalent doping of smaller Co in $Ni_{0.9}Co_{0.1}MoO_4$ and $Ni_{0.7}Co_{0.3}MoO_4$ (Figure 4.3(f, g) and 4.3(j, k)). The nano rod like morphology of the particles (Figure 4.3(a, e, i)) was disrupted to agglomerated one (Figure 4.3(m)) with gradual doping of Co as was also observed in FE-SEM micrographs. The presence of the β phase in $Ni_{0.5}Co_{0.5}MoO_4$ was confirmed by the observation of (002) plane with a spacing of 0.35 nm as shown in Figure 4.3(n, o) [288]. The corresponding SAED patterns in Figure 4.3(p) also verified the presence of these lattice planes from α and β phases.

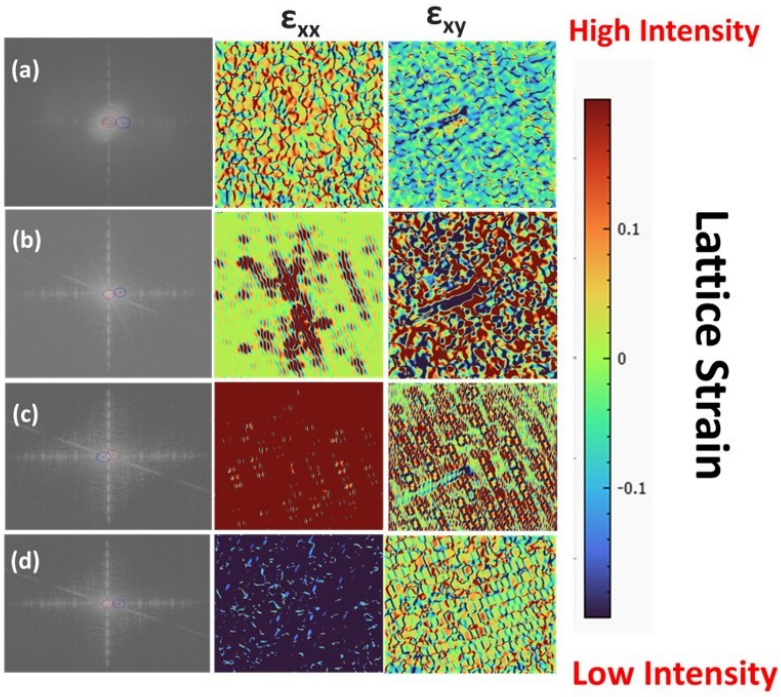

FIGURE 4.4: Strain distribution diagrams ε_{xx} and ε_{xy} of (a) $NiMoO_4$, (b) $Ni_{0.9}Co_{0.1}MoO_4$, (c) $Ni_{0.7}Co_{0.3}MoO_4$ and (d) $Ni_{0.5}Co_{0.5}MoO_4$

Analysis of local atomic spacing variations in HR-TEM micrographs enables the precise measurement of local strain with high spatial resolution. FFT patterns were obtained from the HR-TEM images to analyse the lattice strain in the synthesized molybdate systems. For enhanced comprehension of the structural attributes exhibited by $Ni_{1-x}Co_xMoO_4$, an investigation employing GPA of FFT was conducted utilizing high-resolution TEM imagery. The inset of the Figure 4.3(g,k and o) shows the enlarged TEM images obtained from GPA analysis which confirms the presence of strain in the lattice planes. As depicted in the Figure 4.4 the lattice manifests pronounced strain in ε_{xx} and ε_{xy} . In the image, the transition from blue to red corresponds to a strain profile in lattice from lower to higher intensity. The corresponding strain distribution diagram in Figure 4.4. shows that with the introduction of Co, the lattice strain distribution became more pronounced with $Ni_{0.7}Co_{0.3}MoO_4$ overwhelming the highest strain depicting significant colour changes in the strain field implying lattice distortion in the crystal interior. Further Co doping increased the β phase of $NiMoO_4$, however didn't exhibit prominent strain.

XPS analysis was employed to probe the surface chemical bonding and electronic states of the elements in hydrothermal synthesized $Ni_{1-x}Co_xMoO_4$. The survey spectra in Figure 4.5(a) indicate the inclusion of Ni, Co, and Mo on the surface in their expected atomic ratio. The

high-resolution Mo spectrum (Figure 4.5(b)) demonstrates that the typical spin–orbit doublet corresponding to Mo $3d_{5/2}$ and Mo $3d_{3/2}$ with binding energies of 233.1 and 236.2 eV, respectively, evidencing the prevalence of the Mo^{6+} oxidation state [295–297].

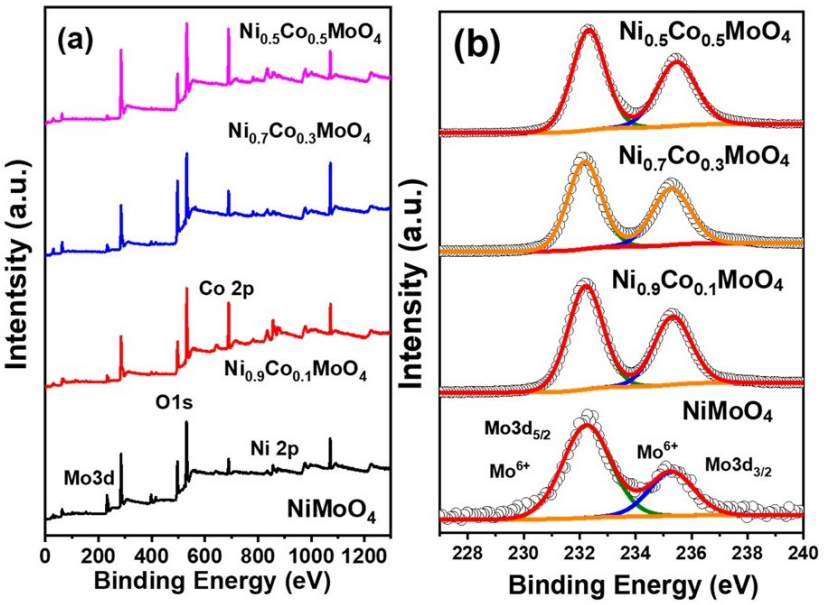

FIGURE 4.5: (a) XPS survey spectra and (b) Mo 3d core level spectra of (a)$NiMoO_4$ and (b) $Ni_{1-x}Co_xMoO_4$

The deconvoluted Ni 2p spectrum in Figure 4.6(a) revealed the simultaneous presence of Ni^{2+} and Ni^{3+}. The high-resolution deconvoluted Ni 2p spectrum shows main peaks at 855.3 and 873.3 eV corresponding to Ni^{2+} $2p_{3/2}$ and $2p_{1/2}$, whereas at 857.8 and 876.3 eV corresponding to Ni^{3+} $2p_{3/2}$ and $2p_{1/2}$, respectively [295, 298]. Interestingly, the concentration of Ni^{3+} gradually increased from 22.8% in pristine $NiMoO_4$ to 28.1% in $Ni_{0.7}Co_{0.3}MoO_4$ with increasing doping of Co. However, the Ni^{3+} concentration was diminished at maximum doping of Co in $Ni_{0.5}Co_{0.5}MoO_4$. The details are provided in Table 4.2. The core level spectra of Co 2p in Figure 4.6(b) exhibited the spin-orbit doublet of the Co $2p_{3/2}$ and Co $2p_{1/2}$ corresponding to the 3+ and 2+ oxidation states of Co. The peaks at 780.6 and 796.7 eV correspond to $2p_{3/2}$ and $2p_{1/2}$ of Co^{3+}, whereas the peaks at 783.9 and 798.7 eV corresponds to $2p_{3/2}$ and $2p_{1/2}$ of Co^{2+}, respectively. Two satellite peaks were also observed at 787.7 and 802.7 eV for the Co core level spectra.

The O1s core level spectra from the pristine and the doped oxides exhibited three distinguishable peaks at 530.6, 532.2, and 533.2 eV, ascribed to the lattice oxygen (O_L), oxygen vacancies (O_V), and lattice bound water molecules (O_w), respectively.

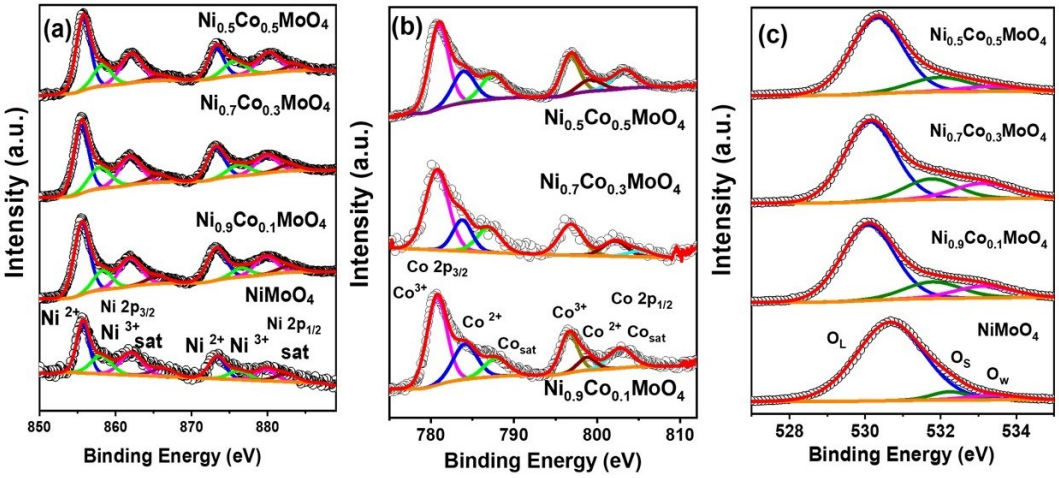

FIGURE 4.6: (a) Ni 2p (b) Co 2p and (c)O 1s core level spectra of $NiMoO_4$ and $Ni_{1-x}Co_xMoO_4$

The binding energies of the present peaks are in good agreement with the reported values [299–302]. A notable and gradual increase of oxygen vacancies was observed with the increment in Co doping. The percentage of O_V increased from 5.4% in pristine $NiMoO_4$ to the maximum of 34.2% in $Ni_{0.7}Co_{0.3}MoO_4$ (vide Table 4.2). It is worth noting that the optimal Co doping in $Ni_{0.7}Co_{0.3}MoO_4$ not only induced maximum lattice strain but also facilitated the formation of Ni^{3+} and oxygen vacancies, the crucial species for the generation of Ni - OOH intermediates during MOR.

TABLE 4.2: Ni^{3+} Concentration, Defect site oxygen species, and surface Ni - OOH concentration

Catalysts	**Ni^{3+}**	**Ov**	**Surface concentration Ni-OOH (τ^*) (mol cm^{-2})**
$NiMoO_4$	22.8	5.4	6.53×10^{-8}
$Ni_{0.9}Co_{0.1}MoO_4$	23.1	16.6	5.73×10^{-7}
$Ni_{0.7}Co_{0.3}MoO_4$	28.1	34.2	6.66×10^{-6}
$Ni_{0.5}Co_{0.5}MoO_4$	19.6	20.4	1.90×10^{-6}

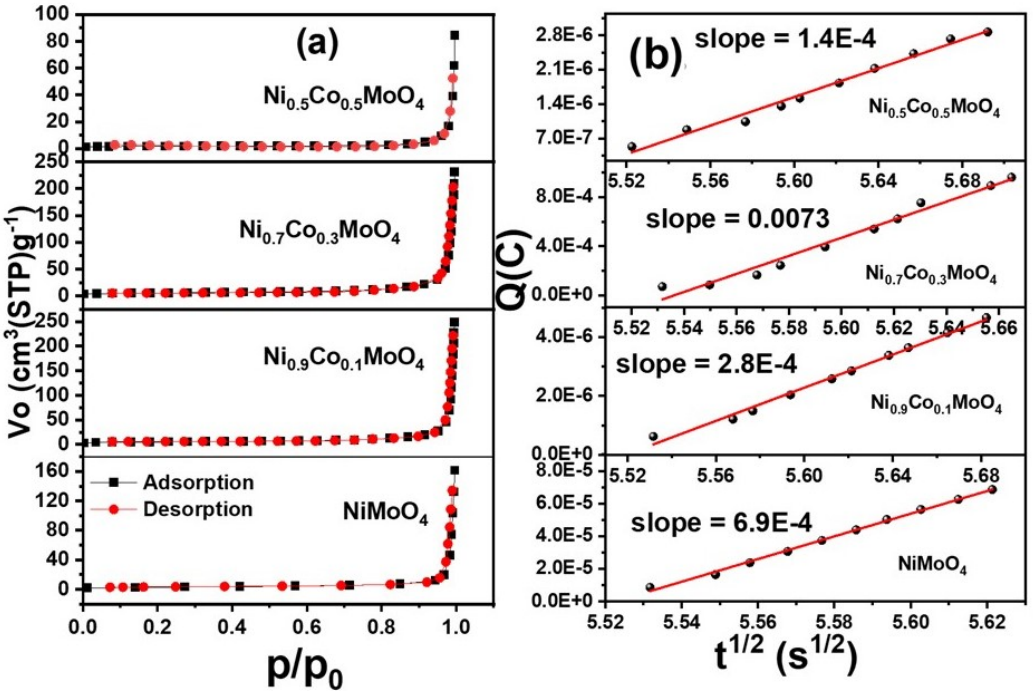

FIGURE 4.7: (a) N_2 Adsorption - desorption profile and (b) Plot of charge against time according to Cottrell equation over $NiMoO_4$, $Ni_{0.9}Co_{0.1}MoO_4$, $Ni_{0.7}Co_{0.3}MoO_4$ and $Ni_{0.5}Co_{0.5}MoO_4$

Electrocatalysis predominantly occurs at the surface interface, where a higher specific surface area and suitable pore volume play pivotal roles in enhancing electrocatalytic activity. This is attributed to the increased exposure of active sites and the reduction of ion diffusion lengths. Analysis of N_2 adsorption-desorption isotherms, as depicted in Figure 4.7(a), revealed type II isotherms with minimal hysteresis for both pristine $NiMoO_4$ and solid solutions of $Ni_{1-x}Co_xMoO_4$, suggesting a macro-porous surface nature with an average pore diameter of 55 nm. The surface area calculations presented in Table 4.3 indicate that $Ni_{0.7}Co_{0.3}MoO_4$ possesses a notably higher surface area compared to other materials. The ECSA was calculated with the help of CA studies using the Cottrell equation Apparently, $Ni_{0.7}Co_{0.3}MoO_4$ exhibited the highest ECSA compared to the other synthesized molybdates indicating a better MOR efficacy of the material (Table 4.3).

TABLE 4.3: BET and ECSA of $NiMoO_4$ and $Ni_{1-x}Co_xMoO_4$

Catalysts	**BET Surface area (m^2g^{-1})**	**ECSA (cm^2)**
$NiMoO_4$	10.01	0.23
$Ni_{0.9}Co_{0.1}MoO_4$	17.66	0.09
$Ni_{0.7}Co_{0.3}MoO_4$	18.63	2.45
$Ni_{0.5}Co_{0.5}MoO_4$	6.37	0.048

4.3.2 Electrocatalytic Oxidation of Methanol

The MOR electrocatalytic activity of pristine $NiMoO_4$ and doped $Ni_{1-x}Co_xMoO_4$ was thoroughly explored with the aid of CV in 0.5 M NaOH and 0.5 M MeOH at a scan rate of 50 mV s^{-1}. The materials were initially activated by cycling several scans in a potential window of 1.0 – 2.0 V vs. RHE in alkaline 0.5 M NaOH electrolyte solution before the MOR. The CV traces in alkaline solution without methanol in Figure 4.9 show an anodic peak at 1.25 V vs RHE corresponding to the formation -OOH species associated with oxidation of Ni^{2+} and a counter cathodic peak at 1.1 V vs RHE with the corresponding reduction process of $Ni^{3+} \rightarrow Ni^{2+}$ process in the experimental potential window [147, 277, 300, 301, 303]. As the Ni oxidation peak is masked by the oxygen evolution reaction occurring at a higher potential, CVs at a zoomed-in potential window of 0.8 to 1.8 V vs RHE is shown in the inset of Figure 4.9(a). The particular peak current density associated with the Ni - OOH formation increased with the increment in the scan rate along with an anodic shift (Figure 4.8). The peak shift was probably due to the less time available at higher scan speed for the complete formation of Ni - OOH species. The concentration of the Ni - OOH layer formed on the surface of the catalyst was quantified using the anodic and cathodic peak current densities as shown in Figure 4.8. A good linear dependence of anodic and cathodic peak current densities (j_{ap} and j_{cp}) with the square root of the sweep rate was observed. The significantly higher slope revealed a better diffusion property of the OH^-, in favour of the generation of electroactive Ni - OOH species. It was observed that $Ni_{0.7}Co_{0.3}MoO_4$ exhibited the highest formation of Ni - OOH equivalent to 6.66×10^{-6} mol cm^{-2} among all the catalysts (Table 4.2). Interestingly, the Ni^{2+}/Ni^{3+} redox peak, which was at 1.41 V vs RHE over $NiMoO_4$ reduced to 1.25 V vs RHE over $Ni_{0.7}Co_{0.3}MoO_4$. The presence of lattice strain due to the Co doping in $NiMoO_4$ might have facilitated the extent of peroxidation of Ni^{2+} at a lower potential for the formation of Ni - OOH species.

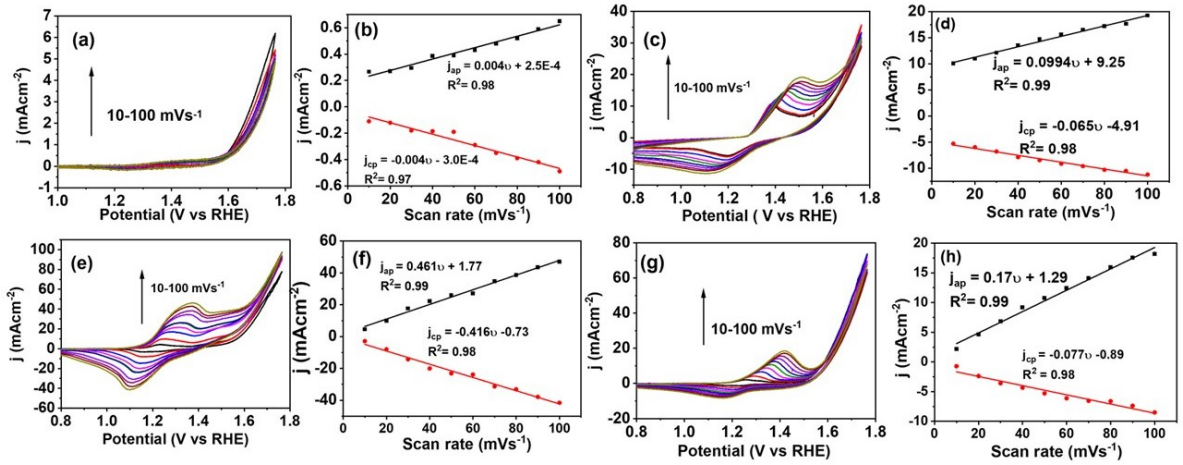

FIGURE 4.8: CVs and linear plot of scan rate vs current density of $NiMoO_4$(a,b), $Ni_{0.9}Co_{0.1}MoO_4$ (c,d), $Ni_{0.7}Co_{0.3}MoO_4$(e,f) and $Ni_{0.5}Co_{0.5}MoO_4$(g,h) in 0.5 M NaOH

Further, the materials were assessed for their MOR activity in 0.5 M MeOH and 0.5 M NaOH at scan rate of 50 mV s^{-1} as shown in Figure 4.9(b). The presence of methanol modified the CV curves dramatically, and a rapid surge in the anodic peak was observed confirming the oxidation of methanol. It was observed that the peak corresponding to the oxidation of Ni diminished and the methanol oxidation peak became more prominent. It could be conferred that the backward cathodic peak corresponds to the oxidation of intermediates formed on the surface of the catalyst. The pristine $NiMoO_4$ exhibited a distinguishable peak for MOR at 1.81 V vs RHE with current density of 19.8 mA cm^{-2}. With the doping of Co, there was drastic increment in the current density with $Ni_{0.7}Co_{0.3}MoO_4$ exhibiting the highest current density of 169.5 mA cm^{-2}. Interestingly, the potential was also shifted to lower value of 1.77 V vs RHE with Co doping compared to the pristine $NiMoO_4$. Further increment in Co^{2+} doping resulted in decrease in the MOR current density. This could be due to the significant increment in β phase interfering the catalytic process of Ni^{2+} to form active sites. It can be inferred that the maximum lattice-strain in $Ni_{0.7}Co_{0.3}MoO_4$ along with the maximum presence of Ni^{3+} and oxygen vacancies might have played a pivotal role in enhancing the MOR activity [304, 305].

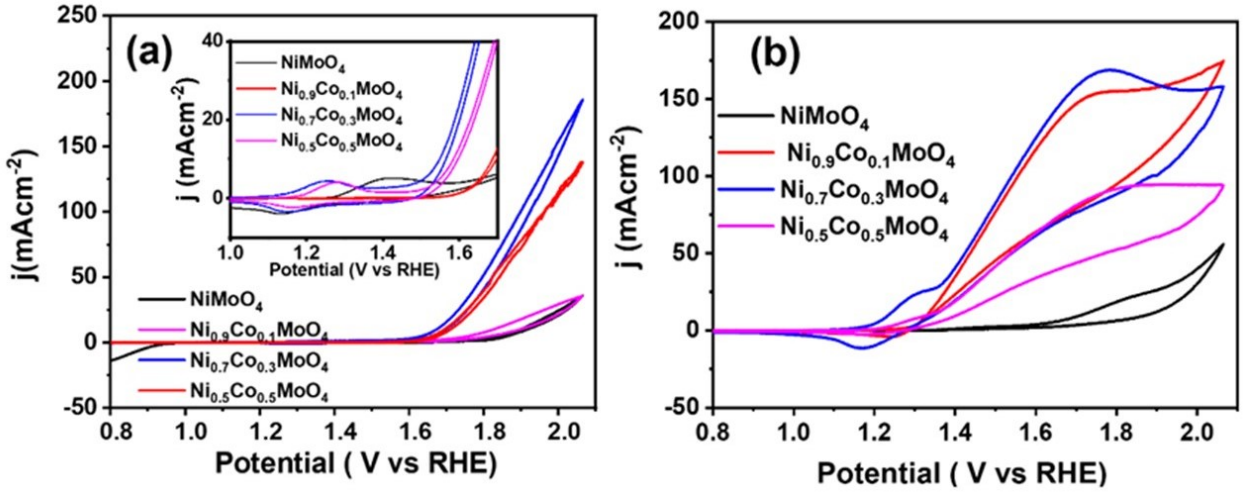

FIGURE 4.9: CVs of $NiMoO_4$, Ni0.9Co0.1MoO4, $Ni_{0.7}Co_{0.3}MoO_4$, and $Ni_{0.5}Co_{0.5}MoO_4$ in (a) 0.5 M NaOH with a scan rate of 50 mV s^{-1}, (b) in 0.5 M NaOH and 0.5 M MeOH with a scan rate of 50 mV s^{-1}

4.3.3 Kinetic Parameters and Durability study

The activation energy (Figure 4.10(a)) was determined through the Arrhenius plot of current density (ln j) vs temperature (T^{-1}) at methanol oxidation potential over $NiMoO_4$ and $Ni_{1-x}Co_xMoO_4$ and the temperature was varied from 25 to 50 °C with a gap of 5 °C in alkaline 0.5 M MeOH electrolyte solution [163, 306]. $Ni_{0.7}Co_{0.3}MoO_4$ exhibited the lowest slope signifying least activation energy and thereby rationalized the fastest MOR kinetics. The superior MOR kinetics significantly depends on the charge-transfer property of the material. Therefore, the electrical conductivity and charge-transfer behaviour on the catalyst – electrolyte interface were also evaluated with the help of EIS measurements at constant potential of 1.77 V vs RHE in an alkaline 0.5 M MeOH solution (Figure 4.10(b)). Semicircles observed in the higher frequency region for all catalysts attributed to the R_{ct} value along with double layer capacitance and the semicircle in the low frequency region corresponds to intermediate adsorption and their consequent to final products [293, 307]. It is worth noting that $Ni_{0.7}Co_{0.3}MoO_4$ exhibited the lowest arcs among the materials indicating the lowest charge transfer resistance as well as fastest rate of electron transfer for a facile electro-oxidation process. To delve deeper into the material's impedance characteristics, we conducted an analysis of its Bode phase and admittance (Figure 4.10(c and d)). In the Bode plot, the phase angle (θ) and impedance ($|Z|$) are allied with the frequency, and it further indicates the electron transfer kinetics of the catalysts [197, 198]. A low phase angle and low slope at a higher frequency region indicates a shorter electron lifetime, indicating a swifter electron transfer between the surface of $Ni_{0.7}Co_{0.3}MoO_4$ and methanol [198].

The corresponding circuits were obtained after fitting the Nyquist plot (Figure 4.10(e)) and the corresponding resistance and capacitance values are tabulated in Table 4.4. The low R_{ct} (22.8 Ω) observed for $Ni_{0.7}Co_{0.3}MoO_4$ indicates rapid charge transfer across the electrode–electrolyte interface. This is also evidenced by the superior C_{dl} value (2.9×10^{-3} F) of $Ni_{0.7}Co_{0.3}MoO_4$ compared to pristine $NiMoO_4$ (5.4×10^{-6} F). Furthermore, the decrease in adsorption resistance confirms the complete removal of intermediates from the surface of $Ni_{0.7}Co_{0.3}MoO_4$. The DFT study was done to understand a deeper insight into the electronic structure of the mixed phase $Ni_{0.7}Co_{0.3}MoO_4$ catalysts. The band - gap (ΔEg) was calculated upon doping with Co from the density of states (DOS, Figure 4.11(a, b)) analysis. We observed a band gap of ∼ 1.05 eV for $NiMoO_4$ (black), and $Ni_{0.9}Co_{0.1}MoO_4$ (green, Figure 4.11(a)). Whereas, the reduced band gap of ∼ 0.3 eV for $Ni_{0.7}Co_{0.3}MoO_4$ suggests that the catalyst exhibits superior conductivity.

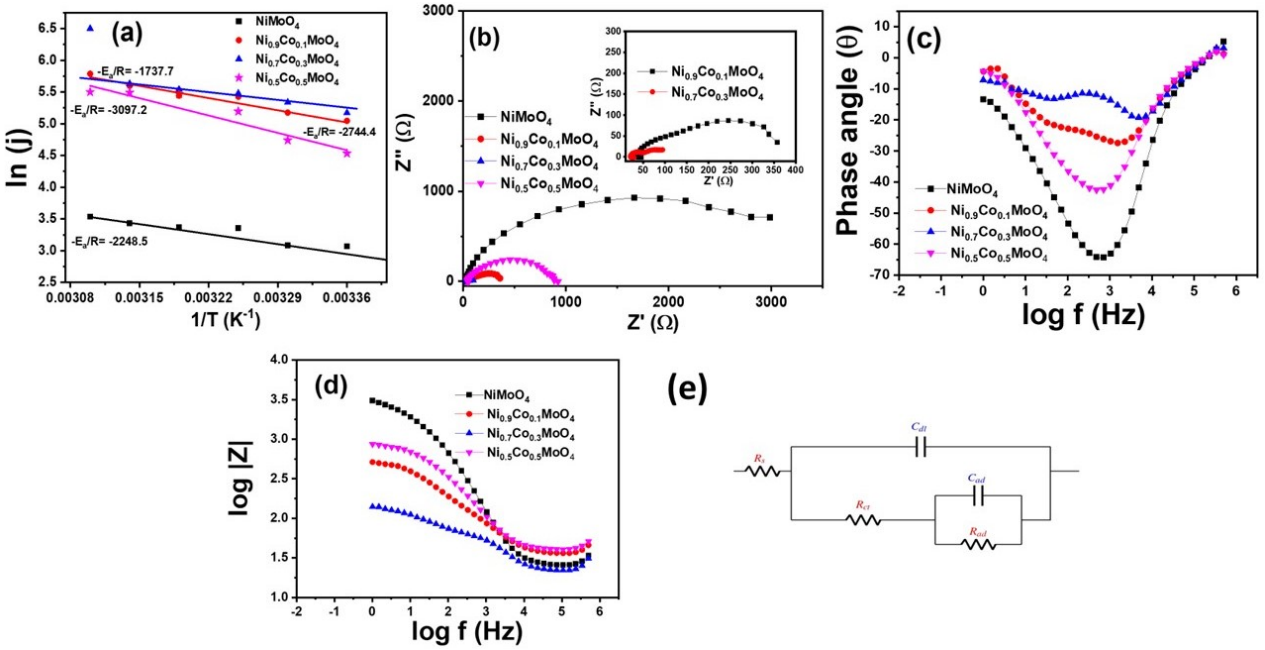

FIGURE 4.10: (a) Activation Energy, (b) Nyquist plot of MOR (c) Bode Phase angle (d) Bode absolute impedance and (d) equivalent circuit of $NiMoO_4$, $Ni_{0.9}Co_{0.1}MoO_4$, $Ni_{0.7}Co_{0.3}MoO_4$, and $Ni_{0.5}Co_{0.5}MoO_4$

TABLE 4.4: EIS parameters obtained from fitting of Nyquist plot

Catalysts/ Parameters	**$NiMoO_4$**	**$Ni_{0.9}Co_{0.1}MoO_4$**	**$Ni_{0.7}Co_{0.3}MoO_4$**	**$Ni_{0.5}Co_{0.5}MoO_4$**
R_s(Ω)	23.06	39.4	22.8	54.6
R_{ct}(Ω)	144.2	76.6	46.4	429.9
C_{ad}(Ω)	8873	263.4	61.1	374.1
C_{dl}(F)	5.4×10^{-6}	1.4×10^{-6}	2.9×10^{-3}	2.8×10^{-6}
Cad (F)	0.14×10^{-3}	0.14×10^{-3}	0.1×10^{-3}	33.3×10^{-6}

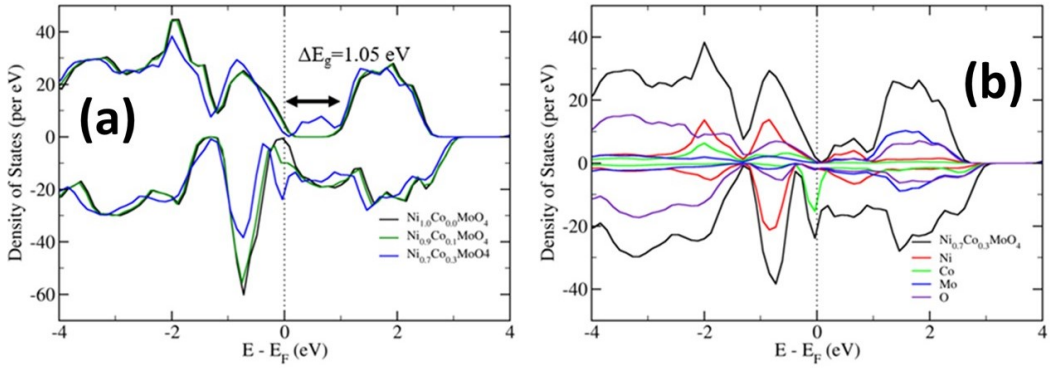

FIGURE 4.11: (a) DOS plots for $NiMoO_4$ (black), $Ni_{0.9}Co_{0.1}MoO_4$ (green) and $Ni_{0.7}Co_{0.3}MoO_4$ (blue), and (b) Projected DOS for $Ni_{0.7}Co_{0.3}MoO_4$

As $Ni_{0.7}Co_{0.3}MoO_4$ stands out to be the superior catalysts among the synthesized molybdates, further evaluation of the MOR kinetic parameters was carried out only with this optimized material. The order of the methanol oxidation reaction over $Ni_{0.7}Co_{0.3}MoO_4$ was evaluated from the voltametric responses of $Ni_{0.7}Co_{0.3}MoO_4$ towards MOR at different methanol concentrations as shown in (Figure 4.12(a)). A linear relationship was obtained by plotting the current density with logarithmic scale of methanol concentration (inset of Figure 4.12(a)). The equation log I = log nFk + m log C was utilized to determine the slope, where n represents the number of electrons, F is the Faraday constant, k denotes the reaction constant, m stands for the reaction order, and C signifies the concentration of methanol. A slope of 0.37 corresponds to the $\frac{1}{2}$ reaction order of $Ni_{0.7}Co_{0.3}MoO_4$towards MOR. The further kinetic introspection of MOR over the optimized catalyst was done with the help of scan rate-dependent studies. The scan rate was varied from 10-100 mV s^{-1} in alkaline 0.5 M MeOH solution. As observed in Figure 4.12(b), a gradual increase in anodic current density was observed as scan rate is varied from 10 - 100 mV s^{-1}. A linear correlation was observed on plotting the square root of scan rate vs current density with regression coefficient R^2= 0.99 following Randles Sevick equation as shown in the inset of Figure 4.12(b). Additionally, the logarithmic relationship between peak current density and scan rate Figure 4.12(c) displayed a slope of 0.51, indicating that the mechanism is diffusion-controlled rather than surface-controlled mechanisms in the observed phenomenon.

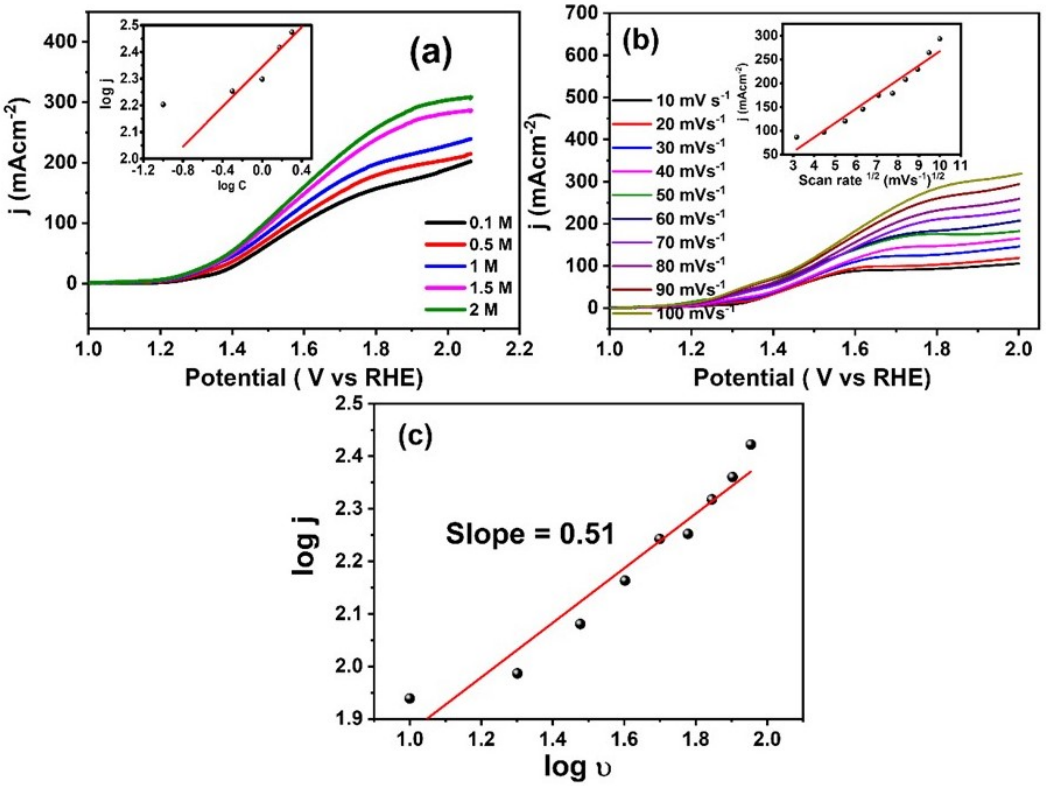

FIGURE 4.12: (a) Methanol concentration study of $Ni_{0.7}Co_{0.3}MoO_4$ (inset: log C Vs log I plot of $Ni_{0.7}Co_{0.3}MoO_4$ for MOR showing order of the reaction) (b) scan rate dependent study of $Ni_{0.7}Co_{0.3}MoO_4$ in 0.5 M NaOH and 0.5 M MeOH (inset square root of scan rate vs current density) (c) logarithmic plot of scan rate with current density for $Ni_{0.7}Co_{0.3}MoO_4$

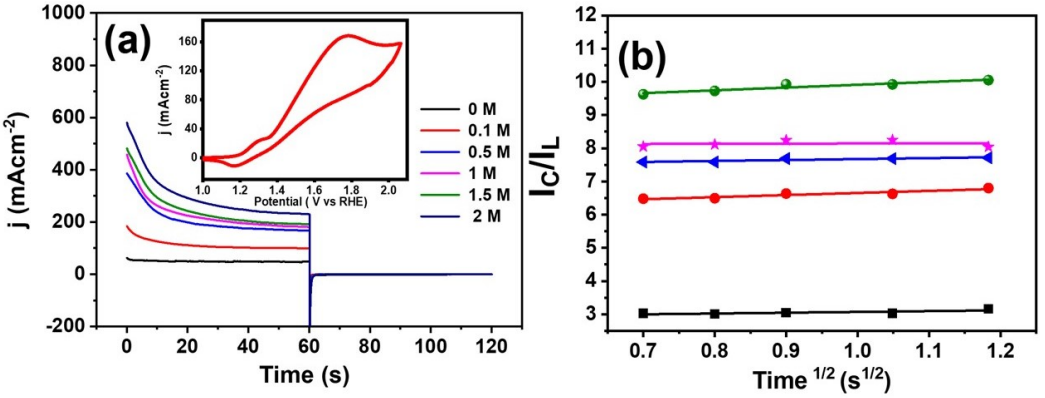

FIGURE 4.13: (a) Double step chrono amperometry of $Ni_{0.7}Co_{0.3}MoO_4$with and without methanol at 1.77 V and 1.0V vs RHE. (b) Ic vs IL vs Time (s) of $Ni_{0.7}Co_{0.3}MoO_4$

Double step chronoamperometry was adopted to study on the rate constant of MOR over $Ni_{0.7}Co_{0.3}MoO_4$. Figure 4.13(a) displays the results obtained from double-step chronoamperometry experiment of $Ni_{0.7}Co_{0.3}MoO_4$conducted under two different potentials. MOR potential of 1.77 V vs RHE was applied for a period of 60 s with further change in the potential to 1.0 V vs RHE to next 60 s. With an increase in methanol concentration, there was a corresponding increase in current density at 1.77 V compared to the RHE. However, there was no alteration in current density at 1.0 V versus RHE regardless of methanol concentration. The rate constant for methanol electro-oxidation was calculated from the double step chrono amperometry using the following equation.

$$I_c/I_L = \gamma^{1/2}\left[\pi^{1/2}\mathrm{erf}\left(\gamma^{1/2}\right) + \exp\left(-\gamma\right)/\gamma^{1/2}\right] \tag{4.3}$$

where I_C is the catalytic current of $Ni_{0.7}Co_{0.3}MoO_4$ in presence of methanol, I_L is the limiting current in the absence of methanol. γ is the argument of error function and is equal to kC_ot, where k is the rate constant in cc $mol^{-1}s^{-1}$, t being the elapsed time in s, and C_o is the bulk methanol concentration in mol cc^{-1}. The above-mentioned equation can be simplified as the following one by considering the value of $\gamma > 2$.

$$I_c/I_L = \gamma^{1/2}\pi^{1/2} = (kC_0t)^{1/2}\pi^{1/2} \tag{4.4}$$

A MOR rate constant of 0.36×10^3 cc $mol^{-1}s^{-1}$ was determined analysing the plot of I_c/I_L versus $t^{1/2}$ (Figure 4.13(b)) with the variation of methanol concentration. This obtained rate constant aligns well with earlier reports, suggesting that $Ni_{0.7}Co_{0.3}MoO_4$ effectively overcomes the kinetic barrier for methanol oxidation as well as notably reduces the overpotential [308].

The assessment of $Ni_{0.7}Co_{0.3}MoO_4$ for long term MOR was studied with the help of CA measurements in 0.5 M NaOH and 0.5 M MeOH electrolyte solution at potential of 1.77 V vs RHE for 12 h. As shown in Figure 4.14(a), the currents quickly decreased at the initial stage probably due to the formation of intermediate species during MOR. $Ni_{0.7}Co_{0.3}MoO_4$ exhibits excellent electrochemical stability, as evidenced by the minimal change in current density even after continuous electrolysis for 12 h. Further, long term stability of $Ni_{0.7}Co_{0.3}MoO_4$ was confirmed using the CV cycling for 300 cycles in 0.5 M MeOH at scan rate of 50 mV s-1 as shown in Figure 4.14(b). The current density remained consistent after 300 cycles, affirming the outstanding stability of $Ni_{0.7}Co_{0.3}MoO_4$.

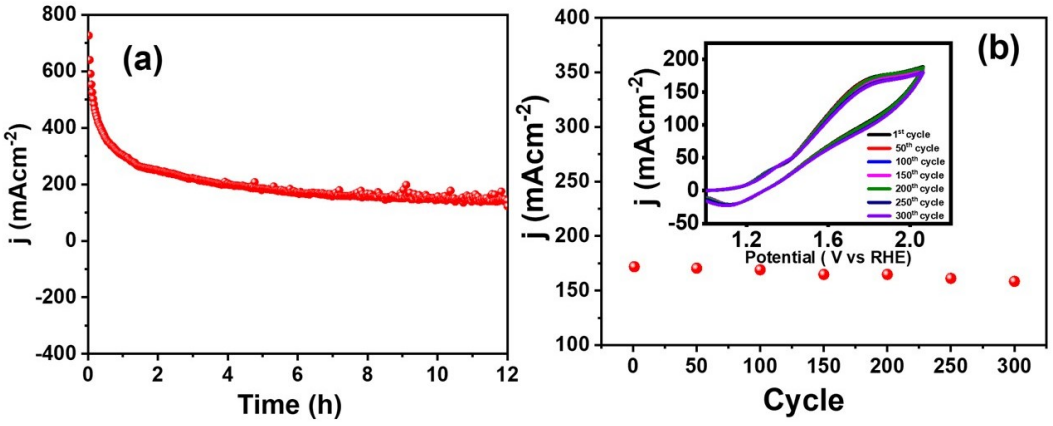

FIGURE 4.14: (a) CA of $Ni_{0.7}Co_{0.3}MoO_4$at 1.77 V vs RHE in 0.5 M NaOH and 0.5 M MeOH for 10 h (b) Stability study of $Ni_{0.7}Co_{0.3}MoO_4$up to 300 cycles (inset: CV up to 300th cycle)

4.3.4 Methanol Upgradation and Assisted HER

Upon completing the CA studies, the electrolyte was subjected to ^{1}HNMR analysis to determine the liquid products and the data are presented in Figure 4.15. Apparently, formic acid was found as only liquid product upon electro-oxidation of methanol and its concentration was found to be 1.95 $\times$ 10^{-3} mol over $Ni_{0.7}Co_{0.3}MoO_4$. Figure 4.16(a) highlights the highest conversion of methanol to the upgraded value-added product formic acid over $Ni_{0.7}Co_{0.3}MoO_4$ among the synthesized molybdate catalysts. The yield of formic acid as product has intrigued us to explore the molybdate catalysts for alcohol assisted HER. This is an innovative process to attain energy-efficient hydrogen generation with the combination of HER along with selective oxidation reaction that lowers the potential barrier of the anodic site and also improves the hydrogen evolution efficiency at the cathode [13, 309, 310]. To evaluate the combined hydrogen production and methanol oxidation, we conducted voltammetric analysis on the most promising material, $Ni_{0.7}Co_{0.3}MoO_4$, in 0.5 M NaOH solutions, both with and without methanol. As depicted in Figure 4.16(b), $Ni_{0.7}Co_{0.3}MoO_4$ demonstrated significant HER activity in an alkaline environment, with an overpotential of -0.59 and -0.64 V vs RHE at current densities of -10.0 and -20.0 mA cm^{-2}, respectively. Upon the addition of 0.5 M MeOH to the alkaline electrolyte, the overpotential notably decreased to -0.57 and -0.60 V vs RHE at current densities of -10.0 and -20.0 mA cm^{-2}, respectively. Evidently, $Ni_{0.7}Co_{0.3}MoO_4$ proves to be a proficient catalyst for MOR-reinforced HER performance. The durability of the electrode was also verified by chronopotentiometry in the absence and presence of methanol. In Figure 4.16(c), it can be observed that $Ni_{0.7}Co_{0.3}MoO_4$ demonstrated notable stability both in the presence and absence of methanol electrolyte at -20.0 mA $cmcm^{-2}$, with the potential being steadily maintained

constant for 12 h.

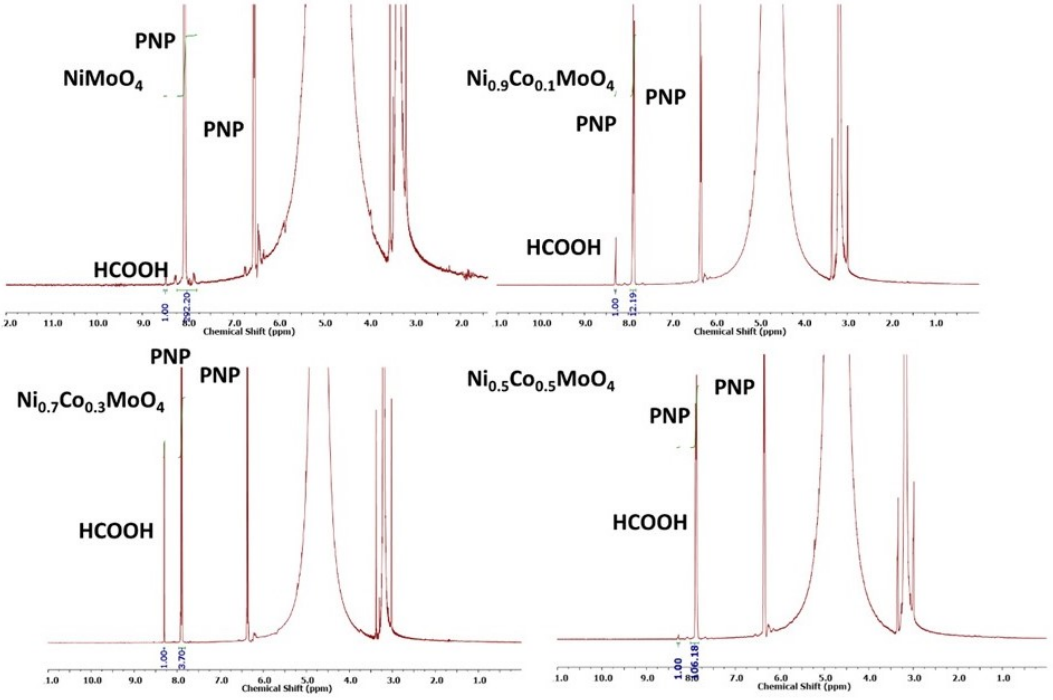

FIGURE 4.15: ^{1}HNMR spectra of the electrolyte of $NiMoO_4$, $Ni_{0.9}Co_{0.1}MoO_4$, $Ni_{0.7}Co_{0.3}MoO_4$, and $Ni_{0.5}Co_{0.5}MoO_4$ after 4 h of CA in 0.5 M MeOH and 0.5 M NaOH medium

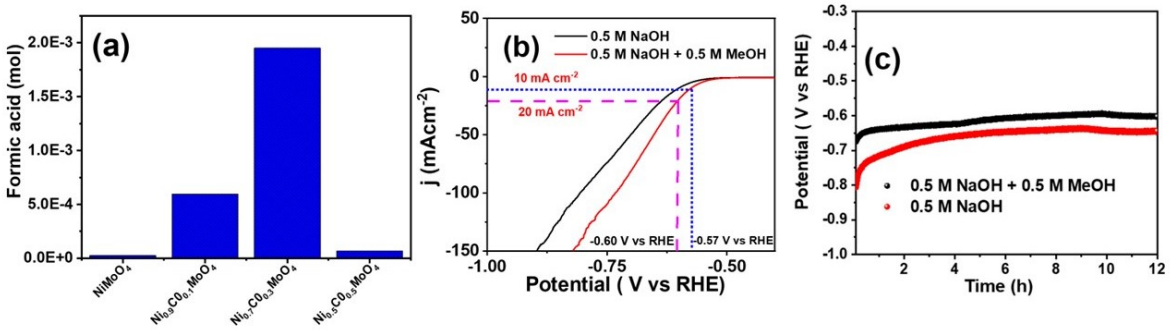

FIGURE 4.16: (a) Bar plot depicting the concentration of formic acid with respect to the catalysts, (b) LSV showing HER performance over $Ni_{0.7}Co_{0.3}MoO_4$,in presence and in absence of methanol, and (c) Chronopotentiometry of $Ni_{0.7}Co_{0.3}MoO_4$ in 0.5 M NaOH and in 0.5 M NaOH + 0.5 M MeOH electrolyte

Intrigued by the excellent activity and stability of $Ni_{0.7}Co_{0.3}MoO_4$ in MOR assisted HER, $Ni_{0.7}Co_{0.3}MoO_4$ were drop-casted onto the surface of carbon cloth as the electrodes to construct a two-electrode system ($Ni_{0.7}Co_{0.3}MoO_4$/CC||$Ni_{0.7}Co_{0.3}MoO_4$/CC) for evaluating the methanol-assisted water splitting performances. The schematic representation and the corresponding experimental set-up are shown in Figure 4.17(a & b). The performance of $Ni_{0.7}Co_{0.3}MoO_4$ for methanol-assisted water splitting was evaluated in the absence and presence of methanol. The comparative LSV traces of $Ni_{0.7}Co_{0.3}MoO_4$/CC in 0.5 M NaOH and in 0.5 M MeOH + 0.5 M

NaOH electrolyte are shown in Figure 4.17(c). Apparently, the overall water electrolysis (OER coupled with HER) required a cell voltage of 1.84 V to achieve 10 mA cm^{-2} current density, while the methanol-assisted water electrolysis (MOR coupled with HER) required a lower cell voltage of 1.68 V to attain the same current density, revealing great cell efficiency and good kinetics for electrolysis of MeOH-NaOH solution. The peak at 1.87 V vs RHE corresponds to Ni^{2+}/Ni^{3+} redox peak. The practical suitability of large-scale hydrogen generation in presence of methanol at a lower cell voltage was revealed by stability study at different current density via chrono potentiometric experiments as shown in Figure 4.17(d). The minor positive shift is credited to the surface blockage due to irreversible intermediate formation and bubble attachment that decreases the effective contact portion between the electrode and electrolyte.

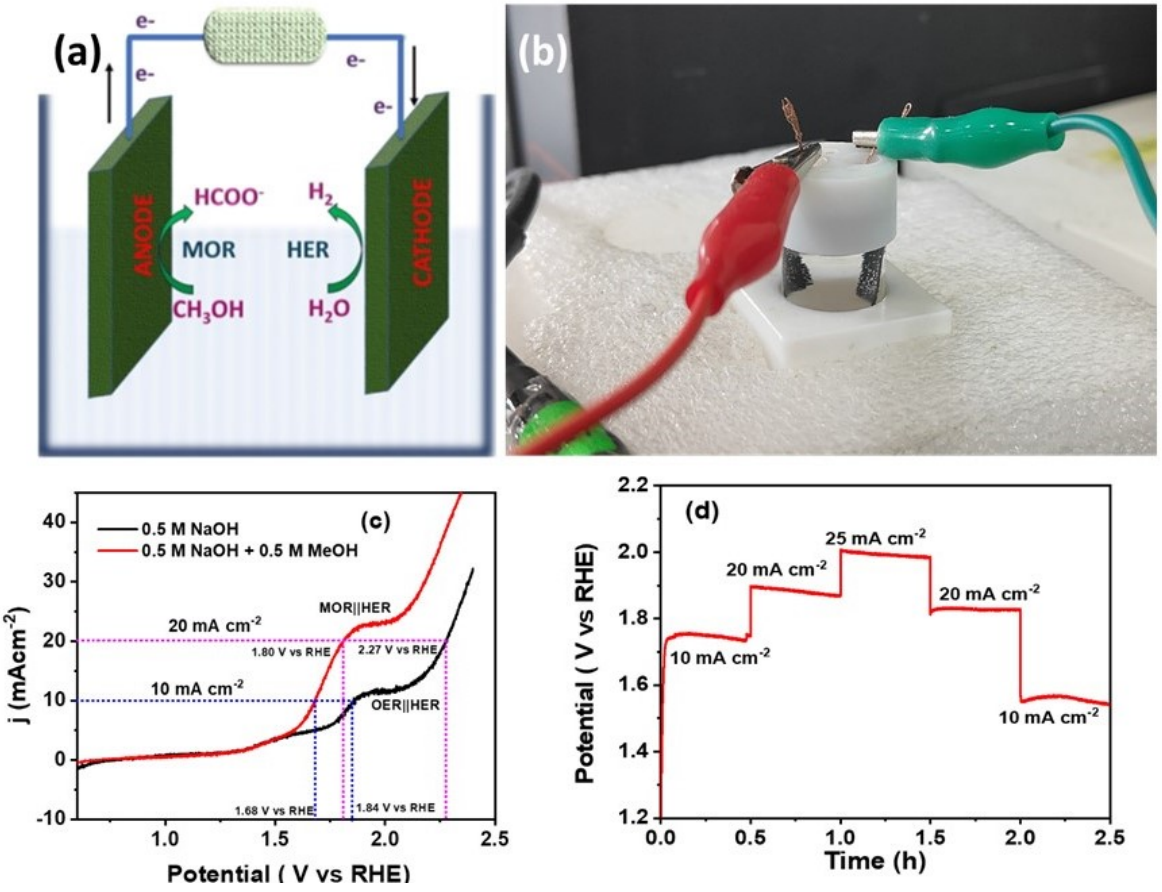

FIGURE 4.17: (a) Schematic representation of two electrode system (b) pictorial representation of experimental set up (c) LSV curves of $Ni_{0.7}Co_{0.3}MoO_4$ in 0.5 M NaOH + 0.5 M MeOH electrolyte (d) chronopotentiometry at different current density

4.4 Conclusion

The pristine $NiMoO_4$and the Co-doped $Ni_{1-x}Co_xMoO_4$ were synthesized via a facile hydrothermal method. While the pristine material exhibited crystallization in a monoclinic α-phase with a nano-rod-like morphology, an increase in the Co doping level led to the presence of mixed α and β phases. Analysis of micro-strain using diffraction data and HR-TEM micrographs revealed a notable development of strain in optimally doped mixed-phase $Ni_{0.7}Co_{0.3}MoO_4$. Additionally, the presence of Ni^{3+} ions, oxygen vacancies, and ECSA was most pronounced in the specific doped molybdate. This combination resulted in superior electrocatalytic methanol oxidation activity over $Ni_{0.7}Co_{0.3}MoO_4$. Detailed kinetic analysis indicated that methanol oxidation over $Ni_{0.7}Co_{0.3}MoO_4$ followed a diffusion-controlled mechanism with a significantly low activation energy barrier. Furthermore, the electrocatalytic oxidation of methanol over $Ni_{0.7}Co_{0.3}MoO_4$ yielded the value-added product of formic acid and demonstrated a significant enhancement in methanol oxidation rate reinforced by HER performance. Overall, the findings highlight the promising potential of $Ni_{0.7}Co_{0.3}MoO_4$ water splitting with implications for sustainable energy conversion technologies.

Chapter 5

Polyaniline supported g-C_3N_4 quantum dots surpass benchmark Pt/C: development of morphologically engineered g-C_3N_4 catalysts towards "metal-free" methanol electro-oxidation

5.1 Introduction

In the earlier chapters, we have explored the role of Ni in different crystalline environments for methanol oxidation in alkaline medium. In this chapter, we tried to develop an efficient metal-free electrocatalyst for MOR. Recently, N-doped carbon electrocatalysts, like N-doped graphene and carbon nanotubes, are popular choice of metal-free catalysts due to their significant activity. Here, in this work, we have explored the catalytic efficacy and improved the mass activity of metal-free g-C_3N_4 materials towards methanol oxidation. Since Wang and Domen [311] reported that polymeric defecteous g-C_3N_4 can efficiently produce hydrogen from water, the study towards this promising metal-free catalyst has attracted serious attention. Among the several allotropes of C_3N_4 like α, β, cubic, pseudocubic, and graphitic structures, g-C_3N_4 that

is structured with the help of polyheptazine (or tris-s-triazine) unit is considered to be most stable chemical structure under a varied extreme environment, and pyridine-like N in the triazine configuration is believed to be the active sites for electrocatalytic reactions [312]. Dissecting the 3 D bulk g-C_3N_4 into 2 D nano-sheets, 1 D nano-rods and finally to 0 D quantum dots are the happening research areas due to the desired combination of high reactive specific surface area and direct molecular transport phenomenon [313, 314]. The nitrogen configurations and content, including quaternary N (or graphitic N), pyridinic N, and pyrrolic N vary accordingly with the size and the surface morphology. And, it is believed that pyridinic N and quaternary N are the main active sites for OER and HER [315]. The 2 D g-C_3N_4 nanosheets have a typical sp^2 network with weak van der Waals interactions across the layers showed an obvious increase in density of states at the conduction band edge and specific surface area with respect to the bulk counterpart [316]. Further, the controlled cutting of the nano-sheets to 1 D nano-rods, and 0 D quantum dots also showed significant quantum confinement effects and possess excellent properties like bright fluorescence, water solubility, and above all, non-toxicity [317–319]. However, these morphologically engineered g-C_3N_4 materials were never studied as active catalysts for methanol oxidation. Additionally, in spite of significant studies on N-doped carbon electrocatalysts, the glaring challenges are: comparatively poor nitrogen content, unstable framework structure of carbon, and the moderate catalytic efficacy in extreme electrochemical conditions. Therefore, it is of high interest to introspect the role of the N- and the C- skeleton of g-C_3N_4 as a function of size and morphology of g-C_3N_4 towards methanol oxidation. Here, in this work, 2 D, 1 D, and 0 D g-C_3N_4 were successfully prepared from bulk g-C_3N_4 directly by a thermal-chemical etching process. The materials were thoroughly characterized and were studied for methanol oxidation reaction in basic condition. The 0 D g-C_3N_4 when supported on conducting polyaniline, not only showed higher electrocatalytic methanol oxidation activity than the commercial Pt/C but also demonstrated excellent CO tolerance to be a suitable and applicable metal free catalyst.

5.2 Experimental Section

5.2.1 Controlled Synthesis of Nano-sheets, Nano-rods and Quantum dots of g-C_3N_4

The synthesis of different nano morphologies of g-C_3N_4 is presented in Figure 5.1. The process starts with melamine to synthesize the bulk g- C_3N_4, and then its consequent CNNS,

CNNR and CNQD. The bulk g-C_3N_4 was produced by calcining melamine (Sigma Aldrich, 99%) at 550 °C for 4 h at a ramping rate of 2.5 °Cmin^{-1}. The synthesized bulk g-C_3N_4 was grounded to fine powders with the help of mortar and pestle. The exfoliated nano-sheets of g- C_3N_4 was synthesized by thermal etching of bulk g-C_3N_4 [320–322]. About 0.5 g of bulk g-C_3N_4 was calcined at 550 °C for 2 h with a heating rate of 5 5 °Cmin^{-1} in a muffle furnace. A light-yellow colour powder of exfoliated CNNS was obtained. The 0.25 g of CNNS were acid etched by a mixture of concentrated H_2SO_4 and HNO_3 for 16 h under ultra-sonication, and the formed clear acid solution was diluted with deionized water (1 L) to produce a colloidal suspension. The colloidal suspension was filtered through a 0.22 µm microporous membrane to get rid of the acids to obtain the CNNR. Following that, the nano-rods were further redispersed in 30 mL of deionized water under ultra-sonication. The suspension was shifted to a teflon-lined 50 mL autoclave and was heated at 200 °C for 10 h. After the completion of heating, once the room temperature was reached, the yellowish solution of CNQD was produced, which was further filtered through a 0.22µm microporous membrane.

5.2.2 Synthesis of Quantum Dot g-C_3N_4 Embedded Polyaniline Nano-Fibres

About 20 mg of CNQD was homogeneously dispersed in 100 mL of deionized water, and 20 mg of aniline (19.6 µL) (Advent Chemicals, 99%) was added to it under constant stirring for 2 h at room temperature. The reaction mixture was ice-cooled, and a freshly prepared aqueous solution of ammonium per sulphate (250 mg in 100 mL water) (SRL Chemicals, 98.0%) was added drop-wise to the reaction mixture. The reaction mixture was at a constant temperature of 5 °C for another 24 h without stirring for polymerization [323, 324]. A deep green-coloured precipitate was formed, which was washed with water, acetone, and methanol to get rid of the oligomers and excess ammonium per sulphate. The washed precipitation was finally dried to obtain CNQD - PANI.

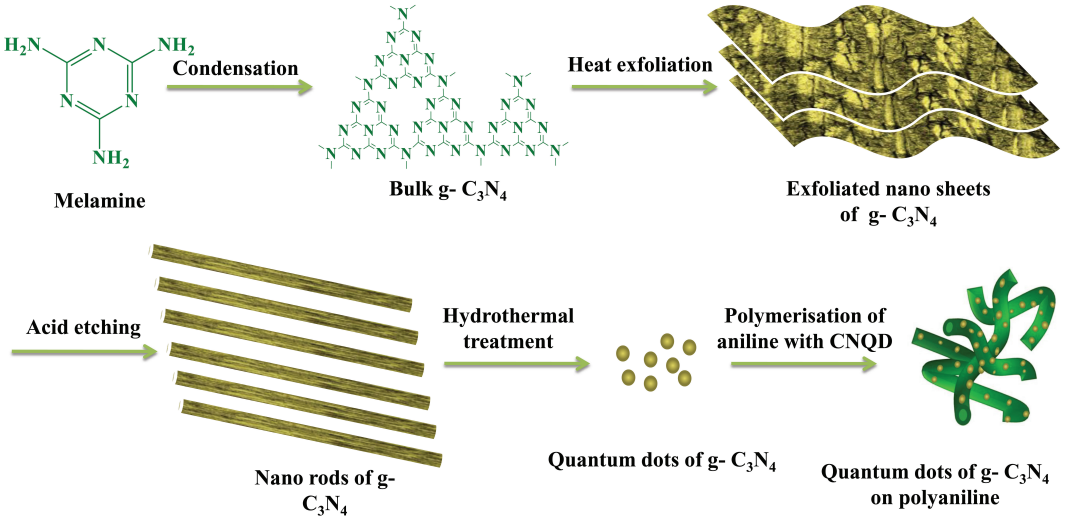

FIGURE 5.1: Schematic illustration of the synthesis of exfoliated CNNS, CNNR and CNQD. The quantum dots of g - C_3N_4 were embedded on polyaniline nano-fibers in the last step

5.2.3 Structural, Morphological and Electronic Characterization

The studies on the crystalline nature of the synthesized g-C_3N_4 materials was carried out by Rigaku Ultima IV XRD with Cu K$-\alpha$ radiation ($\lambda = 1.5418\mathring{A}$). The scan rate during data collection was 1° min^{-1} and step size of 0.01° in the 2θ range between 10° - 60°. Average crystallite size (D) has been estimated by using Debye-Scherrer's formula:

$$D = \frac{0.9\lambda}{B\text{Cos}\theta} \tag{5.1}$$

where B is the full-width at half-maximum, λ is the wavelength of the radiation, and θ is the corresponding angle. The structural information was also derived from HRTEM (JEOL/JEM 2100). The samples were prepared by dispersing in water followed by soaking with a 200 mesh Cu grid. The FT-IR of the synthesized g-C_3N_4 were collected on a JASCO FT-IR- 4200 with KBr pellet, and the Raman spectra were obtained using a UNIRAM 3300 Raman spectrometer with 532 nm laser source. The surface morphology and the particle sizes of the synthesized nano g-C_3N_4 materials were studied using FE-SEM (FEI-Apreo S). XPS of the materials were collected on thermoscientific K$-\alpha$ surface analysis spectrometer with Al K_α as X-ray source. The PL spectra were recorded at room temperature using a Horiba scientific Flurolog steady state spectro-flurometer under excitation wavelength ranging from 320 nm to 400 nm. DRS was carried out on JASCO V-670 UV-visible spectrophotometer.

5.2.4 Electrocatalytic Oxidation of Methanol

The electrochemical experiments were performed by an Auto lab potentiostat PGSTAT128N using a conventional three-electrode system. The electrodes were CNNS, CNNR, CNQD, and CNQD - PANI modified GCE as a working electrode, a Pt-wire as an auxiliary electrode, a saturated Ag/AgCl as a reference electrode. The polished GCE was of 3 mm in diameter with 0.07 cm^2 surface area. About 10 µL solution of synthesized nano materials in methanol dispersion were drop casted on GCE, and methanol was evaporated at ambient temperature for electrochemical studies. The electrochemical MOR was recorded by CV technique at 0.05 V s^{-1} scan rates in an alkaline mixture 0.5 M methanol with 0.5 M NaOH. The current per weight of active catalysts (active mass) was used for all calculations.

5.2.5 Electrochemical Impedance Studies During Oxidation of Methanol

Electrochemical impedance studies were carried out using Biologic Sp-150 with the conventional three electrode system over a frequency range of 50 kHz to 50 mHz with a sinusoidal excitation signal of 10 mV. The three electrode system include CNNS, CNNR, CNQD and CNQD PANI modified glassy carbon as the working electrode, Pt wire as the counter electrode, and a saturated Ag/AgCl as the reference electrode. Impedance of all samples were measured in an alkaline mixture of 0.5 M methanol and 0.5 M NaoH. The Nyquist plot fitted to appropriate equivalent circuit using EC-Lab V11.31.

5.3 Results and discussion

The thermal etching of bulk g-C_3N_4 in aerobic condition is a cost effective, and easy to scale-up top-down approach to synthesize CNNS. The hydrogen-bonds in cohesion with polymeric melon strands in the bulk layers are unstable during oxidization, and produced the nano sheets. The obtained CNNS were acid etched to produce CNNR. During this step, CN bonds combined with tri-s-triazine units were oxidized to produce oxygen-based functional groups, including carboxylate, on the margin and on the substrate. This lead to orientational cleavage of nano-sheets to CNNR. At the end, CNQDs were produced from CNNR under the hydro-thermal process of controlled chemical scissoring.

5.3.1 Crystallinity and Morphology

The pristine g-C_3N_4 shows a weaker diffraction peak at about 13 ° corresponding to in-plane structural packing motif of tri-s-triazine units along (100), and a stronger one at about 27° corresponding to interlayer stacking of aromatic segments along (002) [320, 325, 326]. Consistent with the literature reports, CNNS showed these two peaks in Figure 5.2(a). The weak (100) reflection appeared at $2\theta = 12.8°$ with a d_{100} spacing of 0.69 nm, whereas the strong (002) appeared at 27.9° with d_{002} spacing of 0.319 nm. The XRD profile of bulk g-C_3N_4 shows very high crystallinity and the (002) peak is positioned at 27.5°. Upon thermal etching, the position of the highest intense peak in CNNS is increased by $\sim 0.4°$ from the bulk materials indicating denser packing due to exfoliation, which is also in accordance with existing literature [321, 327]. The crystallite size of CNNS calculated from Scherrer's formula with the help of stronger (002) reflection was found to be 8.19 nm. The CNNR produced from the sheets did not show any significant (100) reflection, and the (002) position was shifted to lower angle by 0.25° than that of CNNS. Due to acid etching of the g-C_3N_4 sheets, the in-plane packing of tri-s-triazine units were ruptured, and consequently the aromatic stacking might have widened in CNNR showing a shift in lower angle reflection. The corresponding d_{002} was calculated to be 0.322 nm for CNNR confirmed the lighter packing compared to CNNS. Further, the hydrothermal treatment of CNNR that produced CNQD did retain the weak diffraction of (100) and almost insignificant (002) suggesting the rupture of aromatic stacking in the quantum dots. This was further proved by the FT-IR spectra in Figure 5.2(b). The peak at 1640 cm^{-1} in CNNS corresponds to the typical stretching modes of CN heterocycles of triazine units which gradually disappeared in CNNR and CNQD [328, 329]. The other sharp aromatic CN stretching frequencies at 1240, 1330, 1425 and 1580 cm^{-1} were apparently present in CNNS, and were obscured after acid etching and hydrothermal treatment suggesting gradual rupture of aromatic stacking [330, 331]. However, the characteristic breathing mode of triazine units at 805 cm^{-1} stayed in CNNS as well as in CNQD [332]. On the other hand, hydrothermally produced CNQD possessed a strong peak at 1385 cm^{-1} due to the bending vibrations of – O– H along with a – C = O stretching peak at 1723 cm^{-1} in the hydrophilic carboxylate groups [333, 334]. The broad bands at around 3200 cm^{-1} were indicative of stretching vibration modes for – NH of g-C_3N_4 [326]. Raman spectroscopy was also used to understand the vibrational properties of C_3N_4 materials, however, the resolution of the recorded Raman spectra of CNNS, CNNR, and CNQD samples with 532 nm laser source (Figure 5.2(c)) was fairly poor due to fluorescence interference. Several feeble

characteristic peaks of CN stretching frequencies at 1280, 1480, 1600 cm^{-1} were observed in CNNS [335–337] which disappeared in CNNR and CNQD materials.

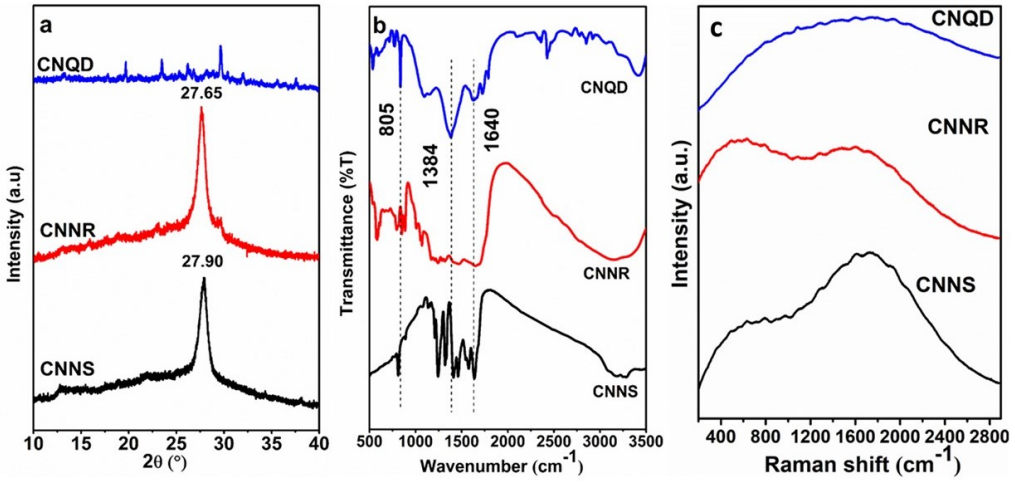

FIGURE 5.2: (a) XRD, (b) FT-IR of bulk g-C_3N_4, CNNS, CNNR and CNQD and (c) Raman spectra of CNNS, CNNR, and CNQD

The electron micrographs studies in Figure 5.3 revealed the successful formation of the nano-sheets, nano-rods and quantum dots. Apparently, the free-standing nanosheets were with thickness of few nanometres, and the edges of the sheets were ragged in order to minimize their TEM images of as-prepared CNQD revealed the formation of well separated quantum dots with average diameter of 7 nm (Figure 5.4(d)). The HR-TEM images (Figure 5.4(e)) showed the lattice fringes of CNQD corresponding to d_{002} spacing 0.313 nm which was consistent with the d_{002} spacing derived from XRD study. The distribution of particle size of CNQD is shown in (Figure 5.4(f). surface area as observed in the FE-SEM in Figure 5.3(a-c) and TEM images in Figure 5.4(a). The CNNR was 40–50 nm long with a width of 5–7 nm (Figure 5.4(c)).

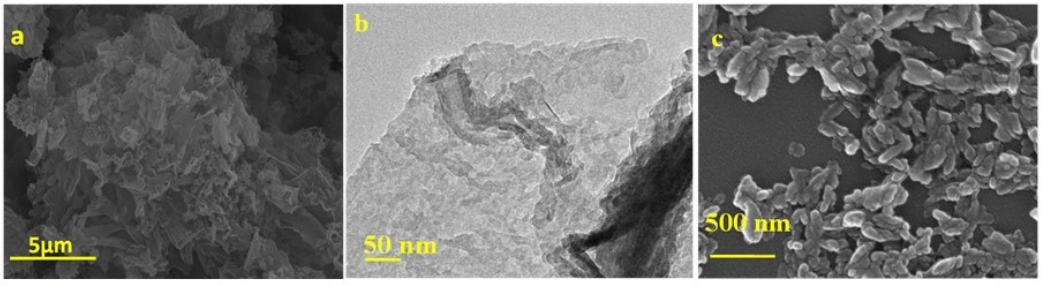

FIGURE 5.3: (a) FESEM image of CNNS, (b) TEM image of CNNS, (c) FESEM image of CNNR

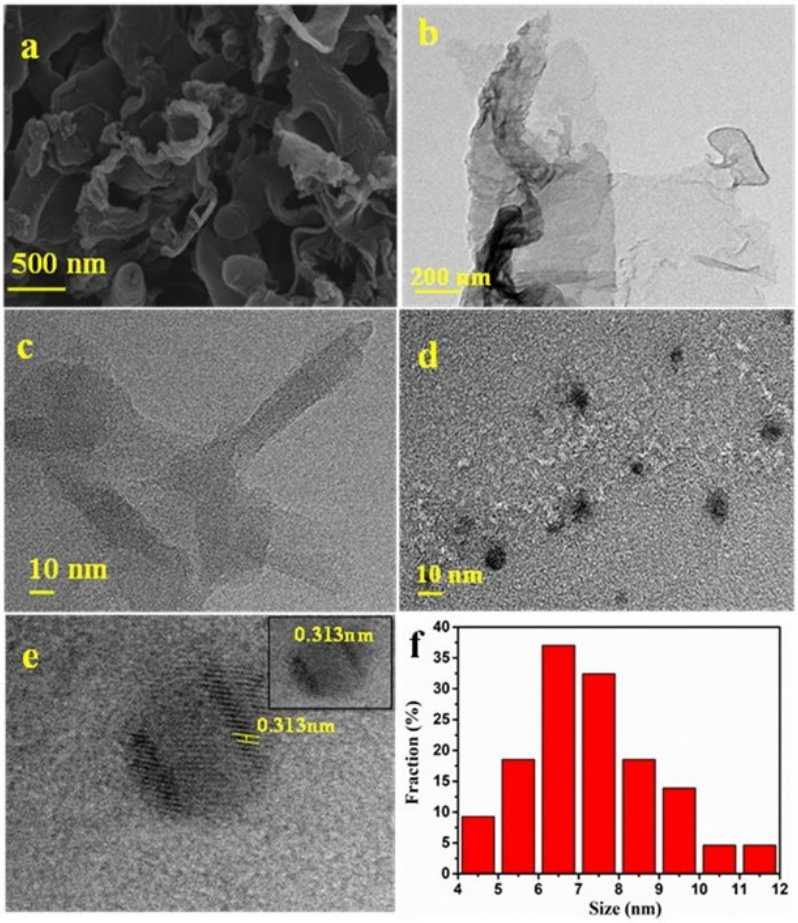

FIGURE 5.4: (a) FE-SEM of CNNS; (b) TEM of CNNS; (c) TEM of CNNR; (d) TEM of CNQD; (e) HR-TEM of CNQD; (f) particle size distribution of CNQD

The PL investigations further probe the formation of quantum dots of g-C_3N_4, which emit bright blue luminescence under UV excitation (Figure 5.5). The quantum dots also showed the excitation wavelength-dependent PL spectra. When the excitation wavelength was varied from 320 to 400 nm, the maxima of the PL profile shifted to longer wavelengths (Figure 5.5). The intrinsic luminescence mechanism of CNQD may be attributed to the π– π^* transition in the aromatic ring, however, depending on the polydispersity of the size, it exhibited the excitation wavelength dependent PL.

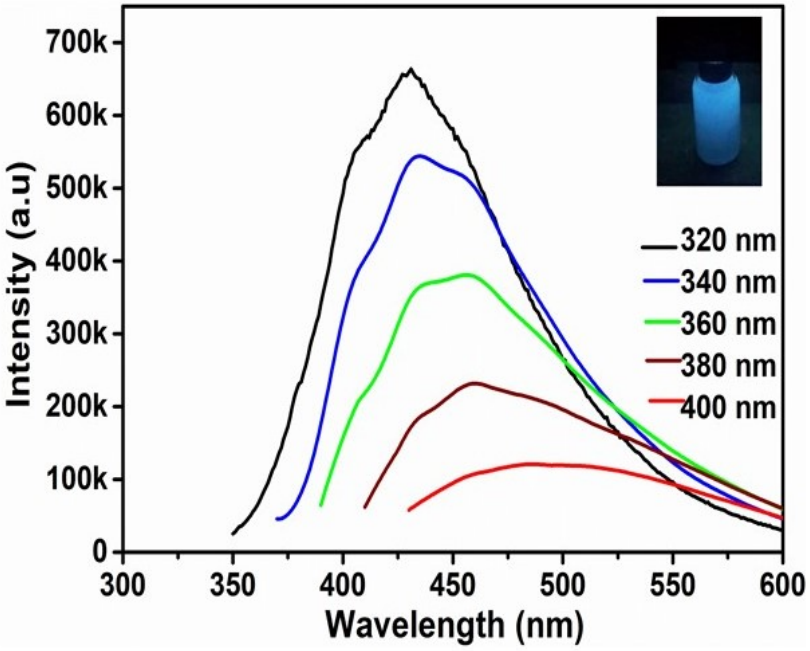

FIGURE 5.5: PL spectra of CNQD excited at different wavelength.

5.3.2 Electronic Properties

The chemical states of CNNS, CNNR, and CNQD were analysed by XPS. The survey spectra showed three major peaks corresponds to C 1s, N 1s, and O 1s in Figure 5.6(a). The intensity of the O 1s peak steadily increased from nano-sheets to nano-rods and was found highest with the quantum dots. The surface composition of C, N and O are provided in supporting information (Table 5.1). The significant increase in oxygen content indicates the oxidation of nano sheets due to acid treatment, and further oxidation of nano-rods due to hydrothermal treatment. The number of energy level decreases upon quantization of the bulk material, and therefore the band gets narrower resulting higher band gap. The VB spectra of the synthesized

TABLE 5.1: Surface composition of C, N and O in CNNS, CNNR and CNQD

Sample	**C (%)**	**N (%)**	**O (%)**
CNNS	35.72	57.54	6.74
CNNR	21.65	31.71	46.61
CNQD	201.17	9.12	70.81

materials are plotted in Figure 5.6(b). The binding energies of the onset edge signifies the gap in the energy between top of VB and Fermi level, and practically the VB spectra coincide with the DOS [83]. The onset edge of VB has shifted from 1.95 eV in CNNS to 2.15 eV in CNNR. This clearly indicates the widening of band gap in CNNR than that of CNNS. The glaring widening of

the band gap was observed in CNQD, where the onset was at 3.05 eV. To confirm the quantum confinement, the band gap of the CNNS, CNNR, and CNQD samples were estimated from the DRS by using the Kubelka–Munk equation, and represented in Figure 5.6(c-d). The g-C_3N_4 is an indirect band gap material with allowed transition. Therefore, K was estimated with the following formula K $=\frac{(1-R)^2}{2R}$, where R is % reflectance. The band gap of CNNS, CNNR, and CNQD was found to be 2.25, 3.67, and 4.82 eV, respectively. The enlarged band gap of the CNNR with respect to CNNS may be ascribed to higher degrees of oxidation in the nano rod. The maximum band gap of the quantum dots than the nano-rods and nano-sheets are due to the quantum confinement, which is in agreement with the literature [338]. The chemical states control the band gap of the materials, and therefore, the core level spectra of C and N were collected. Figure 5.6 (e) shows the high-resolution C 1s spectrum with a doublet peak, which is deconvoluted into sub-peaks. The peak at 284.3 eV may originate from adventitious carbon (sp^3 C - C) or sp^2 C - C bonds, while 285.6 eV may correspond to C - NH_2 species [314, 339–341]. The other two higher binding energy peaks at 287.6 and 288.5 eV are attributed to N = C - N coordination and the N - C - O groups, respectively. It should be noted that the oxidized samples contain more N - C - O species. The N 1s core level spectra in Figure 5.6(f) show a broad peak that could be deconvoluted into three component peaks at 398.5, 399.8, and 401.1 eV. The dominant nitrogen peak centered at 398.5 eV is due to sp^2-bonded N bound to two carbon atoms (C- N = C, s-triazine rings, pyridine-like nitrogen atoms). The peak at 399.8 eV originates from tertiary nitrogen N–$(C)_3$ groups. Another binding energy peak at 401.1 eV is ascribed to amino functional groups (C - NH_2). It is apparent from the spectra that the atomic percentages of pyridinic N, which are considered to be the main active sites for various electrocatalytic reactions [315, 342], are highest with the CNQD (54.8%), and marginally lower in CNNS and CNNR ($\sim$ 50.6%). The highest binding energy peak at 406.1 eV observed only with CNNR and CNQD could be due to the NO_2 that is derived from the oxidation of amino groups. The thermochemical oxidative etching of the nano-sheets oxidized the amino group in CNNR and CNQD.

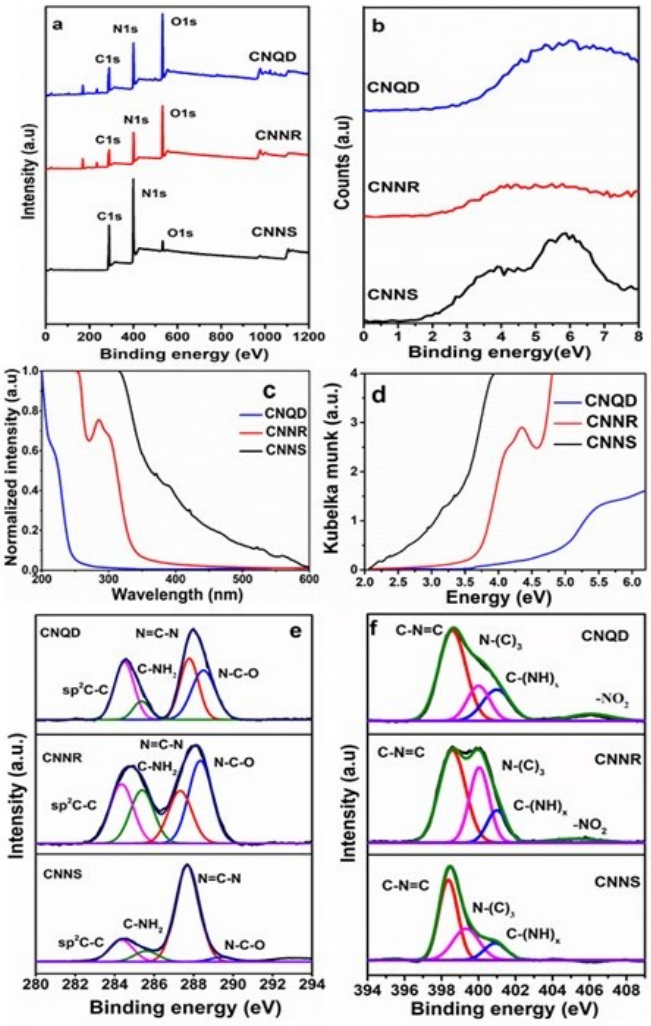

FIGURE 5.6: (a) XPS survey spectra, (b) XPS valence band spectra, (c) UV- visible spectra, and (d) Kubelka-Munk plot of CNNS, CNNR, and CNQD. High resolution core level spectra of (e) C 1s, and (f) N 1s of CNNS, CNNR, and CNQD

5.3.3 Electrocatalytic Oxidation of Methanol

After through characterization of the CNNS, CNNR, and CNQD samples, the electrocatalytic methanol oxidation properties were studied in alkaline solution (Figure 5.7). The CV plots of CNNS, CNNR, and CNQD catalyst in 0.5 M NaOH electrolyte in Figure 5.7(a-c) showed no characteristic peak in alkaline medium in the potential range of -0.2 to 0.8 V. However, the respective current densities were slightly different in 100th cycle compared to the first cycle. The MOR activities of three samples were performed by adding 0.5 M MeOH in electrolyte solution of 0.5 M NaOH. As revealed in Figure 5.7(d-f), the electrocatalytic oxidation of methanol over CNNS, CNNR, and CNQD modified electrodes were noticeable as all the samples showed the characteristic peak for methanol oxidation around 0.58 V with the anodic current density of

10.6, 6.8, and 13 A g^{-1}, respectively in first cycle. Apparently, the MOR activity of CNQD is maximum among the three C N-based catalysts.

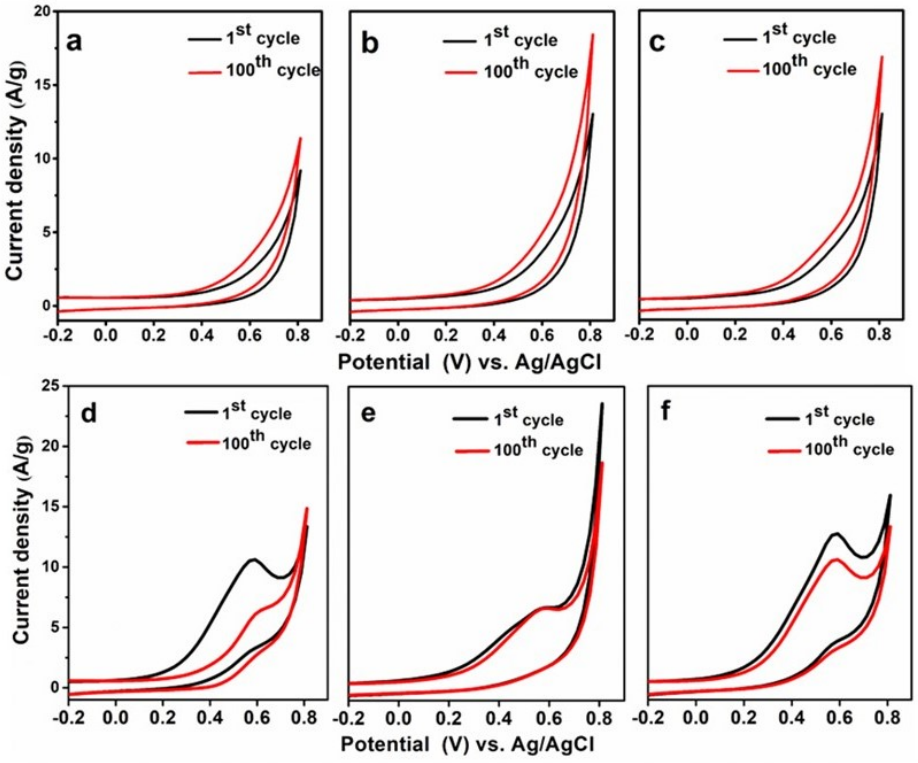

FIGURE 5.7: CVs of CNNS (a) CNNR (b) CNQD (c) in 0.5 M NaOH with a scan speed of 50 mV s^{-1}. CV traces of MOR of CNNS (d) CNNR (e) CNQD (f) modified GCE in the mixture of 0.5 M Methanol in 0.5 M NaOH solution

Again, to get better insight, we measured the ECSA of different CN based catalysts using cottrell equation from double step CA experts and the slope obtained is shown in Figure 5.8. To calculate ECSA was calculated using Cortell equation. The calculated ECSA values in Table 5.2 indicated the area of electroactive surface in CNQD (0.0011 cm^2) is way higher than other two electrodes. Compared to nano-sheets and nano-rods, the higher surface area along with the abundant edges of CNQD [343] made it a superior MOR catalyst among the three.

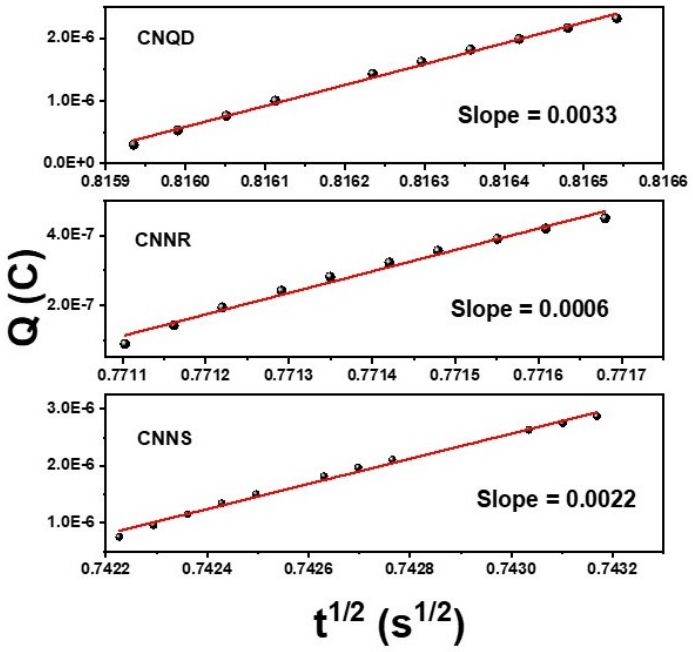

FIGURE 5.8: ECSA of CNNS, CNNR and CNQD

The catalytic activities were further compared by analysing electrochemical impedance spectroscopy during MOR activity of the g-C_3N_4 catalysts at 0.58 V using 0.5 M Methanol in 0.5 M NaOH solution. The Nyquist plots are given in Figure 5.9(a) along with the corroborated equivalent circuit to fit the experimental data in Figure 5.9(b). The results of EIS study are summarized in Table 5.3. The lowest semicircle arc of the Nyquist plot and the lowest value of charge transfer resistance (R_{ct}) in CNQD signified the faster interfacial charge transport on CNQD electrode to provide the best MOR activity among the CN based electrocatalysts. Nonetheless, the anodic current densities of MOR were drastically dropped in 100 th cycle as shown in Figure 5.7(d-f). The anodic current densities of MOR for CNNS, CNNR, and CNQD were 6.1, 6.5, and 10.8 A g^{-1}, respectively after 100^{th} cycle. The decrement of anodic peak current with cycles is quite less for CNQD in comparison with CNNS. Again, the appearance of a small but noteworthy oxidation peak around the same position of 0.58 V in reverse scan during the MOR activity of CNNS and CNQD modified electrodes denoted the oxidation of adsorbed carbonaceous species like CO in backward scan. We may assume that the carbonaceous species like CO, which were produced in forward scan during MOR, were adsorbed on the surface of the electrocatalyst, and effectively produced the catalyst poisoning to provide oxidation in reverse scan [344]. Therefore, we conclude that CNQD is very promising for electro catalytic methanol oxidation, though, the cycle stability and little CO poisoning were the matter of concern. It should be recalled that N 1s spectra showed CNQD possessed maximum atomic percentages of

active site of pyridinic N, which could be responsible for highest MOR activity of the quantum dot [315, 342]. However, probably the slow dissolution in the electrolyte solution of the CNQDs with electrochemical cycle in addition to poor electronic conductivity of the material are the reasons of the electrochemical instabilities. The homogeneous decoration of CNQDs with proper chemical interaction on a conducting polymer may resolve the issue of dissolution and limited electronic conductivity. Henceforth, we have prepared a homogeneous nanocomposite of CNQDs with conducting PANI by effective chemical interactions between –COOH groups of CNQDs and –NH- in PANI polymer chains [345, 346].

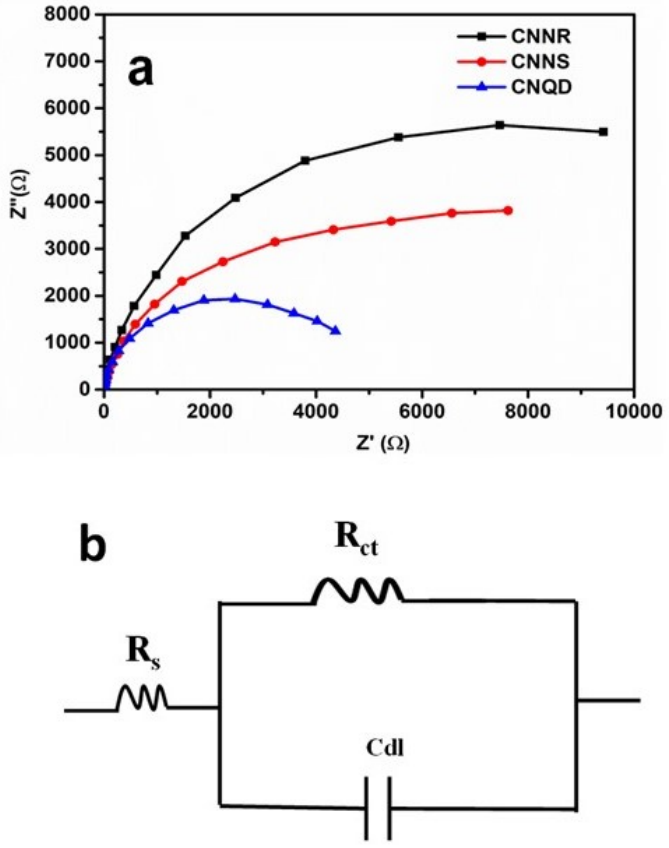

FIGURE 5.9: (a) Nyquist plots and (b) equivalent circuit of CNNS, CNNR, CNQD during MOR

5.3.4 Characterization of CNQD - PANI Nanocomposite

The CNQD - PANI nanocomposite was prepared by in-situ polymerization of aniline in presence of CNQD (1:1 wt. ratio) and ammonium per sulphate at low temperature. In this process, the CNQD acted as an organic acid (as it is having with – COOH groups) as well as the structure-directing agent. CNQD protonated the aniline to form anilinium cations. The anilinium cations provided a self-assembly with the organic acid to form an aniline filled vesicle

which directs the polymerization after addition of APS into PANI nanotubes [330]. Basically, the electrostatic interaction between the -COO^- part of CNQD and N centres of PANI would provide a homogeneous distribution of CNQD in composite structure and restricted the agglomeration of it to improve the catalytic activity. In the UV-Vis studies, CNQD exhibited a small hump around 225 nm as shown in Figure 5.10(a). However, CNQD - PANI nanocomposite revealed three absorbance peaks at 362 nm (π - $\pi*$ transition), 500 nm (polaron - π^* transition), and 880 nm (π- polaron transition). The appearance of the typical absorption peaks in CNQD - PANI confirmed the occurrence of emeraldine salt state of PANI chains in the nanocomposite [347]. The PL spectroscopy in Figure 5.10(b) displayed the effective quenching of the CNQD fluorescence after formation of the CNQD - PANI nanocomposite. The earlier studies reported that the complexation between the QDs with π - conjugated polymers can effectively quench the luminescence of the QDs by intermolecular interaction induced static quenching [348]. Herein, the in-situ polymerization of aniline in presence of CNQD provided a cooperative interaction between CNQD and PANI polymer chains as CNQDs are electrostatically interacting with PANI chains in emeraldine salt state of CNQD - PANI nanocomposite.

The comparative XRD study of CNQD and CNQD - PANI is shown in Figure 5.10(c). The powder XRD pattern revealed that the feeble (100) peak of CNQD was shifted towards lower angle at 12.28 ° in CNQD - PANI. The enhancement of d_{100} spacing in CNQD - PANI clearly confirmed the interaction between CNQDs with PANI in the composite. The XRD pattern of CNQD - PANI also confirmed the amorphous nature of the composite as it showed a broad peak cantered at 25.21 ∘, which was the typical periodicity of PANI polymers reported earlier [323]. The FT-IR spectrum of CNQD in Figure 5.10(d) exhibited the typical bands at 1723, 1640, 1385, 1090, and 805 cm^{-1} were respectively for carboxylic -C=O stretching, -C=N stretching, carboxylic -OH bending, -C-N stretching, and bending vibration of the triazine unit [328]. Appearance of a broad absorbance band at 3430 cm^{-1} was exclusively by the vibration of N - H and O - H bonds. After formation of CNQD - PANI composite, CNQD retained its typical bands for triazine unit at 803 cm^{-1} along with -C = O stretching, -C = N stretching, and -C - N stretching at 1715, 1620 and 1070 cm^{-1}, respectively. The appearance of characteristic bands at 3220, 1505, 1410, 1294, 1140 cm^{-1} for N – H stretching, C = C stretching of quinoid rings, C = C stretching of benzenoid rings, -C – N stretching respectively, which proved the formation of PANI chains by in-situ polymerization in presence of CNQDs. The core level XPS of C1s of CNQD - PANI shows the highest peak from adventitious carbon (sp^3 C–C) or sp^2 C-C bonds (Figure 5.10(e)). On the contrary, CNQD showed the higher content of C 1s from N = C – N

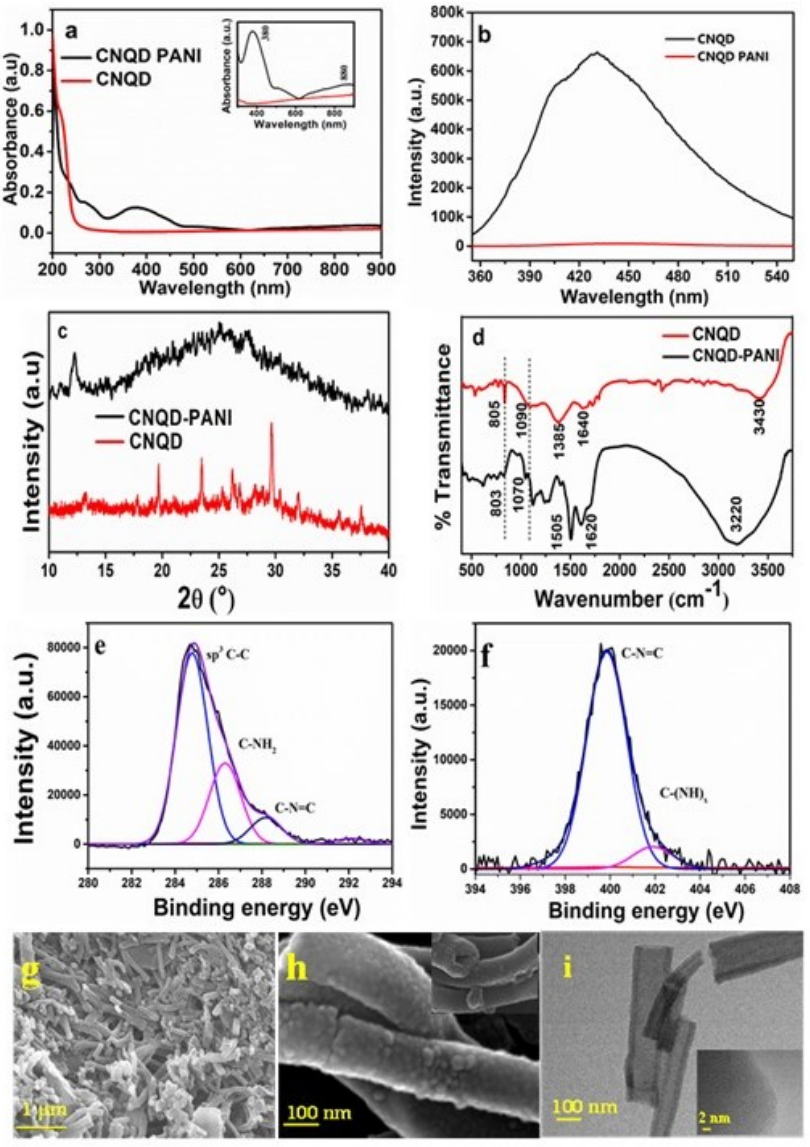

FIGURE 5.10: (a) UV - visible spectra (b) PL spectra excited at 320 nm (c) XRD profile and (d) IR spectra of CNQD and CNQD - PANI. High resolution core level spectra of (e) C 1s, and (f) N 1s of CNQD - PANI. (g-h) FE-SEM, and (i) TEM images of CNQD - PANI

and N – C - O coordination. The N 1s spectra (Figure 5.10(f)) showed significant differences than that of CNQD. The atomic percentages of pyridinic N in CNQD - PANI was found be highest ($\sim$ 90.8%), which is almost double the content in pristine CNQD. The SEM image study in Figure 5.10 (g-h) revealed the one-dimensional nanofibers with different diameters and several micrometre length in CNQD - PANI nanocomposite. The SEM study also evidenced the rougher surface of the nanofibers. The rougher surface in the high aspect ratio nanofibers would increase the available surface area and escalate the ion diffusion process for the electrocatalyst which may accelerate the electro catalysis activities. In HR-TEM images shown in Figure 5.10(i), the CNQD - PANI composite again showed the nanofibrous morphology with various diameters.

The clear contrast difference between the edges and the central part of the nanofibers denoted the nanotube morphology. The CNQDs are residing on the wall of the nanotubes as it directed (as an organic acid) the nanotubular structures in in-situ CNQD - PANI composite.

5.3.5 MOR Activity of CNQD - PANI

The MOR activity of CNQD - PANI nanocomposite was investigated in alkaline medium. The CV plot of the CNQD - PANI modified electrode in alkaline medium is shown in Figure 5.11(a). In comparison with the CV in alkaline medium of CNQD modified electrode in Figure 5.11(a), the CNQD - PANI composite showed 10 fold increment of current density in similar condition. Introduction of PANI into CNQD effectively increased the current density herein. The MOR study using 0.5 M methanol in alkaline medium of CNQD and CNQD - PANI is given in Figure 5.11(b). The CNQD - PANI nanocomposite revealed a significant oxidative peak for MOR around 0.54 V. It was found that the current density (mass activity) of MOR reaction was increased from 13 A g^{-1} in CNQD to 28.4 A g^{-1} in CNQD - PANI, which was 120% of enhancement of electro catalytic activity over CNQD - PANI nanocomposite compared to the pristine quantum dot. It should be noted that the presence of active site of pyridinic N was double in CNQD - PANI than that of pristine CNQD. Again, in Figure 5.11(c), it was very encouraging to observe that there was no significant decrease in peak current density for MOR even after 150^{th} cycle of electro-oxidation by CNQD - PANI. The current density of methanol oxidation by CNQD - PANI in first cycle (28.4 A g^{-1}) was remained consistent in 150^{th} cycle, which was measured to be 27.7 A g^{-1}. The voltammograms recorded at various concentrations of methanol from 0.5 to 5.0 M in Figure 5.11(d) divulged the effect of the concentrations of methanol on the MOR efficacy of the CNQD - PANI modified electrode. The MOR current densities increased with the enhancement of methanol concentration in alkaline medium [349]. Noticeably, the inset of Figure 5.11(d) revealed the linear relation of MOR current densities with methanol concentration. We have also studied the EIS to exhibit the better MOR activity over CNQD - PANI electrode. The EIS spectra shown in Figure 5.11(e) depicted the lesser semicircle arc in CNQD - PANI modified electrode and corresponding equivalent circuit Figure 5.11(f) received by fitting the EIS data revealed the lower R_{ct} value (shown in Table 5.3) confirmed the better interfacial charge transport on CNQD - PANI which elevated the MOR activity in CNQD - PANI.

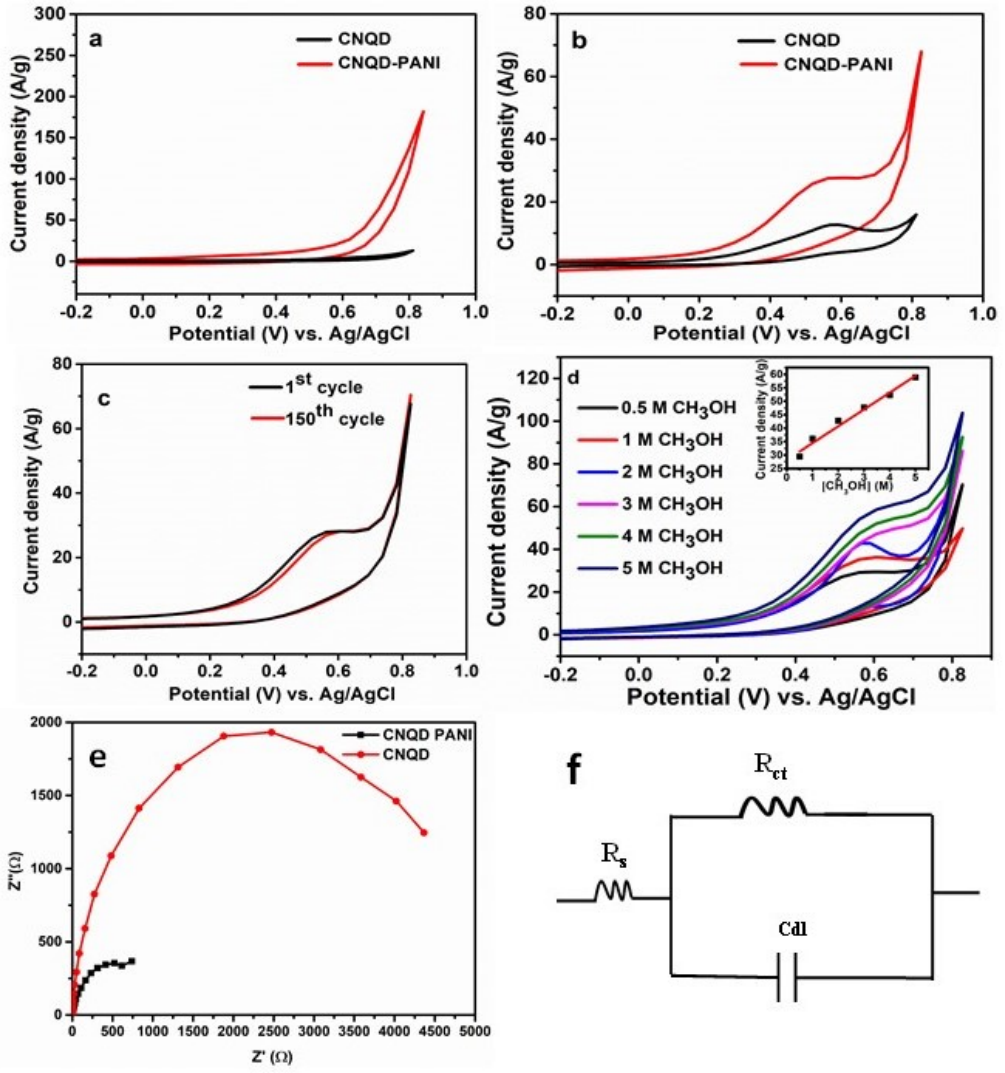

FIGURE 5.11: (a) CVs of CNQD and CNQD PANI in 0.5 M NaOH with a scan speed of 50mV s^{-1}, (b) CV traces of MOR of CNQD and CNQD PANI modified GCE in the mixture of 0.5 M Methanol and 0.5 M NaOH, (c) CV traces of first (black line) and 150th cycle (red line) in 0.5 M Methanol and 0.5 M NaOH, (d) CV curves of MOR of CNQD - PANI in different methanol concentration. (e) Nyquist plots and (f) equivalent circuit of two electrodes during MOR above mentioned conditions

The exceptional ECSA of CNQD - PANI as shown in Table 5.2 gave a piece of strong evidence for enhanced MOR reaction with the proper dispersion of CNQD on PANI with very less agglomeration (Figure 5.12(a)). To evaluate the stability of catalyst, CA study of MOR was performed on CNQD and CNQD - PANI modified electrodes. As shown in the Figure 5.12(b), CA curves showed current density change in 3600 s at 0.54V. In the starting, the current densities decreased steeply because of the adsorption of the reaction intermediate on the surface of the catalyst and then turn to stable with the time.

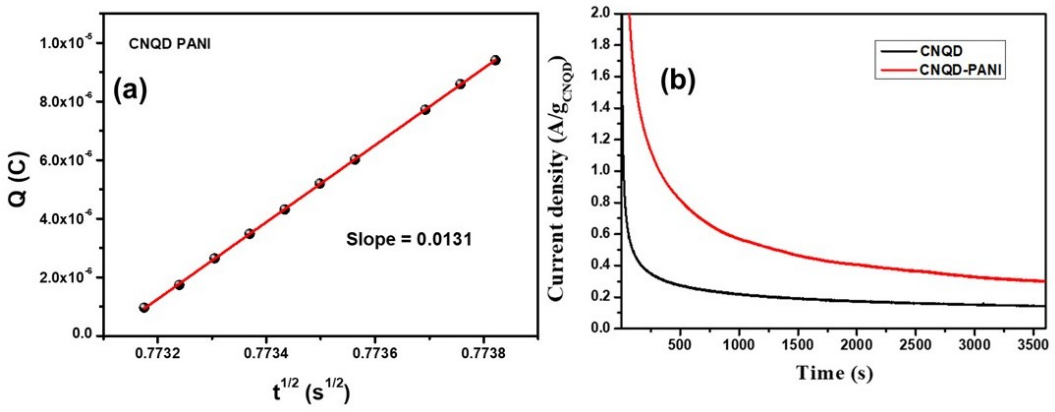

FIGURE 5.12: (a) ESCA of CNQD PANI (b) CA curves of CNQD and CNQD - PANI based electrodes at 0.54 V during MOR using 0.5 M Methanol in 0.5 M NaOH.

TABLE 5.2: Summary of MOR activity and ECSA of all the catalysts

Catalysts	I_f (A g^{-1})	I_g(A g^{-1})	Current density (mA cm^{-2})	ECSA (cm^2)	If/Ib
CNQD - PANI	28.4	7.93	1.06	0.0043	3.58
CNQD	13	3.78	0.18	0.0011	3.43
CNNR	6.8	No peak	0.09	0.0002	4.43
CNNS	10.6	2.58	0.10	0.0007	4.10

Furthermore, the stability of the CNQD - PANI based electrocatalyst was tested by cycle study up to 1000 cycles by two different concentrations of methanol. The Figure 5.13(a) clearly indicated that the current density is stable at above 92% of the initial value even after 1000 cycles irrespective of concentration. This study clearly confirmed the extremely stable catalytic activity of CNQD - PANI nanocomposite for methanol electro-catalytic oxidation in alkaline medium. The restriction of dissolution of the quantum dots from interacted polymer matrix along with the higher electrical conductivity due to integration of PANI in the CNQD - PANI composite are probably the prime factors for enhanced electrocatalytic activity of quantum dot herein. To compare the MOR activity of CNQD - PANI nanocomposite with commercially available Pt/C material, we have performed the MOR of all the materials in 0.5 M NaOH electrolyte using 0.5 M methanol and the voltammograms are shown in Figure 5.13(b). The 20% Pt/C modified electrode exhibited the characteristic methanol oxidation peak at -0.15 V (vs. Ag/AgCl) in alkaline medium. Interestingly, the CNQD - PANI nanocomposite based composite outperformed the 20% Pt/C based catalyst as the Pt/C based electrode exhibited the MOR current density (mass activity) of 12.15 A g^{-1}, which was much lower than the current density of 28.4 A g^{-1} shown by CNQD - PANI based electrode. It is noteworthy that, Cui et al. earlier reported the MOR current density of commercial 20% Pt/C (Johnson Matthey) in 0.5 M methanol to be ~9 A g^{-1} in similar alkaline condition [350]. The comparison of the MOR current densities of CNQD - PANI with other materials can clearly be shown by a representative bar plot in Figure

5.13(c), which indicated the best MOR performance of CNQD - PANI composite compared to Pt/C, PANI and CNQD itself. To benchmark our catalyst, we have compared the MOR performance of CNQD - PANI with other metallic catalysts under alkaline medium, and the data is presented in Table 5.2. It is clear that the metal free CNQD - PANI even outperforms many metallic catalysts.

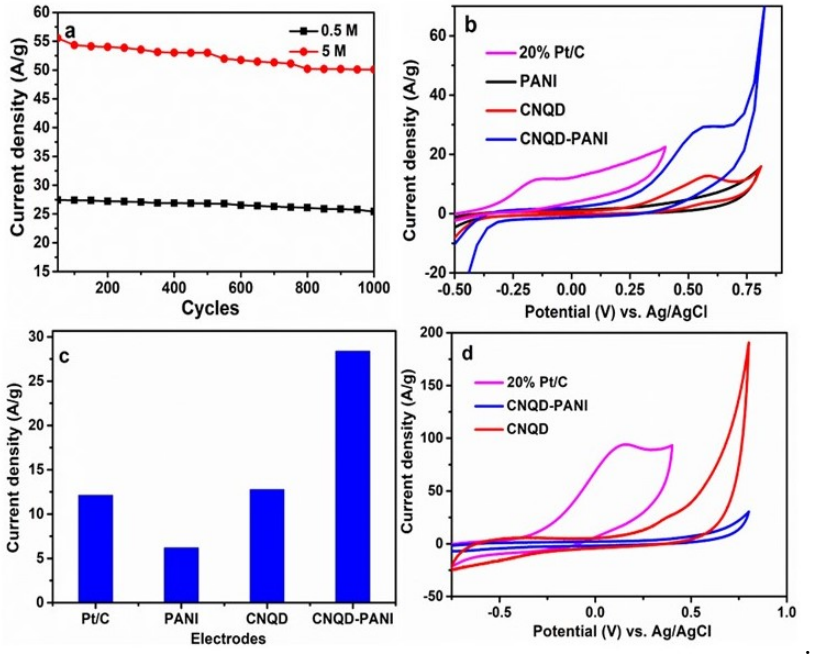

FIGURE 5.13: (a) The change of current density of MOR with cycles over CNQD PANI in 0.5 M and 5M methanol concentration, (b) CV curves of different samples for methanol oxidation, (c) Bar diagram to show the comparison of MOR current density, and (d) CO stripping curve of the samples in 0.5 M NaOH as electrolyte

The CO poisoning is another impending problem in Pt or other metal based electrocatalysts and it is always challenging to avert the CO poisoning in an electrocatalyst to enhance the catalytic activity. To compare the CO tolerance, we preformed the CO stripping evolution studies on CNQD, CNQD - PANI, and Pt/C modified electrodes and the corresponding voltammograms are shown in in Figure 5.13(d). In the CO-stripping experiment, the intense peak at 0.16 V was observed in commercial Pt/C based electrode after bubbling CO for 15 min over the catalyst-modified working electrode. Typically, the generated oxidation peak is fairly attributed to the oxidation of adsorbed CO to CO_2 on the electrocatalyst surface and catalyst poisoning is linearly related with the intensity of the peak. The CNQD modified electrode also exhibited a small hump around 0.3 V vs Ag/AgCl in CO purged condition to show a minimal CO adsorption on its surface. The limited CO adsorption over CNQD was also noticed during MOR study in Figure 5.13(d), where a small CO oxidation peak was perceived in reverse scan. Very interestingly, the

CNQD - PANI based electrode did not exhibit any trace of CO oxidation even after similar CO gas feeding. This experiment clearly advocated the better CO tolerance of CNQD - PANI based electrocatalyst compare to CNQD, and most importantly, to Pt/C based commercial electrodes. The presence of PANI can contribute the conversion of CO to CO_2 during electro catalytic MOR to upsurge the CO tolerance of the modified electrode material by interacting with water in electrolyte [351, 352]. Again, CO has stable resonance [+ C≡O–], with a positive charge at the carbon atom, which can be attracted by the lone pair electron at the N-atoms in PANI to provide CO adsorption on PANI nitrogen [353]. Thus CNQD becomes free from CO poisoning. The postulate mechanism of the MOR by CNQD based catalyst in alkaline medium is shown in Figure 5.14 [354, 355]. In a probable mechanism, the CH_3OH is absorbed on the catalyst surface firstly. Afterwards, it can form CNQD-CO_{ad} which provides CO_2 interacting with OH- or the CNQD - OH_{ad} which are present in alkaline medium. Additionally, the methanol oxidation can undergo by two partial oxidation pathways having HCOOH or HCHO as intermediate. However, in all cases the complete reaction is associated with $6e^-$ and the final product is CO_2. We didn't probe the exact mechanism, although, anticipated the mechanism as shown in Figure 5.14. Overall, the prepared CNQD - PANI nanocomposite demonstrates not only the high electrocatalytic MOR activity but also shows exceptional CO endurance, which can make it a potential metal free anode catalyst in DMFCs applications.

TABLE 5.3: Summary of the electrochemical parameters for MOR

Catalysts	R_s (Ω)	R_{ct} (Ω)	C_{dl} (μF)
CNQD - PANI	37.54	755.63	55.77
CNQD	58.50	4532.56	33.52
CNNR	62.77	7507.51	21.53
CNNS	68.53	9100.20	25.78

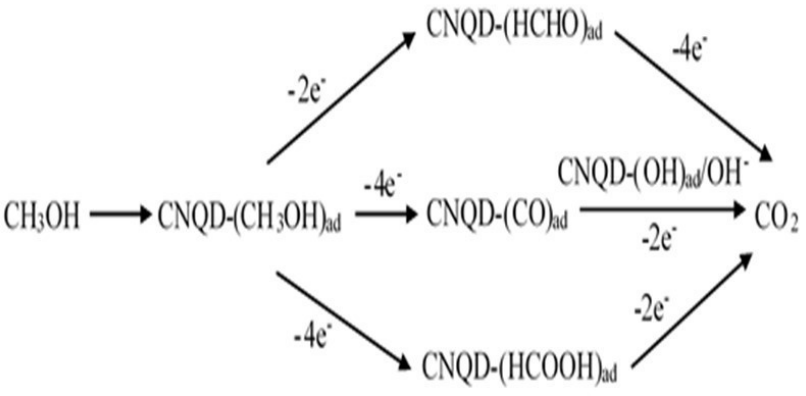

FIGURE 5.14: The possible mechanisms of MOR activity on CNQD electrocatalyst in alkaline medium.

5.4 Conclusion

In conclusion, three morphologically engineered g-C_3N_4 materials (2 D CNNS, 1 D CNNR, and 0 D CNQD) has been successfully synthesized from bulk g-C_3N_4 by a thermo-chemical etching process and are though characterized through XRD, FT-IR, XPS, FE-SEM, TEM, PL spectroscopy. The g-C_3N_4 materials are employed as completely metal free electrocatalyst for MOR in alkaline medium. Among the three different dimensional g-C_3N_4 materials, CNQD shows best electro catalytic methanol oxidation activity owing to its abundant edges in quantum dot morphology and maximum atomic percentages of active site of pyridinic N which are responsible for better MOR. However, electro catalytic process on CNQD is not stable as it shows a significant current density drop from 13 A g^{-1} in first cycle to 10.8 A g^{-1} in 100^{th} cycle. The instability is attributed to slow dissolution of catalyst in alkali medium and less electrical conductivity of the electrode materials. The issue was solved by incorporation of PANI nanofibers with CNQD by synthesizing novel CNQD - PANI nanocomposite through in-situ polymerization of aniline in presence of CNQD. The completely metal free CNQD - PANI nano composite shows high current density of 28.4 A g^{-1} in first cycle which retains up to 92% even after 1000 electro catalysis cycles. The composite catalyst also reveals better MOR activity to the commercial 20 wt% Pt/C catalyst, and much higher CO tolerance property than the latter in MOR. The electrostatic interaction between CNQD and conducting PANI fibres can effectively hold the CNQDs to restrict the dissolution. Again, presence of PANI can also improve the electrical conductivity and methanol adsorption of CNQD - PANI electrocatalyst which led to better MOR activity of the metal free catalyst. The PANI nanofibers also play a role of catalysing the adsorbed CO species into CO_2 during MOR in alkaline solution to upsurge the CO tolerance. Finally, the enhanced durability, better electro catalytic activity compare to commercial 20% Pt/C, and great CO tolerance of synthesized metal free CNQD - PANI can make it greatly favourable to provide efficient and cost-effective electrocatalyst for DMFC in real fuel cell applications.

Chapter 6

Conclusion and Outlook

The study herein offers a systematic and chronological assessment of the descriptors concerning Ni-based oxide catalysts, aiming to enhance our comprehension and optimization of the MOR. While extensive research has already been conducted on evaluating catalytic descriptors in OER, these comprehensive investigations mark the inaugural endeavour to systematically unravel the catalytic descriptors relevant to MOR. The study delves into descriptors such as (i) the facile redox ability of active metal sites, (ii) occupancy of eg orbitals, (iii) metal-oxygen covalency, and (iv) defect engineering and lattice strain.

In Chapters 2A and 2B, we investigated descriptors such as electron occupancy in the eg level and covalency in Ni-based $La_2NiO_{4+\delta}$ Ruddlesden-Popper oxides. Employing solution combustion synthesis, we produced pure Ruddlesden-Popper oxides with abundant surface oxygen vacancies. Chapter 2A revealed intriguing structural insights, particularly with Sr^{2+} doping in $La_2NiO_{4+\delta}$, where we observed tetragonal elongation accompanied by a reduction in lattice constant a/b and an increase in the c parameter, resulting in Jahn-Teller distortion. This was confirmed through refinement and XAFS studies. Optimal Sr^{2+} doping induced a high degree of Ni^{3+} 3d–O 2p hybridization, positioning the O 2p center close to the Fermi level, thereby transitioning the material from insulator to semi-metal and facilitating electron mobility. Consequently, $La_{1.4}Sr_{0.6}NiO_{4+\delta}$ exhibited enhanced MOR activity due to increased conductivity and facile oxidation of lattice oxygen. Conversely, additional doping on the B-site with (Mn/Fe/Co) in Chapter 2B reversed this trend, leading to a sharp decrease in the 'c' parameter and gradual increase in 'a'/'b'. The heightened concentration of Ni^{3+} resulting from B-site doping potentially prompted a shift in the electronic configuration to $t_{2g}^6\ d_{x^2-y^2}^1$ from

$t_{2g}^6 d_z^2$, transitioning from semi-metallic to metallic behavior, as corroborated by DFT calculations. This transition culminated in $La_{1.4}Sr_{0.6}Ni_{0.9}(Mn/Fe/Co)_{0.1}O_{4+\delta}$ exhibiting high MOR activity.

In subsequent chapters focusing on fluorites (Chapter 3A and 3B), we employed ionic doping of CeO_2 with Ni^{2+}, Sr^{2+}, and Zr^{2+} via the solution combustion method, aiming to enhance reducibility and oxygen vacancies. The study investigated the use of reducible solid solution supports to promote the oxidation of $Ni^{2+} \rightarrow Ni^{3+}$ at active sites and improve MOR kinetics, employing $Ce_{1-x-y}Ni_xSr_yO_{2-\delta}$ and $Ce_{1-x-y}Zr_xNi_yO_{2-\delta}$ solid solutions. Increased reducibility in these catalysts facilitated lattice oxygen evolution within the positive potential window, enhancing CO tolerance through reaction with adsorbed CO. The enhanced ease of lattice oxygen evolution due to increased Ce^{4+} reducibility significantly contributed to superior CO oxidation.

The concept of lattice strain was studied with doped $NiMoO_4$ in chapter 4. Hydrothermal synthesis was adopted for $NiMoO_4$ and Co doped $NiMoO_4$ to create strain in the system. Lattice-strain engineering via lattice compression or tension paved away to enhance MOR in $NiMoO_4$ by surface reconstruction by adjusting the metal surface's electronic structure and promoting the intrinsic activity of the reaction site. During MOR, significant concentration of formic acid led to explore the molybdates for methanol assisted HER.

As we moved from metallic to non-metal-based catalyst, in the last and final chapter, controlled synthesis was adopted to make metal-free g C_3N_4 with different morphology from bulk to quantum dot. The controlled cutting of the nano-sheets to 1D nano-rods, and 0D quantum dots also showed significant active catalysts for methanol oxidation. The implementation of thermal etching in aerobic condition followed by hydrothermal treatment to create CNQD from CNNS via CNNR resulted in creating abundant edges. The maximum percentages of active site of pyridinic N and abundant edges were responsible for MOR. Incorporation of PANI solved the stability issue by the electrostatic interaction between CNQD and conducting PANI fibres that effectively hold the CNQDs to restrict the dissolution.

6.1 Future Scope of Work

The research presented in this thesis makes a significant contribution to the realm of catalysis via various descriptors on electrocatalytic MOR. Through meticulous investigation and analysis, the work seeks to shed light on underlying mechanisms and descriptors of various

Ni-based oxides and a metal free catalyst aiming to uncover fundamental insights into their performance. In the future, there are numerous promising directions for further research and development. These potential areas of concentration include:

(i) Taking advantages of high-throughput computing and machine learning methods, the structure-activity relation can be studied from a wide range of degrees of freedom and descriptors can be effectively extracted from the atomic microscale.

(ii) Using operando techniques to probe active sites will be a direct means of identifying the active centre and improving the certainty of the reaction processes that underlying it. This will be more useful to clarify what parameter governs and what pathway is more thermodynamically favourable for MOR. These include in-situ XAS, in situ DRIFT corroborated with DFT computations, femtosecond spectra, NAP-XPS, NAP-STM, etc.

(iii) The majority of earlier studies were only carried out in the half-cell. Setting up of DMFC which is cost effective, economically practical and easy to handle in real devices would be desired to further probe their promising application property. Methanol assisted green hydrogen production is currently a focal point in the realm of hydrogen generation. This method offers the potential to create clean hydrogen energy with reduced energy consumption. Efforts in combining hydrogen generation and methanol oxidation reactions necessitate highly efficient bifunctional catalysts.

Bibliography

(1) Scheffran, J.; Felkers, M.; Froese, R. *Green energy to sustainability: strategies for global industries* **2020**, 1–44.

(2) Olah, G. A.; Goeppert, A.; Prakash, G. S., *Beyond oil and gas: the methanol economy*; John Wiley & Sons: 2011.

(3) Simon Araya, S.; Liso, V.; Cui, X.; Li, N.; Zhu, J.; Sahlin, S. L.; Jensen, S. H.; Nielsen, M. P.; Kær, S. K. *Energies* **2020**, *13*, 596.

(4) Mondal, U.; Yadav, G. D. *Green Chemistry* **2021**, *23*, 8361–8405.

(5) Li, K.; Jiang, D. *Journal of Molecular Catalysis A: Chemical* **1999**, *147*, 125–130.

(6) Lange, J.-P. *Industrial & engineering chemistry research* **1997**, *36*, 4282–4290.

(7) Payra, S.; Devaraj, N.; Tarafder, K.; Roy, S. *ACS Applied Energy Materials* **2022**, *5*, 4945–4955.

(8) Payra, S.; Kanungo, S.; Roy, S. *Nanoscale* **2022**, *14*, 13352–13361.

(9) Payra, S.; Shenoy, S.; Chakraborty, C.; Tarafder, K.; Roy, S. *ACS applied materials & interfaces* **2020**, *12*, 19402–19414.

(10) Marchionna, M.; Lami, M; Galletti, A. M. *Chemtech* **1997**, *27*.

(11) Al Shouny, A.; Rezk, H.; Sayed, E. T.; Abdelkareem, M. A.; Issa, U. H.; Miky, Y.; Olabi, A. G. *Biomimetics* **2023**, *8*, 557.

(12) Kamarudin, S. K.; Achmad, F; Daud, W. R. W. *International Journal of hydrogen energy* **2009**, *34*, 6902–6916.

(13) Arshad, F.; Haq, T. u.; Hussain, I.; Sher, F. *ACS Applied Energy Materials* **2021**, *4*, 8685–8701.

(14) Liu, C.; Feng, L. *Chinese Journal of Structural Chemistry* **2023**, 100136.

(15) Hao, Y.; Yu, D.; Zhu, S.; Kuo, C.-H.; Chang, Y.-M.; Wang, L.; Chen, H.-Y.; Shao, M.; Peng, S. *Energy & Environmental Science* **2023**, *16*, 1100–1110.

(16) Gao, X.; Deng, H.; Dai, Q.; Zeng, Q.; Qiu, S.; Lu, X. *Catalysts* **2021**, *12*, 2.

(17) Chen, L.; Shi, J. *Journal of Materials Chemistry A* **2018**, *6*, 13538–13548.

(18) Liu, Q.; Du, S.; Liu, T.; Gong, L.; Wu, Y.; Lin, J.; Yang, P.; Huang, G.; Li, M.; Wu, Y., et al. *Angewandte Chemie International Edition* **2024**, *63*, e202315157.

(19) Wei, X.; Wang, S.; Hua, Z.; Chen, L.; Shi, J. *ACS applied materials & interfaces* **2018**, *10*, 25422–25428.

(20) Yuda, A.; Ashok, A.; Kumar, A. *Catalysis Reviews* **2022**, *64*, 126–228.

(21) Zhao, X.; Yin, M.; Ma, L.; Liang, L.; Liu, C.; Liao, J.; Lu, T.; Xing, W. *Energy & Environmental Science* **2011**, *4*, 2736–2753.

(22) Abdullah, M. I.; Hameed, A.; Zhang, N.; Islam, M. H.; Ma, M.; Pollet, B. G. *ACS Applied Materials & Interfaces* **2021**, *13*, 30603–30613.

(23) Anantharaj, S.; Sugime, H.; Noda, S. *ACS Applied Materials & Interfaces* **2020**, *12*, 27327–27338.

(24) El-Shafei, A. *Journal of Electroanalytical Chemistry* **1999**, *471*, 89–95.

(25) Yaqoob, L.; Noor, T.; Iqbal, N. *International Journal of Energy Research* **2021**, *45*, 6550–6583.

(26) Liu, S. X.; Liao, L. W.; Tao, Q.; Chen, Y. X.; Ye, S. *Physical Chemistry Chemical Physics* **2011**, *13*, 9725–9735.

(27) Liu, Y.; Wang, Q.-L.; Yang, Y.-Y. *Langmuir* **2022**, *38*, PMID: 36205573, 12510–12520.

(28) Qi, X.; Ye, N.; Zhang, R.; Jiang, Z.; Fang, T. *Fuel* **2023**, *350*, 128773.

(29) Zhang, Z.-C.; Tian, X.-C.; Zhang, B.-W.; Huang, L.; Zhu, F.-C.; Qu, X.-M.; Liu, L.; Liu, S.; Jiang, Y.-X.; Sun, S.-G. *Nano Energy* **2017**, *34*, 224–232.

(30) Wang, J.; Zhang, B.; Guo, W.; Wang, L.; Chen, J.; Pan, H.; Sun, W. *Advanced Materials* **2023**, 2211099.

(31) Meenu, P. C.; Datta, S. P.; Singh, S. A.; Dinda, S.; Chakraborty, C.; Roy, S. *Molecular Catalysis* **2021**, *510*, 111710.

(32) Meenu, P. C.; Roy, S.; Chakraborty, C.; Roy, S. *Advanced Powder Technology* **2021**, *32*, 2663–2689.

(33) Abdel-Hady, E.; Gamal, A.; Hamdy, H.; Shaban, M.; Abdel-Hamed, M.; Mohammed, M. A.; Mohammed, W. M. *Scientific Reports* **2023**, *13*, 4870.

(34) Papadimitriou, S.; Armyanov, S.; Valova, E.; Hubin, A.; Steenhaut, O.; Pavlidou, E.; Kokkinidis, G.; Sotiropoulos, S. *The Journal of Physical Chemistry C* **2010**, *114*, 5217–5223.

(35) Jamil, R.; Sohail, M.; Baig, N.; Ansari, M. S.; Ahmed, R. *Scientific Reports* **2019**, *9*, 15273.

(36) Candelaria, S. L. et al. *ACS Catalysis* **2017**, *7*, 365–379.

(37) Kropp, T.; Paier, J.; Sauer, J. *Journal of the American Chemical Society* **2014**, *136*, 14616–14625.

(38) Wang, Y.; Li, Z.; Zheng, X.; Wu, R.; Song, J.; Chen, Y.; Cao, X.; Nie, Y. *Applied Catalysis B: Environmental* **2023**, *325*, 122383.

(39) Wang, X. et al. *Nature Communications* **2020**, *11*, 4647.

(40) Roy, S.; Hegde, M. *Catalysis Communications* **2008**, *9*, 811–815.

(41) Mazumder, T.; Dandapat, S.; Baidya, T.; Likhar, P. R.; Clark, A. H.; Bera, P.; Tiwari, K.; Payra, S.; Srinivasa Rao, B.; Roy, S., et al. *The Journal of Physical Chemistry C* **2021**, *125*, 20831–20844.

(42) Baidya, T. et al. *The Journal of Physical Chemistry C* **2020**, *124*, 14131–14146.

(43) Tan, Q.; Shu, C.; Abbott, J.; Zhao, Q.; Liu, L.; Qu, T.; Chen, Y.; Zhu, H.; Liu, Y.; Wu, G. *ACS Catalysis* **2019**, *9*, 6362–6371.

(44) Kaur, B.; Srivastava, R.; Satpati, B. *ACS Catalysis* **2016**, *6*, 2654–2663.

(45) Suntivich, J.; May, K. J.; Gasteiger, H. A.; Goodenough, J. B.; Shao-Horn, Y. *Science* **2011**, *334*, 1383–1385.

(46) Suntivich, J.; Gasteiger, H. A.; Yabuuchi, N.; Nakanishi, H.; Goodenough, J. B.; Shao-Horn, Y. *Nature chemistry* **2011**, *3*, 546–550.

(47) Vojvodic, A.; Nørskov, J. K. *Science* **2011**, *334*, 1355–1356.

(48) Grimaud, A.; Hong, W. T.; Shao-Horn, Y; Tarascon, J.-M. *Nature materials* **2016**, *15*, 121–126.

(49) Kuznetsov, D. A.; Han, B.; Yu, Y.; Rao, R. R.; Hwang, J.; Román-Leshkov, Y.; Shao-Horn, Y. *Joule* **2018**, *2*, 225–244.

(50) Li, S.; Ma, R.; Hu, J.; Li, Z.; Liu, L.; Wang, X.; Lu, Y.; Sterbinsky, G. E.; Liu, S.; Zheng, L.; Liu, J.; Liu, D.; Wang, J. *Nature Communications* **2022**, *13*, 2916.

(51) Dubale, A. A.; Zheng, Y.; Wang, H.; Hübner, R.; Li, Y.; Yang, J.; Zhang, J.; Sethi, N. K.; He, L.; Zheng, Z., et al. *Angewandte Chemie International Edition* **2020**, *59*, 13891–13899.

(52) Li, W.; Wang, D.; Zhang, Y.; Tao, L.; Wang, T.; Zou, Y.; Wang, Y.; Chen, R.; Wang, S. *Advanced Materials* **2020**, *32*, 1907879.

(53) Yan, X.; Zhuang, L.; Zhu, Z.; Yao, X. *Nanoscale* **2021**, *13*, 3327–3345.

(54) Chattot, R.; Bordet, P.; Martens, I.; Drnec, J.; Dubau, L.; Maillard, F. *ACS Catalysis* **2020**, *10*, 9046–9056.

(55) Zhu, K.; Shi, F.; Zhu, X.; Yang, W. *Nano energy* **2020**, *73*, 104761.

(56) Kumar, T. N.; Swamynadhan, M; Ghosh, S.; Neppolian, B *Sustainable Energy & Fuels* **2022**, *6*, 3573–3581.

(57) Shi, X; Zheng, H; Kannan, A. M.; Pérez-Salcedo, K; Escobar, B *Inorganic chemistry* **2019**, *58*, 5335–5344.

(58) Phan, V. T. T.; Nguyen, Q. P.; Wang, B.; Burgess, I. J. *Journal of the American Chemical Society* **2024**, *146*, 4830–4841.

(59) Yang, W.; Yang, X.; Jia, J.; Hou, C.; Gao, H.; Mao, Y.; Wang, C.; Lin, J.; Luo, X. *Applied Catalysis B: Environmental* **2019**, *244*, 1096–1102.

(60) Huang, Z.; Li, W.; Jiang, J.; Zhou, W.; Zhang, M.; Mao, R.; Wang, Z.; Xie, J.; Hu, Z. *Journal of Colloid and Interface Science* **2024**, *654*, 164–173.

(61) Seselj, N.; Engelbrekt, C.; Ding, Y.; Hjuler, H. A.; Ulstrup, J.; Zhang, J. *Advanced Energy Materials* **2018**, *8*, 1702609.

(62) Huynh, T. T.; Huynh, Q.; Nguyen, Q. V.; Pham, H. Q. *Inorganic Chemistry* **2023**, *62*, 20477–20487.

(63) Hwang, J.; Feng, Z.; Charles, N.; Wang, X. R.; Lee, D.; Stoerzinger, K. A.; Muy, S.; Rao, R. R.; Lee, D.; Jacobs, R., et al. *Materials Today* **2019**, *31*, 100–118.

(64) Yang, X.; Wang, Y.; Tong, X.; Yang, N. *Advanced Energy Materials* **2022**, *12*, 2102261.

(65) Zhang, X.; Wang, H.; Key, J.; Linkov, V.; Ji, S.; Wang, X.; Lei, Z.; Wang, R. *Journal of the Electrochemical Society* **2012**, *159*, B270.

(66) Li, L.; Tan, S.; Salvatore, K. L.; Wong, S. S. *Chemistry – A European Journal* **2019**, *25*, 7779–7797.

(67) Yavari, Z.; Noroozifar, M.; Khorasani-Motlagh, M. *Journal of Applied Electrochemistry* **2015**, *45*, 439–451.

(68) Du, J.; You, S.; Li, X.; Tang, B.; Jiang, B.; Yu, Y.; Cai, Z.; Ren, N.; Zou, J. *ACS applied materials & interfaces* **2019**, *12*, 686–697.

(69) Nakamura, T.; Oike, R.; Ling, Y.; Tamenori, Y.; Amezawa, K. *Physical Chemistry Chemical Physics* **2016**, *18*, 1564–1569.

(70) Zhao, H.; Mauvy, F.; Lalanne, C.; Bassat, J.-M.; Fourcade, S.; Grenier, J.-C. *Solid State Ionics* **2008**, *179*, 2000–2005.

(71) Zhou, N.; Chen, G.; Zhang, H.; Zhou, C. *Physica B: Condensed Matter* **2009**, *404*, 4150–4154.

(72) Egger, A.; Schrödl, N.; Gspan, C.; Sitte, W. *Solid State Ionics* **2017**, *299*, 18–25.

(73) Ma, X.; Wang, B.; Xhafa, E.; Sun, K.; Nikolla, E. *Chemical Communications.* **2015**, *51*, 137–140.

(74) Mizoguchi, T.; Sonoki, H.; Niwa, E.; Taminato, S.; Mori, D.; Takeda, Y.; Yamamoto, O.; Imanishi, N. *Solid State Ionics* **2021**, *369*, 115708.

(75) Aguadero, A.; Escudero, M. J.; Pérez, M.; Alonso, J. A.; Pomjakushin, V.; Daza, L. *Dalton Transactions* **2006**, 4377–4383.

(76) Forslund, R. P.; Hardin, W. G.; Rong, X.; Abakumov, A. M.; Filimonov, D.; Alexander, C. T.; Mefford, J. T.; Iyer, H.; Kolpak, A. M.; Johnston, K. P.; Stevenson, K. J. *Nature Communications* **2018**, *9*.

(77) Akbay, T.; Staykov, A.; Druce, J.; Téllez, H.; Ishihara, T.; Kilner, J. A. *Journal of Material Chemistry A* **2016**, *4*, 13113–13124.

(78) Ishikawa, K.; Kondo, S.-i.; Okano, H.; Suzuki, S.; Suzuki, Y. *Bulletin of the Chemical Society of Japan* **2006**, *60*, 1295–1298.

(79) Inprasit, T.; Limthongkul, P.; Wongkasemjit, S. *Journal of The Electrochemical Society* **2010**, *157*, B1726.

(80) Suntivich, J.; May, K. J.; Gasteiger, H. A.; Goodenough, J. B.; Shao-Horn, Y. *Science* **2011**, *334*, 1383–1385.

(81) Zhou, S.; Miao, X.; Zhao, X.; Ma, C.; Qiu, Y.; Hu, Z.; Zhao, J.; Shi, L.; Zeng, J. *Nature Communications* **2016**, *7*, 11510.

(82) Duan, Y.; Sun, S.; Xi, S.; Ren, X.; Zhou, Y.; Zhang, G.; Yang, H.; Du, Y.; Xu, Z. J. *Chemistry of Materials* **2017**, *29*, 10534–10541.

(83) Challagulla, S.; Tarafder, K.; Ganesan, R.; Roy, S. *The Journal of Physical Chemistry C* **2017**, *121*, 27406–27416.

(84) Payra, S.; Ganeshan, S. K.; Challagulla, S.; Roy, S. *Advanced Powder Technology* **2020**, *31*, 510–520.

(85) Roy, S.; Viswanath, B.; Hegde, M. S.; Madras, G. *The Journal of Physical Chemistry C* **2008**, *112*, 6002–6012.

(86) Lin, Y.-F.; Chen, C.-H.; Xie, W.-J.; Yang, S.-H.; Hsu, C.-S.; Lin, M.-T.; Jian, W.-B. *ACS Nano* **2011**, *5*, 1541–1548.

(87) Huang, J.; Kaner, R. B. *Angewandte Chemie International Edition* **2004**, *43*, 5817–5821.

(88) Inprasit, T.; Wongkasemjit, S.; Skinner, S. J.; Burriel, M.; Limthongkul, P. *RSC Advances* **2015**, *5*, 2486–2492.

(89) Forslund, R. P.; Alexander, C. T.; Abakumov, A. M.; Johnston, K. P.; Stevenson, K. J. *ACS Catalysis* **2019**, *9*, 2664–2673.

(90) Perdew, J. P.; Burke, K.; Ernzerhof, M. *Phys. Rev. Lett.* **1996**, *77*, 3865–3868.

(91) VargasHernández, R. A. *The Journal of Physical Chemistry A* **2020**, *124*, 4053–4061.

(92) Kresse, G.; Furthmüller, J. *Computational Materials Science* **1996**, *6*, 15–50.

(93) Kresse, G.; Hafner, J. *Physical review B* **1993**, *47*, 558.

(94) Zhang, L.; Yao, F.; Meng, J.; Zhang, W.; Wang, H.; Liu, X.; Meng, J.; Zhang, H. *Journal of Material Chemistry A* **2019**, *7*, 18558–18567.

(95) Valderrama, G.; Kiennemann, A.; Goldwasser, M. R. *Journal of Power Sources* **2010**, *195*, 1765–1771.

(96) Hyeok Yang, E.; Noh, Y. S.; Hong, G. H.; Moon, D. J. *Catalysis Today* **2018**, *299*, Special Issue of Catalysis Today for NGCS 11 Tromsø., 242–250.

(97) Halat, D. M.; Dunstan, M. T.; Gaultois, M. W.; Britto, S.; Grey, C. P. *Chemistry of Materials* **2018**, *30*, 4556–4570.

(98) Marrocchelli, D.; Perry, N. H.; Bishop, S. R. *Physical Chemistry Chemical Physics* **2015**, *17*, 10028–10039.

(99) Choisnet, J.; Bassat, J.; Pilliere, H.; Odier, P.; Leblanc, M. *Solid State Communications* **1988**, *66*, 1245–1249.

(100) Qiao, L.; Bi, X. *Europhysics Letters* **2011**, *93*, 57002.

(101) Mullica, D.; Lok, C.; Perkins, H.; Young, V *Physical Review B* **1985**, *31*, 4039.

(102) McBean, C. L.; Liu, H.; Scofield, M. E.; Li, L.; Wang, L.; Bernstein, A.; Wong, S. S. *ACS Applied Materials & Interfaces* **2017**, *9*, 24634–24648.

(103) Yang, X.; Li, L.; Yang, Z.; Hu, J.; Lei, Y.; Li, P.; Zheng, Z. *The Journal of Chemical Physics* **2020**, *153*, 024701.

(104) Li, J. P. H.; Zhou, X.; Pang, Y.; Zhu, L.; Vovk, E. I.; Cong, L.; van Bavel, A. P.; Li, S.; Yang, Y. *Physical Chemistry Chemical Physics* **2019**, *21*, 22351–22358.

(105) Ha, M. N.; Lu, G.; Liu, Z.; Wang, L.; Zhao, Z. *Journal of Material Chemistry A* **2016**, *4*, 13155–13165.

(106) Merino, N. A.; Barbero, B. P.; Eloy, P.; Cadús, L. E. *Applied Surface Science* **2006**, *253*, 1489–1493.

(107) Xue, Y.; Miao, H.; Sun, S.; Wang, Q.; Li, S.; Liu, Z. *RSC Advances* **2017**, *7*, 5214–5221.

(108) Ponce, S; Peña, M.; Fierro, J. *Applied Catalysis B: Environmental* **2000**, *24*, 193–205.

(109) Bott-Neto, J. L.; Martins, T. S.; Machado, S. A. S.; Ticianelli, E. A. *ACS Applied Materials & Interfaces* **2019**, *11*, 30810–30818.

(110) Ghouri, Z. K.; Al-Meer, S.; Barakat, N. A. M.; Kim, H. Y. *Scientific reports* **2017**, *7*, 1738.

(111) Asgari, M.; Maragheh, M. G.; Davarkhah, R.; Lohrasbi, E.; Golikand, A. N. *Electrochimica Acta* **2012**, *59*, 284–289.

(112) Li, J.; Luo, Z.; Zuo, Y.; Liu, J.; Zhang, T.; Tang, P.; Arbiol, J.; Llorca, J.; Cabot, A. *Applied Catalysis B: Environmental* **2018**, *234*, 10–18.

(113) Xiu, R.; Zhang, F.; Wang, Z.; Yang, M.; Xia, J.; Gui, R.; Xia, Y. *RSC Advances* **2015**, *5*, 86578–86583.

(114) Das, A. K.; Layek, R. K.; Kim, N. H.; Jung, D.; Lee, J. H. *Nanoscale* **2014**, *6*, 10657–10665.

(115) Ko, T.-H.; Devarayan, K.; Seo, M.-K.; Kim, H.-Y.; Kim, B.-S. *Scientific reports* **2016**, *6*, 20313.

(116) Tammam, R.; Fekry, A.; Saleh, M. *International Journal of Hydrogen Energy* **2015**, *40*, 275–283.

(117) Li, J.; Luo, Z.; He, F.; Zuo, Y.; Zhang, C.; Liu, J.; Yu, X.; Du, R.; Zhang, T.; Infante-Carrió, M. F.; Tang, P.; Arbiol, J.; Llorca, J.; Cabot, A. *Journal of Material Chemistry A* **2018**, *6*, 22915–22924.

(118) Elgrishi, N.; Rountree, K. J.; McCarthy, B. D.; Rountree, E. S.; Eisenhart, T. T.; Dempsey, J. L. *Journal of Chemical Education* **2018**, *95*, 197–206.

(119) Wang, J.; Zhao, Q.; Hou, H.; Wu, Y.; Yu, W.; Ji, X.; Shao, L. *RSC Advances* **2017**, *7*, 14152–14158.

(120) Sheikhi, S.; Jalali, F. *Fuel* **2021**, *296*, 120677.

(121) Zhang, X.; Ma, J.; Yan, R.; Cheng, W.; Zheng, J.; Jin, B. *Journal of Alloys and Compounds* **2021**, *867*, 159017.

(122) Chokkiah, B.; Eswaran, M.; Alothman, A. A.; Alsawat, M.; Ifseisi, A. A.; Alqahtani, K. N.; Dhanusuraman, R. *Journal of Materials Science: Materials in Electronics* **2022**, *33*, 8768–8776.

(123) Suroviec, A. H. *The Chemical Educator* **2012**, *17*, 83–85.

(124) Eswaran, M.; Dhanusuraman, R.; Tsai, P.-C.; Ponnusamy, V. K. *Fuel* **2019**, *251*, 91–97.

(125) Lashkenari, M. S.; Ghorbani, M.; Silakhori, N.; Karimi-Maleh, H. *Materials Chemistry and Physics* **2021**, *262*, 124290.

(126) Yu, M.; Wang, S.; Hu, J.; Chen, Z.; Bai, Y.; Wu, L.; Chen, J.; Weng, X. *Electrochimica Acta* **2014**, *145*, 300–306.

(127) Anu Prathap, M.; Srivastava, R. *Nano Energy* **2013**, *2*, 1046–1053.

(128) Knížek, K; Novák, P; Jirák, Z *Physical Review B* **2005**, *71*, 054420.

(129) Mefford, J. T.; Rong, X.; Abakumov, A. M.; Hardin, W. G.; Dai, S.; Kolpak, A. M.; Johnston, K. P.; Stevenson, K. J. *Nature Communications* **2016**, *7*, 11053.

(130) Payra, S.; Roy, S. *The Journal of Physical Chemistry C* **2021**, *125*, 8497–8507.

(131) Nagashree, K. L.; Ahmed, M. F. *J. Solid State Electrochem.* **2010**, *14*, 2307–2320.

(132) Chandrasekharan Meenu, P.; Samanta, P. K.; Yoshida, T.; English, N. J.; Datta, S. P.; Singh, S. A.; Dinda, S.; Chakraborty, C.; Roy, S. *ACS Applied Energy Materials* **2022**, *5*, 503–515.

(133) Shin, D.; Zu, F.; Nandayapa, E. R.; Frohloff, L.; Albert, E.; List-Kratochvil, E. J. W.; Koch, N. *Advanced Functional Materials* **2023**, *33*, 2208980.

(134) Whittingham, A. W. H.; Liu, X.; Smith, R. D. L. *ChemCatChem* **2022**, *14*, e202101684.

(135) Xiao, H.; Liu, P.; Wang, W.; Ran, R.; Zhou, W.; Shao, Z. *Energy & Fuels* **2020**, *34*, 9208–9221.

(136) Xu, X.; Pan, Y.; Zhong, Y.; Ran, R.; Shao, Z. *Materials Horizons* **2020**, *7*, 2519–2565.

(137) Varma, A.; Mukasyan, A. S.; Rogachev, A. S.; Manukyan, K. V. *Chemical Reviews* **2016**, *116*, 14493–14586.

(138) Deganello, F.; Tyagi, A. K. *Progress in Crystal Growth and Characterization of Materials* **2018**, *64*, 23–61.

(139) Notario-Estévez, A.; Kozlov, S. M.; Viñes, F.; Illas, F. *Chemical Communications.* **2015**, *51*, 5602–5605.

(140) Zavodinsky, V.; Kuyanov, I. *Computational Materials Science* **1996**, *6*, 240–244.

(141) Kresse, G; Furthmüller, J; Hafner, J *Europhysics Letters* **1995**, *32*, 729.

(142) Kresse, G.; Furthmüller, J.; Hafner, J. *Physical Review B* **1994**, *50*, 13181–13185.

(143) Yatoo, M. A.; Skinner, S. J. *Materials Today: Proceedings* **2022**, *56*, First International Conference on Design and Materials, 3747–3754.

(144) Zhu, W.; Chen, J.; Liu, D.; Yang, G.; Zhou, W.; Ran, R.; Yu, J.; Shao, Z. *Materials Chemistry Frontiers* **2023**, *7*, 4526–4534.

(145) Ananyev, M. V.; Tropin, E. S.; Eremin, V. A.; Farlenkov, A. S.; Smirnov, A. S.; Kolchugin, A. A.; Porotnikova, N. M.; Khodimchuk, A. V.; Berenov, A. V.; Kurumchin, E. K. *Physical Chemistry Chemical Physics* **2016**, *18*, 9102–9111.

(146) Gopalakrishnan, J.; Colsmann, G.; Reuter, B. *Journal of Solid State Chemistry* **1977**, *22*, 145–149.

(147) Meenu, P. C.; Roy, S. *ACS Applied Energy Materials* **2023**, *6*, 11212–11225.

(148) Mullica, D. F.; Lok, C. K. C.; Perkins, H. O.; Young, V. *Physical Review B* **1985**, *31*, 4039–4042.

(149) Vignesh, A.; Prabu, M.; Shanmugam, S. *ACS Applied Materials & Interfaces* **2016**, *8*, PMID: 26887571, 6019–6031.

(150) Zhu, Y.; Zhou, W.; Yu, J.; Chen, Y.; Liu, M.; Shao, Z. *Chemistry of Materials* **2016**, *28*, 1691–1697.

(151) Baeumer, C.; Liang, A. Y.-L.; Trstenjak, U.; Lu, Q.; Waser, R.; Mefford, J. T.; Gunkel, F.; Nemšák, S.; Chueh, W. C. *Journal of Material Chemistry A* **2021**, *9*, 19940–19948.

(152) Gilev, A. R.; Kiselev, E. A.; Cherepanov, V. A. *RSC Advances* **2016**, *6*, 72905–72917.

(153) Tomon, C.; Sarawutanukul, S.; Phattharasupakun, N.; Duangdangchote, S.; Chomkhuntod, P.; Joraleechanchai, N.; Bunyanidhi, P.; Sawangphruk, M. *Communications Chemistry* **2022**, *5*, 54.

(154) Mittal, R.; Awasthi, S. K. *ACS Applied Nano Materials* **2022**, *5*, 7831–7840.

(155) Feng, J.; Meng, Y.; Lian, Z.; Fang, L.; Long, Z.; Li, Y.; Song, Y. *RSC Advances* **2019**, *9*, 9729–9736.

(156) Li, L.; Yuan, Q.; Ye, S.; Fu, Y.; Ren, X.; Zhang, Q.; Liu, J. *Materials Chemistry Frontiers* **2021**, *5*, 6171–6181.

(157) Song, L.; Zhu, S.; Tong, L.; Wang, W.; Ouyang, C.; Xu, F.; Wang, Y. *Materials Advances* **2021**, *2*, 5622–5628.

(158) Zhang, R.; Zhou, T.; Wang, L.; Zhang, T. *ACS Applied Materials & Interfaces* **2018**, *10*, PMID: 29341589, 9765–9773.

(159) Yin, X.; Tang, C.; Zhang, L.; Yu, Z. G.; Gong, H. *Scientific Reports* **2016**, *6*, 21566.

(160) Dong, X.-C.; Xu, H.; Wang, X.-W.; Huang, Y.-X.; Chan-Park, M. B.; Zhang, H.; Wang, L.-H.; Huang, W.; Chen, P. *ACS Nano* **2012**, *6*, 3206–3213.

(161) Chen, F.; Guo, S.; Yu, S.; Zhang, C.; Guo, M.; Li, C. *Journal of Colloid and Interface Science* **2023**, *646*, 43–53.

(162) Rezaee, S.; Shahrokhian, S. *Applied Catalysis B: Environmental* **2019**, *244*, 802–813.

(163) Cohen, J. L.; Volpe, D. J.; Abruña, H. D. *Physical Chemistry Chemical Physics* **2007**, *9*, 49–77.

(164) Zegeye, T. A.; Chen, W.-T.; Hsu, C.-C.; Valinton, J. A. A.; Chen, C.-H. *ACS Energy Letters* **2022**, *7*, 2236–2243.

(165) Velasco-Plascencia, M.; Vázquez-Gómez, O.; Olmos, L.; Reyes-Calderón, F.; Vergara-Hernández, H. J.; Villalobos, J. C. *Catalysts* **2023**, *13*, 517.

(166) Renjith, A.; Lakshminarayanan, V. *Journal of Material Chemistry A* **2015**, *3*, 3019–3028.

(167) Azizi, S. N.; Ghasemi, S.; Chiani, E. *Electrochimica Acta* **2013**, *88*, 463–472.

(168) Deshpande, P. S.; Chaudhari, V. R.; Prasad, B. L. V. *Energy Technology* **2020**, *8*, 1900955.

(169) Azizi, S.; Ghasemi, S.; Yazdani-Sheldarrei, H. *International Journal of Hydrogen Energy* **2013**, *38*, 12774–12785.

(170) Durai, L.; Gopalakrishnan, A.; Badhulika, S. *Energy & Fuels* **2021**, *35*, 12507–12515.

(171) Amin, R.; Abdel Hameed, R.; El-Khatib, K.; Elsayed Youssef, M. *International Journal of Hydrogen Energy* **2014**, *39*, 2026–2041.

(172) Chen, P.; Zhang, S.; Fan, Y.; Yang, W.; Luo, X. *Materials Advances* **2023**, *4*, 1363–1371.

(173) Fingerle, M.; Tengeler, S.; Calvet, W.; Mayer, T.; Jaegermann, W. *Journal of The Electrochemical Society* **2018**, *165*, H3148.

(174) Huang, J.; Li, Z.; Liaw, B. Y.; Zhang, J. *Journal of Power Sources* **2016**, *309*, 82–98.

(175) Laschuk, N. O.; Easton, E. B.; Zenkina, O. V. *RSC Advances* **2021**, *11*, 27925–27936.

(176) Grosvenor, A. P.; Biesinger, M. C.; Smart, R. S.; McIntyre, N. S. *Surface Science* **2006**, *600*, 1771–1779.

(177) Tong, X.; Qin, Y.; Guo, X.; Moutanabbir, O.; Ao, X.; Pippel, E.; Zhang, L.; Knez, M. *small* **2012**, *8*, 3390–3395.

(178) Meher, S. K.; Rao, G. R. *ACS Catalysis* **2012**, *2*, 2795–2809.

(179) Roy, S.; Hegde, M. *Catalysis Communications* **2008**, *9*, 811–815.

(180) Mazumder, T.; Dandapat, S.; Baidya, T.; Likhar, P. R.; Clark, A. H.; Bera, P.; Tiwari, K.; Payra, S.; Srinivasa Rao, B.; Roy, S.; Biswas, K. *The Journal of Physical Chemistry C* **2021**, *125*, 20831–20844.

(181) Dong, Z.; Hu, Q.; Liu, H.; Wu, Y.; Ma, Z.; Fan, Y.; Li, R.; Xu, J.; Wang, X. *Sensors and Actuators B: Chemical* **2022**, *357*, 131227.

(182) Miri, A.; Sarani, M.; Khatami, M. *Rsc Advances* **2020**, *10*, 3967–3977.

(183) Bellakki, M. B.; Baidya, T.; Shivakumara, C.; Vasanthacharya, N.; Hegde, M.; Madras, G. *Applied Catalysis B: Environmental* **2008**, *84*, 474–481.

(184) Shannon, R. D. *Acta crystallographica section A: crystal physics, diffraction, theoretical and general crystallography* **1976**, *32*, 751–767.

(185) Hezam, A.; Namratha, K.; Drmosh, Q. A.; Ponnamma, D.; Wang, J.; Prasad, S.; Ahamed, M.; Cheng, C.; Byrappa, K. *ACS Applied Nano Materials* **2020**, *3*, 138–148.

(186) Ravishankar, T. N.; Ramakrishnappa, T.; Nagaraju, G.; Rajanaika, H. *ChemistryOpen* **2015**, *4*, 146–154.

(187) Wu, D.; Zhang, W.; Cheng, D. *ACS Applied Materials & Interfaces* **2017**, *9*, 19843–19851.

(188) Chandrasekharan Meenu, P.; Datta, S. P.; Singh, S. A.; Dinda, S.; Chakraborty, C.; Roy, S. *Journal of Power Sources* **2020**, *461*, 228150.

(189) Sun, M.; Wang, S.; Li, Y.; Xu, H.; Chen, Y. *Applied Surface Science* **2017**, *402*, 323–329.

(190) Sun, M.; Wang, S.; Li, Y.; Wang, Q.; Xu, H.; Chen, Y. *Journal of the Taiwan Institute of Chemical Engineers* **2017**, *78*, 401–408.

(191) Wang, J.; Teschner, D.; Yao, Y.; Huang, X.; Willinger, M.; Shao, L.; Schlögl, R. *Journal of Materials Chemistry A* **2017**, *5*, 9946–9951.

(192) Cao, Y.; Ge, J.; Jiang, M.; Zhang, F.; Lei, X. *ACS Applied Materials & Interfaces* **2021**, *13*, 29491–29499.

(193) Rebekah, A.; Anantharaj, S.; Viswanthan, C.; Ponpandian, N. *International Journal of Hydrogen Energy* **2020**, *45*, 14713–14727.

(194) Qi, Y.; Zhang, Y.; Yang, L.; Zhao, Y.; Zhu, Y.; Jiang, H.; Li, C. *Nature Communications* **2022**, *13*, 4602.

(195) Antony, R. P.; Satpati, A. K.; Jagatap, B. N. *ChemElectroChem* **2017**, *4*, 2989–2996.

(196) Adekunle, A. S.; Ozoemena, K. I. *Electrochimica Acta* **2008**, *53*, 5774–5782.

(197) Bredar, A. R.; Chown, A. L.; Burton, A. R.; Farnum, B. H. *ACS Applied Energy Materials* **2020**, *3*, 66–98.

(198) Huang, T.; Mao, S.; Zhou, G.; Zhang, Z.; Wen, Z.; Huang, X.; Ci, S.; Chen, J. *Nanoscale* **2015**, *7*, 1301–1307.

(199) Renjith, A.; Lakshminarayanan, V *Journal of Materials Chemistry A* **2015**, *3*, 3019–3028.

(200) Hou, G.; Parrondo, J.; Ramani, V.; Prakash, J. *Journal of The Electrochemical Society* **2013**, *161*, F252.

(201) Anantharaj, S.; Sugime, H.; Chen, B.; Akagi, N.; Noda, S. *The Journal of Physical Chemistry C* **2020**, *124*, 9673–9684.

(202) Wang, B.; Tao, L.; Cheng, Y.; Yang, F.; Jin, Y.; Zhou, C.; Yu, H.; Yang, Y. *Catalysts* **2019**, *9*, 387.

(203) Wu, F.; Zhang, Z.; Zhang, F.; Duan, D.; Li, Y.; Wei, G.; Liu, S.; Yuan, Q.; Wang, E.; Hao, X. *Catalysts* **2019**, *9*, 749.

(204) Chung, D. Y.; Kim, H.-i.; Chung, Y.-H.; Lee, M. J.; Yoo, S. J.; Bokare, A. D.; Choi, W.; Sung, Y.-E. *Scientific Reports* **2014**, *4*, 7450.

(205) Dunnick, K. M.; Pillai, R.; Pisane, K. L.; Stefaniak, A. B.; Sabolsky, E. M.; Leonard, S. S. *Biological Trace Element Research* **2015**, *166*, 96–107.

(206) Kuntaiah, K.; Sudarsanam, P.; Reddy, B. M.; Vinu, A. *Rsc Advances* **2013**, *3*, 7953–7962.

(207) Guan, B.; Li, Y.; Yin, B.; Liu, K.; Wang, D.; Zhang, H.; Cheng, C. *Chemical Engineering Journal* **2017**, *308*, 1165–1173.

(208) Liu, L.; Zhang, H.; Fang, L.; Mu, Y.; Wang, Y. *Journal of Power Sources* **2016**, *327*, 135–144.

(209) Bao, J.; Zhang, X.; Fan, B.; Zhang, J.; Zhou, M.; Yang, W.; Hu, X.; Wang, H.; Pan, B.; Xie, Y. *Angewandte Chemie* **2015**, *127*, 7507–7512.

(210) Wang, C.; Fan, H.; Ren, X.; Fang, J. *Applied Physics A* **2018**, *124*, 99.

(211) Su, Y.; Zhang, Q.; Chen, L.; Bao, L.; Lu, Y.; Shi, Q.; Wang, J.; Chen, S.; Wu, F. *ACS Applied Materials & Interfaces* **2020**, *12*, PMID: 32814409, 37208–37217.

(212) Wang, B.; Zhu, B.; Yun, S.; Zhang, W.; Xia, C.; Afzal, M.; Cai, Y.; Liu, Y.; Wang, Y.; Wang, H. *NPG Asia Materials* **2019**, *11*, 51.

(213) Fingerle, M.; Tengeler, S.; Calvet, W.; Mayer, T.; Jaegermann, W. *Journal of The Electrochemical Society* **2018**, *165*, H3148.

(214) Zhu, H.; Qin, Z.; Shan, W.; Shen, W.; Wang, J. *Journal of Catalysis* **2004**, *225*, 267–277.

(215) Wang, Y.; Shen, Q.; Tong, Y.; Zhan, Z. *International Journal of Hydrogen Energy* **2022**, *47*, 6827–6836.

(216) Lee, J.; Ryou, Y.; Chan, X.; Kim, T. J.; Kim, D. H. *The Journal of Physical Chemistry C* **2016**, *120*, 25870–25879.

(217) Tang, K.; Liu, W.; Li, J.; Guo, J.; Zhang, J.; Wang, S.; Niu, S.; Yang, Y. *ACS Applied Materials & Interfaces* **2015**, *7*, PMID: 26573213, 26839–26849.

(218) Ma, Z.; Zhao, S.; Pei, X.; Xiong, X.; Hu, B. *Catalysis Science & Technology* **2017**, *7*, 191–199.

(219) Luisetto, I.; Stendardo, S.; Senthil Kumar, S. M.; Selvakumar, K.; Kesavan, J. K.; Iucci, G.; Pasqual Laverdura, U.; Tuti, S. *Processes* **2021**, *9*, 1899.

(220) Ma, Y.; Liu, J.; Chu, M.; Yue, J.; Cui, Y.; Xu, G. *Catalysis Letters* **2022**, *152*, 872–882.

(221) Lee, S. M.; Lee, Y. H.; Moon, D. H.; Ahn, J. Y.; Nguyen, D. D.; Chang, S. W.; Kim, S. S. *Industrial & Engineering Chemistry Research* **2019**, *58*, 8656–8662.

(222) Chandrasekharan Meenu, P.; Roy, S. *ACS Applied Materials & Interfaces* **2023**, *15*, 36154–36166.

(223) Laosiripojana, N.; Kiatkittipong, W.; Assabumrungrat, S. *AIChE journal* **2011**, *57*, 2861–2869.

(224) Wang, X.; Wang, J.; Sun, Y.; Li, K.; Shang, T.; Wan, Y. *Frontiers in Chemistry* **2022**, *10*, 1089708.

(225) Yoko, A.; Kamonvarapitak, T.; Seong, G.; Tomai, T.; Adschiri, T. *ChemNanoMat* **2022**, *8*, e202100495.

(226) Zhang, K.; Han, Y.; Qiu, J.; Ding, X.; Deng, Y.; Wu, Y.; Zhang, G.; Yan, L. *Journal of Colloid and Interface Science* **2023**, *630*, 570–579.

(227) Zhang, X.; Kong, L.; Xing, W.; Zhang, Y.; Yang, J.; Zhou, C.; Liu, H.; Yang, Z.; Zhu, W.; Wei, H. *ACS Applied Energy Materials* **2022**, *5*, 12485–12495.

(228) Jiang, W.-J.; Niu, S.; Tang, T.; Zhang, Q.-H.; Liu, X.-Z.; Zhang, Y.; Chen, Y.-Y.; Li, J.-H.; Gu, L.; Wan, L.-J.; Hu, J.-S. *Angewandte Chemie International Edition* **2017**, *56*, 6572–6577.

(229) Cui, X.; Xiao, P.; Wang, J.; Zhou, M.; Guo, W.; Yang, Y.; He, Y.; Wang, Z.; Yang, Y.; Zhang, Y.; Lin, Z. *Angewandte Chemie International Edition* **2017**, *56*, 4488–4493.

(230) Elsawy, H.; Thamer, B. M.; Sedky, A.; El-Newehy, M. H. *Materials Chemistry and Physics* **2023**, *297*, 127361.

(231) Gopalakrishnan, A.; Durai, L.; Ma, J.; Kong, C. Y.; Badhulika, S. *Energy & Fuels* **2021**, *35*, 10169–10180.

(232) Wang, H.; Li, S.; Sun, G.; Lu, G.; Bu, Q.; Kong, X.; Liu, Q. *Inorganic Chemistry Communications* **2022**, *145*, 109984.

(233) Zhang, S.; Chen, P.; Fan, Y.; Zhao, Y.; Yang, W.; Gao, H.; Luo, X. *New Journal of Chemistry.* **2023**, *47*, 875–881.

(234) Neppolian, B et al. *Ceramics International* **2022**, *48*, 29025–29030.

(235) Li, W.; Song, Z.; Deng, X.; Fu, X.-Z.; Luo, J.-L. *Electrochimica Acta* **2020**, *337*, 135684.

(236) Shi, Y.; Li, H.; Ao, D.; Chang, Y.; Xu, A.; Jia, M.; Jia, J. *Journal of Alloys and Compounds* **2021**, *885*, 160919.

(237) Han, L.; Li, H.; Yang, L.; Liu, Y.; Liu, S. *ACS Applied Materials & Interfaces* **2023**, *15*, 9392–9400.

(238) Zahedi, F.; Shabani-Nooshabadi, M. *Fuel* **2023**, *335*, 127083.

(239) Hou, G.; Shen, Z.; Tang, Y.; Chen, Q.; Cao, H.; Zhang, H.; Zheng, G.; Zhang, J. *International Journal of Hydrogen Energy* **2023**, *48*, 991–1000.

(240) Sajeev, A.; Sathyaseelan, A.; Bejigo, K. S.; Kim, S. J. *Journal of Colloid and Interface Science* **2023**, *637*, 363–371.

(241) Luo, Q.; Peng, M.; Sun, X.; Asiri, A. M. *Catalysis Science & Technology* **2016**, *6*, 1157–1161.

(242) Liu, S.; Sun, Y.-Y.; Wu, Y.-P.; Wang, Y.-J.; Pi, Q.; Li, S.; Li, Y.-S.; Li, D.-S. *ACS Applied Materials & Interfaces* **2021**, *13*, 26472–26481.

(243) Shin, Y.; Doh, K.-Y.; Kim, S. H.; Lee, J. H.; Bae, H.; Song, S.-J.; Lee, D. *Journal of Material Chemistry A* **2020**, *8*, 4784–4789.

(244) Mizusaki, J.; Sasamoto, T.; Cannon, W. R.; Bowen, H. K. *Journal of the American Ceramic Society* **1983**, *66*, 247–252.

(245) Li, H.; Zhang, C.; Xiang, W.; Amin, M. A.; Na, J.; Wang, S.; Yu, J.; Yamauchi, Y. *Chemical Engineering Journal* **2023**, *452*, 139104.

(246) Cui, X.; Yang, Y.; Li, Y.; Liu, F.; Peng, H.; Zhang, Y.; Xiao, P. *Journal of The Electrochemical Society* **2015**, *162*, F1415.

(247) Udachyan, I.; Zidki, T.; Mizrahi, A.; Patra, S. G.; Meyerstein, D. *ACS Applied Energy Materials* **2022**, *5*, 12261–12271.

(248) Kandoi, S.; Greeley, J.; Sanchez-Castillo, M. A.; Evans, S. T.; Gokhale, A. A.; Dumesic, J. A.; Mavrikakis, M. *Topics in Catalysis* **2006**, *37*, 17–28.

(249) Hou, G.; Parrondo, J.; Ramani, V.; Prakash, J. *Journal of The Electrochemical Society* **2013**, *161*, F252.

(250) Fang, Y.-H.; Liu, Z.-P. *Surface Science* **2015**, *631*, Surface Science and Electrochemistry - 20 years later, 42–47.

(251) Anantharaj, S.; Noda, S.; Driess, M.; Menezes, P. W. *ACS Energy Letters* **2021**, *6*, 1607–1611.

(252) Khadke, P.; Tichter, T.; Boettcher, T.; Muench, F.; Ensinger, W.; Roth, C. *Scientific Reports* **2021**, *11*, 8974.

(253) Velázquez-Palenzuela, A.; Centellas, F.; Garrido, J. A.; Arias, C.; Rodríguez, R. M.; Brillas, E.; Cabot, P.-L. *Journal of Power Sources* **2011**, *196*, 3503–3512.

(254) Samanta, S.; Bhunia, K.; Pradhan, D.; Satpati, B.; Srivastava, R. *ACS Sustainable Chemistry & Engineering* **2018**, *6*, 2023–2036.

(255) Prathap, M. A.; Satpati, B.; Srivastava, R. *Electrochimica Acta* **2014**, *130*, 368–380.

(256) Zegeye, T. A.; Chen, W.-T.; Hsu, C.-C.; Valinton, J. A. A.; Chen, C.-H. *ACS Energy Letters* **2022**, *7*, 2236–2243.

(257) Bortamuly, R.; Konwar, G.; Boruah, P. K.; Das, M. R.; Mahanta, D.; Saikia, P. *Ionics* **2020**, *26*, 5747–5756.

(258) Channei, D.; Inceesungvorn, B.; Wetchakun, N.; Phanichphant, S. *International Journal of Photoenergy* **2013**, *2013*, 484831.

(259) Rameshan, R.; Pentyala, P.; Singh, S. A.; Deshpande, P. A.; Roy, S. *Journal of Environmental Chemical Engineering* **2022**, *10*, 108966.

(260) Romero-Núñez, A.; Gómez-Cortés, A.; Tiznado, H.; Díaz, G. *Catalysis Today* **2020**, *349*, XXVI IIMRC (2017) Symposium F3: Advanced Catalytic Materials, 10–16.

(261) Li, W. Q.; Goverapet Srinivasan, S.; Salahub, D. R.; Heine, T. *Physical Chemistry Chemical Physics* **2016**, *18*, 11139–11149.

(262) Nolan, M. *Journal of Materials Chemistry* **2011**, *21*, 9160–9168.

(263) Chen, S.; Li, L.; Hu, W.; Huang, X.; Li, Q.; Xu, Y.; Zuo, Y.; Li, G. *ACS Applied Materials & Interfaces* **2015**, *7*, 22999–23007.

(264) Cheng, M.; Fan, H.; Song, Y.; Cui, Y.; Wang, R. *Dalton Transactions* **2017**, *46*, 9201–9209.

(265) Song, D.; Wang, L.; Wang, B.; Yu, J.; Li, Y.; Qu, Y.; Duan, C.; Yang, Y.; Miao, X. *International Journal of Electrochemical Science* **2020**, *15*, 1949–1963.

(266) Jain, S.; Shah, J.; Negi, N. S.; Sharma, C.; Kotnala, R. K. *International Journal of Energy Research* **2019**, *43*, 4743–4755.

(267) Trinh, Q. T.; Bhola, K.; Amaniampong, P. N.; Jérôme, F.; Mushrif, S. H. *The Journal of Physical Chemistry C* **2018**, *122*, 22397–22406.

(268) Jiang, Y.; Liu, B.; Yang, W.; Yang, L.; Li, S.; Liu, X.; Zhang, X.; Yang, R.; Jiang, X. *Nanoscale* **2017**, *9*, 11713–11719.

(269) Liu, A.; Liu, G.; Zhu, H.; Shin, B.; Fortunato, E.; Martins, R.; Shan, F. *Applied Physics Letters* **2016**, *108*, 233506.

(270) Cao, X.; Zhang, C.; Wang, Z.; Liu, W.; Sun, X. *RSC Advances* **2020**, *10*, 4664–4671.

(271) Kim, T.; Vohs, J. M.; Gorte, R. J. *Industrial & Engineering Chemistry Research* **2006**, *45*, 5561–5565.

(272) Roy, S.; Marimuthu, A.; Hegde, M.; Madras, G. *Applied Catalysis B: Environmental* **2007**, *71*, 23–31.

(273) Lin, F.; Delmelle, R.; Vinodkumar, T.; Reddy, B. M.; Wokaun, A.; Alxneit, I. *Catalysis Science & Technology* **2015**, *5*, 3556–3567.

(274) Gao, Y.; Teng, S.; Wang, Z.; Wang, B.; Liu, W.; Liu, W.; Wang, L. *Journal of Materials Science* **2020**, *55*, 283–297.

(275) Liu, L.; Shi, J.; Zhang, X.; Liu, J. *Journal of Chemistry* **2015**, *2015*, 254750.

(276) Chen, S.; Huang, D.; Liu, D.; Sun, H.; Yan, W.; Wang, J.; Dong, M.; Tong, X.; Fan, W. *Applied Catalysis B: Environmental* **2021**, *291*, 120065.

(277) Meenu, P. C.; Samanta, P. K.; Datta, S. P.; Singh, S. A.; Dinda, S.; Chakraborty, C.; Roy, S. *Inorganic chemistry* **2023**, *63*, 526–536.

(278) Hassan, F.; Naeem, R.; Shabbir, S.; Sharif, S.; Mushtaq, M.; Sattar, R. *New Journal of Chemistry* **2024**.

(279) Maarisetty, D.; Hang, D.-R.; Chou, M. M.; Parida, S. *ACS Applied Energy Materials* **2022**, *5*, 14059–14070.

(280) Sarkar, S.; Ramarao, S.; Das, T.; Das, R.; Vinod, C.; Chakraborty, S.; Peter, S. C. *ACS catalysis* **2021**, *11*, 800–808.

(281) Wu, T.; Sun, M.; Huang, B. *Small* **2020**, *16*, 2002434.

(282) Sharma, P.; Minakshi Sundaram, M.; Watcharatharapong, T.; Laird, D.; Euchner, H.; Ahuja, R. *ACS Applied Materials & Interfaces* **2020**, *12*, 44815–44829.

(283) Chamani, S.; Sadeghi, E.; Unal, U.; Peighambardoust, N. S.; Aydemir, U. *Catalysts* **2023**, *13*, 798.

(284) Perdew, J. P.; Burke, K.; Ernzerhof, M. *Physical review letters* **1996**, *77*, 3865.

(285) Kresse, G.; Furthmüller, J. *Physical review B* **1996**, *54*, 11169.

(286) Kresse, G.; Furthmüller, J. *Computational materials science* **1996**, *6*, 15–50.

(287) Ghoreishian, S. M.; Raju, G. S. R.; Pavitra, E; Kwak, C. H.; Han, Y.-K.; Huh, Y. S. *Ceramics International* **2019**, *45*, 12041–12052.

(288) Zhang, Y.; Guo, H.; Li, X.; Ren, W.; Song, R. *Materials Chemistry Frontiers* **2022**, *6*, 1477–1486.

(289) Sharma, P.; Minakshi Sundaram, M.; Watcharatharapong, T.; Jungthawan, S.; Ahuja, R. *ACS Applied Materials & Interfaces* **2021**, *13*, 56116–56130.

(290) De Moura, A. P.; de Oliveira, L. H.; Rosa, I. L.; Xavier, C. S.; Lisboa-Filho, P. N.; Li, M. S.; La Porta, F. A.; Longo, E.; Varela, J. A., et al. *The Scientific World Journal* **2015**, *2015*.

(291) Padmanathan, N.; Shao, H.; Razeeb, K. M. *International Journal of Hydrogen Energy* **2020**, *45*, 30911–30923.

(292) Xu, Y.; Xuan, H.; Gao, J.; Liang, T.; Han, X.; Yang, J.; Zhang, Y.; Li, H.; Han, P.; Du, Y. *Journal of materials science* **2018**, *53*, 8483–8498.

(293) Rajput, A.; Adak, M. K.; Chakraborty, B. *Inorganic Chemistry* **2022**, *61*, 11189–11206.

(294) Prabhu, S.; Maruthapandi, M.; Durairaj, A.; Arun Kumar, S.; Luong, J. H.; Ramesh, R.; Gedanken, A. *ACS Applied Energy Materials* **2023**, *6*, 1321–1331.

(295) Aishwarya, K; Maruthasalamoorthy, S; Mani, J; Anbalagan, G; Nirmala, R; Navaneethan, M; Navamathavan, R *Physical Chemistry Chemical Physics* **2022**, *24*, 25620–25629.

(296) Kumar, R. S.; Mannu, P.; Prabhakaran, S.; Nga, T. T. T.; Kim, Y.; Kim, D. H.; Chen, J.-L.; Dong, C.-L.; Yoo, D. J. *Advanced Science* **2023**, *10*, 2303525.

(297) Liu, H.; Dai, M.; Zhao, D.; Wu, X.; Wang, B. *ACS Applied Energy Materials* **2020**, *3*, 7004–7010.

(298) Fu, Z.; Hu, J.; Hu, W.; Yang, S.; Luo, Y. *Applied Surface Science* **2018**, *441*, 1048–1056.

(299) Ren, Y.; Li, X.; Wang, Y.; Gong, Q.; Gu, S.; Gao, T.; Sun, X.; Zhou, G. *Journal of Materials Science & Technology* **2022**, *102*, 186–194.

(300) Liu, N.; Wu, R.; Liu, Y.; Liu, Y.; Deng, P.; Li, Y.; Du, Y.; Cheng, Y.; Zhuang, Z.; Kang, Z., et al. *Inorganic Chemistry* **2023**, *62*, 11990–12000.

(301) Acharya, J.; Pant, B.; Ojha, G. P.; Park, M. *Journal of Colloid and Interface Science* **2022**, *610*, 863–878.

(302) Zhang, K.; Zeng, H.-Y.; Ge, K.-W.; Wang, M.-X.; Li, H.-B. *Inorganic Chemistry* **2023**, *62*, 8219–8231.

(303) Huang, J.; Li, Y.; Zhang, Y.; Rao, G.; Wu, C.; Hu, Y.; Wang, X.; Lu, R.; Li, Y.; Xiong, J. *Angewandte Chemie* **2019**, *131*, 17619–17625.

(304) Hou, Z.; Cui, C.; Li, Y.; Gao, Y.; Zhu, D.; Gu, Y.; Pan, G.; Zhu, Y.; Zhang, T. *Advanced Materials* **2023**, 2209876.

(305) Jothi, P. R.; Kannan, S.; Velayutham, G *Journal of Power Sources* **2015**, *277*, 350–359.

(306) Matthews, T.; Chabalala, M. P.; Mbokazi, S. P.; Maumau, T.; Mugadza, K.; Gallenberger, J.; Hofmann, J. P.; Dolla, T. H.; Maxakato, N. W. *Fuel* **2024**, *359*, 130460.

(307) Yin, Z.; Zhang, S.; Chen, W.; Xinzhi, M.; Zhou, Y.; Zhang, Z.; Wang, X.; Li, J. *New Journal of Chemistry* **2020**, *44*, 17477–17482.

(308) Feng, L.; Li, K.; Chang, J.; Liu, C.; Xing, W. *Nano Energy* **2015**, *15*, 462–469.

(309) Arshad, F.; Tahir, A.; Haq, T. u.; Duran, H.; Hussain, I.; Sher, F. *Energy & Fuels* **2023**, *37*, 14161–14170.

(310) Zhang, Y.; Wu, X.; Fu, G.; Si, F.; Fu, X.-Z.; Luo, J.-L. *International Journal of Hydrogen Energy* **2022**, *47*, 17150–17160.

(311) Wang, X.; Maeda, K.; Thomas, A.; Takanabe, K.; Xin, G.; Carlsson, J. M.; Domen, K.; Antonietti, M. *Nature Materials* **2009**, *8*, 76–80.

(312) Han, Q.; Wang, B.; Gao, J.; Qu, L. *Angewandte Chemie* **2016**, *128*, 11007–11011.

(313) Niu, W.; Yang, Y. *ACS Energy Letters* **2018**, *3*, 2796–2815.

(314) Wang, W.; Yu, J. C.; Shen, Z.; Chan, D. K. L.; Gu, T. *Chemical Communications.* **2014**, *50*, 10148–10150.

(315) Liang, H.-W.; Zhuang, X.; Brüller, S.; Feng, X.; Müllen, K. *Nature communications* **2014**, *5*, 4973.

(316) Zhang, X.; Xie, X.; Wang, H.; Zhang, J.; Pan, B.; Xie, Y. *Journal of the American Chemical Society* **2013**, *135*, 18–21.

(317) Li, X.-H.; Wang, X.; Antonietti, M. *Chemical Science* **2012**, *3*, 2170–2174.

(318) Liu, J.; Huang, J.; Zhou, H.; Antonietti, M. *ACS Applied Materials & Interfaces* **2014**, *6*, PMID: 24800656, 8434–8440.

(319) Wang, S.; Li, C.; Wang, T.; Zhang, P.; Li, A.; Gong, J. *Journal of Material Chemistry A* **2014**, *2*, 2885–2890.

(320) Challagulla, S.; Payra, S.; Chakraborty, C.; Roy, S. *Physical Chemistry Chemical Physics* **2019**, *21*, 3174–3183.

(321) Niu, P.; Zhang, L.; Liu, G.; Cheng, H.-M. *Advanced Functional Materials* **2012**, *22*, 4763–4770.

(322) Wang, W.; Yu, J. C.; Xia, D.; Wong, P. K.; Li, Y. *Environmental Science & Technology* **2013**, *47*, 8724–8732.

(323) Mondal, S.; Rana, U.; Malik, S. *Chemical Communications.* **2015**, *51*, 12365–12368.

(324) Roy, S.; Payra, S.; Challagulla, S.; Arora, R.; Roy, S.; Chakraborty, C. *ACS omega* **2018**, *3*, 17778–17788.

(325) Wang, A.; Wang, C.; Fu, L.; Wong-Ng, W.; Lan, Y. *Nano-micro letters* **2017**, *9*, 1–21.

(326) Fang, S.; Xia, Y.; Lv, K.; Li, Q.; Sun, J.; Li, M. *Applied Catalysis B: Environmental* **2016**, *185*, 225–232.

(327) Gomez, I. J.; Arnaiz, B.; Cacioppo, M.; Arcudi, F.; Prato, M. *New Journal of Chemistry B* **2018**, *6*, 5540–5548.

(328) Yang, L.; Wu, X.; Luo, L.; Liu, Y.; Wang, F. *New Journal of Chemistry.* **2019**, *43*, 3174–3179.

(329) Liao, G.; Chen, S.; Quan, X.; Yu, H.; Zhao, H. *Journal of Materials Chemistry* **2012**, *22*, 2721–2726.

(330) Qin, J.; Huo, J.; Zhang, P.; Zeng, J.; Wang, T.; Zeng, H. *Nanoscale* **2016**, *8*, 2249–2259.

(331) Li, H.; Jing, Y.; Ma, X.; Liu, T.; Yang, L.; Liu, B.; Yin, S.; Wei, Y.; Wang, Y. *RSC Advances* **2017**, *7*, 8688–8693.

(332) Bing, W.; Chen, Z.; Sun, H.; Shi, P.; Gao, N.; Ren, J.; Qu, X. *Nano Research* **2015**, *8*, 1648–1658.

(333) Hu, S.-L.; Niu, K.-Y.; Sun, J.; Yang, J.; Zhao, N.-Q.; Du, X.-W. *Journal of Materials Chemistry* **2009**, *19*, 484–488.

(334) Zhu, H.; Wang, X.; Li, Y.; Wang, Z.; Yang, F.; Yang, X. *Chemical Communications.* **2009**, 5118–5120.

(335) Xiang, Q.; Yu, J.; Jaroniec, M. *The Journal of Physical Chemistry C* **2011**, *115*, 7355–7363.

(336) Li, J.; Shen, B.; Hong, Z.; Lin, B.; Gao, B.; Chen, Y. *Chemical Communications.* **2012**, *48*, 12017–12019.

(337) Jiang, J.; Ou-yang, L.; Zhu, L.; Zheng, A.; Zou, J.; Yi, X.; Tang, H. *Carbon* **2014**, *80*, 213–221.

(338) Zhu, S.; Song, Y.; Zhao, X.; Shao, J.; Zhang, J.; Yang, B. *Nano Research* **2015**, *8*, 355–381.

(339) Reddy, A. L. M.; Srivastava, A.; Gowda, S. R.; Gullapalli, H.; Dubey, M.; Ajayan, P. M. *ACS Nano* **2010**, *4*, PMID: 20931996, 6337–6342.

(340) Fujimoto, A.; Yamada, Y.; Koinuma, M.; Sato, S. *Analytical Chemistry* **2016**, *88*, PMID: 27264720, 6110–6114.

(341) Zhou, L.; Tian, Y.; Lei, J.; Wang, L.; Liu, Y.; Zhang, J. *Catalysis Science & Technology* **2018**, *8*, 2617–2623.

(342) Shibuya, R.; Kondo, T.; Nakamura, J. In *Carbon-Based Metal-Free Catalysts*; John Wiley Sons, Ltd: 2018; Chapter 8, pp 227–249.

(343) Li, Y.; Zhao, Y.; Cheng, H.; Hu, Y.; Shi, G.; Dai, L.; Qu, L. *Journal of the American Chemical Society* **2012**, *134*, PMID: 22136359, 15–18.

(344) Hsin, Y. L.; Hwang, K. C.; Yeh, C.-T. *Journal of the American Chemical Society* **2007**, *129*, PMID: 17658804, 9999–10010.

(345) Eisazadeh, H.; Ghorbani, M. *Journal of Vinyl and Additive Technology* **2009**, *15*, 204–210.

(346) Ghorbani, M.; Eisazadeh, H. *World Applied Sciences Journal* **2008**, *5*, 204–210.

(347) Rana, U.; Malik, S. *Chemical Communications.* **2012**, *48*, 10862–10864.

(348) Selmarten, D.; Jones, M.; Rumbles, G.; Yu, P.; Nedeljkovic, J.; Shaheen, S. *The Journal of Physical Chemistry B* **2005**, *109*, PMID: 16853021, 15927–15932.

(349) Yang, X.; Jia, Q.; Duan, F.; Hu, B.; Wang, M.; He, L.; Song, Y.; Zhang, Z. *Applied Surface Science* **2019**, *464*, 78–87.

(350) Cui, X.; Zhu, Y.; Hua, Z.; Feng, J.; Liu, Z.; Chen, L.; Shi, J. *Energy & Environmental Science* **2015**, *8*, 1261–1266.

(351) Wang, A.-L.; Xu, H.; Feng, J.-X.; Ding, L.-X.; Tong, Y.-X.; Li, G.-R. *Journal of the American Chemical Society* **2013**, *135*, PMID: 23837995, 10703–10709.

(352) Yang, Z.; Berber, M. R.; Nakashima, N. *Journal of Material Chemistry A* **2014**, *2*, 18875–18880.

(353) Zhao, J.; Wu, G.; Hu, Y.; Liu, Y.; Tao, X.; Chen, W. *Journal of Material Chemistry A* **2015**, *3*, 24333–24337.

(354) Ozoemena, K. I. *RSC Advances* **2016**, *6*, 89523–89550.

(355) Lu, S.; Li, H.; Sun, J.; Zhuang, Z. *Nano Research* **2018**, *11*, 2058–2068.

List of Publications and Conferences

1. **Meenu P. C.**, Datta, S. P., Singh, S. A., Dinda, S., Chakraborty, C., & Roy, S. Polyaniline supported g-C_3N_4 quantum dots surpass benchmark Pt/C: Development of morphologically engineered g-C_3N_4 catalysts towards "metal-free" methanol electro-oxidation. Journal of Power Sources, **2020**, 461, 228150.

2. **Meenu P. C.**, Datta, S. P., Singh, S. A., Dinda, S., Chakraborty, C., & Roy, S. A compendium on metal organic framework materials and their derivatives as electrocatalyst for methanol oxidation reaction. Molecular Catalysis, **2021**, 510, 111710.

3. **Meenu P. C**, Saraswati Roy, Chanchal Chakraborty, & Sounak Roy. Electro catalytic oxidation reactions for harvesting alternative energy over non noble metal oxides: Are we a step closer to sustainable energy solution? Advanced Powder Technology. Advanced Powder Technology, **2021**, 32 (8), 2663-2689.

4. **Meenu P.C**, Pralok K. Samanta, Takefumi Yoshida, Niall J. English, Santanu Prasad Datta, Satyapaul A. Singh, Srikanta Dinda, Chanchal Chakraborty, & Sounak Roy. Electro-Oxidation Reaction of Methanol over $La_{2-x}Sr_xNiO_{4+\delta}$ Ruddlesden–Popper Oxides. ACS Applied Energy Materials **2022**, 5, 503-515.

5. **Meenu P.C**, Sounak Roy. Electro-oxidation Reaction of Methanol over Reducible $Ce_{1-x-y}Ni_xSr_yO_{2-\delta}$: A Mechanistic Probe of Participation of Lattice Oxygen. ACS Appl. Mater. Interfaces. **2023**, 15, 30, 36154-36166.

6. **Meenu. P.C**, Sounak Roy. Unveiling the Mechanistic Significance of Reducibility and Lattice Oxygen Evolution in $Ce_{1-x-y}Zr_xNi_yO_{2-\delta}$. Catalyst for Methanol Electro-oxidation. ACS Applied Energy Material. ACS Appl. Energy Mater. **2023**, 6, 21, 11212-11225.

7. **Meenu. P.C**, Pralok K. Samanta, Santanu Prasad Datta, Satyapaul A. Singh, Srikanta Dinda, Chanchal Chakraborty, & Sounak Roy. Electro-oxidation Reaction of Methanol over $La_{2-x}Sr_xNi_{1-y}(Mn/Fe/Co)_yO_{4+\delta}$ Ruddlesden-Popper oxides. Inorg. Chem. **2024**, 63, 1, 526–536

8. **Meenu. P.C**, & Sounak Roy. Rationalizing Descriptors for Electrocatalysts in Methanol Oxidation Reaction. Catalysis Today, **2024**, 439, 114802.

Book Chapter

Sounak Roy, Aathira Bhaskaran, **Preetha Chandrasekharan Meenu**. Chapter Title: Chapter 4: Microwave-assisted Synthesis of Porous Materials. Royal Society of Chemistry, Catalysis Series. E book Edition.

Conferences

• **Poster presentation** on National Symposium on Convergence of Chemistry and Materials, BITS Hyderabad, 17-18th December, 2019.

• **Oral Presentation** in Research award 2021-2022, Rasayanam at K V Rao scientific society- Electro-oxidation Reaction of Methanol over $La_{2-x}Sr_xNiO_{4+\delta}$ Ruddlesden-Popper Oxides.

• **Oral presentation** in International Conference on Chemistry and Allied sciences at Pingle College for Women, Warangal on 25-27th August 2022.

• **Poster presentation** at National Symposium on Convergence of Chemistry and Materials (CCM-2023) at BITS Pilani, Hyderabad campus. January 6-7th 2023.

• **Oral presentation** in Research award 2022 - 2023, Rasayanam at K V Rao scientific society - Role of Lattice Oxygen for Electro - oxidation Reaction of Methanol over Reducible $Ce_{1-x-y}Ni_xSr_yO_{2-\delta}$.

• **Poster presentation** at Indo- German workshop on Catalysis for Circular Economy Towards Sustainable Energy ($CatCE^2$) at BITS Pilani, Hyderabad Campus. 20th-23rd September 2023.

Biography of Meenu P C

Meenu P C completed her M. Phil in Chemistry from University of Kerala. She started her career as Project Assistant at University of Kerala. Later she has been pursuing her Ph.D. from Birla Institute of Technology and Science, Pilani, Hyderabad Campus under the supervision of Prof. Sounak Roy. Her research interest includes materials synthesis, electrochemistry and application towards environmental remediation.

Biography of Prof. Sounak Roy

Prof. Sounak Roy is serving as a professor in the Department of Chemistry in Birla Institute of Technology and Science, Pilani, Hyderabad Campus, India. He received his Ph.D. from the Indian Institute of Science, Bangalore in 2008. Later, he worked as a Post-Doctoral fellow at ETH Zurich Switzerland, University of Delaware and University of Pennsylvania. His research interests encompasses around solid state chemistry, energy and environmental catalysis, and understanding the reaction mechanism in light of structure-property relationship. He has published many research articles in national and international peer-reviewed journals. Currently, his group is engaged in the area of catalytic NO_x abatement, conversion of CO_2 to biofuels, water splitting and fuel cells.

Biography of Prof. Chanchal Chakraborty

Prof. Chanchal Chakraborty is working as Assistant Professor in the Department of Chemistry in Birla Institute of Technology and Science, Pilani, Hyderabad Campus, India. He received his Ph.D. from Indian Association for the Cultivation of Science, Kolkata. He worked as a Post-Doctoral fellow at National Institute of Materials Science (NIMS), Japan. His research interests include designing and fabricating polymer-based solid state electrochromic materials, structure-property relationships and developing self-powered electrochromic devices. Currently, his group is engaged in the area of electrocatalytic energy conversion and storage, fuel cells, and electrochromic devices.

Biography of Prof. Santanu Prasad Datta

Prof. Santanu Prasad Datta is working as an Associate Professor in the Department of Mechanical Engineering in Birla Institute of Technology and Science, Pilani, Hyderabad Campus, India. He received his Ph.D. from the Indian Institute of Technology, Kharagpur, India. His research interests include refrigeration and air-conditioning, hybrid vehicle thermal management, energy and environmental impact on society, compact heat exchangers, evaporative cooling, and experimental thermo- fluid science.